The Behaviour of Spent Nuclear Fuel in Wet Interim Storage

Elizabeth Anne Howett,
B.Sc.(Hons.), M.Sc

Lancaster University

Submitted to Lancaster University in partial fulfilment for the requirements for the degree of **Doctor of Philosophy**

23rd August 2019

Abstract

The UK is currently transitioning from a closed nuclear fuel cycle to an open cycle. During this transition, wet interim storage of AGR spent nuclear fuel in the UK will be extended until a long term disposal facility becomes operational. The current THORP Receipt and Storage pond is to be converted into an interim storage facility. Spent fuel will be more densely packed in this pond to accommodate current and future spent nuclear fuel. There will a resulting rise in pond water temperature from 24 °C to between 45-60 °C. This necessitates further research into the long term stability of stored spent nuclear fuel. This thesis describes the corrosion behaviour of AGR fuel cladding and AGR spent fuel under conditions relevant to the lengthened storage periods.

An electrochemical study of the corrosion behaviour of unirradiated and unsensitised 20/25/Nb stainless steel under alkaline spent nuclear fuel interim storage pond water conditions is presented. The results give preliminary indications that dosing pond water to a pH≃11.4, with an expected chloride concentration of ∼1 ppm and hydrogen peroxide concentration of ∼1 ppm, provides corrosion protection to unstressed cladding samples at the temperatures studied, 24 °C (current conditions), 45 °C (projected future pond temperature) and 60 °C (predicted peak operating conditions).

Analogues for fuel cladding affected by radiation induced sensitisation were developed by the National Nuclear Laboratory. For both heat treated 20/25/Nb stainless steel and heat treated 304H stainless steel, experiments provide initial evidence that for sensitised 20/25/Nb SS dosing pond water to a pH≃11.4, with an expected chloride concentration of ∼1 ppm and hydrogen peroxide concentration of ∼1 ppm, will lead to the passivation of the cladding surface for pond water temperatures between 24 and 60 °C. However general corrosion rates are higher

than those of the unsensitised counterparts and spent fuel stringers likely to be affected by RIS should be monitored more closely.

In the unlikely event that the fuel cladding is perforated, the fuel itself will be exposed to pond water. Thus in order to assist in the generation of a thorough safety case, the corrosion of pure UO_2 and AGR SIMFuels was studied under conditions typical of those found in interim spent fuel storage pond waters. With respect to the dissolution of spent fuel, it appears to be advantageous to dose the ponds to pH$\simeq$11.4. The alkaline conditions in the pond water suppress the dissolution as UO_2^{2+} which may otherwise occur. A U_3O_7/U_4O_9 oxide layer is predicted to be developing on the surface of the samples at the open circuit potentials, for the samples exposed to simulant pond water.

Acknowledgements

I would like to give a special thanks to my director of studies Prof Colin Boxall for all his help, support and encouragement throughout my PhD tenure. I would also like to thank my industrial supervisor Dr David Hambley at the National Nuclear Laboratory for his scientific guidance and valuable comments.

I am grateful to the DISTINCTIVE consortium and NDA focus group for providing the opportunity to discuss my project with other researchers and industry experts whose contributions were invaluable.

This thesis would not have been possible without the aid of the staff and students in the Engineering Department at Lancaster University. Thanks must be given for their technical and administrative support.

Thanks to my parents for their continued support both emotionally and financially through the entirety of my education and to my closest friends for their reassurance and constant banter.

Declaration

The work described in this thesis was conducted in the Department of Engineering, Lancaster University between October 2014 and August 2019. I, Elizabeth Anne Howett, declare that the work in this thesis has been done by myself and has not been submitted elsewhere for the award of any other degree unless stated otherwise.

Signature: _____

Elizabeth Howett

Contents

List of Figures

List of Tables

List of Abbreviations

AGR   Advanced Gas-cooled Reactor

CV   Cyclic Voltammetry

DL-EPR   Double Loop Electrochemical Potentiokinetic Reactivation

EIS   Electrochemical Impedance Spectroscopy

FWHM   Full width half maximum

GDF   Geological Disposal Facility

IGA   Intergranular Attack

IGSCC   Intergranular Stress Corrosion Cracking

LSV   Linear Sweep Voltammetry

LWR   Light Water Reactor

MOX   Mixed Oxide Fuel

NHE   Normal Hydrogen Electrode

NNL   National Nuclear Laboratory

OCP   Open Circuit Potential

PUREX   Plutonium Uranium Extraction

SCE   Saturated Calomel Electrode

SEM   Scanning Electron Microscope

SHE   Standard Hydrogen Electrode

SIMFuel   Simulant spent nuclear fuel

SNF   Spent Nuclear Fuel

SS   Stainless Steel

SCC   Stress Corrosion Cracking

THORP   Thermal Oxide Reprocessing Plant

WAGR   Windscale Advanced Gas Cooled Reactor

XPS   X-ray Photoelectron Spectroscopy

List of Symbols

β_A Anodic Tafel slope

β_C Cathodic Tafel slope

ϵ Dielectric constant of a material

ϵ_0 Permittivity of free space

ν Scan rate

A Area

C_{dl} Double layer capacitance

d Density

E Potential

E^0 Standard electrode potential

E_{corr} Corrosion Potential

E_{FB} Flat-band Potential

E_{ZC} Potential of zero current

EW Equivalent weight

F Faraday constant

i Current

i_{corr} Corrosion current

i_p Peak current

k_B The Boltzmann constant

n Number of electrons transfer in a reaction

N_D Dopant density

Q The reactant quotient

q Elementary charge

R The gas constant

R_{ct} Charge transfer resistance

R_p Polarisation resistance

R_s Solution resistance

T Temperature

Z Impedance

Z' Real component of impedance

Z'' Imaginary component of impedance

Z_0 Magnitude of impedance

Chapter 1

Introduction

1.1 Research Motivation and Project Objectives

The bulk of the UK's current operating fleet of nuclear reactors are of the Advanced Gas-cooled Reactor type (AGR). These were constructed during the 1970s and 1980s, and utilize a graphite moderator and CO_2 gas coolant. The fuel used in AGR reactors consists of low enriched UO_2 annular ceramic pellets, encased in a 20/25/Nb stainless steel cladding. Up until November 2018, the UK operated a closed fuel cycle where spent nuclear fuel (SNF) from these reactors underwent reprocessing at the Thermal Oxide Reprocessing Plant (THORP) in Sellafield, Cumbria. This resulted in a separated uranium product, which was sent to form new fuel and a separated plutonium product also available for fuel manufacturing. The highly active fission products and minor actinides formed in spent fuel were removed for disposal as high-level waste.

However, due to THORP's recent closure an open fuel cycle is now being adopted. The plan for current holdings of un-reprocessed SNF and SNF that will be discharged from AGRs in the future is to send it to a UK Geological Disposal Facility (GDF). The intention is for the GDF to start taking intermediate level waste (ILW) in the late 2030s, with spent fuel to follow around 2075. Until then UK AGR SNF will be kept in interim wet storage ponds at Sellafield, ultimately being consolidated into a single, long term storage pond.

There are currently three large ponds that house AGR fuel at Sellafield: the fuel handling plant, the AGR interim storage pond and the THORP Receipt and Storage (R & S) pond. Sellafield Ltd have decided to use existing facilities for AGR SNF storage until the GDF is ready for receipt rather than have a purpose built facility [1]. As such the THORP Receipt and Storage pond will be converted into an interim storage facility.

The spent fuel currently in the AGR interim storage ponds is stored in demineralized water with a chloride concentration typically < 0.1 ppm, a temperature of 24 °C and dosed with NaOH to achieve a pH of 11.4. Such an alkaline pH acts as a corrosion inhibitor for fuel cladding. This storage regime has been shown to be effective for the safe storage of AGR fuel for up to ∼25 years. Without such treatment, and specifically in the absence of NaOH as a corrosion inhibitor, cladding corrosion is observed - cladding perforation occurring within 1 - 2 years in the presence of 0.2 – 0.3 ppm chloride in inhibitor-free / undosed pond water [2]. For higher chloride concentrations of 1 - 10 ppm, perforation was observed after only 100 - 200 days [2].

Due to the success of the current AGR storage regime, the THORP Receipt and Storage pond will mirror the water chemistry of the current storage facility i.e. pH≃11.4. This pond currently has a pH≃8.5; again achieved by dosing the pond with NaOH. The pH will be gradually increased to 11.4 to accommodate the longer term storage of AGR SNF.

In order to accommodate all future AGR SNF arisings, until such time as a permanent disposal facility becomes available, a new racking system for the THORP Receipt and Storage pond has also been proposed. This new arrangement will mean that fuel will be packed closer together than previously, with a resultant increase in the temperature of pond water from the 24 °C that is currently maintained. Present assessments indicate that pond water temperature could rise to approximately 53 °C with an average temperature of close to 40 °C (Personal communications, D.I Hambley, NNL). Note that in this thesis

conservative temperatures approximately 5 °C greater than these values are considered - specifically 60 °C and 45 °C.

Further, current storage periods are typically less than 10 years, although this may extend to as long as 100 years depending on when a GDF will be ready to receive irradiated AGR fuel. It is therefore necessary to determine if AGR SNF can be stored safely, as it is currently, without significant corrosion of the cladding at these elevated temperatures and over this extended time scale.

During storage, only the AGR fuel cladding should be in direct contact with the pond water. However, if the cladding is breached due to stress corrosion cracking, an unexpected rise in chloride levels or in the unlikely event that the cladding has been damaged during dismantling of the fuel assembly, the ceramic UO_2 fuel itself will be exposed to the pond water. Therefore, it is essential to study both the evolution of the cladding and fuel surfaces under the pond water conditions described above.

The objective of this thesis is therefore to carry out an exhaustive electrochemical study of the corrosion behaviour of 20/25/Nb stainless steel and AGR SNF in alkaline spent nuclear fuel interim storage pond water conditions. The results of this work will contribute to the mechanistic understanding of the AGR cladding corrosion and corrosion inhibition, so contributing to the technical underpinning of Sellafield's extended interim storage safety case.

This thesis is structured as follows. This chapter (Chapter 1) gives an introduction to the nuclear fuel cycle, interim storage conditions and operating experiences. The design of AGR reactors including their fuel assembly is also discussed. Chemical and physical conditions affecting the corrosion behaviour of the stainless steel fuel cladding and UO_2 fuel are considered and the need for fuel and clad analogues highlighted.

Chapter 2 describes the materials investigated and outlines the experimental methods pertaining to the work undertaken towards establishing a thorough understanding of fuel cladding and fuel matrix corrosion in pond water

environments.

Chapters 3, 4 and 5 focus on fuel cladding corrosion in simulated pond water. Both unsensitised and heat treated stainless steels are examined and the results of rigorous electrochemical testing of 20/25/Nb SS and 304H SS, a cladding analogue, are presented. Chapter 6 deals with the corrosion behaviour of UO_2 and SIMFuels under conditions relevant to interim storage.

Finally, Chapter 7 summarises the main conclusions drawn from the research carried out and suggests possible future work.

1.2 The Nuclear Fuel Cycle

The nuclear fuel cycle refers to the collective processes involved in the generation of electricity from nuclear reactions. Figure 1.1 shows a schematic of the major activities in the nuclear fuel cycle, from mining of uranium ore to final disposal. The fuel cycle can be divided into two sections the front-end, pertaining to the production of fuel and the back-end, referring to waste management operations [3].
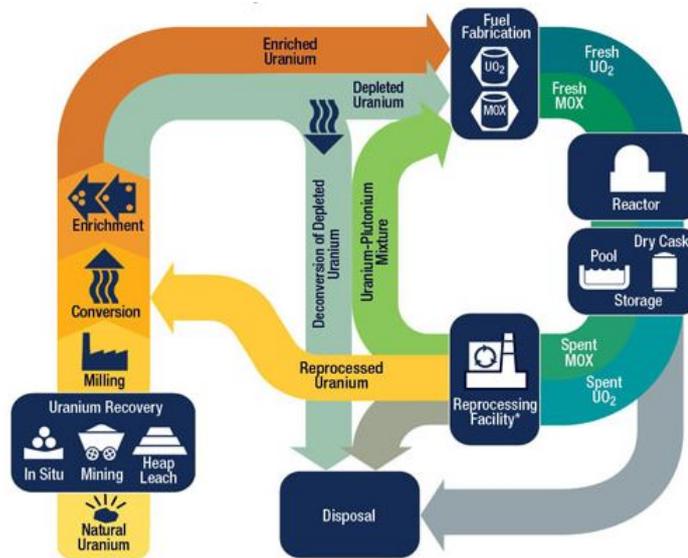
Figure 1.1: The Nuclear Fuel Cycle [4].

Globally, fissile Uranium-235 is currently the most important component of nuclear fuel for sustaining fission reactions. However, only approximately 0.7% of natural uranium is U-235, the rest consisting of predominantly non-fissile U-238. The majority of nuclear reactors (including AGRs) require fuel to be between 3% and 5% U-235 in order to compensate for the neutron absorption cross-section of the cladding and moderator (at least one neutron created during fission must cause another fission event in order to have a self-sustaining chain reaction). Therefore, it is necessary to enrich the natural uranium [5]. The current enrichment levels are designed to achieve target burn-ups that are most efficient for the utilities (i.e. allow utility companies meet their planned cycle length). Uranium is enriched

using gas phase centrifugation with separation being achieved by exploiting the difference in mass between, and thus centrifugal forces experienced by, the two principal isotopes of uranium (U-238 and U-235). This necessarily requires that uranium is in a gas phase.

The enrichment process is just one step in the wider fuel cycle. Referring to Figure 1.1, the front-end of the nuclear fuel cycle starts with the mining of uranium ore. This ore is then milled to produce U_3O_8 concentrate known as yellowcake [5]. Milling involves grinding the ore and leaching the resulting slurry with sulphuric acid. Subsequently the leached uranium is precipitated as U_3O_8, generally through the addition of ammonia to produce a wet concentrate of ammonium diuranate (ADU) and followed by drying and calcination.

The yellowcake is then converted into gaseous uranium hexafluoride, UF_6, suitable for enrichment. This conversion occurs in three steps: (i) purified U_3O_8 is mixed with hydrogen and nitrogen to give UO_3, (ii) the UO_3 is heated with hydrogen fluoride to produce UF_4 and (iii) UF_4 is heated with fluorine to produce UF_6. Enrichment is carried out in a gas centrifuge where the uranium isotopes are separated due to their mass difference, as described above. Enriched UF_6 is converted into UO_2 powder by either a dry (Integrated Dry Route Powder Process) or wet (ADU or AUC (ammonium uranyl carbonate)) process [6]. The UO_2 powder is then pressed and sintered into pellets [4]. The pellets are then arranged into fuel assemblies for LWRs or elements for AGRs (see Figure 1.2 below for the latter). Depending on the burnup, AGR fuel usually spends approximately 6-7 years in the reactor.
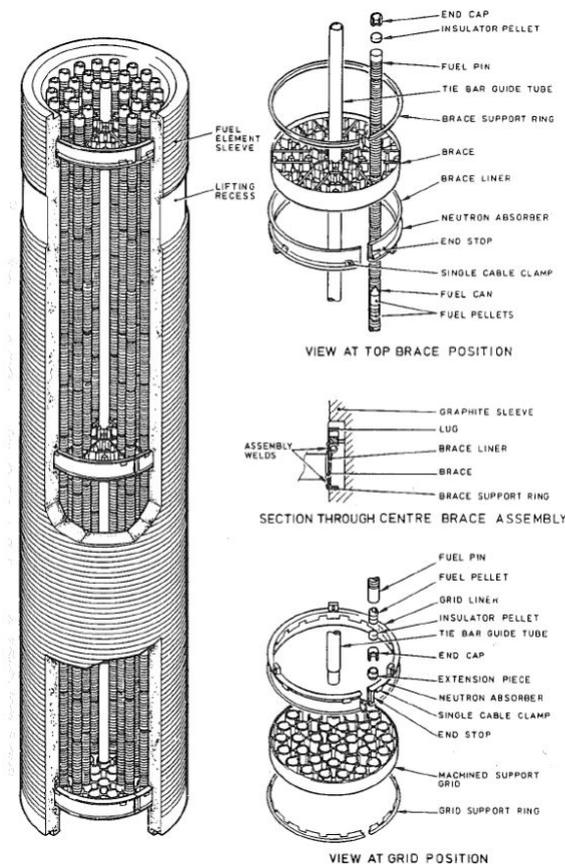
Figure 1.2: Commercial AGR fuel element [7].

The back-end of the fuel cycle starts when the spent fuel is removed from the reactor. The fuel assemblies/stringers are kept in storage ponds at the reactor site until the decay heat is significantly decreased and the fuel can be safely transported. The fuel is then transferred to interim storage facilities where it is held for a period of approximately 10 years to allow for a further reduction of heat and radioactivity before reprocessing or disposal.

In a closed fuel cycle, such as that which operated in the UK until November 2018, the spent nuclear fuel undergoes reprocessing and is then sent to be converted to UF_6 or mixed oxide fuel (MOX) and the cycle repeats. Reprocessing separates uranium and plutonium from fission products and minor actinides generated in the fuel during its time in the reactor [5]. In the UK, this separation is carried out with a liquid-liquid extraction technique known as PUREX - Plutonium Uranium Redox EXtraction. In the first instance, the spent fuel assemblies are dismantled, sheared and dissolved in nitric acid. Chemical separation is carried out through mixing

of the dissolved spent fuel with tributyl phosphate (TBP) in odourless kerosene. This involved conditioning of the U and Pu into their 6+ and 4+ oxidation states respectively which, due to their capacity to complex with TBP, enter the organic phase. The majority of the other constituents of the spent fuel stay in the aqueous nitric phase, so forming a so-called Highly Active Raffinate (HAR) waste stream. The Pu(IV) is then selectively reduced to Pu(III) which then partitions back to the aqueous phase due to its weaker affinity for complex formation with TBP in the organic phase [8]. The resulting separated Pu and U products can then be recycled and the waste products solidified (i.e. the HAR is vitrified) and sent for disposal [9]. It is noteworthy that, in the UK, the Pu has not been recycled into fuel since the Sellafield MOX plant closed in 2011.

The UK followed a closed fuel cycle until 2018. However as discussed in section 1.1 it is now transitioning to an open cycle. In an open fuel cycle there is no reprocessing step and the spent nuclear fuel goes straight for final disposal after a period of interim storage. In the UK, the proposed final disposal facility is a GDF. This involves burying the spent fuel and radioactive waste in a specially built facility deep underground. Assuming selection of an appropriate site the host rock should provide a natural geological barrier to radioactive release to the environment. However, there will also be engineered barriers to radioactive release, so providing resistance in depth. These include the waste/spent fuel container, the backfill around the containers and mass backfill of all shafts and tunnels [10]. For radioactive wastes as opposed to spent fuel, these also include the waste form itself and for spent fuel the fuel cladding itself can also act as a barrier to release. Site selection and safety case development are currently under way. Current predictions suggest the facility could be operational by the 2030s [10, 11].

1.3   Advanced Gas-Cooled Reactor Design

Fourteen of the 15 operational reactors in the UK are AGRs and nearly all of the spent fuel arisings generated in the UK going forward will be from this type

of reactor. It is therefore necessary to consider the effects that the fuel design will have on disposal strategy.

Figure 1.3 shows a schematic for the AGR design. AGRs use a graphite moderator and are cooled using carbon dioxide. The graphite moderator consists of graphite bricks with channels for fuel assemblies, control rods and coolant flow. Carbon dioxide coolant is circulated through the reactor core with an output temperature ∼650 °C before passing through the steam generator assembly.
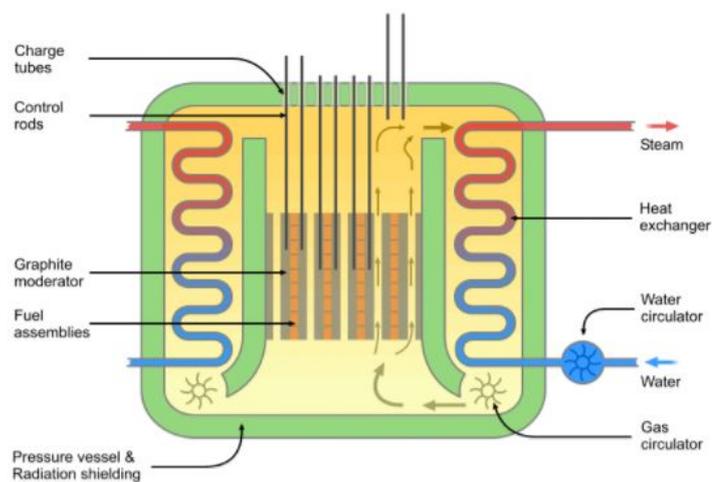
Figure 1.3: Schematic of the AGR design [12].

AGR fuel consists of low enriched UO_2 in the form of hollow cylindrical pellets (see Figure 1.4 (a)). Typical enrichment of UO_2 is between 2.7 and 3.4% and the average burn-up is around 30 GWd/tU [13] with a current maximum irradiation of 43 GWd/tU. However this may increase in the future, with a maximum possible burn-up of ≈50 GWd/tU [7].
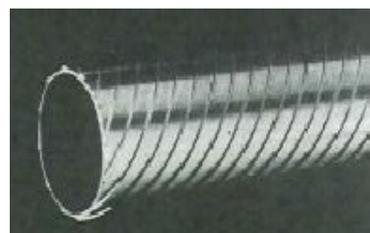
(a)   (b)

Figure 1.4: AGR components, (a) fuel pellets [14] and (b) fuel cladding [15].

The pellets are surrounded in a 0.37 mm thick alloyed stainless steel cladding

with machined helical ribs to enhance heat transfer between the clad and coolant gas (see Figure 1.4 (b)). AGR fuel cladding is a 20/25/Nb stainless steel, with a composition as given in Table 1.1. Fuel cladding pins are ≈ 1 m in length with an outer diameter of ≈ 15 mm and contain 64 fuel pellets [7]. They are filled with helium and sealed at both ends. There are 36 pins in a fuel element, with the support structure and fuel placement shown in Figure 1.2 in the previous section. Eight fuel elements are stacked together to make a fuel stringer and 332 fuel channels surrounded by a graphite lattice make up a single reactor core [7].

Steel	Cr	Ni	C	Mn	Si	Nb	P	N	Fe
20/25/Nb	19.33	24.05	0.062	0.79	0.58	0.56	0.014	0.01	Balance

Table 1.1: Composition (wt %) of 20/25/Nb stainless steel.

1.4   Interim Storage Conditions

As stated in section 1.2, AGR fuel usually spends approximately 6 - 7 years in the reactor. After this time it is removed and, in the first instance, spends a short period At the Reactor (AR) in ponds after which it is moved to interim storage Away From the Reactor (AFR). Table 1.2 shows typical water chemistries for AGR storage ponds. The AR ponds contain borated water (due to the twin abilities of boron to both inhibit corrosion and criticality, the latter by absorption of neutrons) and are dosed with sodium hydroxide to maintain a pH of ~7. In the case of the AFR ponds, given the longer time spent fuel spends in these ponds, demineralised water is used to improve visibility in the ponds. Use of demineralised water places two requirements on the ponds:

1. That it is continually replaced to maintain high purity levels and low concentrations of harmful ions (e.g actinide/lanthanide ions from damaged fuel or ionic products of clad dissolution). It is also especially important to maintain very low concentrations of chloride and sulphate in the ponds, both of which can accelerate clad corrosion.

2. That a larger amount of sodium hydroxide is added to act as a corrosion inhibitor for the stainless steel cladding, keeping the ponds at a pH of approximately 11.4.

Regular measurement of ion concentrations, pH, water conductivity and activity of the ponds allows for the water chemistry to be carefully controlled and so minimize clad corrosion. The latter is particularly important in order to keep radiation doses to facility operators as low as reasonably practicable. As described above, the cause of activity in pond water can vary from active corrosion products (e.g ^{59}Fe, ^{51}Cr) to fission products (if the fuel has been damaged). Ion exchangers and filters are used to lower water activity [16]. Table 1.2 gives typical parameters for the water chemistry of AR and AFR ponds for AGR spent fuel.

Fuel Type	AGR	
Pond Type	AR pond	AFR pond[a]
Fuel Container (if any)		Flooded containers
Cooling	Borated water	Demineralized water
pH	7	11.4
Chloride	0.5 ppm	<1.2 ppm
Sulphate	0.5 ppm	0.9 ppm
^{137}Cs	10MBq/m^3	29.4 MBq/m^3 [b]
Water Activity	40 MBq/m^3	29.5 MBq/m^3

[a]Purged ponds, no in-pond ion exchange systems. Ion exchange takes place downstream of the storage pond in a separate facility, prior to sea discharge
[b]Pond contains small quantities of fuel with perforated cladding

Table 1.2: Typical examples of water chemistry parameters in storage ponds for AGR spent fuels [16].

Temperatures in the AFR ponds are lower than those of the AR ponds as the decay heat has significantly decreased. Consequently, AFR interim storage ponds do not exceed 40°C under normal circumstances, having a typical temperature of $\sim 20 - 25$°C. Such a pond temperature range is beneficial as lower temperatures reduce corrosion rates and less activity is transferred from the fuel to the water [16].

Having described the general aqueous conditions of AR and AFR ponds, the

next section describes operating experience and observations of fuel and clad condition during storage.

1.5   Wet Storage Experience

AGR spent fuel has been successfully stored at Sellafield in ponds for periods as long as 23 years. In this section the operating experience in relation to fuel cladding and exposed uranium dioxide fuel surfaces in AFR ponds is described.

1.5.1   Fuel Cladding in Wet Storage

Unirradiated stainless steel is generally very resistant to corrosion. However, during its time in the reactor stainless steel may undergo thermal and radiation sensitisation leaving it more susceptible to corrosion. These effects are discussed in detail in section 1.9.4. Corrosion of stainless steel in an aqueous pond is affected by several factors (portrayed more explicitly in Figure 1.5), including but not limited to: (i) the quality of the metal, (ii) the stress level, (iii) the water conditions, eg. pH, impurities, temperature etc. and (iv) the layer formed on the surface of the cladding [17]. The specific corrosion mechanisms of stainless steel in aqueous environments are reviewed in section 1.8.

However, LWR SS cladding has been successfully stored for up to 28 years in demineralized water of pH$\simeq$6 without any signs of degradation. Indeed, uniform corrosion rates of LWR SS cladding is found to be between 2.5 and 3 μm/year [17].

For AGR cladding, calculations estimate that general corrosion rates of 0.5 μm/year would be expected for cladding stored in deionised water [18]. It is therefore, predicted that AGR fuel pins with intact cladding can survive a maximum storage period of $\sim$152 years in pond water at pH$\simeq$11.4, while leaving the cladding thick enough for safe mechanical handling. It must be noted that this model assumes that only uniform corrosion will result in failure i.e. assuming no localised attack.
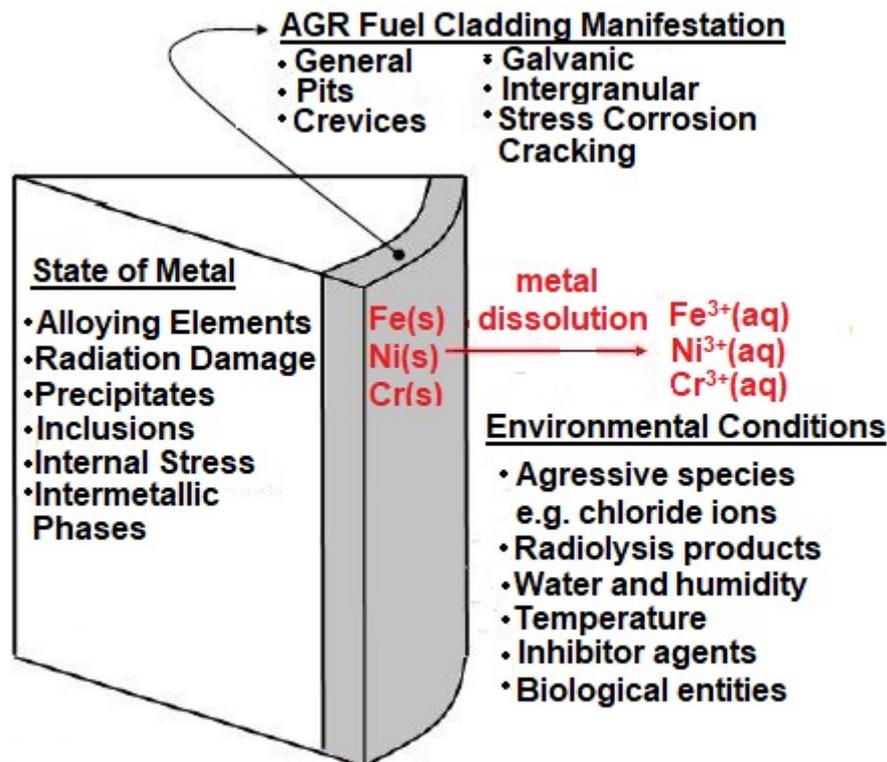
Figure 1.5: Factors effecting the corrosion of AGR fuel cladding [19]

Historically, intergranular stress corrosion cracking (IGSCC) is the primary mechanism of corrosion of irradiated cladding in reactor and in wet storage. This form of attack has been the cause of many past failures in AGR cladding [18]. However, since dosing the ponds with NaOH, cladding perforation has been successfully inhibited and no fuel failure has occurred since 1986 [18].

1.5.2 Uranium Dioxide in Wet Storage

The understanding of interactions between UO_2 with possible pond water compositions is one of the principal aims of this project. This section gives an overview of the operating experience of fuel rods with exposed UO_2 surfaces. A more in-depth discussion on the factors influencing UO_2 corrosion is found in section 1.10.

UO_2 pellets may become exposed to water in the pond if the cladding is (i) breached during handling, (ii) exposed in reactor or (iii) corroded through whilst in storage. Breaching can be in the form of pinhole defects, cracks, holes or broken

fuel rods [20]. Breached fuel is normally identified at the reactor and all the fuel from the suspect stringer is put into sealed bottles to prevent contamination of station ponds. Fuel that has failed in reactor is located by NNL at Windscale and the defective fuel is put into welded cans to protect the fuel from pond water. Fuel that is visibly damaged during dismantling is put into sealed cans that again prevent water access to the defective fuel. Fuel that is cut or punctured during PIE is put into welded cans to prevent water access. Nevertheless there is a possibility that some fuel with minor defects may reach the fuel ponds or that fuel can become exposed as a result of handling damage (to intact fuel cladding or sealed containers).

If the fuel rod is breached during handling (mechanism (i)), fission gases will be released into the environment and subsequent radioactive release into the storage ponds would be determined by the dissolution rate of the fuel matrix at the breach point. Likewise, if the fuel is punctured while it is in the reactor (mechanism (ii)), fission gases are discharged into the coolant and thus radioactive release into interim storage pond water would be non-gaseous and is controlled by dissolution of the bulk UO_2 matrix [21]. Further, any release of activity to pond via mechanism (iii) is kept between 3.7 and 37 Bq/ml through filtration and ion exchange.

Internationally, there have been a number of instances where defective fuel rods have resulted in the exposure of UO_2 fuel to pond water. A few are summarised below, especially with respect to effect on fuel integrity.

Electric Power Research Inst. and Atomic Energy of Canada Ltd conducted a wet storage study starting in 1977. CANDU spent fuel with exposed UO_2 pellets was examined after $\sim$21 years in demineralised water at pH$\simeq$7 [20]. Surface oxidation of the UO_2 was evident and the surface layer was determined to be $UO_3 \cdot yH_2O$ through x-ray photoelectron spectroscopy. Importantly the integrity of the fuel seemed unaffected. Through extrapolation of the results of these investigations it appears that water storage periods of greater than 50 years

could be safely achieved as long as the oxidation rate of UO_2 does not change significantly [22]. In addition to this, intentionally perforated CANDU fuel has been stored in this water composition for around 10 years with no signs of swelling or degradation around the hole [23].

British SGHWR (Steam Generating Heavy Water Reactor) spent fuel which had incurred cladding defects in-reactor, leaving some of the UO_2 surface exposed was studied after 9 years in demineralised water. It was found that the rods diameter had increased slightly in the vicinity of the defects and 5 ppm ^{137}Cs had been released over the 9 years by two defective rods. It was possible to measure the concentration of ^{137}Cs release as the fuel was stored in a sealed canister. There was no indication that any significant oxidation of the UO_2 had occurred [17,23].

PWR and BWR fuel bundles with defective rods stored in demineralised water at the Wiederaufarbeitungsanlage Karlsruhe (WAK) reprocessing plant pond, Germany, underwent regular visual assessments over a six year period in deionised water. Again, radioactivity release rates were very low and there was no apparent dissolution of the exposed UO_2 pellets [17,20].

The Oskarshamn ponds in Sweden house BWR spent fuel rods in demineralised water. In these ponds, radioactivity levels of $\sim$7.4 Bq/ml were found in ponds containing defective fuel rods whereas for ponds with non-defective fuel the activity was $\sim$0.37 Bq/ml [20]. The 20 fold increase in radioactivity levels in ponds containing exposed spent fuel suggests that radionuclides from the spent fuel are being released into the storage ponds.

In the USA, the General Electric Company, who have been storing defective fuel rods in demineralised water with a pH$\simeq$5, did not identify any fission gases in these ponds. Released radioactivity was kept between $\sim$3.7 - 14.8 Bq/ml with the aid of a purification process [17,20]. This indicates that there is a possible release of radionuclides through dissolution of the exposed UO_2 spent fuel; however, radioactivity and dose rates can be controlled.

From the operating experiences described above, it is evident that for UO_2

spent fuel exposed to storage pond water the integrity of the spent fuel is maintained over periods up to 21 years. Radioactive release rates are low and a $UO_3 \cdot yH_2O$ surface has been observed to form on the fuel surface. Thus, the formation of $UO_3 \cdot yH_2O$ appears to protect the spent fuel from dissolution.

The next section presents an exploration of key corrosion concepts in this context.

1.6   Electrochemical Corrosion Concepts

Corrosion of metal and metal oxides in aqueous solutions are electrochemical processes. Therefore, the corrosion behaviour of SNF and fuel cladding can be studied using electrochemical techniques. The following sections describe basic electrochemical corrosion concepts that are essential to understanding oxidation and dissolution mechanisms that may occur under wet interim storage conditions.

Corrosion occurs when a metal reacts with its environment causing destructive alterations to the metal's exposed surface. In aqueous solution, corrosion is an inherently electrochemical process and thus can be studied using electrochemical measurement techniques [24]. Electrochemical reactions involve the transfer of electrons to or from the environment to the metal. Oxidation is the loss of electrons and reduction is the gain of electrons. The surface at which oxidation occurs is called an anode and the surface where reduction takes place a cathode.

If a metal is oxidised it loses one or more electrons. An example of this type of process is the anodic oxidation of iron:

$$Fe(s) \longrightarrow Fe^{2+}(aq) + 2e^- \tag{1.1}$$

where (s), (aq), (l) and (g) refer to the solid, aqueous, liquid and gas phases respectively. Processes of the type shown in equation 1.1 are referred to as half-cell reactions. In the context of a general whole cell reaction, the electrons freed in the oxidation reaction must be consumed by a reduction reaction. In the specific

case of a corrosion process this usually occurs at a cathodic site on the metal surface [25]. For example, for the oxidation reaction of iron in equation 1.1, an associated reduction half reaction in the context of a corrosion process would be:

$$2H_2O(l) + O_2(g) + 4e^- \longrightarrow 4OH^-(aq) \qquad (1.2)$$

The total reaction is then written as:

$$2Fe(s) + 2H_2O(l) + O_2(g) \longrightarrow 2Fe^{2+}(aq) + 4OH^-(aq) \qquad (1.3)$$
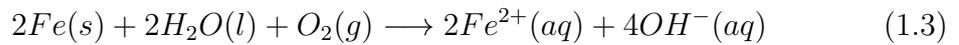
A schematic of these coupled reaction processes is shown in Figure 1.6.
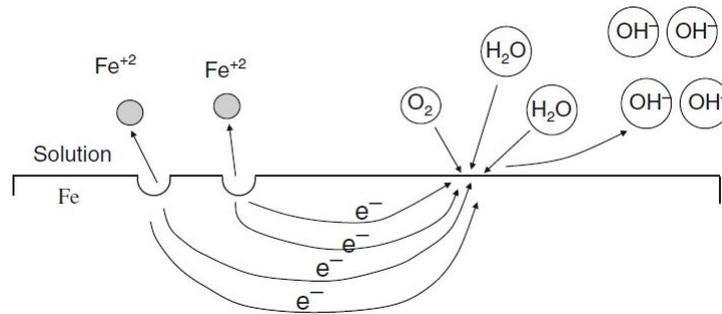
Figure 1.6: Coupled electrochemical reactions on an Fe surface in a neutral or alkaline solution [26].

Electrochemical reactions such as these occur at the surface of the metal until solution equilibrium is attained. This creates a potential difference across the interface, known as the electrode potential. The absolute potential of the metal with respect to solution is impossible to measure as it involves introducing a second electrode into the solution and thus a second electrode/electrolyte potential difference. The potential of the metal is thus measured with respect to an agreed standard electrode system, commonly referred to as a reference electrode [25]. For the studies conducted in this thesis a simple metal/metal chloride electrode system, namely Ag/AgCl, is used.

A simple relationship exists between the measured potential and the activity of the solution phase metal ions, the Nernst equation. This allows for the prediction of

the measured potential for a system based on the concentration of the electroactive metal ions therein and vice versa. It is given by:

$$E = E^0 - \frac{RT}{nF} lnQ \tag{1.4}$$

where E^0 is the standard potential for the reaction, Q is the reaction quotient, n is the number of electrons transferred in the reaction, F is Faraday's constant, R is the ideal gas constant and T is the temperature in Kelvin. For the general reaction $Ox + e^- \longrightarrow Red$, Q=Red/Ox.

Externally imposed changes in the electrical potential cause different anodic and cathodic reactions to occur.

The open circuit potential (OCP) is the resting electrode potential without any external potential perturbation in a solution. The value of this potential on a single electrode is determined by the equilibrium between the anodic and cathodic processes that might obtain on the electrode i.e. the potential adjusts to a value at which both the anodic and cathodic processes occur at the same rate. this value may be such that the rate of metal oxidation is very low (no or little corrosion) or very high (active corrosion) - so allowing for the prediction of expected corrosion behaviour of the metal surface in a specific environment. Specifically, this value can be compared to Pourbaix diagrams, see section 1.6.2 or voltammograms as described in the next section to identify the reactions occurring.

1.6.1   Voltammetry

Voltammetry involves sweeping the potential that has been deliberately applied to the electrode and measuring the resulting current. Altering the potential results in the oxidation/reduction of the electrode surface or the oxidation/reduction of electroactive ions in solution; the charge passed is directly related to the amount of oxidation/reduction by Faraday's first law of electrolysis [26]. In a typical linear sweep voltammagram of an electroactive

metal in aqueous solution, as current density increases so to does the corrosion rate.

Plotting the logarithm of the current density versus the applied potential is a typical way of presenting this data. These are known as polarisation curves or Tafel plots, an example of which is shown in Figure 1.7.
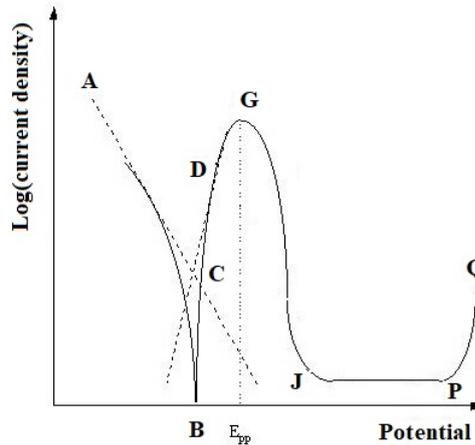
Figure 1.7: Schematic of a typical polarisation curve for a passivating metal [27].

The curve of Figure 1.7 has been broken down into a number of characteristic regions, AB, BC etc. and these can be described as follows. AB is a cathodic reaction, namely hydrogen evolution. The hydrogen evolution reaction is:

$$2H^+ + 2e^- \longrightarrow H_2 \tag{1.5}$$

At potential B the metal corrodes freely. This potential is called the corrosion potential. Corrosion of the metal occurs from B to G, this is the active region. As the potential increases from G to J a protective oxide film begins to grow on the surface of the electrode reducing the current density. The potential at G is referred to as the passivation potential, E_{pp}. Between J and P the current density remains at this passivation limited reduced current density. The associated corrosion rate is low so the surface is protected. This region is referred to as the passive region. In stainless steels the passive layer consists mainly of iron/chromium oxides and hydroxides (see section 1.6.2). At P the oxide layer

begins to breakdown intermittently and pitting is likely to occur. This potential is known as the critical pitting or breakdown potential (E_{pit}). As the potential increases further from P to Q dissolution of the passive layer takes place. This is called the transpassive region.

Importantly, in a corrosion context, polarisation curves can also be used to calculate corrosion rates of a metal in aqueous solution. It is necessary first to determine the corrosion current, I_{corr}, by extrapolating the linear portion of the anodic and cathodic reactions to the corrosion potential. This corresponds to the dashed lines AC and DC in Figure 1.7. If the anodic and cathodic Tafel lines have an equal gradient then I_{corr} is the current at the intersection of these lines. Alternatively, if the Tafel line gradients are unequal then polarisation resistance (R_p) can be used. The polarisation resistance is equivalent to the gradient of the line $\approx$ 10 to 20 mV either side of E_{corr} on a standard potential versus current plot. This may then be used along with the Tafel constants to calculate I_{corr}:

$$I_{corr} = \frac{\beta_A \beta_C}{2.3(\beta_A + \beta_C)} \frac{1}{R_p} \tag{1.6}$$

where β_A and β_C are the Tafel slopes of the anodic and cathodic reactions respectively.

I_{corr} can then be used to determine the corrosion rate using the following equation:

$$Corrosion\,rate = \frac{3272 I_{corr} EW}{dA} \tag{1.7}$$

where EW is the equivalent weight of the stainless steel in grams, d is the density in g/cm^{-3} and A is the exposed area in cm^2, giving the corrosion rate in mm/year.

1.6.2 Contribution of Alloying Elements to Corrosion Resistance

A widely used grade of stainless steel is austenitic stainless steel. These are non-magnetic steels that contain high levels of nickel and chromium and low levels

of carbon. They are known for their corrosion resistance and formability. AGR cladding material is an austenitic stainless steel.

Another way to interpret the influence of the major components of stainless steel on corrosion and passivity is the use of pH-potential diagrams, commonly known as Pourbaix diagrams. Pourbaix diagrams are electrode potential versus pH diagrams that encompass thermodynamic data for the system in question. For this work metal/water system diagrams are of most relevance. Based on physical experiments and thermodynamic modelling these diagrams show the expected oxidation state of the metal at a given potential and pH. This allows the identification of potential and pH ranges where soluble species or passive species are expected. It is important to remember that such diagrams are thermodynamic only and therefore the kinetic rates of formation of each species are not accounted for. Example Pourbaix diagrams for the main components of stainless steel, Fe, Cr and Ni, are shown in Figure 1.8 - Figure 1.10.

The dashed diagonal lines in these diagrams mark the potential-pH region of water stability. Between these lines water is thermodynamically stable. Above the upper line, water is thermodynamically unstable due to oxygen evolution. Below the lower line, water is thermodynamically unstable due to hydrogen gas evolution.

The dominant component of stainless steel is iron. As mentioned above, the Pourbaix diagram for the iron/water system is shown in Figure 1.8. At low pH values, soluble Fe^{2+} ($\sim$-0.6 to $\sim$0.8 V vs SHE) and Fe^{3+} ($\sim$0.8 to $\sim$2 V vs SHE) are formed whereas in alkaline conditions passive Fe_2O_3 is generated for potentials $\sim$-0.5 to $\sim$1 V vs SHE. This potential range is where the OCP of stainless steels is expected to lie under most conditions.
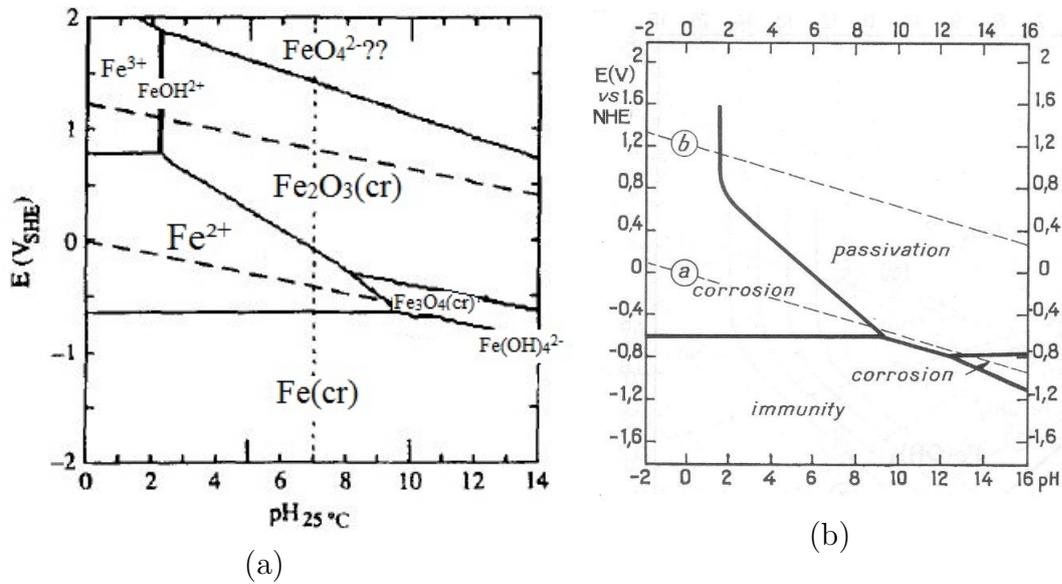
Figure 1.8: (a) Pourbaix diagram for iron at 10^{-6} mol dm^{-3} at 25 °C [28] and (b) theoretical conditions of corrosion, immunity and passivation of the iron/water system [29].

Chromium enhances the steels ability to resist oxidation and pitting corrosion. Concentrations greater than $\sim$12 wt% are necessary to give beneficial corrosion resistance. This resistance is derived from a strong protective Cr_2O_3 layer formed over wide potential ranges at pH>5, as seen in the Cr-H_2O Pourbaix diagram in Figure 1.9 [30]. At pH$\simeq$5 Cr_2O_3 is the dominent species between $\sim$-0.5 and $\sim$1 V vs SHE. However, this potential range shifts with pH and at pH$\simeq$14 Cr_2O_3 dominates between $\approx$-1.5 and $\approx$0 V vs SHE. The OCP of stainless steels may lie outside this predominance area in very alkaline conditions. In agreement with this, it has been observed that at pH>5 Cr makes up between 50 and 70% of the cation fraction of the protective oxide layer on stainless steels but as the pH increases Cr solubility increases and the fraction of Cr in the surface film decreases [31]. As stated above, protection is instead provided by the increased resistance of Fe_2O_3 at such pH values.

(a)

(b)
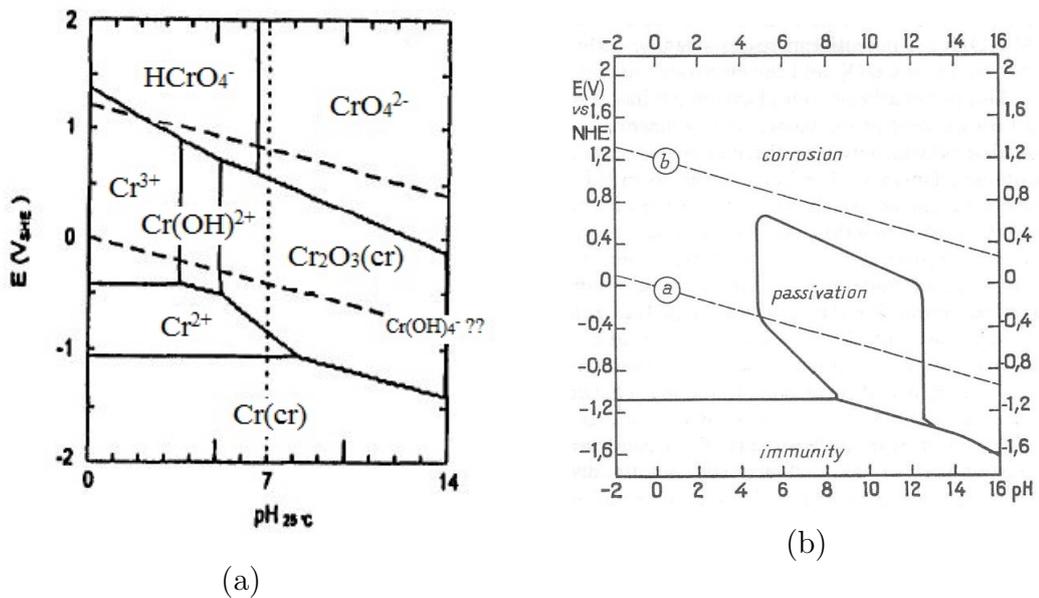
Figure 1.9: Pourbaix diagrams for chromium at 10^{-6} mol dm^{-3} at 25 and 100 °C [30] and (b) theoretical conditions of corrosion, immunity and passivation of the chromium/water system [29].

Austenitic stainless steels usually also contain 8-20 wt% nickel [24]. AGR cladding contains 25 wt% Ni. The addition of nickel to iron alloys increases the hardness and tensile strength. For stainless steels the presence of nickel causes the formation of a more formidable austenitic phase providing it high tensile strength at high temperatures (>500 °C) and increased toughness[1] [24]. Nickel also increases the resistance of the stainless steel to oxidation and corrosion [32]. For example, the addition of Ni decreases the chromium carbide formation in the steel [33], the formation of carbides being the cause of many historic failures in steels, see section 1.7.4 [34].

Oxidation of nickel occurs at a slower rate than that of iron and chromium. Therefore, Ni enrichment is not seen in the outer oxide layer on stainless steel but appears enriched in the metal at the metal/oxide interface [31]. Figure 1.10 shows the Pourbaix diagram for the Ni-H_2O system, for pH<8.5 Ni is in the form of soluble Ni^{2+} for potentials >-0.5 V vs SHE. At pH>8.5 Ni oxides oxidise to a passive β-Ni(OH)$_2$ at potentials >-0.7 V vs SHE, before transforming to a non-

---

[1]Toughness describes the ability of a metal to adsorb energy and deform plastically without rupturing.

passivating gamma phase oxide at potentials >0.6 V vs SHE (these potential values are pH dependant) [35].

(a)   (b)
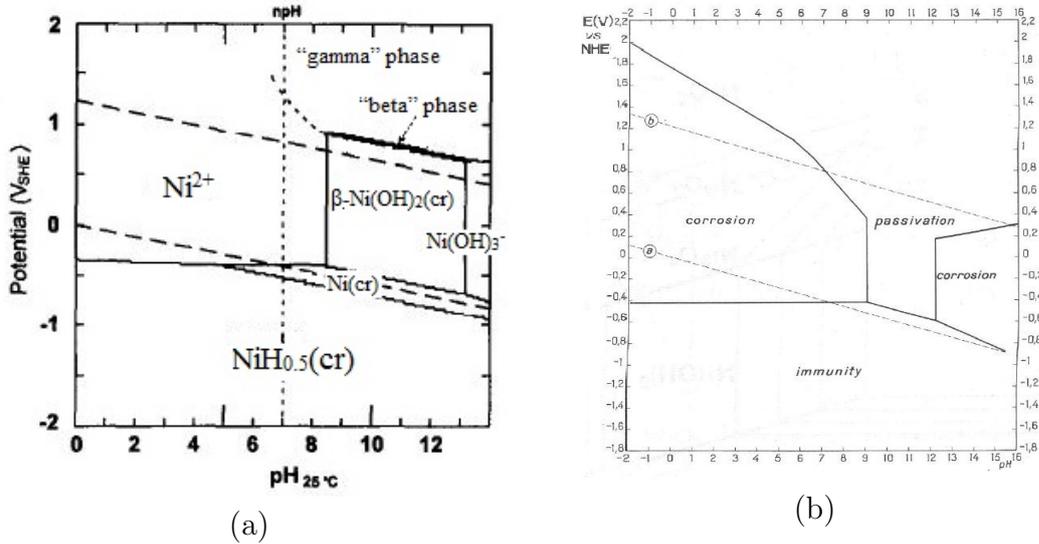
Figure 1.10: Pourbaix diagrams for nickel at 10^{-6} mol dm^{-3} at 25 °C [35] and (b) theoretical conditions of corrosion, immunity and passivation of the nickel/water system [29].

A comparison of the regions of passivity for iron, chromium and nickel is shown in Figure 1.11. At a storage pond water pH of 11.4, all three metals offer protection against corrosion by formation of a passive oxide layer provided the natural potential of the stainless steel in solution is between approximately -0.8 and 0.4 V vs NHE i.e the area of overlap in Figure 1.11. Cr alone extends passive protection to -1.3 V and Ni alone extends passivation to 0.8 V.
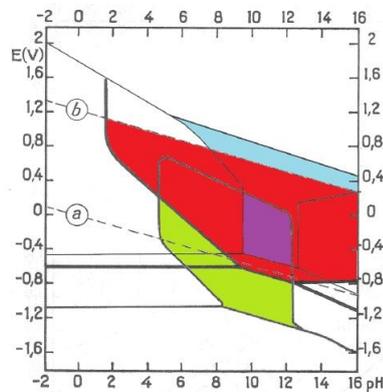
Figure 1.11: Overlay of theoretical conditions of passivation for iron (red), chromium (green) and nickel (blue), potential is referenced vs NHE. The purple area shows the potential-pH window where the passive region of the three metals overlap [36].

1.7   Corrosion Processes of Stainless Steels

One of the major aims of the work described in this thesis is to discern the corrosion behaviour of stainless steel fuel cladding under various aqueous solution conditions relevant to pond storage. It is therefore important to understand the fundamental physical mechanisms by which stainless steels corrode. Thus, this section describes the most common corrosion processes for stainless steels.

1.7.1   Uniform Corrosion

Uniform or general corrosion is when material loss occurs at approximately the same rate across the whole exposed surface [24,25,37–39]. From an electrochemical point of view, there is no favoured location for cathodic or anodic reactions, they occur randomly across the surface and alter positions with time as seen in Figure 1.12 [24, 37]. The result is that the metal thins evenly over the entire surface. Uniform corrosion is usually slow for stainless steel, especially in neutral to alkaline environments due to the presence of a passive surface film.
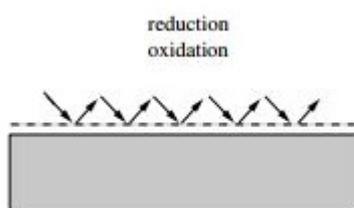
Figure 1.12: Uniform corrosion [25].

1.7.2   Pitting Corrosion

Pitting corrosion is an intense, extremely localised attack, giving rise to the formation of holes/pits, on the surface of a metal. Pits can be wide and shallow or narrow and deep [37]. They can penetrate quickly through the metal and are known to be initiators of stress corrosion cracking [40], which is discussed later in this section. In general pits are small, typically a few micrometres in diameter

but it is possible for them to grow to a few millimetres in diameter under suitably aggressive conditions [24] [25].

The initiation of pitting only occurs above a certain electrode potential, known as the pitting potential [39]. This potential depends on a variety of factors including, but not limited to: composition and microstructure of the metal; surface defects; the presence of non-metallic inclusions; composition of the electrolyte; temperature and convection conditions [25].

Generally, pitting is initiated by aggressive anions, often Cl^-, via breakdown of the passive film. Cl^- competes with OH^- and O_2 for adsorption sites in the passive layer. If the Cl^- is adsorbed, a metal-chloride (MCl) complex is generated instead of a passivating oxide. MCl only forms weak bonds with oxides, therefore film dissolution can more readily occur. Thus, the presence of Cl^- at the bare metal surface creates a break in passivation and the Cl^- attacks sites of least resistance causing the formation of a pit [41]. A pit may be metastable, where pit propagation shuts down after a few seconds [26] or stable, whereby an autocatalytic corrosion process begins [42].
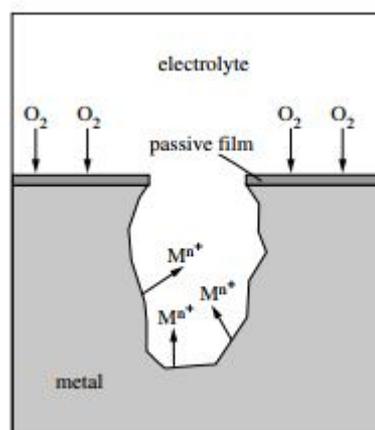
Figure 1.13: Partial reactions in pitting corrosion [25].

This autocatalytic process proceeds as follows. Firstly, anodic reactions inside the pit cause the ionisation of the metal. The so formed M^{n+} ions cause the migration of Cl^- into the pit to maintain charge balance. M^{n+} ions then react with Cl^- to form a metal chloride (MCl) [42] [43]. The MCl then reacts with

water to form hydrochloric acid causing the pH in the pit to drop significantly to pH$\simeq$2 [43]. Acidic conditions accelerate metal dissolution resulting in an excess of positive charge in the pit and Cl$^-$ ions are once again required to maintain the charge balance, hence creating an autocatalytic cycle. Dissolution at the base of the pit continues until the metal is perforated. Figure 1.13 shows partial reactions for the overall pitting corrosion process.

1.7.3 Crevice Corrosion

Crevice corrosion is another form of localised attack. It propagates with a similar mechanism to pitting corrosion but occurs in gaps between metal-metal interfaces, metal-non-metal interfaces or within cracks in a single metal [24]. A schematic of the mechanism for crevice corrosion is seen in Figure 1.14.
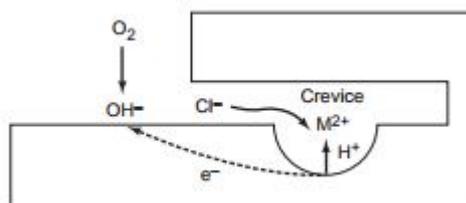
Figure 1.14: Schematic of crevice corrosion propagation mechanism [24].

The chemistry inside the crevice differs from that of the bulk electrolyte. Anodic metal dissolution occurs inside the crevice and cathodic reactions occur just outside the mouth of the crevice [39]. The cathodic reaction (equation 1.8), shown in Figure 1.14, consumes oxygen and causes the crevice to be depleted of O$_2$ [42] [39]. Within the crevice, metal cations M^{n+} are generated via the anodic reaction, leading to the migration of OH$^-$ and other solution anions such as Cl$^-$, from the bulk electrolyte into the crevice to maintain charge neutrality. As a consequence metal chloride can form and be subsequently hydrolysed to give a non-passivating metal hydroxide and free acid, reducing the pH inside the crevice. The combination of low pH, increased Cl$^-$ and O$_2$ depletion prevents passivation

within the crevice and dissolution of the metal proceeds uninhibited [42].

$$O_2 + 2H_2O + 4e^- \rightarrow 4OH^- \tag{1.8}$$
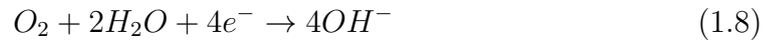
1.7.4   Intergranular Corrosion

Intergranular corrosion occurs at, or beside, the grain boundaries in a metal without any significant dissolution of the bulk grains. The electrochemical properties of the grain boundary can be different to those of the grain itself. This originates from a potential difference between the grain boundary and the bulk grain caused by precipitates or intermetallic phases that may form at the grain boundary [24] [25]. As such the exact propagation mechanism is sample dependent.
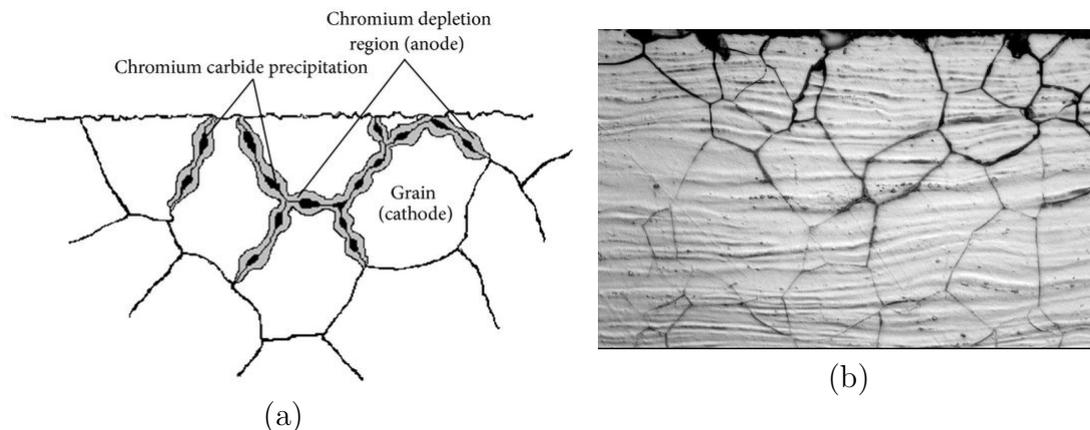
Figure 1.15: (a) Schematic representation of the carbide precipitation at grain boundaries in austenitic stainless steel [44] and (b) an SEM image of intergranular corrosion in austenitic stainless steel [45].

The most common cause of intergranular corrosion in stainless steels is chromium carbide precipitation at grain boundaries when exposed to elevated temperatures [24] [25]. This is shown schematically in Figure 1.15 (a). The formation of Cr carbides at grain boundaries leaves an area incapable of forming the Cr_2O_3 passive state (depletion region). This depletion zone offers a path of least corrosion resistance as the weaker Cr carbide deposits are attacked (acting as an anode) while cathodic processes occur at the Cr_2O_3 protected grain bulk.

The result is corrosion that propagates along the grain boundary as shown in Figure 1.15(b) [37]. Stabilisers such as niobium are often added to stainless steels to reduce Cr carbide formation and reduce susceptibility to intergranular corrosion, e.g. Nb locks up carbon by forming niobium carbides and therefore there is less available carbon in solid solution to form Cr carbides.

1.7.5 Stress Corrosion Cracking

Stress corrosion cracking (SCC) involves the joint action of a tensile stress and a corrosion process [39] [25]. The tensile stress may be due to an externally applied load or due to residual stresses caused by heat or mechanical treatment. There are two major stages to SCC, initiation and propagation. In the former, there are many ways in which a crack may be initiated, the most widely recognised phenomena include [37]: pitting or crevice corrosion; intergranular corrosion; hydrogen embrittlement; mechanical film rupture; and chemical breakdown of the passive film.

Figure 1.16 shows the propagation mechanism for SCC in an anion (e.g. Cl^-) containing solution. In a similar way to pitting and crevice corrosion the pH at the crack tip is significantly lower than that of the bulk electrolyte [26]. In the case of SCC the sides of the crack repassivate and corrosion occurs at the tip only. Thus, crack propagation occurs via the active dissolution of the crack tip only.
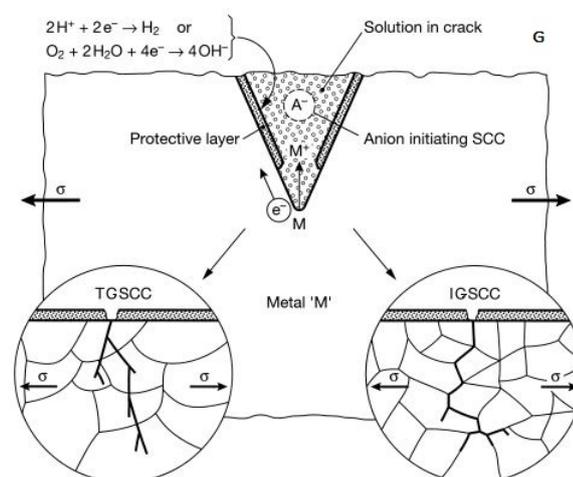
Figure 1.16: Mechanism for common SCC in an anion containing solution [46].

Cracks propagate perpendicularly to the applied stresses [24]. Cracks can be transgranular (TGSCC) or intergranular (IGSCC), as shown in Figure 1.16. Transgranular cracks propagate straight through the grains and intergranular cracks propagate along the grain boundaries [39].

1.8   Corrosion Behaviour of Stainless Steels under Conditions Relevant to Interim Storage

This section focuses on the key solution properties of pond storage water that are likely to effect the corrosion behaviour of stainless steels. The effects of varying chloride concentration, solution pH, solution temperature and radiolytically produced oxidants on corrosion susceptibility are discussed.

1.8.1   Effect of Chloride Concentration on the Corrosion Behaviour of Stainless Steels

The aggressive nature of Cl^- ions comes from their small ionic size, high charge density and high diffusivity [47]. Cl^- encourages the localised breakdown of Cr_2O_3 or Fe_2O_3 passive films i.e. the layer is penetrated rather than thinned. Cl^- ions migrate through the passive film by replacing the water and hydroxyl groups in the surface oxide layer on the stainless steel. As such, the mechanism of corrosion will be of the form of pitting, crevice or SCC, as discussed previously. While attack is usually localised, general stability of the passive layer may also be effected by incorporation of Cl^- [48].

As described in section 1.6.1, there is a critical potential above which the pitting/breakdown in the passive layer is likely to proceed. Increases in chloride concentration reduce this breakdown potential and the potential range over which the stainless steel is passive is significantly decreased. Alternatively, if the corrosion

potential lies in the transpassive region, uniform corrosion will dominate because the formation rate of soluble CrO_4^{2-} is greater than the rate of Cl^- absorption [49].

Mitigation of Cl^- induced pitting can be achieved by the addition of excess OH^- into the electrolyte. OH^- ions have a high affinity for the metal surface making them effective inhibitors of pitting [50]. The OH^- blocks the adsorption sites in the passive oxide film, inhibiting metal chloride formation. The higher the Cl^- concentration the more OH^- is required to block Cl^- adsorption and inhibit localised corrosion.

1.8.2 Effect of pH on the Corrosion Behaviour of Stainless Steels

In terms of electrochemical behaviour, described in section 1.6.1, altering the pH of the electrolyte can affect the current density, the passivation potential and the pitting potential. The most probable natural oxide phases formed on the surface of a stainless steel change with pH and this behaviour can be predicted and understood using Pourbaix diagrams, see section 1.6.2.

Acids tend to form soluble salts when interacting with metals causing increased dissolution of the surface. Fe dissolves rapidly in acidic solutions and if a passive film develops on a steel under such conditions it is enriched with Cr at the outer surface [51]. Indeed, mass loss has been observed in acidic solutions even at potentials where the Cr-rich passive layer is growing due to the selective dissolution of iron at low pH and potential [52].

If the pH is increased to more alkaline conditions there is a significant lowering of the disolution rates of stainless steels. Passive layers grown under alkaline conditions tend to be thicker and more stable [31]. Specifically, the stability of Fe and its oxides at alkaline pHs is greatly increased, resulting in the outer sections of the passive layer becoming enriched with Fe, Fe cations travelling through the passive film at greater rates than Cr cations [52]. As stated in the previous section the addition of OH^- ions to the solution is also an effective way of inhibiting

corrosion due to their affinity for the metal surface.
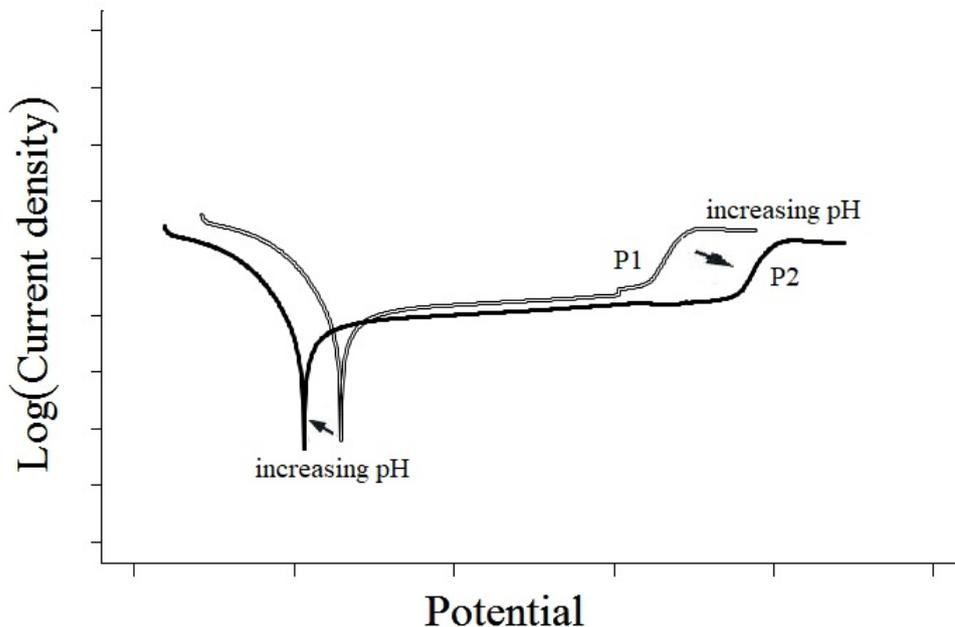
Figure 1.17: Tafel plot illustrating the effect of pH increasing from P1 to P2.

With regards to the voltammetric behaviour of stainless steel as a function of pH, Figure 1.17, both the current density in the passive range and the passivation potential are decreased with increased pH (i.e. towards alkaline conditions). As well as this the onset of transpassivity shifts to higher potentials increasing the potential range over which stainless steel are expected to be passive [52] [25] [53]. From the Nernst equation, the potential range over which the passive layer exists increases by $\approx$ 60 mV with each unit increase in pH [54]. Thus, the selection of an alkaline pH for the optimum storage of stainless steel clad appears justified and as noted previously AGR fuel pins have been held in storage ponds of pH$\simeq$11.4 without pin failure for periods as long as 20 years.

1.8.3   Effect of Electrolyte Temperature on the Corrosion Behaviour of Stainless Steels

For the majority of chemical reactions an increase in the rate of formation of reaction products is seen with increasing temperature. The general influence of

temperature on corrosion processes can be described by three effects: (i) changes in the dissociation of water, (ii) changes in the breakdown potential of the passive film and (iii) alterations in the physical and chemical properties of the passive film.

Considering first the effect of temperature on the dissociation of water, Table 1.3 shows the effect of varying temperature on the pH of a solution of pH=11.4 at 24 °C. The dissociation of water increases with temperature and results in consequent decrease in solution pH. As discussed in section 1.8.2 as the pH becomes more acidic the passive potential range of stainless steels is reduced.

Temperature /°C	Ionisation constant for water		pH
	$-\log_{10}K_w$	K_w	
0	14.9435	1.1389×10^{-15}	12.34
10	14.5346	2.9201×10^{-15}	11.93
20	14.1669	6.8093×10^{-15}	11.57
24	14	1×10^{-14}	11.4
30	13.833	1.4689×10^{-14}	11.23
40	13.5348	2.9188×10^{-14}	10.93
50	13.2617	5.4739×10^{-14}	10.66
60	13.0171	9.6139×10^{-14}	10.42
90	12.4	3.9811×10^{-13}	9.8
100	12.2899	5.13×10^{-13}	9.69

Table 1.3: Effect of temperature on the pH of a solution of pH=11.4 at 24°C [2].

Secondly, cathodic shifts in the breakdown potential are commonly observed with an increase in temperature [55] [56]. Increasing the temperature to 70°C can shift the breakdown potential by a approximately 200 mV [2]. It must be noted that this is a greater difference than would be expected solely as a result of the reduction in pH derived from increased water dissociation with increasing temperature (described above) [2]. Thus, the shift in breakdown potential most likely is also due to increased solubility of metal oxides at elevated temperatures. Figure 1.18 demonstrates the expected voltammetric shifts in behaviour of a typical steel under heating in an aqueous solution. As the temperature increases from T1 to T2 there is an increase in current density at all applied potentials, an anodic movement in the corrosion potential and a cathodic shift in the

breakdown potential, i.e. higher steel corrosion rates and a smaller passive window as temperature increases.

Finally, it has also been reported that the physical and chemical properties of the passive layer may be affected by temperature [55]. Thicker oxide layers may form but said layers have increased porosity and thus offer less corrosion resistance [57]. Thus, even under passive conditions general corrosion rates of stainless steel have been seen to increase progressively with temperature. For the temperatures of interest in this thesis, previous work by Langevoort *et al.* on 304 SS suggests that the passive layer may be slightly more enriched with Cr as temperature increases [58].
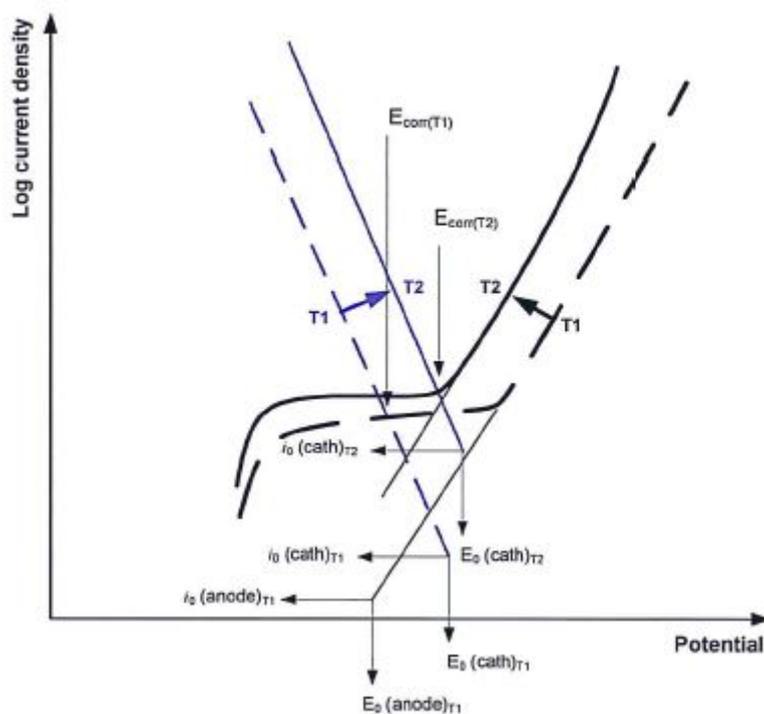
Figure 1.18: Tafel plot illustrating the effect of temperature increasing from T1 to T2 [2]. E_0 is the standard electrode potential, i_0 is the current associated with the standard electrode potential and E_{corr} is the corrosion potential

1.8.4   Effect of Radiolysis Products on the Corrosion Behaviour of Stainless Steels

Due to the presence of a radiation field generated by the SNF, radiolysis of the pond water will occur during fuel storage. Both molecular and radical products

are formed during radiolysis, that can be oxidising or reducing. These include H_2, H_2O_2, O_2^-, $OH^\bullet$, e_{aq}^-, $HO_2^\bullet$ and $H^\bullet$ [59]. The concentrations of the radiolysis products in water depends on the type of radiation emitted, the amount of energy deposited, the solution pH, the temperature of the solution and the presence of other ions in solution. Radiolysis products can interact between themselves or become involved in electrochemical reactions resulting in corrosion enhancement [60]. Figure 1.19 shows the dose rates, as a function of time, in the water layer in contact with a CANDU fuel bundle with a burnup of 220 MWh/kgU.
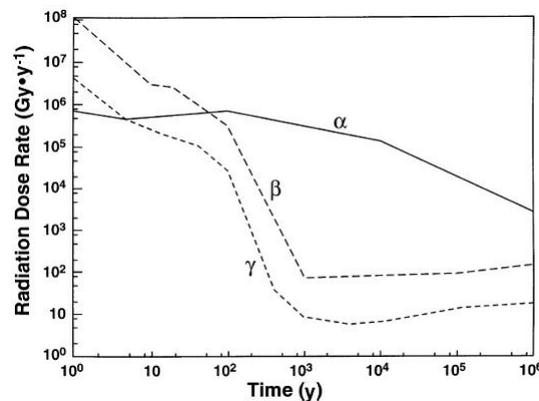
Figure 1.19: Alpha (α), beta (β) and gamma (γ) dose rates in the water layer in contact with a CANDU fuel bundle with a burnup of 220 MWh/kgU [61].

From Figure 1.19 it can be seen that β and γ are the most dominant types of radiation emitted by SNF for approximately the first 10 years after removal from the reactor. α, β and γ contribute similar dose rates up to 100 years, after which α radiation alone begins to dominate. For intact cladding, γ radiation would be expected to be the main contributor to radiolysis at the surface of the fuel pin, as α and β particles are unlikely to penetrate the exterior clad. However, if perforation of the cladding occurs α radiation will have the highest impact at the UO_2 surface. In this case all of the α particles energy is transferred to a thin layer of solution surrounding the UO_2 fuel pellets [62].

	Gamma	Alpha
Species	Water	
H_2O_2	0.7	0.98
$\bullet HO_2$	0	0.22
H_2	0.45	1.3
$\bullet H$	0.55	0.21
e_{aq}	2.65	0.06
$\bullet OH$	2.7	0.25
H^+	2.65	0.06
H_2O	-4.1	-2.65

Table 1.4: Gamma and alpha particle G-values in neutral water [63].

The yield of each radiolysis product can be expressed using G-values. A G-value is the number of moles produced (or consumed) per 100 eV of energy deposited. Table 1.4 shows the G-values for irradiated water. From Table 1.4 it can be seen that for the lower energy transfers associated with γ radiation (and potentially β) more radicals than molecules are produced in water containing no chloride, in particular $\bullet OH$. The opposite is true for higher energy transfers via α radiation. This is because for α radiation the density of ionizations is higher and radicals tend to recombine to form molecules (i.e. the radicals formed are closer together and therefore more likely to react) [64].

As free radicals have a shorter lifetime in aqueous solutions than molecules, the time it would take for radicals to diffuse to the fuel surface could be greater than their half-lives in solution [65]. Thus, H_2O_2 is considered to be the most significant oxidising agent generated during radiolysis [66].

Generally, the γ radiation induced generation of H_2O_2 decreases as pH and temperature increase. Said reduction at higher temperatures is due to an increased rate of relaxation (decombination) of the ion-pairs generated along the track of ionising radiation [67]. Increasing the pH of a solution reduces H_2O_2 generation slightly due to the interaction of $\bullet OH$ radicals with hydroxide ions, equation 1.9. Since it is generally accepted that the majority of H_2O_2 production occurs via equation 1.10, if some of the $\bullet OH$ radials are consumed by their reaction with

OH^- there will be a resultant decrease in peroxide formation [68].

$$\bullet OH + OH^- \rightleftharpoons O^{\bullet -} + H_2O \qquad (1.9)$$

$$\bullet OH + \bullet OH \longrightarrow H_2O_2 \qquad (1.10)$$
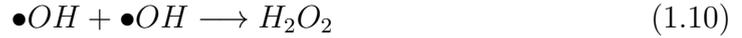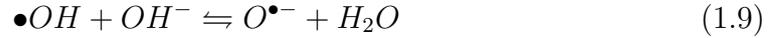
Even considering the above decrease in H_2O_2 production in alkaline conditions, H_2O_2 produced through radiolysis is still likely to be the most dominant oxidising species in interim storage pond waters. Thus, the rest of this section will solely focus on the effect H_2O_2 has on the corrosion behaviour of stainless steel. Decomposition of H_2O_2 involves the coupling of the following redox half-reactions [69]:

$$H_2O_2 + 2e^- \longrightarrow 2OH^- \qquad (1.11)$$

$$H_2O_2 \longrightarrow O_2 + 2H^+ + 2e^- \qquad (1.12)$$
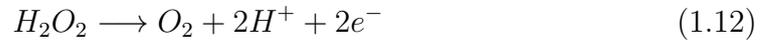
The rate of H_2O_2 decomposition is affected by pH, temperature and presence of a suitably catalytic surface. Considering pH first, H_2O_2 is more unstable in alkaline solutions, however the decomposition rate appears to be slow enough for an adsorbed hydroxyl radical layer to form at a metal surface, even if the bulk H_2O_2 concentration is suppressed [2]. In alkaline solutions the decomposition of H_2O_2 occurs via the following reaction [70]:

$$H_2O_2 + OH^- + 2e^- \longrightarrow 3OH^- \qquad (1.13)$$

H_2O_2 in neutral/alkaline solution oxidises the Fe of stainless steel via the following reaction to produce a partially protective iron oxide [71]:

$$2Fe^{2+} + H_2O_2 + 4OH^- \longrightarrow 2Fe(OH)_3 (precipitate) \qquad (1.14)$$

Fe also catalyses H_2O_2 decomposition [72]. In acidic solutions the decomposition of H_2O_2 in the presence of Fe^{2+} occurs via Fenton reactions (equations 1.15 - 1.17) which also cause further rapid dissolution of the Fe metal surface due to the production of strongly oxidising radicals [73].

$$Fe^{2+} + H_2O_2 \longrightarrow Fe^{3+} + \bullet OH + OH^- \tag{1.15}$$

$$Fe^{3+} + H_2O_2 \longrightarrow Fe^{2+} + \bullet OOH + H^+ \tag{1.16}$$

$$Fe^{2+} + 2 \bullet OH \longrightarrow Fe^{2+} + 2OH^- \tag{1.17}$$
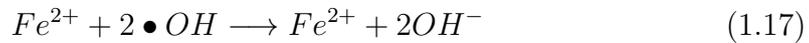
For 304 SS, Song *et al.* found that in neutral 0.02 mol dm^{-3} NaCl solutions, H_2O_2 decreases pitting potential (i.e. moves it to more cathodic potentials) and increases passivation potential (i.e. moves it to more anodic potentials), leading to a reduction in the passive potential range [74]. In solution of pH$\simeq$10 Sharma *et al.* found that for a range of stainless steels increases in peroxide concentrations (300 to 600 ppm) resulted in increased corrosion rates and increased localised attack [75]. Therefore it appears that corrosion resistance is decreased in the presence of H_2O_2. However, at higher pH values the impact of H_2O_2 is likely to be reduced due to the accelerated decomposition of H_2O_2.

Turning now to the effect of temperature, as temperature increases the solubility of O_2 in water decreases while the inverse is true for H_2O_2 [2,76]. Also, increasing temperature accelerates H_2O_2 decomposition and bulk H_2O_2 concentrations are expected to decrease as a result. Research on stainless steel corrosion by action of H_2O_2 at elevated temperatures is limited to studies conducted on 304 SS in BWR conditions of high temperature ($\sim$285 °C) and pressure. In this environment the thickness of oxide films decrease with increasing H_2O_2 concentrations and increase with increasing O_2 concentration. Oxide layers consist of a α-Fe_2O_3 outer layer and Ni rich Fe_3O_4 spinel inner layer in H_2O_2 solutions [77]. Higher dissolution rates are observed in H_2O_2 solutions and open circuit potentials are greater in the presence of H_2O_2 than in O_2 [78].

Finally, there appears to be a limited concentration range of H_2O_2 outside which the concentration is unimportant with regards to the corrosion behaviour of stainless steel. Below this critical range O_2 reactions dominate and above this concentration range the surface is saturated with OH^-. For 304 SS Whillock found the upper limit is 0.5 mg/L [79] and Song found the lower limit to be 0.2 mg/L [74].

1.9 AGR Specific Corrosion Behaviour

The previous section gave an overview of the corrosion behaviour of stainless steel in environments relevant to wet interim storage. This section reviews the corrosion behaviour of AGR fuel clad stainless steel specifically.

As stated in section 1.3 AGR cladding is made of 20/25/Nb SS, the dominant components being approximately 20 wt% Cr, 25 wt% Ni and 54 wt% Fe, as shown in Table 1.5. The effects of the addition of Cr and Ni to Fe were discussed in section 1.6.2. Particularly, the high Ni content is necessary to the protect the stainless steel against corrosion at elevated reactor temperatures (exit temperatures $\sim$650°C).

	Cr	Ni	C	Mn	Si	Nb	P	N	Fe
20/25/Nb	19.33	24.05	0.062	0.79	0.58	0.56	0.014	0.01	Balance

Table 1.5: Composition (wt %) of 20/25/Nb stainless steel.

An important addition to 20/25/Nb stainless steel is the 0.56 wt% niobium, which is added to stabilise carbides. Nb bonds with carbon to form NbC precipitates which are very stable and difficult to dissolve within the steel matrix. This limits the generation of chromium carbides at the grain boundaries, making sure the chromium is instead available to offer corrosion resistance against intergranular attack [32]. Furthermore, Nb also limits the effect of radiation induced segregation (discussed later in section 1.9.4).

Although there is limited published work on AGR specific cladding corrosion, the following subsections describe the available information relevant to corrosion in interim storage conditions. The effects of irradiation on cladding structure and

behaviour are also described and along with the criteria for successfully producing a suitable spent clad analogue through non-active techniques.

1.9.1 Effect of Chloride on the Corrosion Behaviour of 20/25/Nb Stainless Steel

Anwyl *et al.* found that for unsensitised 20/25/Nb SS in neutral electrolyte solutions containing increasing amounts of chloride there is a shift in the pitting/breakdown potential to more negative potentials [80], reducing the window of passivity. This is consistent with the behaviour expected for typical stainless steels, highlighted in section 1.8.1.

Phuah [19] found that for 20/25/Nb SS in a chloride environment, corrosion is often initiated at NbC precipitate sites. There are four main corrosion mechanisms for this:

1. **Galvanic coupling at NbC precipitates**: NbC precipitates act as cathodes in galvanic dissolution of the metal region around the precipitates;

2. **Pitting corrosion:** The presence of chloride ions can result in pitting corrosion preferentially occurring at a vulnerable area adjacent to NbC precipitates (the mechanism of which is described in 1.7.2);

3. **Formation of lacy covers:** Formation of a porous metallic cover over a hemispherical pit. Such a feature prevents repassivation of the metal surface and inhibits the internal chloride environment from diffusing into bulk solution (a similar process to crevice corrosion). This feature is known as a lacy corrosion cover [81].

4. **Heat induced stress as a result of growth of NbC precipitates:** When the stainless steel was heated during casting or in reactor NbC particles may grow in size. This induces regions of high stress in the steel and results in increased corrosion susceptibility in these regions.

Finally, intergranular SCC is known to occur in irradiated AGR fuel cladding during pond storage in the presence of Cl^- [82]. The mechanism for SCC is explained in detail in section 1.7.5.

1.9.2   Effect of Wet Storage Temperature on the Corrosion Behaviour of 20/25/Nb Stainless Steel

There is limited experimental data on the temperature dependence of the corrosion of AGR cladding. Those studies that are available in the open literature, have been carried out at elevated temperature in order to artifically accelerate corrosion processes. Marsh and Cavell [83] studied WAGR (Windscale Advanced Gas Cooled Reactor) pins in aqueous solution at 60 °C with 10 ppm $[Cl^-]$ and 200 ppm $[OH^-]$, the pH was 12.1 at 24 °C (before heating the solution). Under such conditions, there were no pin failures over a 8400 hour immersion period. However, intergranular attack was observed in pins that were irradiated at temperatures between 350 and 520 °C, where radiation induced segregation is expected. This phenomena is addressed later in this chapter, section 1.9.4. Pins irradiated outside this temperature range exhibited no signs of intergranular attack. Penetration of the cladding was observed for all pins in the absence of OH^- [2] [83].

1.9.3   Effect of Radiolysis Products on the Corrosion Behaviour of 20/25/Nb Stainless Steel

Anwyl *et al.* [80] also performed electrochemical experiments on 20/25/Nb SS in anoxic evaporite simulant groundwater containing 10 μmol dm^{-3} H_2O_2, pH$\simeq$6.8. The presence of H_2O_2 causes an increase in the OCP of the stainless steel and a decrease in the passive potential window. However, the addition of H_2O_2 appears to result in the growth of a thicker oxide layer in the passive region compared to in the absence of peroxide, indicated by decreased current density for this range of potentials in the presence of peroxide. Thus, H_2O_2 could provide additional

corrosion protection to 20/25/Nb SS. The shortened potential passive range is the same effect observed for standard stainless steels in aqueous H_2O_2 solutions, discussed in section 1.8.4.

1.9.4   Radiation Induced Segregation in Stainless Steels

Irradiating stainless steels, in a reactor for example, produces a flux of point defects, vacancies or interstitials, in the steel [84] [85] [86]. The number of point defects created is far above equilibrium concentrations. At high temperatures, these point defects preferentially migrate to low energy sites such as grain boundaries and other defect or dislocation sites. Radiation induced segregation (RIS) occurs because each alloying element travels at a different rate in response to the defect flux [84]. Thus, interactions of these species with the defect flux results in areas that are enriched or depleted of certain elements. Note that at very high temperatures (>520 °C for AGR cladding) the rate of diffusion of all alloying elements is sufficiently high that the concentration differences are small. However, there are intermediate temperatures (350 - 520 °C for AGR cladding) where the differences in vacancy and elemental diffusion rates are sufficiently different that significant variations in concentrations occur near grain boundaries. As such, the result is that the physical, mechanical and chemical properties of stainless steels can be critically degraded by RIS [87]. For austenitic Fe-Ni-Cr stainless steels RIS causes the depletion of Cr and the enrichment of Ni at grain boundaries [86].

Indeed, for AGR cladding RIS can reduce the Cr concentration at the grain boundaries to as low as 10% [82, 88]. The grain boundary of an AGR fuel pin affected by RIS is seen in Figure 1.20. AGR fuel pins operating between 350 and 520 °C undergo RIS. This phenomenon has a peak impact at ≈ 420 °C [89]. Not all fuel elements run in this temperature range so RIS is only expected for a small fraction of fuel elements.
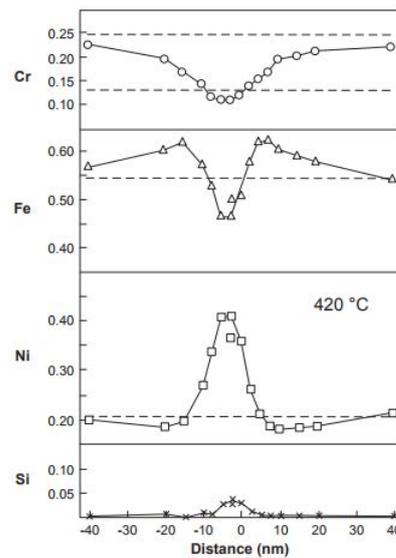
Figure 1.20: Grain boundary compositional profiles, wt%, for portion of AGR fuel pin irradiated to ≈20 GWd/te at a cladding temperature of 420 °C [90].

As a result of RIS, affected pins are more susceptible to corrosion during post-irradiation storage. These fuel pins corrode through intergranular attack leading to either intergranular stress corrosion cracking or a network of loose grains [82]. Figure 1.21 shows both forms of intergranular corrosion on RIS affected AGR cladding.
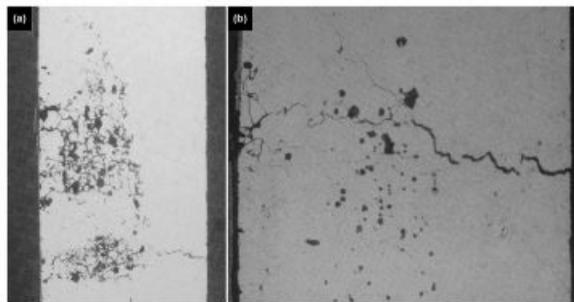
Figure 1.21: Typical morphology of IGA in RIS affected AGR cladding, (a) a network of loose grains and (b) intergranular attack [91].

Anodic polarisation curves for RIS-affected grain boundaries differ from those of the bulk metal. The breakdown potential of RIS-affected grain boundaries is significantly lower and in neutral solutions is approximately the same as the free corrosion potential, see Figure 1.22 [2]. Intergranular attack thus proceeds easily, as evidenced by previous imaging of fuel pins in historic pond water storage (Figure

1.21) [91].
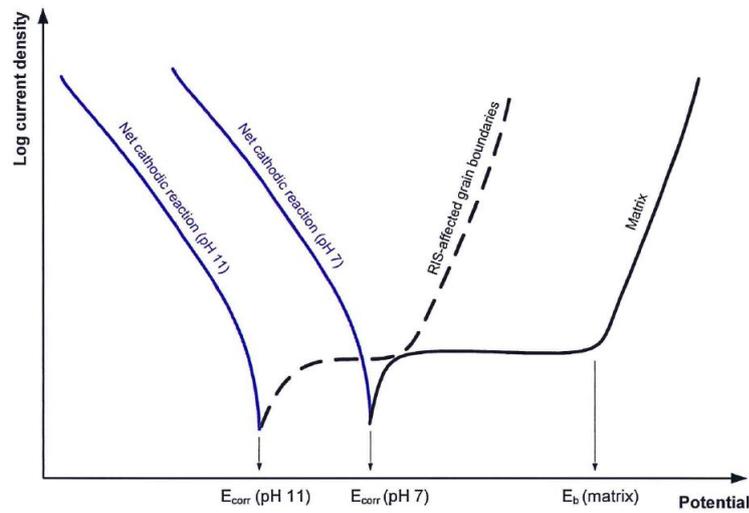
Figure 1.22: Polarisation curves for RIS-affected stainless steel in solutions of two different pH values [2]

In order to protect against such attack the free corrosion potential could be shifted in the cathodic direction, making passivation a possibility. As described previously, dosing the ponds with NaOH decreases the corrosion potential, this allows passivation of RIS sensitised material. This is the primary reason for the alkaline conditions maintained in interim storage ponds.

1.9.5 Thermal Treatment of Stainless Steels

For research purposes, stainless steels are thermally aged in an attempt to replicate the effect of RIS without the experimental difficulties associated with irradiated materials. Some stainless steels become sensitised i.e. grain boundary chromium concentrations dip below 12%, when heated in the temperature range 550 - 800 °C [92]. In this temperature range chromium rich carbides precipitate along the grain boundaries leaving the grain boundaries depleted of Cr and thus more susceptible to corrosion [93]. The level of Cr depletion at the grain boundary is comparable to that seen for RIS affected steels and thus corrosion is expected to proceed in a relatively similar manner. The specific thermal treatments used for samples investigated in this thesis can be found in section 2.1.4. More information

on the scientific basis for the thermal treatment process can be found in reference [94].

However, it must be recognised that Cr profiles of irradiated and thermally sensitised materials will differ. In Nb stabilised stainless steels, such as AGR fuel cladding, carbon forms precipitates with Nb during manufacture. Therefore there is limited free carbon in solid solution. NbC will only dissolve if the temperature is between 1093-1179°C [95, 96], which is outside the range of where RIS will occur and reactor operating conditions. There is likely to be $\leq 0.0075\%$ free carbon present and when aged at 550 °C, providing equilibrium is achieved, Cr concentrations at the grain boundary will drop to a $\sim 15\%$ if maximum $Cr_{23}C_6$ precipitation occurs [97]. Hence significant chromium carbide precipitation is unlikely to occur in irradiated AGR cladding compared to heat treated analogues where chromium carbide precipitation will be the cause of Cr depletion. Indeed precipitates formed in RIS-affected 20/25/Nb SS tend to be Ni and Si rich, with any chromium carbide precipitates observed typically formed due to carbon pick-up from the CO_2 coolant in reactor [88]. Another difference between thermally aged and RIS-affected 20/25/Nb SS is that enrichment of Si at the grain boundaries is only seen for irradiated cladding. Si is added to SS to improve oxidation resistance. However, grain boundaries with Si enrichment have been associated with greater spatial depth of Cr depletion, so it is possible that these areas have greater corrosion susceptibility despite Cr depletion not reaching a critical level (<12 wt%) [90]. Whether this has a significant impact when comparing corrosion resistance of heat treated samples and irradiated 20/25/Nb SS is unclear.

1.9.6   AGR Fuel Cladding Analogues

As discussed in section 1.9.4 fuel cladding becomes RIS sensitised during its time in the reactor. Because of this the microstructure of irradiated cladding and fresh cladding will differ. Hence, the National Nuclear Laboratory (NNL) have

been developing non-radioactive SNF fuel cladding analogues. Requirements for an appropriate analogue have been set based on previous interim storage experience, and are as follows [82]:

1. The sample must be susceptible to IGSCC

2. Initiation and propagation of IGSCC at 1ppm Cl^-, pH=7 at 30 °C must be evident. This has been seen for historic fuel pins kept in open storage ponds

3. Initiation and propagation of IGSCC at $\sim$0.3 mg/L Cl^-, pH=7, at 45 °C must be seen. This is representative of the experience in enclosed, undosed storage ponds where a brief Cl^- excursion occurred

4. The initiation of IGSCC must be stopped by dosing solution containing 1-10 ppm Cl^- (at 30 °C) with NaOH to a pH of 11.4 (at 24 °C). This represents the storage environment that has been maintained since 1986

The stainless steel analogues used in the research described in Chapters 4 and 5 were prepared by the NNL with the above criteria in mind. Section 2.1 discusses the pretreatment of these stainless steels and their viability as analogues in more detail.

Having given an overview of the corrosion behaviour expected on stainless steels specifically AGR fuel cladding, 20/25/Nb SS, it is now necessary to consider the uranium dioxide fuel. In the unlikely event that the 20/25/Nb SS cladding is breached, spent uranium dioxide fuel will become exposed directly to pond water. Thus, to ensure the provision of a comprehensive safety case, the corrosion behaviour of fuel pellets must be discussed. The following section (section 1.10) aims to give a review of current findings on the corrosion behaviour of UO_2 and simulant fuels (SIMFuels) under conditioned relevant to interim storage.

1.10   Uranium Dioxide

During its time in the reactor core the composition of the uranium dioxide fuel is drastically altered through the process of fission, resulting in the formation of a variety of fission products including both new fissile and non-fissile materials amongst the original bulk uranium matrix. Spent fuel typically contains $\sim$96% uranium, 3% fission products and minor actinides and 1% plutonium (based on AGR SNF with a burn-up of $\sim$25 GWd/tU) [98]. The release of fission products is traditionally separated into two components: a rapid release of activity on fuel surfaces and at grain boundaries and a longer term release of activity from the fuel matrix. The former is called instant release fraction in fuel disposal studies and the latter matrix dissolution [98]. This thesis is focused on the long term release related to the dissolution of the fuel matrix which contains the vast majority of the radioactive inventory of the fuel. As noted above, the dominant component of spent fuel is uranium dioxide and therefore under interim storage conditions it can be assumed that the rate of release of retained fission products is directly related to the dissolution of the UO_2 matrix. Thus, understanding the corrosion behaviour of UO_2 in various environments can aid in the interpretation of the behaviour of spent fuel under similar conditions.

1.10.1 UO_2 Structure

UO_2 has a cubic fluorite structure, Figure 1.23, with many empty interstitial sites (shown as white squares in Figure 1.23). Such sites are capable of housing oxygen atoms with little distortion to the lattice itself up to a limiting composition of approximately $UO_{2.33}$. Thereafter, further oxidation causes a complete transformation of the fluorite structure to a tetragonal structure [99]. From simulations and theoretical calculations, there is a general agreement that the formation energies of O vacancies and interstitials are significantly lower than those required to form U point defects [100].

The incorporation of oxygen into the lattice causes structural transitions in the cubic lattice. For x-values up to 0.05, oxygen atoms are randomly distributed throughout the lattice at interstitial sites [101, 102]. Further addition of oxygen in the lattice up to x<0.11 causes point defects to form ordered structures, so-called Willis clusters [101]. Willis clusters are most commonly a linear combination of two O' interstitials, two O vacancies and two O'' interstitials[2] [105]. For x>0.11 there is a significant increase in the conductivity at grain boundaries [102]. Willis clusters transition into densely packed cuboctahedral clusters [101]. When x increases beyond ∼0.23 the majority of defects are cuboctahedral clusters and only a few stoichiometric areas retain their cubic symmetry [102, 106].

In order to incorporate excess oxygen atoms into the lattice it is necessary for some U(IV) to be oxidised to U(V) or U(VI) to maintain charge balance [107]. The effects of oxygen incorporation into the UO_2 matrix on the dissolution behaviour of that matrix are discussed in detail in the following section.
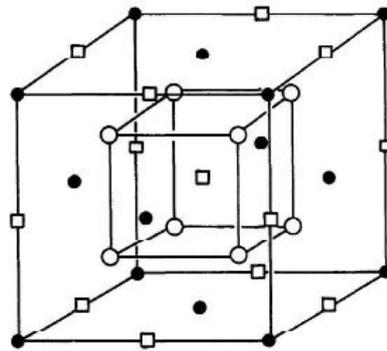
Figure 1.23: Structure of the UO_2 lattice, (●) uranium atom, (○) oxygen atom and (□) empty interstitial sites [99].

1.10.1.1   Hyperstoichiometric UO_2

Spent fuel may contain many non-stoichiometric areas due to production of fission products during irradiation in the reactor or unfinished sintering during fabrication. As defects tend to migrate to low energy sites such as grain boundaries,

---

[2]O' insterstitials lie in the <1 1 0> direction and O'' interstitials lie in the <1 1 1> direction, approximately 1 Å from the centre octahedral site [103, 104].

non-stoichiometric areas are therefore expected to be preferentially found at grain boundaries [100]. However, despite such areas and the presence of fission products, previous studies have identified that, in general, the composition of spent uranium dioxide fuel will remain near to stoichiometric, approximately $UO_{2.001}$ [100].

As stated in the previous section the UO_2 lattice readily accepts oxygen atoms. The addition of such interstitial oxygen atoms creates new electronic levels in the UO_2 band gap. These new defect energy levels, seen in Figure 1.24, come from the U_{7p}, U_{6d} and $O_{2p}^{''}$ bands [108]. Comparatively, for pure UO_2 only the U_{5f} states lie in the band gap. The excess oxygen atoms in hyperstoichiometric UO_2 provide charge carriers by generating holes in the U_{5f} band by production of charge compensating U(V) or U(VI) sites, as discussed at the end of section 1.10.1 above [99]. This increases the conductivity and also alters the Fermi energy level of the UO_{2+x} material [102, 108]. The creation of mobile holes converts UO_2 into a p-type semiconductor, UO_{2+x} [99].
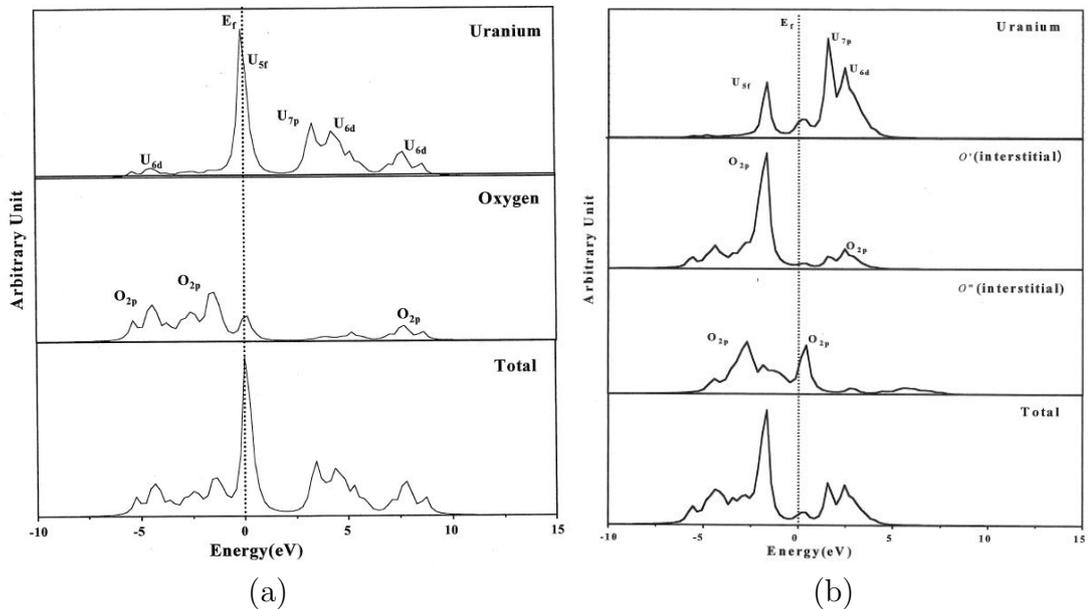
Figure 1.24: Electronic structure of (a) stoichiometric UO_2 and (b) $UO_{2.12}$ represented by a plot of the local density of states vs energy [108].

The creation of donor/acceptor U(IV)/U(V) sites results in increased anodic reactivity. These sites are available to reduce oxidants such as O_2 and H_2O_2 (specific O_2 and H_2O_2 effects will be addressed later in the chapter), so

enhancing corrosion at non-stoichiometric regions, i.e. reactivity is increased at hyperstoichiometric areas such as grain boundaries and oxidation and dissolution is likely to preferentially occur at these areas [62]. Measured corrosion rates of uranium dioxide samples in 0.1 mol/L NaCl solution (pH 9.5) are up to 10^3 times greater for $UO_{2.1}$ than those measured for stoichiometric UO_2 [102].

1.10.2   Typical Voltammetric Behaviour of UO_2

Figure 1.25 shows a typical cyclic voltammogram for UO_2. The regions of interest are labelled I to VI with the following assignments found from references [66,99,109]. Region I corresponds to the oxidation of sites of energy that differ from the bulk UO_2 such as non-stoichiometric areas most likely at the grain boundaries.

Oxidation of the bulk UO_2 matrix from UO_2 to UO_{2+x} occurs in region II, up to a limiting stoichiometry of $UO_{2.33}$. As mentioned previously, film growth occurs by oxidation of adjacent U(IV) to U(V) and further to U(VI) and incorporation of oxygen atoms at interstitial sites in the UO_2 matrix. Oxidation above $UO_{2.33}$ involves restructuring of the lattice via recrystallisation to form orthorhombic $UO_{2.66}$ or dissolution of U(V) or U(VI) species.

In region III further oxidation from UO_2 to UO_2^{2+} (soluble U(VI)) occurs in acid solution. In neutral/alkaline aqueous solutions UO_2^{2+} has a limited solubility and re-precipitates as $UO_3 \cdot yH_2O$ on the surface. This hydrated layer is considered to be porous and therefore may not completely inhibit corrosion reactions and local acidification in the pores may occur promoting further UO_2^{2+} dissolution.
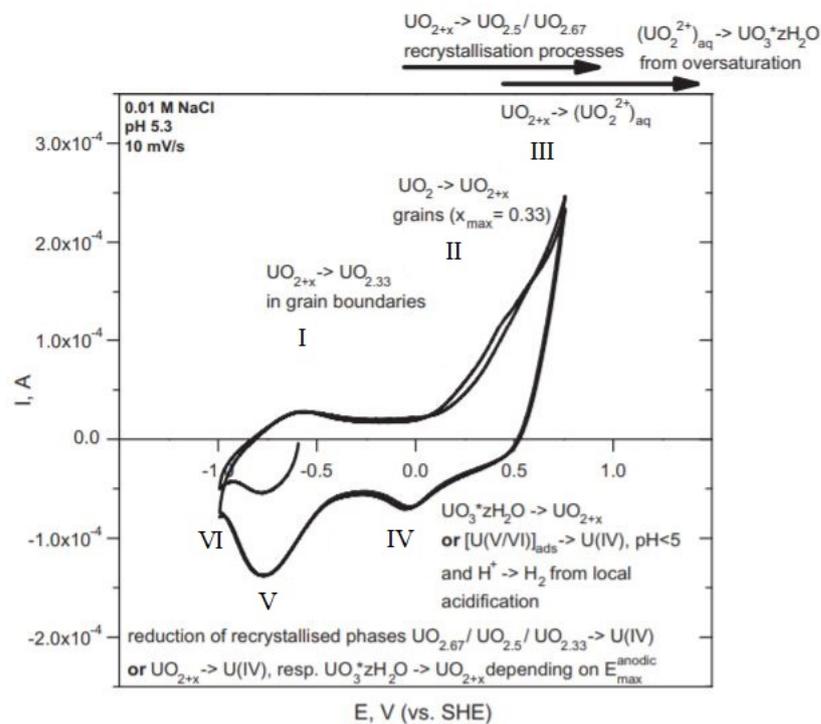
Figure 1.25: Cyclic voltammetric scan of a UO_2 electrode in 0.01 mmol dm^{-3} NaCl (pH$\simeq$5.3) at a scan rate of 10 mV/s [109].

The cathodic peak at region IV is due to the reduction of surface absorbed U(VI) species. This trough may also be attributed to the reduction of H$^+$ to H$_2$ if local acidification has occurred.

The cathodic peak in region V is a result of the reduction of the underlying oxidised surface layer formed in region II or higher oxides adsorbed onto the surface due to recrystallisation/reduction of U(VI) species. Finally, cathodic reduction of water occurs in region VI.

If two CVs from independent studying are compared, increases in the anodic and cathodic currents implies that there is a comparitive increase in the degree of surface oxidation [102].

1.10.3   Effect of pH on the Corrosion of UO$_2$

From the previous sections on the corrosion of stainless steel it is clear that storage of fuel cladding in alkaline media is advantageous. It is important to discern whether this too is the case for UO$_2$. Studies of the pH effects on UO$_2$ corrosion

have been carried out by a variety of authors and their significant findings are presented below.
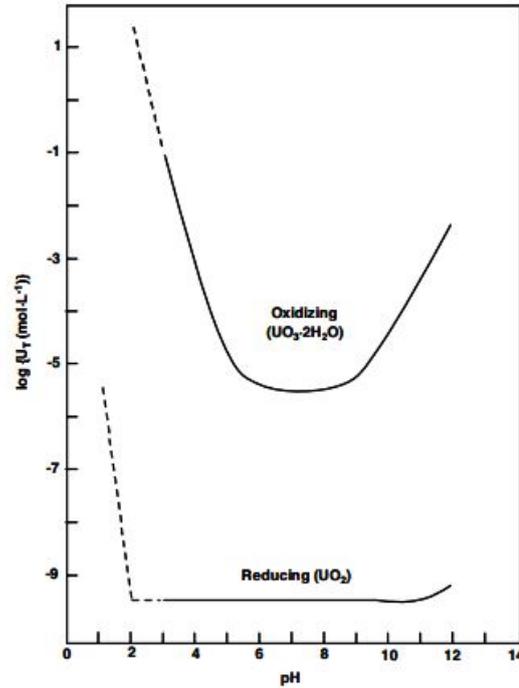
Figure 1.26: Solubilities of uranium dioxide (UO_2) and schoepite ($UO_3 \cdot 2H_2O$) as a function of pH at 25 °C [110].

Figure 1.26 shows the solubility of UO_2 and schoepite as a function of pH. From Figure 1.26 it can be seen that at pH values lower than 5, metaschoepite ($UO_3 \cdot H_2O$) does not form on the surface of UO_2 due to its increased solubility [111] [112]. The dissolution of U(VI) occurs too quickly for any O^{2-} ions to incorporate into the lattice [112]. Thus, the UO_2 surface remains close to stoichiometric in this acidic pH range [112].

Nicol and Needes [113] proposed that the mechanism of anodic dissolution of UO_2 in acidic environments follows equations 1.18 to 1.20.

$$UO_2 + H_2O \leftrightarrow (U^V O_2 OH)_{ads} + H^+ + e^- \tag{1.18}$$

$$(U^V O_2 OH)_{ads} + H_2O \longrightarrow (U^{VI} O_2 OH)_{ads} + O^{2-} + 2H^+ + e^- \tag{1.19}$$

$$(U^{VI} O_2 OH)_{ads} + 2H^+ \longrightarrow UO_2^{2+} + 2H_2O \tag{1.20}$$
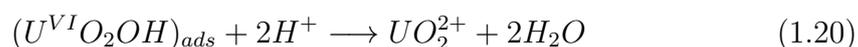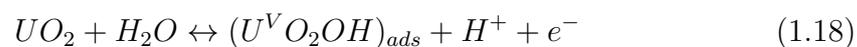
Adsorption of the hydrolysed species occurs before dissolution as U(VI) [110] and therefore, the corrosion rate is dictated by the solubility of said uranyl hydroxides in a particular acidic solution [114].

As shown in Figure 1.26, for 5<pH<10 the solubility of corrosion products is low and almost independent of pH [115]. The lack of pH dependence means that it is uncertain as to whether corrosion rates are controlled by anodic or by cathodic reactions. Film growth proceeds with incorporation of O^{2-} into the UO_2 matrix. Sunder *et al.* [111] found that in neutral to alkaline conditions oxidation to $UO_{2.33}$ occurred between 0 and 10 hours exposure, dependent on dissolved oxygen concentration i.e. ambient redox stress. However, after 100 hours the surface phase was entirely formed of hydrated UO_3 and steady-state dissolution conditions were attained. Torrero *et al.* [112] found that the average composition of the surface of UO_2 in mild alkaline solutions (0.01 mol dm^{-3} NaClO$_4$, pH between 8-9) is $UO_{2.25}$ under open circuit conditions. The uranium oxide film thickness is observed to increase with pH. This thicker surface layer results is a significant decrease in the dissolution rates, for example dissolution rates at pH=2.5 were shown to be 50 times higher than those recorded at pH=9.7 [111]. Santos *et al.* [110] propose the mechanism for the anodic dissolution of UO_2 in alkaline solutions to be as follows (equations 1.21 and 1.22):

$$UO_2 + xH_2O \longrightarrow U^{IV}_{1-2x}U^{V}_{2x}O_{2+x} + 2xH^+ + 2xe^- \tag{1.21}$$

$$U^{IV}_{1-2x}U^{V}_{2x}O_{2+x} + 3OH^- \longrightarrow U^{VI}O_{2+x}(OH)_3^- + 2e^- \tag{1.22}$$
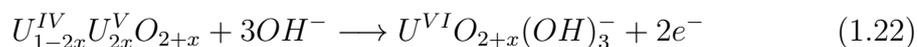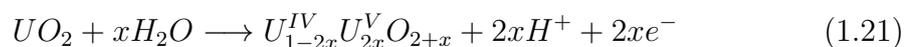
From Figure 1.26 it is seen that solubility of schoepite and UO_2 increase in solutions with pH>10/11. For pH>10 the dissolution rate has been suggested to be controlled by the anodic reaction of equations 1.21 and 1.22 rather than subsequent dissolution (equation 1.20) [111]. U(VI) dissolution is initially enhanced by uranyl corrosion product hydrolysis reactions at high pH via equation 1.23 and the uranyl

corrosion product in solution is stabilised [110].

$$UO_2^{2+} + xOH^- \leftrightarrow UO_2(OH)_x^{(2-x)+} \tag{1.23}$$
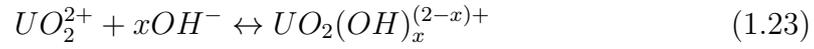
However, as a result Engelhardt *et al.* [114] discovered that when U(VI) reaches a maximum solubility in solution, a protective layer (possibly schoepite, $(UO_2)_8O_2(OH)_{12}\cdot 12H_2O$) begins to form which then lowers corrosion rates through blocking of the underlying surface.

1.10.4   Effect of Oxygen on the Corrosion of UO_2

Oxygen reduction is a slow process because it involves breaking the strong O-O bond [116]. However, this process is catalysed by the presence of donor-acceptor sites on the surface of UO_2 [62,117]. These active sites are made of adjacent U(IV) and U(V) or U(V) and U(VI) cations. Figure 1.27 shows the schematic for such a reduction process. Here the U(V) on the surface is reduced by accepting an electron from the bulk of the material. This electron is then donated to the adsorbed O_2 molecule generating the superoxide ion (O_2^-) [62]. The further reduction of the superoxide ion results in the formation of the hydroxide ion. Thus, the reaction for oxygen reduction is:

$$O_2 + H_2O + 4e^- \longrightarrow 4OH^-$$
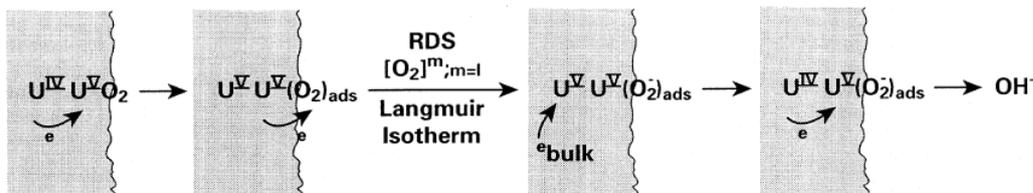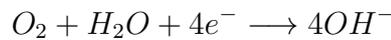
Figure 1.27: Reduction of Oxygen at donor-acceptor sites [62].

As UO_2 becomes increasingly more hyperstoichiometric (UO_2-$UO_{2.33}$) there is only a moderate impact on O_2 reduction, suggesting a large amount of surface

oxidation would need to occur before any change to the rate of O_2 reduction is observed [117].
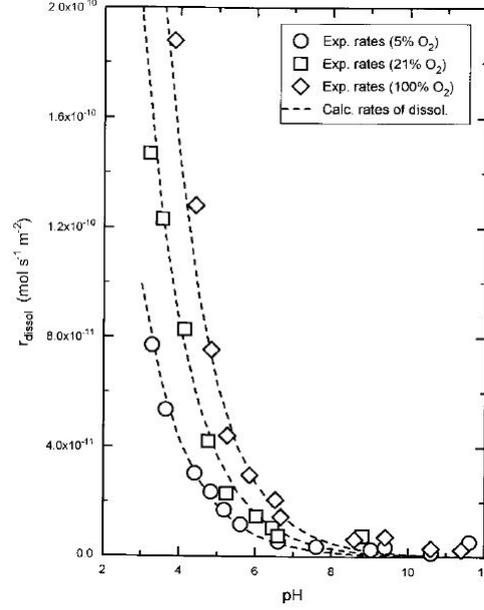
Figure 1.28: Dissolution rates of uranium dioxide as a function of pH and oxygen concentration [112].

Torrero *et al.* [112] investigated the effect of dissolved oxygen on the corrosion of uranium dioxide using a continuous flow through reactor. They discovered that for solutions with pH>6.5 dissolution rates were relatively low (approximately 1×10^{-11} mol s$^{-1}m^{-2}$) and that for oxygen concentrations of 5, 21 and 100% in the purge gas, dissolution rates appear to be almost independent of O_2 concentration in alkaline solutions, shown in Figure 1.28 [112]. They hypothesised that at low pH H^+ and O_2 were competing for surface sites which promotes dissolution of oxidised U(VI) via equations 1.24, 1.25 and 1.27 [118]. The kinetic rate equation for the rate of dissolution is given in equation 1.26.

$$2UO_2 + O_2 \underset{k_{-1}}{\overset{k_1}{\rightleftharpoons}} 2UO_2 \cdot O_2 \equiv 2UO_3 \tag{1.24}$$

$$UO_3 + H^+ \xrightarrow{k_2} UO_3 \cdot H^+ \longrightarrow UO_2(OH)^+ \tag{1.25}$$
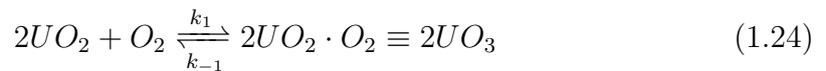
$$r = \frac{k_1[O_2][UO_2]_{tot}(k_3 + k_2[H^+])}{k_{-1} + k_3 + k_2[H^+] + k_1[O_2]} \tag{1.26}$$

$$UO_3 + H_2O \xrightarrow{k_3} UO_3 \cdot H_2O \longrightarrow UO_2(OH)_2 \qquad (1.27)$$
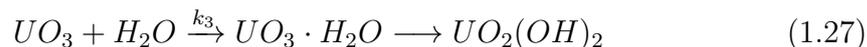
However, at neutral to alkaline pHs, $k_2[H^+]$ in equation 1.26 is negligible i.e. dissolution rates are independent of $[H^+]$ and equation 1.27 is instead favoured, with formation of a surface oxide/hydroxide occurring [118].

Interestingly, Shoesmith *et al.* [111] found that in 0.1 mol dm^{-3} NaClO$_4$ solutions of pH$\simeq$9.5 the steady state corrosion potential is dependent on the oxygen concentration and is seen to lie between 0 and 0.1 V (vs SCE) for higher $[O_2]$ but below 0 V for lower concentrations. In the potential region 0 to 0.1 V the fuel surface is covered with U(VI), on the other hand below 0 V corrosion is slow but can be sustained on the UO_{2+x} surface unencumbered by dissolution of U(VI). From this it can be said that the rate controlling step at high $[O_2]$ is the dissolution of U(VI) and at low $[O_2]$ it is the reduction of O_2.

Unlike in the proposed UK geological disposal conditions post-closure, interim storage ponds contain aerated solutions. However, because dissolution rates are almost independent of oxygen concentration at the high pH levels (pH$\simeq$11.4 in interim storage ponds), dissolved oxygen is unlikely to play a major role in UO$_2$ dissolution during interim storage.

1.10.5   Effect of Hydrogen Peroxide on the Corrosion of UO$_2$

The reduction of hydrogen peroxide on uranium dioxide is a much faster reaction than that of oxygen reduction on the same material. As a result the reduction current of oxygen is one or two orders of magnitude smaller than that of H$_2$O$_2$ [62]. Both observations can be attributed to the ability of H$_2$O$_2$ to generate its own donor-acceptor sites, which can catalyse the decomposition of H$_2$O$_2$. Decomposition of peroxide on U(IV)/U(V) sites is described by equations 1.28 and 1.29. Equation 1.30 then represents the simplified overall reaction for decomposition.

$$2U^{4+} + H_2O_2 \longrightarrow 2U^{5+} + 2OH^- \tag{1.28}$$

$$2U^{5+} + 2e^- \longrightarrow 2U^{4+} \tag{1.29}$$

$$H_2O_2 + 2e^- \longrightarrow 2OH^- \tag{1.30}$$

The electrons required for H_2O_2 reduction in equation 1.29 and the simplified reaction in equation 1.30 is provided by the anodic oxidation of UO_2. Equations 1.31 and 1.32 describe the anodic oxidation process, the simplified overall reaction shown in equation 1.33. The H_2O_2 driven corrosion of UO_2 is considered to be an electrochemical process and therefore involves the coupling of these anodic (oxidation of UO_2) and cathodic (H_2O_2 reduction) reactions.

$$UO_2 + 0.33H_2O \longrightarrow UO_{2.33} + 0.66H^+ + 0.66e^- \tag{1.31}$$

$$UO_{2.33} + 0.66H^+ \longrightarrow UO_2^{2+} + 0.33H_2O + 1.34e^- \tag{1.32}$$

$$UO_2 \longrightarrow UO_2^{2+} + 2e^- \tag{1.33}$$
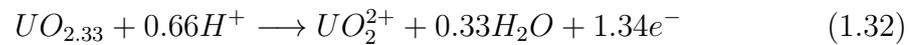
It has been reported that via this coupling the oxidation of UO_2 to $UO_{2.33}$ (equation 1.31) is approximately 200 times quicker in H_2O_2 solutions than in solutions containing the same concentration of oxygen [119]. After H_2O_2 decomposition, the oxidative dissolution of $UO_{2.33}$ to UO_2^{2+}, shown in equation 1.32, progresses at a rate similar to that following O_2 reduction [62].

The recorded corrosion potential UO_2 as a function of H_2O_2 concentration is shown in Figure 1.29. These measurements show 3 distinct regions and these areas have been observed and discussed in [62, 66, 120–122].
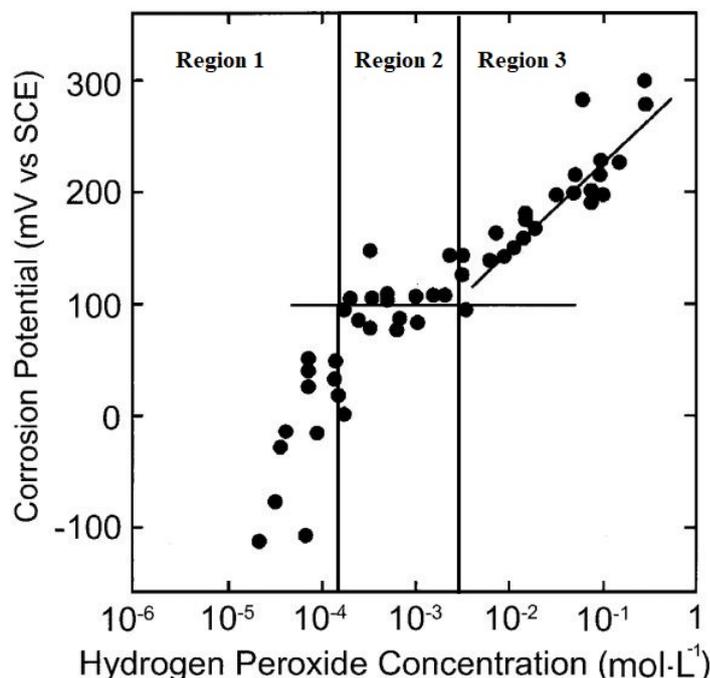
Figure 1.29: Variation in corrosion potential as a function of [H$_2$O$_2$] in solution of 0.1 mol dm^{-3} NaClO$_4$, pH$\simeq$ 9.5 [66].

In region 1, for [H$_2$O$_2$] $< 2 \times 10^{-4}$ mol L^{-1}, the increase in UO$_2$ corrosion potential is directly proportional to the increase in H$_2$O$_2$ concentration. In this region equation 1.30 couples with equation 1.33. Thus, increasing H$_2$O$_2$ concentration results in an increase in the rate of UO$_2$ dissolution. As mentioned above, it has been suggested that the oxidation of UO$_2$ to UO$_{2.33}$, shown in equation 1.31, is most affected by H$_2$O$_2$ concentration and equation 1.32 proceeds at the same rate as in the absence of peroxide [62]. However, since more UO$_{2.33}$ is formed and therefore available to be further oxidised to UO$_2^{2+}$ it follows that the overall dissolution of the surface layer will increase. At these low H$_2$O$_2$ concentrations secondary UO$_3 \cdot$xH$_2$O phases are unlikely to be present in any significant amount at the surface.

In region 2, for 2×10^{-4} mol L^{-1} $<$ [H$_2$O$_2$] $< 5 \times 10^{-3}$ mol L^{-1}, corrosion potentials appear to be independent of H$_2$O$_2$ concentration. In this region peroxide decomposition does not couple with the anodic dissolution of UO$_2$, the reduction of peroxide in equation 1.30 instead couples with peroxide oxidation in equation

1.34 resulting in redox buffering of the UO_2.

$$H_2O_2 \longrightarrow O_2 + 2H^+ + 2e^- \tag{1.34}$$

$$O_2 + 4e^- + 2H_2O \longrightarrow 4OH^- \tag{1.35}$$
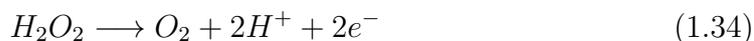
However, dissolution still occurs at a higher rate than in region 1 as signified by the higher corrosion potential compared to $[H_2O_2]{<}2{\times}10^{-4}$ mol L^{-1}. Such behaviour can be explained by the coupling of the H_2O_2 decomposition product, O_2 with the UO_2 dissolution reaction i.e. equation 1.33 couples with equation 1.35. As shown in section 1.10.4 dissolution rates are independent of $[O_2]$ at the alkaline pH studied, thus further increases in $[O_2]$ due to increases in $[H_2O_2]$ do not increase the rate of UO_2 dissolution.

In region 3 at $[H_2O_2] > 5 \times 10^{-3}$ mol L^{-1}, the corrosion potential increases again, showing a first order dependence on $[H_2O_2]$. As such the dissolution rate of UO_2 also becomes dependent on $[H_2O_2]$, increasing as $[H_2O_2]$ increases. However, if the same experiment is performed in carbonate containing solutions the corrosion potential of Figure 1.29 does not increase as significantly. This has been attributed to accumulation of U(VI) deposits on the UO_2 surface under non-carbonate conditions. These deposits form due to the [U(VI)] exceeding its solubility limit local to the electrode surface. Studies by Amme *et al.* [123] have shown that these deposits are most likely studtite at $[H_2O_2]{>}1{\times}10^{-4}$ and at lower concentrations schoepite may form. This surface secondary phase deposition blocks U(IV)/U(V) donor sites and slows down the decomposition of H_2O_2 allowing un-decomposed H_2O_2 to polarise the UO_2 surface to a higher potential, thus increasing the UO_2 dissolution rate. This has also been reported by Corbel *et al.* [124], who observed increased initial U(VI) release to solution from UO_2 as a function of $[H_2O_2]$ concentrations from 10^{-3} to 10^{-1} mol L^{-1}. However, while initial release is more rapid (and overall dissolution rate similarly), Corbel also showed over longer time periods (> 1 hour) and in the

absence of carbonate that most dissolved U(VI) is used in growing the surface secondary phase, rather than being released into bulk solution. The result is that under non-complexing solution conditions (i.e. no carbonate or similar) such peroxide concentrations in region 3 of Figure 1.29 actually inhibit environmental U(VI) release over the time scales expected for uranium storage in either pond or geological repository.

Calculations estimate radiogenic H_2O_2 concentrations to be ~ 30 μmol L^{-1} under pond water conditions [125]. Therefore, H_2O_2 concentrations remain at the lower end of the first region of Figure 1.29, leading to the belief that the corrosion potential will be <-0.1 V vs SCE.

The above experiments were carried out in solutions at pH$\simeq$9.5. However in pond water conditions the pH is around 11.4. Sunder *et al.* [66] observed a decrease in steady-state corrosion potential (region 2 in Figure 1.29) over a pH range of 3 to 13 at $[H_2O_2]\simeq 10^{-3}$ mol L^{-1}, suggesting that H_2O_2 decomposition is more significant than oxidative dissolution in alkaline conditions. They hypothesize that the change in the mechanism of decomposition of H_2O_2 as alkalinity increases (see section 1.8.4) substantially slows down the oxidation of UO_2 and subsequent dissolution and deposition of U(VI) species [66].

This is also supported by the work of Meca *et al.* [126]. They found that in the presence of 1.1×10^{-4} mol L^{-1} H_2O_2 (lower edge of region 2, Figure 1.29) in 0.1 mol L^{-1} $NaClO_4$, at pH$\simeq$11 the surface composition of UO_2 is close to $UO_{2.33}$, whereas at pH$\simeq$13 the surface composition of UO_2 is closer to $UO_{2.07}$ after 500 hours of exposure. Further, a higher U(VI) surface content was present at pH 11 than pH 13.

In contrast, Claren *et al.* [122] investigated the effect of H_2O_2, $[H_2O_2]\simeq 10^{-5}$ (region 1 in Figure 1.29), on UO_2 dissolution for a range of pH values. Dissolution appeared to decrease as the pH increased to 7, then plateaued and began to increase for pH >9. They found the increase in the dissolution rate under alkaline conditions (pH >9) to have a linear relationship with pH. They suggest that the increased

dissolution rate is due to the development of local acidity via equation 1.36, which only occurs under alkaline conditions [122].

$$H_2O_2 + OH^- \leftrightarrow H_2O + HO_2^- \qquad (1.36)$$
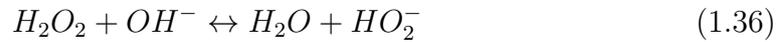
The perhydroxyl anion (HO_2^-) generates radicals which are considered to be stronger oxidising agents than H_2O_2, thus enhancing the oxidation of UO_2 (in alkaline solutions) [69, 122], which in turn increases UO_2 dissolution.

Such inconsistencies between studies may be due to the differences in H_2O_2 concentration. The behaviour observed by Claren *et al.* is reminiscent of that shown in Figure 1.26 which shows the effect of pH on UO_2 solubility. This indicates that at $[H_2O_2] \simeq 10^{-5}$ and pH>11 the observed increase of disolution effect may well be dominated by UO_2 solubility differences rather than the presence of H_2O_2. Considering that concentrations of H_2O_2 in storage ponds are expected to be approximately the same as that studied by Claren *et al.*, enhanced dissolution of UO_2 through the described H_2O_2 reaction coupling may not significantly increase the UO_2 dissolution rate.

1.10.6 The Effect of Temperature on UO_2 Corrosion

There is a gap in the scientific literature with regards to the temperature dependent corrosion of UO_2 under pond water solution conditions and in the temperature range of interest (25 - 90 °C) the majority of studies having been carried out with groundwater simulants.

Studies performed by Thomas and Till [127] and Lahelle and Guillaumont [128] found that increasing the temperature of demineralised, deionised water increased the dissolution rate of UO_2 from approximately 2×10^{-3} g m^{-2} d^{-1} at 30 °C to 7 $\times 10^{-3}$ g m^{-2} d^{-1} at 90 °C. At 70 °C in saline groundwater, similar dissolution rates to those reported for deionised water at the same temperature were observed. However, in granitic groundwater (where

the dominant ion is HCO_3^-) and solutions containing Mg^{2+}, increases in temperature did not lead to increased dissolution rates. This may be due to corrosion product deposits blocking the dissolution of the UO_2 surface, most likely $NaUO_3$ or NaU_2O_7 for granitic water or a magnesium silicate in Mg^{2+} solutions.

Batak *et al.* [129] have reported that for groundwater containing sodium and calcium carbonates, no secondary phases are formed while leaching at 70 °C and bulk surface oxidation to U_4O_9 occurred. Experiments in deionised water yielded the same results.

At a higher temperature range of 150 - 200 °C, a layer of $UO_{2.33}$ developed on UO_2 in demineralised water [130]. As the temperature increased so did the thickness of the $UO_{2.33}$ layer, with similar results also observed at pH $\simeq$ 6 and 10. The thickness of the $UO_{2.33}$ layer increased from $\sim$ 5-8 nm at room temperature to 100-500 nm at elevated temperatures. The thickness had a linear relationship with the square root of time over the 4 hour test period [130]. The growth of the $UO_{2.33}$ layer can be explained by accelerated diffusion of O^{2-} at elevated temperatures, $>100°C$, increasing film formation and growth.

1.10.7   Spent Nuclear Fuel Analogues

Spent nuclear fuel is highly radioactive, making laboratory scale research on real irradiated fuel problematic. Therefore a suitable spent fuel analogue is needed.

Considering that UO_2 makes up $\sim$96% of SNF, it is reasonable to select pure UO_2 as a possible analogue. Generally, the underlying corrosion processes of UO_2 and spent fuel appear to be the same based on experiments using electrochemical corrosion techniques on both UO_2 and real fuel [62, 131, 132]. Such similarities, between materials despite obvious compositional differences, is due to the formation of an oxidised UO_2 surface layer which protects the bulk material from the corroding environment and causes both materials to act in a similar manner [62, 131, 132]. As an example, the effects of pH, carbonate

concentration and temperature on the oxidation/dissolution rate of UO_2 and spent fuel have been examined by Steward and Gray [133]. While the average dissolution rate of UO_2 was ~ 3 times that of spent fuel, this difference is insignificant, as dissolution rates previously reported for pure UO_2 vary by this much for the same experiments carried out by different laboratories [62].

However, the response of spent fuel and UO_2 to changes in oxygen concentration has resulted in dissimilar responses. At room temperature and dissimilarly to UO_2, the corrosion rate of spent fuel is independent of oxygen concentration. It should be noted however, that the true oxygen dependence may have been disguised by the effects of increased radiolysis from spent fuel versus depleted UO_2 [62, 133].

Further, Bottomley *et al.* [62, 131] found that irradiated UO_2 (6.85% ^{235}U; burnup 20-22 GWd/tU in Na_2CO_3) has a lower resistivity than natural UO_2 and the corrosion rate of irradiated UO_2 is approximately twice that of unirradiated UO_2. Such differences in the corrosion processes between SNF and pure UO_2 stem from the effects of radiation damage on the material matrix, variation in surface area and exposure of grain boundaries.

An alternative to pure UO_2 is to use doped UO_2 materials commonly referred to as SIMFuels (Simulated SNF). SIMFuels aim to replicate the chemistry and microstructure of SNF, without the difficulty of an intense radiation field. SIMFuels account for the presence of fission products in irradiated fuel by doping UO_2 with non-radioactive elements to concentrations expected in real SNF.

Spent fuel simulants are manufactured to represent different levels of burnup of spent fuel. Burnup is a measure of the energy extracted per unit mass of fresh fuel. The most common unit for burnup is Wd/tU (Watt-days per metric tonne of the heavy metal). However, burnup can also be expressed as the atomic percent of initial heavy metal ions that have undergone fission, where for UO_2 fuels 1 at% equals 9375 MWd/tU [134].

The following section discusses the specific dopants used in SIMFuels and how they are likely to affect the corrosion behaviour.

1.10.7.1   Physical and Chemical Effects of Fission Products on UO_2

Microscopic and macroscopic changes occur in UO_2 fuel during its time in reactor. This is due to temperature and neutron flux gradients and the generation of fission products that are insoluble in the fuel matrix. UO_2 grains may grow in reactor and thermal stresses can lead to fuel cracking. Simulating the physical effects induced by irradiation is difficult, although creating simulants, with a similar chemical composition where dopants are incorporated at defect sites in the UO_2 structure, is achievable [135].

Within the UO_2 matrix different fission products vary in solubility. These elements can be grouped in the following manner [136] [107]:

1. Elements retained by the UO_2 matrix: This includes actinides (Am, Pu, Np, Cm) and lathanides (La, Ce, Pr, Nd, Eu, Gd), within their limits of solubility in the UO_2 matrix.

2. Volatile elements and inert gases (He, Xe, Kr, Br, Rb, Cs, Te, I): These tend to have limited solubility in the fuel matrix and migrate towards the fuel/cladding gap. Fission gas bubbles result in the expansion of the matrix and these bubbles may connect and form pathways for fission gas release.

3. Precipitates: Less volatile elements may move to grain boundaries and form oxide (Ba, Zr, Mo, Sr) or metallic precipitates (Ru, Pd, Rh, Mo, Tc, Ag, Cd). The oxides have a perovskite-type structure usually having the composition ABO_3 where A is Ba, Sr or Cr and B is Zr, Mo, U, Pu or a rare earth element.

Of these elements, two particular groupings have the greatest effect on the corrosion of spent nuclear fuel. The first group are the solid solution rare earth elements (La, Ce, Pr, Nd, Pm, Sm, Eu, Gd and Y). These elements dwell within the lattice generally with an oxidation state of (III). Rare earth (RE) elements

increase the electrical conductivity of UO_2 by generating holes in the U 5f sub-band. When RE(III) ions enter the lattice U(V) sites are produced to maintain charge neutrality [62] [117] [137]. High levels of RE(III) dopants diminish the anodic oxidation of UO_2 because the number of available oxygen vacancies, required for the incorporation of oxygen interstitials during oxidation, is reduced via the formation of dopant vacancy clusters [138]. Indeed, it has been reported that the oxidation of RE(III) doped UO_2 is kinetically slower than that of pure UO_2 and proceeds via the formation of U_4O_9 rather than U_3O_7 as for pure UO_2 [138] [135]. Thus, dopants also potentially alter the defect cluster ordering which leads to U_3O_7 formation (presumably through the formation of dopant vacancy clusters) [135].

The second group are the noble metal precipitates known as ε-particles. These noble metal particles are unstable as oxides [137] and reside in UO_2 spent fuel as hexangonal close packed alloys (typically at grain boundaries [139]). The mean composition of the ε-phase is Ru-47/Mo-28/Pd-22/Rh-3 (in at.%). These particles make up approximately 4% of the total volume of 6 at% burn-up CANDU SIMFuel [62, 117]. ε-particles can increase UO_2 oxidation by catalysing the decomposition of H_2O_2 and O_2 reduction (see following sections). However the reactivity of ε-particles is suppressed by the formation of a surface film in an oxidising environment [62, 117].

Effects of dopants in the UO_2 matrix (i.e. SIMFuels) under specific conditions are discussed, in the following sections.

1.10.7.2 Effect of Oxygen on the Corrosion of SIMFuels

Rare-earth doping of UO_2 appears to have little effect on O_2 reduction [62]. However, SIMFuels containing ε-particles exhibit enhanced O_2 and H_2O reduction in neutral and alkaline solutions [62, 117]. From this it is concluded that ε-particles are more reactive than UO_2 with regards to O_2 reduction. Indeed metallic Ru and Pd are good O_2 reduction catalysts in their own right [140, 141]. As described in

section 1.10.4, as UO_2 oxidises to UO_{2+x} there is a slight increase in O_2 reduction. However, the opposite appears true for SIMFuels with O_2 reduction decreasing with increased UO_2 oxidation. This has been ascribed to the increasing formation of $UO_{2.33}$ on the fuel surface as the SIMFuel oxidises which covers the ε-particles, blocking any ε-particle sites for O_2 reduction (Figure 1.30). Thus, over longer time scales, or in particularly oxidising environments, ε-particles do not play a significant role in the UO_2 oxidation process in the presence of oxygen [62, 117]. Furthermore, at pH$\simeq$11.4, as found in fuel storage ponds and as with pure UO_2 dissolution (see section 1.10.4) the dissolution of the SIMFuel surface will again be independent of O_2 concentration, see Figure 1.28. Therefore, for the studies carried out under interim storage conditions in this thesis the oxygen concentration of the solution is not considered further.
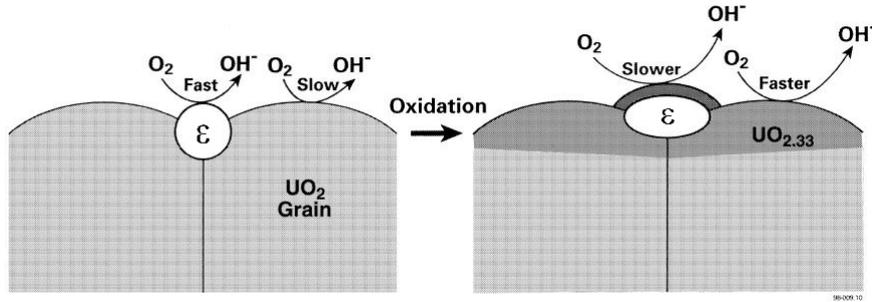
Figure 1.30: Reduction of O_2 on ε-particles in UO_2 [62].

1.10.7.3   Effect of Hydrogen Peroxide on the Corrosion of SIMFuels

It is well known that the decomposition of H_2O_2 is enhanced in the presence of noble metal catalysts, such as ε-particles [107]. Goldik *et al.* [142] found that as the number density of these particles in SIMFuel increases, the rate of reduction of H_2O_2 is accelerated. Trummer *et al.* [143] found similar results using Pd only doped UO_2 in solutions containing 2 mmol dm^{-3} H_2O_2. They reported that the concentration of dissolved UO_2^{2+} increases linearly with Pd loading, suggesting that Pd catalyses UO_2 oxidation. Futhermore, the rate of decomposition of H_2O_2 also increases with Pd loading, suggesting H_2O_2 decomposition is also catalysed by Pd-particles [144]. It is important to note that measurements were carried out

over 50 minutes. In this time frame, acceleration of H_2O_2 reduction occurs via equation 1.37 [143] so enhancing oxidation of UO_2 via equation 1.38.

$$H_2O_2 + e_S^- \longrightarrow OH\cdot + OH^- \tag{1.37}$$

$$(U^{VI})_S \longrightarrow (U^V)_S + e_S^- \tag{1.38}$$

Experiments carried out by Lousada *at el.* [145] over an extended time scale of 120,000 minutes (approx. 3 months) found that in the presence of 5 mmol dm^{-3} H_2O_2 at pH$\simeq$7.5, the rate of dissolution of U(VI) was in fact lower for SIMFuel and Pd/Y_2O_3 doped UO_2 than for pure UO_2. As described previously, such an observation would be consistent with enhanced decomposition of H_2O_2 at the SIMFuel surface, however the concentration of hydroxyl radicals (produced as a result of H_2O_2 decomposition) was found to be the same for both pure and doped UO_2 under the same conditions. Thus, redox reactivity must decrease on doping of UO_2.

Finally, if H_2 is present in solution, OH· radicals generated via equation 1.37 may be scavenged on ε-particles via equation 1.39 [146]. This would either prevent or reverse the oxidation processes at the SIMFuel surface, equation 1.40 [146].

$$H_2 + OH\cdot \longrightarrow H_2O + H^+ + e_{aq}^- \tag{1.39}$$

$$(U^V)_S + e_{aq}^- \longrightarrow (U^{IV})_S \tag{1.40}$$
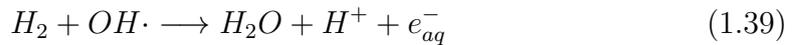
AGR SIMFuel specific corrosion studies in the presence of hydrogen peroxide have been carried out by Rauff-Nisthar *et al.* [147]. They conducted immersion experiments on AGR SIMFuel with a simulated burn-up of 43 GWd/tU immersed in anoxic modified simplified groundwater (10 mmol dm^{-3} NaCl, 2 mmol dm^{-3} NaHCO$_3$, pH$\simeq$6.8) containing 100 μmol dm^{-3} H_2O_2 for 1 hour. Raman spectra of the surface post immersion showed a decrease in the peak associated with lattice damage, indicating enhanced dissolution of the SIMFuel surface is occuring in

the presence of H_2O_2, i.e. conversion of surface UO_{2+x} to UO_2^{2+} in line with the short 50 minute experiments of Trummer *et al.* on Pd-doped UO_2 [143]. This is also consistent with increases in open circuit potentials with increasing peroxide concentration resulting in the oxidation of the surface to soluble UO_2^{2+}. However, similar experiments on AGR SIMFuel with a lower simulated burn-up of 25GWd/tU were also carried out. In this case the 540 cm^{-1} defect peak of the Raman spectra increases on exposure to groundwater containing 100 μmol dm^{-3} H_2O_2 for 1 hour [147]. This suggests that additional oxygen interstitials have been incorporated into the UO_2 lattice and a protective UO_{2+x} surface layer has formed, the lower ε-particle content reduces the degree of UO_2^{2+} release.

1.10.7.4   Effect of Temperature on the Corrosion of SIMFuels

As with undoped UO_2, see section 1.10.6, there is little published work on SIMFuels immersed in pond water or ground water aqueous solutions of temperatures between 45 - 90 °C. Shoesmith *et al.* [102] conducted cyclic voltammetry experiments on CANDU SIMFuels, 1.5 at%, 3 at% and 6 at%, in buffered 0.1 mol dm^{-3} KCl solution (pH$\simeq$9.5) at 10 degree increments from room temperature to 80 °C. For 1.5 at% and 3 at% SIMFuels oxidation currents (Peak II: $UO_2 \longrightarrow UO_{2+x}$ and Peak III: $UO_{2+x} \longrightarrow UO_3 \cdot yH_2O$ from assignments of Figure 1.25) increased with increasing temperature due to accelerated UO_2 oxidation reactions at higher solution temperatures. Interestingly, at high potentials and temperatures there was some evidence of current suppression through the deposition of $UO_3 \cdot yH_2O$ onto the SIMFuel surface which blocks dissolution. There were also indications that local acidification was occurring in the reverse CV scan resulting in the reduction of UO_2^{2+}. However, for 6 at% SIMFuel the influence of increasing temperature appears to be dampened, suggesting that there is lower anodic reactivity of high burn-up fuels in line with the explanation given in section 1.10.7.1.

Having now reviewed currently available literature on the key features of the

corrosion behaviour of stainless steels, UO_2 and SIMFuels, the remainder of this thesis presents a discussion of experiments conducted on AGR cladding, UO_2 and AGR SIMFuels under conditions relevant to wet interim storage. As stated above, Chapter 2 details the experimental methods used and describes the properties of the materials investigated; Chapter 3 discusses the corrosion behaviour of unsensitised 20/25/Nb SS cladding; Chapter 4 presents results of corrosion experiments on heat treated 20/25/Nb SS; Chapter 5 discusses the corrosion behaviour a 304H SS (AGR cladding analogue); Chapter 6 describes the corrosion behaviour of UO_2 and AGR SIMFuel and Chapter 7 presents the conclusions drawn throughout the thesis and offers some recommendations for future work. Some additional information is also given in the Appendices.

Chapter 2

Materials and Experimental Procedure

2.1 Materials

2.1.1 Pond water chemistry

Pond water simulants were prepared in doubly deionized water to the specification given in Table 2.1 and dosed with hydroxide to a pH$\approx$11.4 where appropriate. The simulant composition given in Table 2.1 is based on an average of sample data recorded from the AGR storage pond, at Sellafield, UK, which was analyzed once a week from October to December 2013. Note that these values are those of the current AGR storage pond not the THORP Receipt and Storage pond. However, analysis of the composition of the THORP pond during the same period suggests that use of the composition of Table 2.1 as a THORP pond water simulant would constitute a conservative approach i.e. concentrations of ions in Table 2.1 are higher than those expected in the THORP Receipt and Storage Pond (excluding the dosing to pH 11.4 with NaOH).

Ion	Concentration /μmol dm^{-3}
Na$^+$	5.4×10^3
Ca^{2+}	2
K$^+$	5
Cl$^-$	30
SO$_4^{2-}$	2
OH$^-$	Balance

Table 2.1: Simulant pond water composition.

2.1.2   Fuel cladding material

As described in Chapter 1, the fuel in AGR reactors are encased in 20/25/Nb stainless steel. This is an austenitic steel containing 20 wt% Cr and 25 wt% Ni, and is chosen for its ability to endure the reactor environment, temperatures of up to 825 °C in a CO_2 atmosphere. Nb is included to stabilize the steel matrix, as the presence of NbC precipitates provide creep resistance, improve structural strength at high temperature and prevent chromium carbide formation and subsequent sensitisation.

The composition of 20/25/Nb SS AGR fuel cladding, sourced from Westinghouse's Springfields Fuel Ltd production line at Preston, UK, is given in Table 2.2. The composition of 304H SS is also given in this table. 304H SS was selected as a possible analogue for 20/25/Nb SS due to their similar Cr and C content. 304H SS is more easily sensitised than 20/25/Nb SS as the C is free to react with Cr due to the lack of Nb stabiliser. However, 304H SS has significantly lower Ni content than 20/25/Nb SS.

Steel	Cr	Ni	C	Mn	Si	Nb	P	N	Fe
20/25/Nb	19.33	24.05	0.062	0.79	0.58	0.56	0.014	0.01	Balance
304H	18.24	8.09	0.06	1.38	0.45	-	0.032	0.1	Balance

Table 2.2: Composition (wt %) of 304H and 20/25/Nb stainless steels.

2.1.3   Uranium dioxide simulated spent fuel material

The UK National Nuclear Laboratory (NNL, Springfields, UK) fabricated UO_2 pellets and SIMFuel pellets simulating AGR fuel pellet burn-ups of 25 GWd/tU and 43 GWd/tU. SIMFuel pellets were prepared using sintering powder precursors containing the dopant compositions given in Table 2.3.   The composition calculations were conducted using the FISPIN nuclear inventory calculation code (developed by NNL and distributed by Wood plc) and represent fuel pellets that have been aged for 100 years after removal from the reactor. The fission product surrogates of Table 2.3 were weighed and ball milled for 12 hours using ZrO_2 milling media.   The fission product blend was then mixed with depleted UO_2.   The powder blend was then compacted at 75 MPa to produce granules. These granules were then uniaxially pressed at 400 MPa. Pellets were sintered at a heating rate of 5 °C min^{-1} to 300 °C and then 15 °C min^{-1} to 1730 °C. The pellets were sintered for 300 minutes in a 99.5 vol.% H_2 and 0.5 vol.% CO_2 atmosphere.   The pellets were cooled at a rate of 15 °C min^{-1} to room temperature [136]. A detailed description of the fabrication process and materials characterisation of the pellets can be found in Hiezl *et al.* [136]. Figure 2.1 shows the resulting SIMFuel pellet.
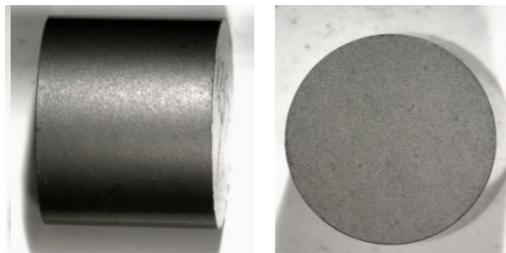
Figure 2.1: SIMFuel pellet [98].

For the majority of the elements represented in SIMFuel there is no significant alteration in wt% with time. However, during the 100 year period post irradiation, ^{90}Sr decays to ^{90}Zr and ^{137}Cs decays to ^{137}Ba.   Therefore, in the time-scale of interim storage, concentrations of Sr and Cs will be higher and concentrations of Zr and Ba will be lower for real irradiated fuel than in the SIMFuel samples

used [98].

Dopant	wt% 25GWd/tU	wt% 43GWd/tU
UO_2	95.705	92.748
Nd_2O_3	0.761	1.284
ZrO_2	0.793	1.284
MoO_3	0.614	1.027
RuO_2	0.512	0.892
$BaCO_3$	0.328	0.576
CeO_2	0.297	0.499
PdO	0.195	0.425
Rh_2O_3	0.080	0.115
La_2O_3	0.156	0.256
SrO	0.081	0.126
Y_2O_3	0.095	0.149
$CsCO_3$	0.311	0.495
TeO_2	0.073	0.130

Table 2.3: The measured composition of AGR SIMFuel pellets with different burn-ups.

Some key physical differences between the SIMFuel samples and pure UO_2 are highlighted in Table 2.4. The change in density is due to the porosity of the doped SIMFuels. This is most likely caused by air being trapped during final compaction or secondary phase formation during oxide reduction [136]. The reduction of grain size with increasing burn-up is an effect not seen in real irradiated fuel where the average grain size is in fact expected to increase slightly [7]. This reduction is probably due to one of the dopants restricting grain growth during sintering [136].

	Undoped UO_2	25 GWd/tU	43GWd/tU
Grain size	9.7±2.3 μm	4.21±0.59 μm	2.95±1.3 μm
Density	10.62 g cm^{-3}	9.76 g cm^{-3}	9.67 g cm^{-3}
R_u (current interrupt @1.2 V)	1386.51 Ω	108.17 Ω	77.39 Ω

Table 2.4: Properties of undoped UO_2 and SIMFuels [136].

2.1.4 Heat Treatment Process for Stainless Steels

Stainless steel samples were heat treated in an attempt to mimic the grain boundary sensitisation seen for RIS-affected cladding. An overview of the mechanism of sensitisation is given in section 1.9.4. The heat treatment processes used are described in sections 2.1.4.1 and 2.1.4.2 below. These regimes are then summarised in Table 2.5, also below.

2.1.4.1 Treatment of 20/25/Nb Stainless Steels

The 20/25/Nb SS samples were solution annealed at high temperatures in an effort to dissolve NbC. Literature suggests for 20/25/Nb SS to be at least in part annealed it should be kept at 1093-1179 °C [95, 96]. However, excessive grain growth may occur at very high temperature [148]. For this reason, experimentalists have suggested an annealing temperature of 1050 °C [148, 149]. Based on previous experimental data, a maximum concentration ∼0.01 wt% carbon could be present in solid solution at 1050 °C for a Nb content of 0.56 wt% [150]. This may not be enough carbon to induce sensitisation of the SS. Increasing the annealing temperature to 1150 °C would increase the free carbon concentration to 0.027 wt% providing a greater chance for the formation of chromium carbides during subsequent ageing treatment [82].

The solution annealing process involved first heating the as-received sample to high temperatures of either 1050 °C and 1150 °C and then rapidly quenching in order to retain any carbon released in solid solution, thereby increasing the carbon available to react with chromium when subsequently given a sensitising heat treatment. To achieve this, the cladding samples were first vacuum-sealed in quartz tubes to suppress oxidation. The samples were then heated to their respective annealing temperatures and held there for 30 minutes. They were then quenched by putting the quartz tubes into a water bath and quickly breaking them. After solution annealing the samples were thermally aged for 48 hours at 600 °C in an argon atmosphere.

2.1.4.2   Treatment of 304H Stainless Steels

The 304H SS samples were thermally aged without any pre-treatment. 304H SS does not have a deliberate Nb addition - thus all of the constituent carbon is already available in solid solution in the as-received samples. 304H SS was therefore aged in as-received condition with no annealing necessary [151–153]. The ageing treatment was performed in air because the accompanying oxidation associated with the treatment can be easily machined off after the ageing is complete. Ageing was carried out at 550 °C and 600 °C. The samples were heated for periods between 24 and 1000 hours, with the longer ageing times used for the lower temperature only.

A full list of heat treatment regimes used for each sample prepared is given in Table 2.5. Grain boundary profiles were assessed by colleagues at the UK National Nuclear Laboratory (NNL) using Transmission electron microscopy (TEM). Due to restricted availability of the TEM only three 304H SS samples were assessed; 48 hours at 600 °C, 72 hours at 600 °C and 500 hours at 550 °C. Grain boundary profiles are shown in the relevant later chapters. All three grain boundaries were found to be decorated with chromium precipitates, with the chromium content adjacent to these precipitates dipping to approximately 15 wt% in the sample aged for 48 hours and to less than 10 wt% in the latter two samples. Grain boundary profiles of 20/25/Nb SS solution annealed for 30 minutes and ages for 48 hours at 600 °C have previously shown chromium concentrations to drop to as low as 10 wt% at the grain boundaries [154].

Material	Solution Annealing		Thermal Ageing Treatment	
	Temperature /°C	Time /hours	Temperature /°C	Time /hours
304H	-	-	-	0
	-	-	550	1000
	-	-		750
	-	-		500
	-	-	600	96
	-	-		72
	-	-		48
	-	-		24
20/25/Nb	-	-		0
	1050	0.5	600	48
	1150	0.5	600	48

Table 2.5: Experimental samples and their heat treatment periods.

Experiments have been conducted by the NNL to show the susceptibility of these heat treated samples to IGSCC and the results are published by Whillock *et al.* [82]. In terms of the selection criteria for a suitable analogue, listed in section 1.9.6, the following was found:

1. 304H SS samples heat treated at 550 °C for 500 hours underwent IGSCC at 45 °C but not at 30 °C

2. 304H SS samples heat treated at 550 °C for 750 hours did not exhibit signs of IGSCC at 30 °C

3. 304H SS samples heat treated at 550 °C for 1000 hours did not reliably undergo IGSCC at 30 °C

4. 304H SS samples heat treated at 600 °C for 24 hours and 96 hours showed no signs of IGSCC

5. For 304H SS samples heat treated at 600 °C for 48 hours IGSCC was seen at 60 °C but not at 30 and 45 °C

6. For 304H SS samples heat treated at 600 °C for 72 hours IGSCC was present

at 30 and 45 °C, IGSCC was also inhibited by dosing the test solution to pH$\simeq$11.4 at 24 °C

As such the experiments described in this thesis focused on 304H SS aged for 48 hours at 600 °C and 304H SS heat treated at 600 °C for 72 hours.

2.1.5   Sample Preparation

The SS samples were mounted on brass bases and set in an epoxy resin mold to form a ring electrode. The exposed surface is a cross-section of the cladding tubes. The surface of the samples were prepared by polishing using a series of abrasives with decreasing size/grade of grit, specifically silicon carbide sandpaper 240 – 1200 standard grit and then diamond paste of 6 μm – 1 μm. The samples were then washed with deionised water on a polishing pad. Polished electrodes of 20/25/Nb SS and 304H SS can be seen in Figure 2.2. The surface areas of the samples are 0.2428 and 1.4045 cm^2 respectively.

(a)   (b)

Figure 2.2: Electrodes of (a) 20/25/Nb SS and (b) 304H SS.

Likewise, the UO$_2$ and SIMFuel samples were mounted on brass bases using silver loaded epoxy and set in an epoxy resin mold to form a disk electrode. The surface of the samples were finished by polishing using silicon carbide sandpaper (600 standard grit). A polished UO$_2$ electrode is shown in Figure 2.3.
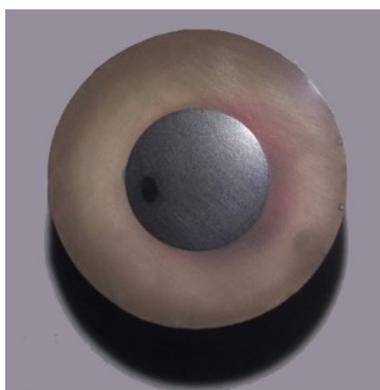
Figure 2.3: UO$_2$ electrode.

2.1.6 Experimental Set-up for Electrochemical Techniques

All electrochemical studies were carried out using a Metrohm Autolab potentiostat model PGSTAT128N using NOVA^{TM} control and data acquisition software. A three electrode cell was employed using a platinum mesh counter (Advent Research Materials Ltd, Oxford, England) and a silver silver chloride, Ag/AgCl, electrode as the reference electrode (Alvatek electrochemical solutions, England). A diagram of the experimental set-up is shown in Figure 2.4.
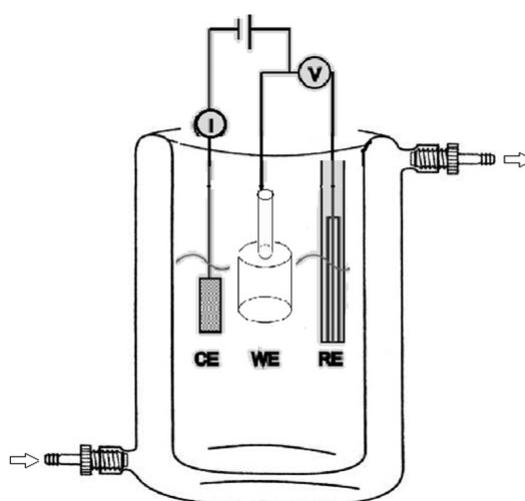
Figure 2.4: Schematic of the experimental set-up for electrochemical experiments, with CE as the counter electrode, WE as the working electrode and RE as the reference electrode.

Linear sweep voltammetry studies on SS sample electrodes immersed in various different solutions were carried out at a scan rate of 1 mV/s over a potential range of -0.8 to 1.5 V, except if otherwise indicated.

Cyclic voltammetry studies on UO_2 and SIMFuel sample electrodes immersed in solution were carried out at a scan rate of 10 mV/s over a potential range of -1.8 to 0.4 V, unless otherwise stated. The electrode was held at -1.8 V for 5 minutes prior to sweeping the potential in order to further remove any absorbed species and altered surface microstructure that may still be present due to the limited polishing [155]. IR compensation was utilized during the voltammetric experiments on account of the resistive nature of UO_2 and SIMFuel electrodes [116].

Those experiments carried out at elevated temperatures used a water-jacketed electrochemical cell, where water was circulated with a pump and a water bath was used to increase the temperature of the solution. The temperature was measured using an alcohol thermometer. For experiments carried out at 90 °C, this method was unable to reach such a high a temperature so solutions were heated using a hot plate. Note, the Ag/AgCl reference electrode has a temperature dependence such that E(mV)=199-1.01*(T-25 °C), where E(mV) is the potential vs NHE and T is the temperature in degrees Celsius [156]. The potential values were adjusted accordingly.

2.2   Electrochemical Characterisation Techniques

2.2.1   Linear Sweep and Cyclic Voltammetry

Linear sweep voltammetry (LSV) involves sweeping the voltage from a start potential to a final potential at a given scan rate (V/s) typically less than 10 mV/s and measuring the response of the current. It is common for the results of an LSV to be analysed using a log current density versus potential plot, also known as

polarisation curves. An example of such a plot is shown in Figure 2.5. These plots allow active, passive and transpassive regions to be identified, with related electrochemical corrosion concepts being discussed in more detail in section 1.6.
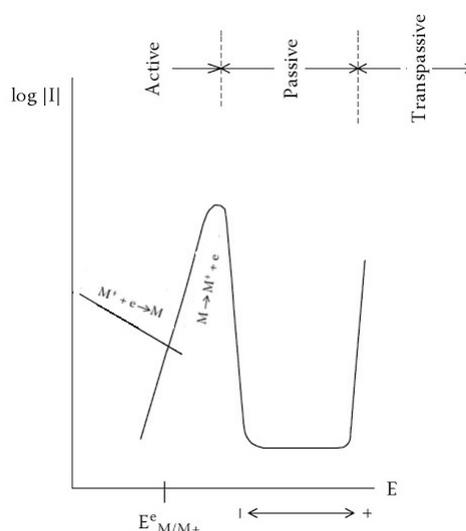
Figure 2.5: Example of a polarisation curve for a metal, with three distinct regions: region of active dissolution, region of passivity and the region of transpassivity [157].

Cyclic voltammetry (CV) is similar to LSV save that: (i) the potential is typically swept at a scan rate faster than 10 mV/s; and (ii) the potential is swept from a start potential or first potential limit to a switching potential or second potential limit and then back to the start potential. The latter allows the full range of oxidation and reduction processes (not seen using LSV) on the surface of the electrode to be seen. Positive current peaks in positive going potential scans indicate oxidation processes whereas negative current peaks in a negative going potential scan indicate reduction processes. Such peaks can be seen in the sample CV in Figure 2.6.
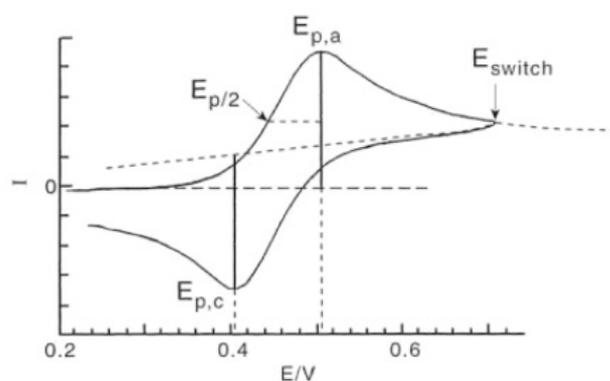
Figure 2.6: Example of a cyclic voltammogram, with $E_{p,a}$ indicating the anodic or oxidation peak potential and $E_{p,c}$ is the cathodic or reduction peak potential [158].

2.2.2   Chronopotentiometry

Chronopotentiometry is the measurement of open circuit potentials (OCPs) as a function of time. It is used to determine the equilibrium potential of an electrode in a particular solution over time. By examining where the OCP lies on either an LSV or CV it is possible to predict the nature of the surface if no external electrochemical stresses are applied.

2.2.3   Testing for Degree of Sensitisation

A stainless steel is considered sensitised if the Cr concentration at the grain boundaries drops below 12 wt%, leaving the SS vulnerable to localised corrosion. The presence of sensitisation can be measured experimentally via either chemical etching or electrochemical etching. In this study both methods were employed with the set up specifics described below.

2.2.3.1   Etching with Oxalic Acid

In order to test for sensitisation, stainless steels were etched using a 10 %(w/v) oxalic acid solution with a voltage of 6 V applied to the stainless steel for 15 seconds.   Cr rich features, austenite grain boundaries and carbides/precipitates are attacked by this process [159]. If there is greater attack

at the grain boundaries, it may signify the presence of chromium carbides and the formation of Cr depleted regions adjacent to these carbides. Imaging of the surface after etching reveals whether the microstructure is sensitised and is classified according to ASTM standard A 262 [160]:

- A step-like structure is indicative of an unsensitised sample.

- A dual structure, when both ditching and steps are observed but no grain is completely encircled, calls for further electrochemical investigation to determine the degree of sensitisation (see below).

- Complete ditching around the grains suggests increased susceptibility to intergranular attack.

Examples of possible microstructures are shown in Figure 2.7.

(a) (b)
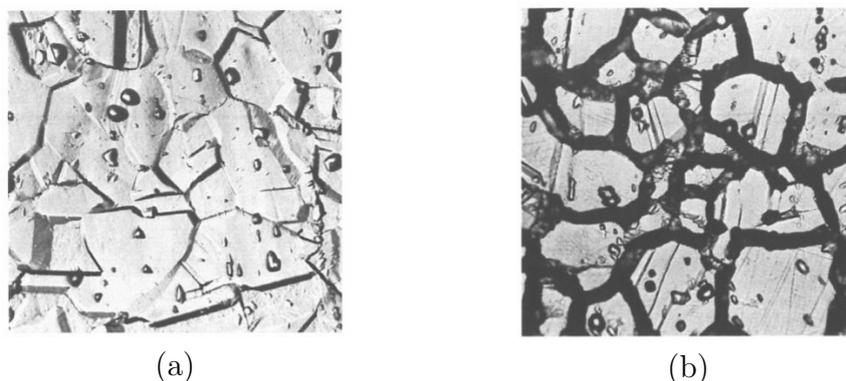
Figure 2.7: Examples of (a) step-like structures and (b) ditch structures resulting from oxalic acid etching [160].

2.2.3.2 Double Loop Electrochemical Potentiokinetic Reactivation Test

The Double Loop Electrochemical Potentiokinetic Reactivation (DL-EPR) test is an alternative method used to check for the sensitisation of stainless steels. This test involves immersing a working electrode into a solution containing 0.5 mol dm^{-3} H_2SO_4 and 0.01 mol dm^{-3} KSCN, in the same three electrode configuration as with cyclic and linear sweep voltammetry. The potential is swept, at a scan rate of 1.6 mV/s, from the hydrogen evolution region to a potential where it is

suspected that a passive layer is developing on the surface. This is the activation process. It is held at this potential for 2 minutes to allow the passive film to form. Then the potential is scanned back to the starting point. This is the reactivation step. On the reverse scan, the passive film tends to preferentially dissolve at areas with chromium depletion. The ratio of the reactivation peak to the activation peak gives a value for the degree of sensitisation. Generally, it is accepted that if a material is significantly sensitised the ratio will be greater than 0.5 and if the ratio is less than 0.1 no sensitisation is present in the sample [161, 162]. An example of a typical potential scan is shown in Figure 2.8.
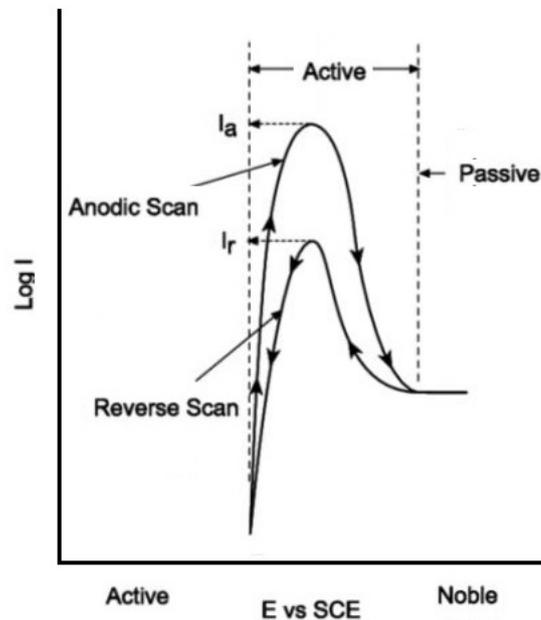
Figure 2.8: Typical potential scan for the DL-EPR test [163].

2.2.4   Electrochemical Impedance Spectroscopy

Impedance is the total opposition an electrical circuit has to the flow of an alternating current. The impedance (Z) is analogous to resistance in Ohm's law and is defined as the ratio of potential (E) to current (I).

$$Z = \frac{E(t)}{I(t)} \tag{2.1}$$

Electrochemical impedance spectroscopy (EIS) involves applying a small

sinusoidal potential to the working electrode and scanning the frequency between 10,000 and 0 Hz. This produces a sinusoidal current response which can be measured and analysed in accordance with Ohm's law, to extrapolate impedance information. Figure 2.9 shows an example sinusoidal input potential and corresponding sinusoidal output current.
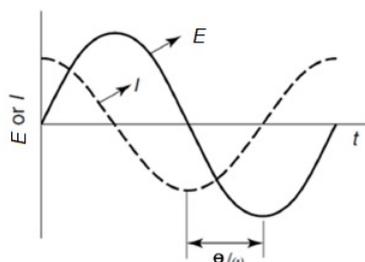
Figure 2.9: Sinusoidal potential perturbation and current response [164].

Impedance has both magnitude and phase and therefore is a vector quantity. Thus, it can be expressed using complex notation via the following equation:

$$Z = Z_0(cos\theta + jsin\theta) = Z' + jZ'' \tag{2.2}$$

where Z' is the real component and Z'' is the imaginary component of impedance. Plotting the imaginary versus the real components of impedance produces what is known as a Nyquist plot. An example of which is shown in Figure 2.10. These plots can be analysed using equivalent circuit modelling (see section 2.2.4.1) to acquire an insight into corrosion behaviour, such as whether passivation or active dissolution is occurring.
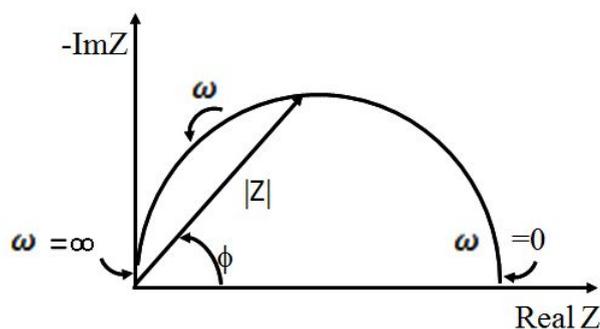
Figure 2.10: Nyquist plot representing the impedance in the complex plane. ω is the frequency of the applied signal and ϕ is the phase angle [165]

However, Nyquist plots offer no frequency information. This can be obtained by using a different plot, the Bode plot. A Bode plot shows the magnitude of the impedance and the phase angle as a function of the logarithm of the frequency. Plateaus in the magnitude versus frequency plots represent the cumulative resistances and slopes the influence of capacitive elements. Each peak in the phase angle plot represents a relaxation constant[1]. An example of such a plot is shown in Figure 2.11.
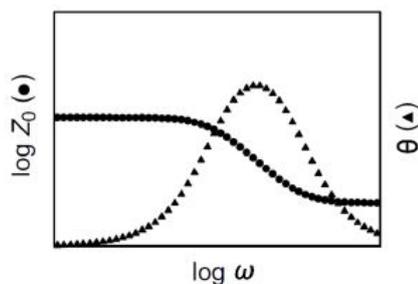
Figure 2.11: Example of a Bode plot; where log ω is the logarithm of the radial frequency, θ is the phase angle and log Z_0 is the logarithm of the magnitude of the impedance [164].

2.2.4.1   Equivalent Circuit Modelling

One of the most common methods for extracting information from either Bode or Nyquist plots is equivalent circuit modelling. The models are described using traditional electrical components (capacitors, resistors, inductors etc.), as

---

[1]Relaxation describes the mobility of molecules at the surface of the material and is related to the resistance and capacitance of the process (e.g. passive layer formation) [166]

well a some more electrochemical specific components. The selected circuit should represent the physical electrochemical system in question [164]. An equivalent circuit with at least three components is necessary to describe a faradaic process such as oxidation and reduction [167]. The Randle cell, seen in Figure 2.12, is a widely used simple model for faradaic processes at a metal-solution interface [164]. The three components here are:

1. R_s: the resistance of the solution between the reference and working electrodes,

2. R_p or R_{ct}: the polarisation resistance or the charge transfer resistance

3. C_{dl}: the electrochemical double layer capacitance.

The Randle cell is a good starting point for the development of more complex models needed to describe different processes. When an appropriate circuit model has been designed, computer modelling software, such as Zview2 (Scribner Associates, UK), can be used to fit the model to the impedance data. Through this analysis, electrical properties of the system, such as R_s, R_p and C_{dl} can be extracted from the data set, allowing for the characterisation of the metal-solution interface.
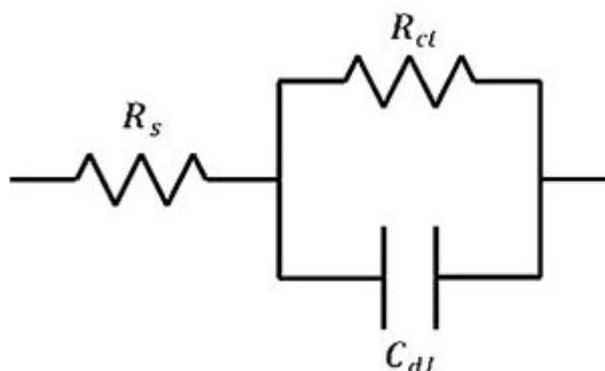
Figure 2.12: Electrical equivalent circuit model used to represent an electrochemical interface undergoing corrosion in the absence of diffusion control (Randle cell).

2.2.4.2   Mott-Schottky Analysis

Semiconductors are materials that have small band gaps between their valence and conduction bands. This is in contrast to metals where the bands overlap, thus allowing for free motion of electrons and electron vacancies (holes) as charge carriers via thermal promotion within the band structure, and insulators where the band gap is typically many times larger than kT, so preventing the flow of charge by simple thermal promotion of electrons within the band structure.

The flow of electrons and holes is critically controlled by the presence of impurities within the semiconductor crystal structure. At 0 K in metals, all available energy states will be occupied up to a particular energy level, this energy level in known as the Fermi level [168]. At temperatures greater than 0 K the Fermi level corresponds to the energy level at which the probability of that level being occupied by an electron is 0.5. In accordance with the latter definition, the Fermi level lies in the centre of the band gap in a pure or intrinsic semiconductor.

The Fermi level shifts with the introduction of impurities. N-type semiconductors contain impurities with filled electron energy levels that lie just below the lowest energy of the conduction band or conduction band edge. These impurities may then be thermally ionised by electron excitation into the conduction band where they may move freely and so carry current. The electrons are then termed the majority carriers and the n-type impurities referred to as electron donors [169]. In such n-type semiconductors, the Fermi level shifts towards the conduction band and, to a first approximation, can be identified with the conduction band edge.

In contrast, p-type semiconductors contain impurities with empty electron energy levels that lie just above the highest energy of the valence band or valence band edge. These impurities may accept electrons that have been thermally promoted from the valence band, leaving behind a valence band electron vacancy or hole with a net positive charge that may then move freely and so carry

current. The holes are then termed the majority carriers and the p-type impurities referred to as electron acceptors [169]. In such p-type semiconductors, the Fermi level shifts towards the valence band and, to a first approximation, can be identified with the valence band edge.

When a semiconductor is immersed in an electrolyte, there is an associated charge area at the semiconductor electrolyte interface, known as the space charge layer [170]. There are three main types of space charge layers; accumulation, inversion and depletion – and the character of this layer can be controlled by electrochemical application of an applied potential to the semiconductor. In an accumulation layer there is a build-up of the majority charge carrier within the layer [171]. In a depletion layer there is a build-up of the minority charge carriers within the layer. Note that the minority charge carriers are electrons for p-type semiconductors and holes for n-type semiconductors. In an inversion layer the layer is devoid of majority charge carriers and therefore minority charge carriers are in excess [171]. Under such circumstances, the space charge layer of the semiconductor behaves as if it were of the opposite type i.e. the space change layer of an n-type electrode under inversion behaves as a p-type semiconductor and vice versa.

Let us consider the depletion case in detail first. For an n-type semiconductor electrode at open circuit, the energy of the Fermi level is typically higher than the redox energy level of the electrolyte, and hence electrons will be transferred from the electrode into the solution until equilibrium is reached. During equilibration the energy of the Fermi level shifts down in energy, as do the conduction and valence bands in the semiconductor bulk. However, the band edges at the semiconductor-electrolyte interface are fixed by the pH of the electrolyte (if the electrolyte is an aqueous solution) and remain unchanged. This is reflected in an apparent upward bending of the band at the semiconductor-electrolyte interface [170]. Due to the loss of electrons from the semiconductor surface there is a positive charge associated with the space charge

region.

In the case of a depletion layer, for a p-type semiconductor, the energy of the Fermi layer is generally lower than the redox energy level in the electrolyte and hence electrons must transfer from the solution to the electrode to attain equilibrium. In this case, the energy of the Fermi level moves to a higher energy level, as do the conduction and valence bands in the bulk. The energies of the band edges, as with n-type semiconductors, are pinned at the surface and thus do not shift in the equilibration process. This causes an apparent downward bending in the band at the semiconductor-electrolyte interface [170]. This generates a negative charge in the space charge region.

Post-equilibration, the extent of this bending can be controlled by application of an electrochemical potential to the semiconductor. Depending upon the direction of application of the potential (i.e. its sign) and its magnitude, this can lead to an increase in the apparent bending or a decrease – or a reversal of the direction of the band bending altogether.

This latter scenario can lead to the formation of an accumulation layer. Thus, in this regime, n-type semiconductors exhibit a downward bending of the bands and p-type semiconductors exhibit an upwards bending of the bands [170]. Under accumulation, the density of majority carriers in the space charge layer is so high that it behaves as a pseudo-metal.

At an applied potential known as the flat-band potential (E_{FB}) no band bending occurs and the electrostatic potential is zero throughout the semiconductor, the flat-band potential is material and electrolyte – especially electrolyte pH – dependent. Again, applying a potential bias to semiconductor materials causes the Fermi level to shift driving the semiconductor into accumulation, depletion or inversion at the semiconductor-electrolyte interface and as a consequence the band-bending changes with applied potential (E) [172, 173]. Figure 2.13 shows how the bands bend at the semiconductor/electrolyte interface with an applied potential, n-type

semiconductors (a-c) and p-type semiconductors (d-f).
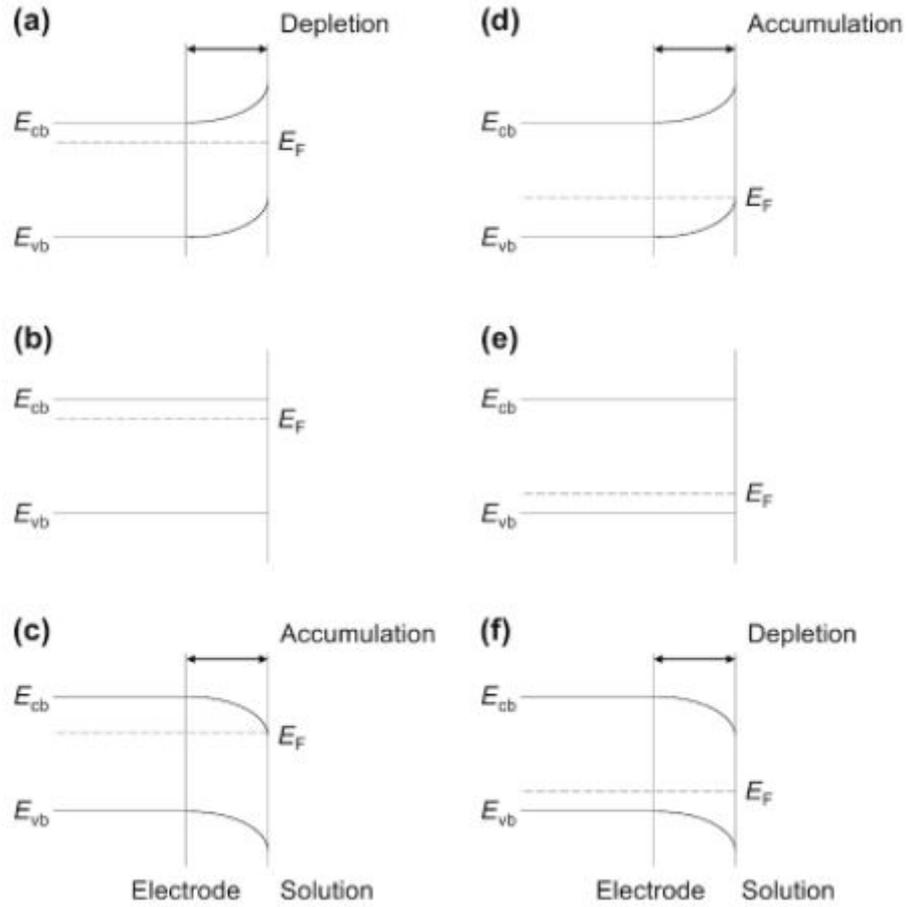
Figure 2.13: Schematic of the semiconductor/electrolyte interface with an applied potential, n-type semiconductors (a-c) and p-type semiconductors (d-f). (a) and (d) E>E_{FB}, (b) and (e) E=E_{FB} and (c) and (f) E<E_{FB} [172].

There is an apparent capacitance related to the space charge layer at the semiconductor-electrolyte interface. The Mott-Schottky equation describes the relationship between the capacitance of the space charge layer and the applied potential as follows:

$$\frac{1}{C^2} = \frac{2}{\varepsilon\varepsilon_0 A^2 q N_D}(-E + E_{FB} + \frac{k_B T}{q})$$ (2.3)

where ε is the dielectric constant of the semiconductor, ε_0 is the permittivity of free space, A is the surface area, q is the elementary charge, N_D is the dopant density, E is the applied potential, E_{FB} is the flatband potential, k_B is the Boltzmann constant and T is the temperature.

In a Mott-Schottky plot the inverse capacitance squared is plotted as a function of the applied potential. This plot may show a linear relationship; if the slope is positive the semiconductor is of an n-type character and if the slope is negative the semiconductor is p-type. Applying this analysis to the data extracted using equivalent circuit models allows the prediction of the composition of the passive layer forming on the surface of the electrodes.

2.2.5   EIS set-up

EIS experiments were set up using the same 3 electrode cell as previously described for voltametry experiments. For stainless steels EIS measurements reported here were started at -0.6 V and were scanned up to 1.2 V. For UO_2 and SIMFuels, EIS measurements reported here were started at -1.5 V and were scanned up to 0.4 V. For all samples, the potential was held every 0.1 V and the frequency scanned between 100,000-0.1 Hz.

2.3   Surface Analysis Techniques

2.3.1   Scanning Electron Microscope

A scanning electron microscope (SEM) is an electron microscope that scans the surface of a solid sample with a focused electron beam to produce images of said surface. The electron in the beam either pass through the sample or are scattered by the sample. The scattered electrons that result in the production of an SEM image are known as secondary electrons, although imaging using backscattered electrons is also a widely used feature of SEM machines.

Secondary electrons are a result of inelastic interactions with the surface or near-surface of the sample. The secondary electrons are useful for imaging the topography of the surface as the electrons are distinguished by the distance travelled to detector [174]. Backscattered electrons originate from deeper in the sample than secondary electrons and are produced by elastic interactions.

Interactions with heavier atoms give rise to strong signals whereas lighter atoms produce weaker signals. Therefore, the number of electrons reaching the detector is proportional to the atomic number [174]. This builds a compositional map of the surface. Figure 2.14 gives a schematic representation of a SEM machine.
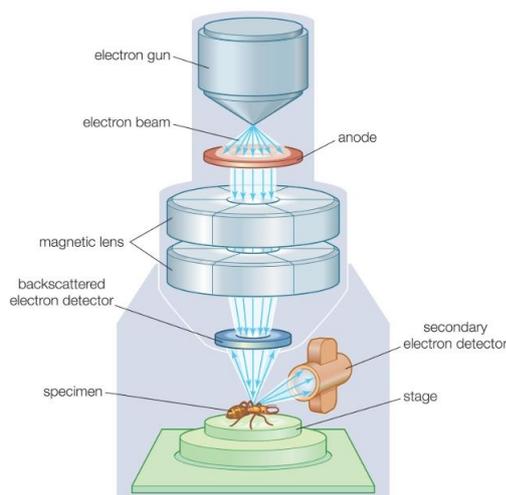
Figure 2.14: Schematic example of a scanning electron microscope [175].

SEM images of the stainless steel electrode surfaces presented in the results section of this thesis were taken using a 6010PLUS SEM-EDS (JEOL, UK).

2.3.2 X-ray Photoelectron Spectroscopy

X-ray Photoelectron Spectroscopy (XPS) is a surface analysis tool that allows the user to measure elemental compositions, determine empirical formula and the chemical and electronic states within the surface layer of a material. XPS has a sampling depth of 3λ, where λ is the inelastic mean free path of an electron in a solid, this is derived from the Beer-Lambert law[2] [176]. Penetration depths are typically between 3 and 30 nm. The basic principle behind XPS is the emission of electrons from an atom or ion due to its interaction with a photon of sufficient energy. The photon is annihilated during this process and total energy transfer to the electron occurs. The kinetic energy of these so called photoelectrons is measured. The kinetic energy is a function of the binding energy of the electron

---

[2]The Beer-Lambert law describes the change in electron intensity via the following equation: $I = I_0 e^{-d/\lambda}$ [176]

and this has a unique value for each element [177]. Figure 2.15 shows a basic schematic for this technique. In general, the results of XPS are presented as energy spectra, spatial images and depth profiles.
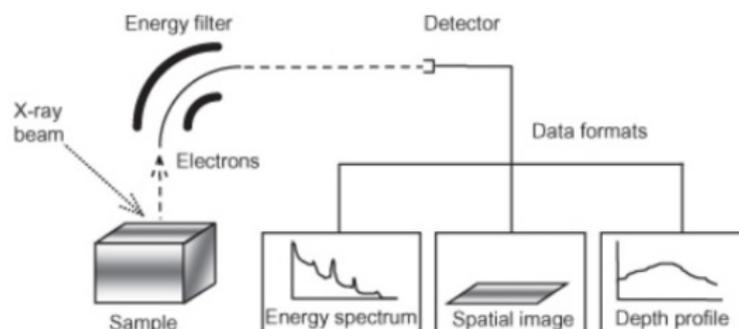
Figure 2.15: Schematic example of an XPS instrument and the three most common ways of relaying the data [177].

For the work presented in this thesis, XPS experiments were carried out on polished 20/25/Nb SS samples at the NEXUS facility at Newcastle University using Thermo Scientific K-Alpha XPS System with a monochromated Al K-alpha X-ray source (1486.6 eV, 12 mA with 15 kV bias). XPS experiments post exposure to simulant pond water were carried out at the School of Materials at Manchester University. The spectrometer was a Kratos Axis Ultra Hybrid using a monochromated Al K-alpha X-ray source (1486.6 eV, 12 mA with 15 kV bias). XPS was performed on as-received sample of 20/25/Nb SS and 304H SS, a sample of 20/25/Nb SS solution annealed at 1150 °C and aged for 48 hour at 600 °C and a 304H SS sample thermally aged for 48 hours at 600 °C. All four samples were immersed in simulant pond water at ∼24 °C, pH≃11.4, for one week. The samples were then dried using nitrogen gas and immediately transferred to the XPS chamber.

Quantitative analysis was carried out at two points on each sample and the data reported is an average of the obtained spectra. Spectra were curve fitted using Shirley background subtraction and a mixed Gaussian-Lorentzian (70:30) function. CasaXPS software (Casa Software Ltd) was used to complete this analysis.

2.3.3 Raman Spectroscopy

Raman spectroscopy is a surface analysis technique that uses molecular vibration information to identify the composition and crystal structure of a material. When light scatters it is either an elastic (Rayleigh scattering) or an inelastic (Raman scattering) process. Raman spectroscopy relies on Raman scattering, this involves a shift in the wavelength (and frequency) of light when it interacts with a molecule. The shift in wavelength is dependant on the molecular vibration and rotational energies of a particular atom or ion. Increases in the wavelength of a photon of light is called a Stokes shift and decreases in wavelength an anti-Stokes shift. In Stokes scattering, energy is absorbed by the molecules and in anti-Stokes, energy is transfer from the molecule, thus at room temperature, when molecules are in their ground state Stokes scattering will dominate. The change in energy is dependant on the chemical bonds and the structural symmetry in the material and therefore can be used to extract useful information about the materials composition and crystallinity. Raman spectra show the intensity of the scattered light as a function of wavenumber (1/wavelength), due to its linear relationship with energy. [178, 179]

In this project, Raman spectroscopy has been used for the determination of the surface state of the UO_2 and SIMFuel samples. This analysis was performed using a Voyage confocal Raman microscope (B & W Tek, Newark, USA) with an excitation wavelength of 785 nm. The penetration depth of the 785 nm laser used in the Raman spectroscopy reported in this thesis is $\sim$12 μm [180]. To prevent the thermal oxidation of UO_2 to U_3O_8 the laser power was set to <5 mW using neutral density filters [181]. The laser beam was focused using a 50x objective lens. Spectra were obtained over a wavenumber range of 190 to 3000 cm^{-1} with an integration time of 40 seconds. For each sample considered, 20 spectra were obtained at different sites across the surface of the sample and the spectra were background subtracted. An average of these spectra was recorded. Sites at or near large noble metal particles or grey-phases were avoided so as to determine

the degree of oxidation of the bulk UO_2 or SIMFuel matrix.

Chapter 3

AGR fuel cladding - Unsensitised 20/25/Nb Stainless Steel

This chapter of work focuses on the corrosion behaviour of unsensitised AGR fuel cladding, 20/25/Nb stainless steel. The reasons for studying unsensitised material are threefold: (i) substantial amounts of cladding will not become sensitised in reactor; (ii) working on real irradiated cladding is challenging from both radiological safety and economic perspectives and (iii) representative analogues of RIS-affected 20/25/Nb SS, whilst under development, still do not fulfil all criteria required of such simulant materials. Therefore, in the first instance unirradiated 20/25/Nb SS is studied to set a baseline for the steel corrosion behaviour before proceeding on to subsequent studies of novel sensitised simulant samples.

The surface of a fuel cladding pin consists of 3 distinct surfaces, the top of the rib, the side of the rib and the surface of the cylindrical shaft. Hence, examining the cross section of a cladding pin gives a simplified system with a homogeneous reproducible surface and the preparation of the studied surface, in contrast to the cladding inner and ribbed outer surface, is wholly under our control. All experiments are carried out using electrodes where the exposed surface is the cross-section of the cladding as shown in Figure 2.2 (a). The electrochemical behaviour of the outer cladding surface was investigated and is included in Appendix A for the interest of the reader. It is found that the cross-section is largely representative of the outer clad surface. The explicit differences and similarities are highlighted

in Appendix A.

The studies on 20/25/Nb SS cladding reported in this section provide information on the corrosion behaviour under various pond water conditions such as altered pH, varying chloride concentration, increasing temperatures and the presence of hydrogen peroxide.

3.1   Degree of Sensitisation

In the first instance, it is necessary to baseline the as-received sample of 20/25/Nb SS and to demonstrate by comparison with the literature that the sample is in fact unsensitised. Thus, both qualitative and quantitative degree of sensitisation tests (as discussed in Section 2.2.3) were performed.

3.1.1   Electrochemical Etching of Unsensitised 20/25/Nb SS

Electrochemical etching was performed by exposure of the sample to 10 %(w/v) oxalic acid solution for 15 seconds with an applied voltage of 6 V. Pre and post exposure, the sample was analysed through the inspection of the surface images, obtained using a scanning electron microscope (SEM). Figure 3.1 shows the acquired SEM images. The unetched samples are broadly featureless, whilst the etched surfaces exhibit step-like structures, the most obvious of which are highlighted in the red boxes of Figure 3.1(b). The step structure results from the different dissolution rates of each grain depending on their orientation [162]. The absence of any obvious ditches at grain boundaries indicates a sensitisation-free surface [160]. These findings are in agreement with similar studies performed on identical as-received 20/25/Nb SS samples by Chan *et al.* [182]. Due to the lack of ditching, grain size is difficult to infer from the images of Figure 3.1; however, in their work, Chan *et al.* observe a grain size of $\sim$10 μm, measured using electron backscatter diffraction (EBSD) [182].

(a) (b)
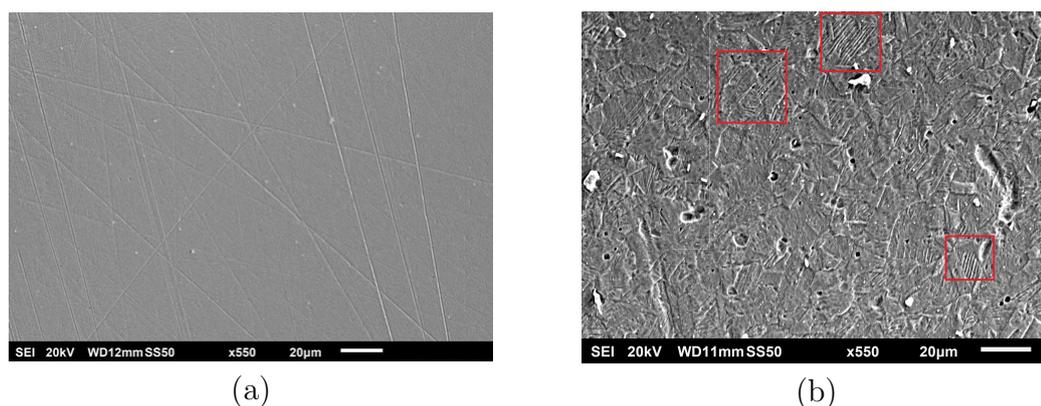
Figure 3.1: SEM image of unsensitised 20/25/Nb SS (a) pre- and (b) post-exposure to oxalic acid at an applied potential of 6 V for 15 seconds.

3.1.2 Double Loop Electrochemical Potentiokinetic Reactivation Tests on Unsensitised 20/25/Nb

Double loop electrochemical potentiokinetic reactivation tests were carried out on the stainless steel sample. The results of which can be seen in Figure 3.2. The ratio of the activation peak to the reactivation peak is found to be 0.015, which is in agreement with the literature value for unsensitised materials [161, 162].
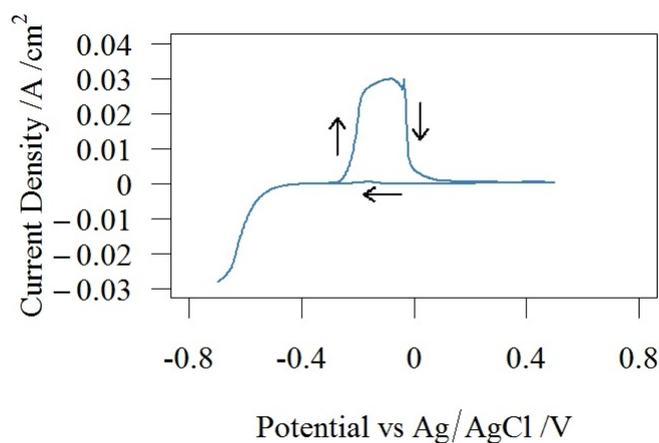
Figure 3.2: DL-EPR curve of unsensitised 20/25/Nb SS in solution of 0.5 mol dm^{-3} H$_2$SO$_4$ and 0.01 mol dm^{-3} KSCN at a scan rate of 1.6 mV/s.

3.2   Compositional Analysis of the Passive Film Formed on unsensitised 20/25/Nb Stainless Steel in Simulant Pond Water

Having determined the unsensitised nature of the 20/25/Nb SS sample, this section attempts to analytically determine surface compositions of as-received samples of 20/25/Nb SS and samples that had been immersed in pH$\simeq$11.4 simulant pond water at $\sim$24 °C for one week using XPS.

XPS has been widely used to interrogate the surface of stainless steels but so far the literature shows limited XPS data for 20/25/Nb SS. XPS data was obtained from our 20/25/Nb samples using a Thermo Scientific K-Alpha XPS System for the as-receieved SS and a Kratos Axis Ultra Hybrid XPS for the SS post-immersion as described in section 2.3.2. As the wavelength of the K-alpha X-ray emission of the aluminium source used for these experiments is 0.834 nm, the XPS-measured compositional data reported here corresponds to no more than the top 2-3 nm of the sample surface. Peak assignments were carried out using the NIST X-ray Photoelectron Spectroscopy Database [183]. The binding energies of the four dominant components, Fe, Cr, Ni and O were used as the basis to the analysis performed in this section. During analysis a Shirley background correction was utilised and the peak positions were charge corrected by setting the adventitious carbon (C=C) peak to 284.8 eV. XPS spectra at two points on the stainless steel surface were recorded and the results presented in this section represent the average of these two spectra. Curves were fitted to the XPS spectra using CasaXPS and the results are presented in Figure 3.3 and Figure 3.6. The average binding energy and full width half maximum (FWHM) of the spectra for each of the dominant elements is shown in Table 3.1 and Figure 3.2. For cases where FWHM values were larger than expected it is assumed that two or more phases with similar binding energies may be present.

Component	Assignment	Average Peak Position	FWHM
Fe $2p_{3/2}$	Fe^0	706.96	1.08
	$Fe_2O_3/Fe_3O_4/$ $Fe(OH)_2/Fe(OH)_3/$ $FeOOH/$ Fe spinels	710.25	4.43
Cr $2p_{3/2}$	Cr^0	573.84	1.1
	$C_2O_3/Cr(OH)_3$	576.41	2.99
	CrO_3	579.16	1.52
Ni $2p_{3/2}$	Ni^0	852.87	1.26

Table 3.1: Average peak positions and FWHM values obtained for Fe $2p_{3/2}$, Cr $2p_{3/2}$ and Ni $2p_{3/2}$ in as-received 20/25/Nb SS.

Considering first the as-received 20/25/Nb SS; Figure 3.3 and Table 3.1 report the oxide/hydroxide phases present at the SS surface. The Fe profile of unsensitised as-received 20/25/Nb SS shown in Figure 3.3(a). There are two peaks evident. The first peak at 706.96 eV is due to elemental iron, Fe^0. Due to the broadness of the second peak at 710.25 eV, it is likely that a multiphase oxide is present consisting of iron (III) oxide (Fe_2O_3), iron (II,III) (Fe_3O_4) and spinels such as $FeCr_2O_4$ and $NiFe_2O_4$, which also have binding energies $\sim$710.5 eV. It may also contain contributions from iron hydroxides, $Fe(OH)_2/Fe(OH)_3/FeOOH$, which are also known to present spectral features at $\sim$711 eV.

The chromium profile in Figure 3.3(b) shows three peaks which can be attributed to Cr metal, 573.84 eV, chromium (III) oxide Cr_2O_3, 576.41 eV and chromium (IV) oxide CrO_3, 579.16 eV. The Cr_2O_3 peak at $\sim$577.2 eV may also contain contributions from chromium (III) hydroxide, $Cr(OH)_3$.

The nickel profile seen in Figure 3.3(c) shows a single peaks at 852.87 eV which can be assigned to Ni metal Ni^0.

(a)

(b)

(c)
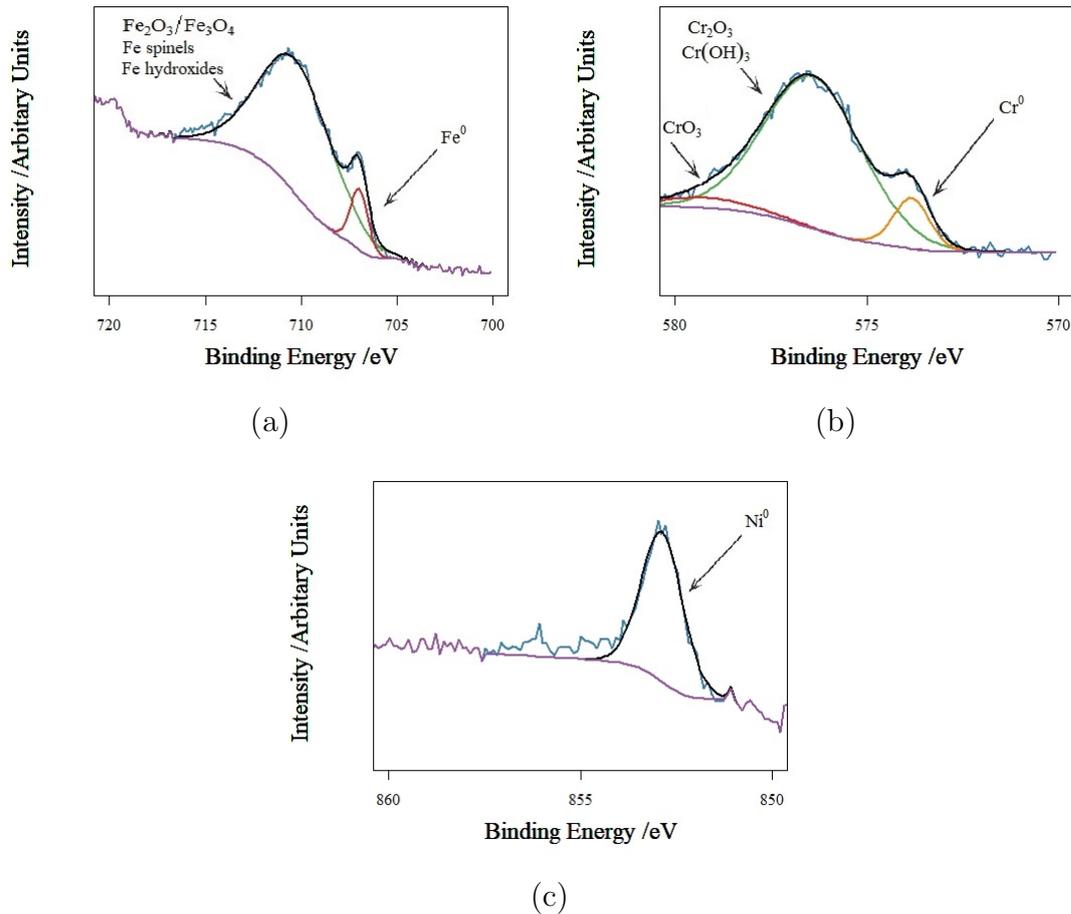
Figure 3.3: XPS profiles of (a) Fe $2p_{3/2}$, (b) Cr $2p_{3/2}$ and (c) Ni $2p_{3/2}$ of as-received 20/25/Nb SS in simulant pond water, pH$\simeq$11.4 at 24 °C.

For ease of interpretation, the full XPS spectrum of 20/25/Nb SS can be represented as a series of bar charts giving the relative atomic percentages of each species observed for the main constituent metals of the steel. Accordingly, in Figure 3.4 bar A, bar B and bar C show such bar charts for the iron, chromium and nickel species observed from the as-received steel respectively. From these, the percentage of oxide/hydroxide present in the passive layer for each of the main constituent metals may be calculated. Specifically, $\sim$90 at% each of the Fe and Cr in the passive layer are present as their respective oxides/hydroxides. In contrast, Ni is present almost entirely as the unoxidised metal.
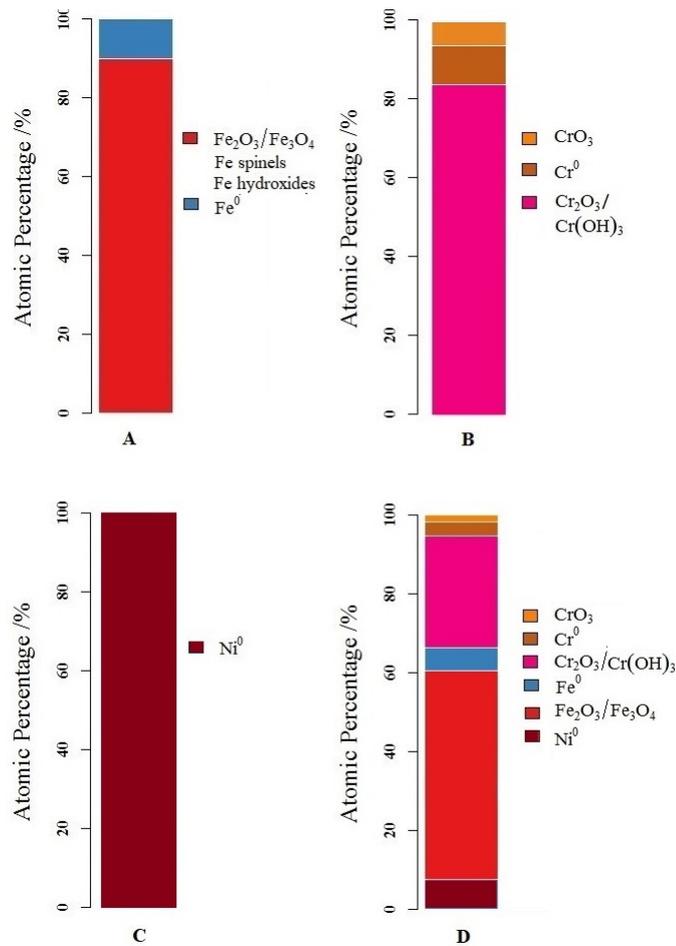
Figure 3.4: Atomic percentage data comparison of **A** Fe $2p_{3/2}$, **B** Cr $2p_{3/2}$ and **C** Ni $2p_{3/2}$ and **D** combined data extracted from XPS profiles of as-received 20/25/Nb SS.

To obtain a more complete description of the true composition of the passive layer, it is necessary to merge the three relative atomic percentage bar charts to obtain a single relative atomic percentage bar chart. This analysis assumes that only these three elements contribute to the passive film and considers only the $2p_{3/2}$ peaks. Since the probability of the emission of a photoelectron is different for each atomic core level and depends on the photon energy of the x-ray source, the intensity of each peak must be normalised by dividing by its unique photoionisation cross-section. The photon energy of the x-ray source used is 1486.6 eV and the relevant cross-sections are reported by Yeh and Lindau in Atomic Data and Nuclear Tables [184]. The resulting bar chart is shown in Figure 3.4 **D**.

This composite bar chart indicates that, as expected from Figure 3.4 **C**, Ni

oxides/hydroxides are absent from the passive layer. It also indicates that CrO_3 comprises only 2 at% of the layer. These results therefore suggest that the electrochemistry and thus the corrosion resistance of as-received 20/25/Nb SS will be dominated by the Cr oxide/hydroxide ($\sim$28 at%) and Fe oxide/hydroxide ($\sim$53 at%) phases.

Before XPS measurements were performed on the immersed samples, simple electrochemical impedance spectroscopy (EIS) measurements where conducted to provide a qualitative initial assessment as to how the composition of the steel passive layer changes as a function of immersion time. Specifically, EIS measurements were conducted every 30 minutes on 20/25/Nb SS immersed in simulant pond water up to a total immersion time of 6 hours. Selected Nyquist and Bode plots from this run are shown in Figure 3.5 from which it can be seen that these plots are invariant with time after only 30 minutes of immersion. In light of this result, it is not unreasonable to assume that the passive layer has stabilised after this relatively short immersion period. As the purpose of the data presented in Figure 3.5 was to simply provide qualitative evidence that the passive film quickly stabilises, equivalent circuit modelling of these plots was not performed. Detailed equivalent circuit modelling of the surface layer is discussed later.

(a)

(b)

(c)
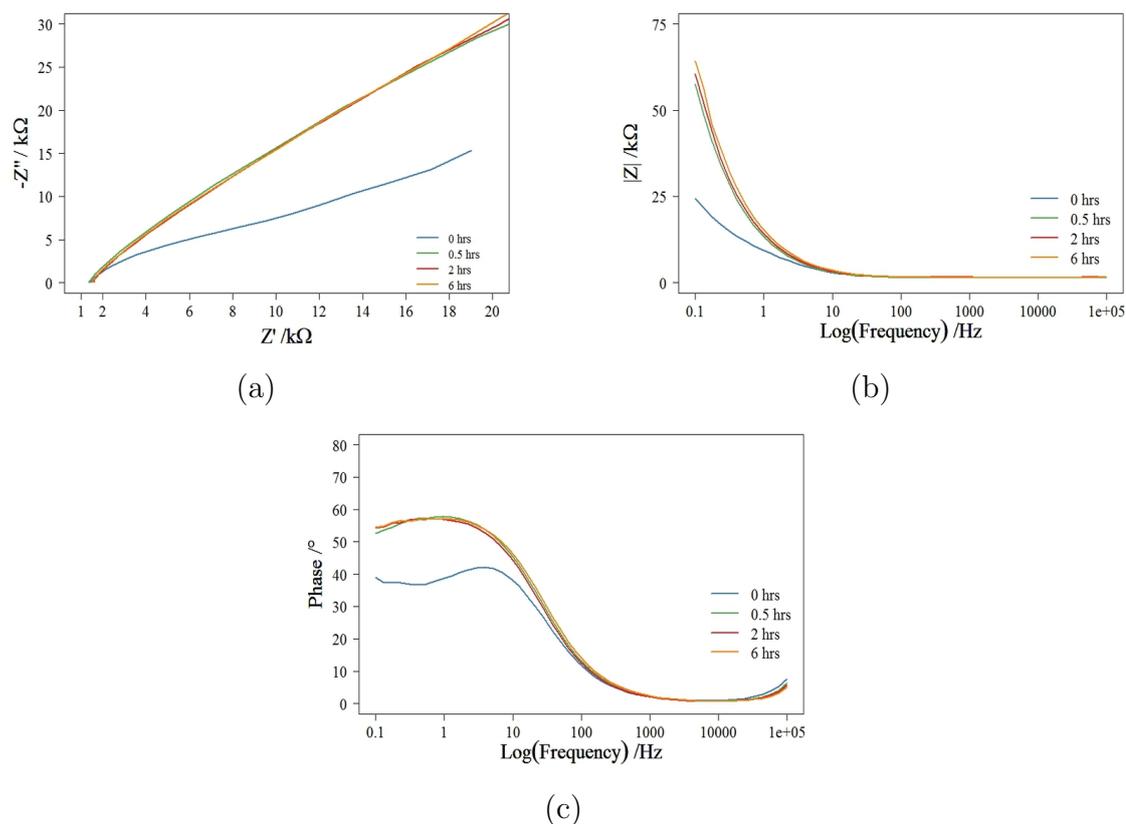
Figure 3.5: Time dependant Nyquist and Bode plots for 20/25/Nb SS in simulant pond water, pH$\simeq$11.4.

The XPS data of Table 3.2 and Figure 3.6 obtained for unsensitised 20/25/Nb SS immersed in simulant pond water for one week at 24 °C can now be considered. During this time the open circuit potential, E_{OCP}, was observed to obtain an equilibrium value of $\sim$0 V vs Ag/AgCl. This XPS data can then be used to inform the analysis of polarisation curves later in this chapter.

Component	Assignment	Average Peak Position	FWHM
Fe 2p$_{3/2}$	Fe^0	706.83	1.06
	Fe$_2$O$_3$/Fe$_3$O$_4$/ Fe(OH)$_2$/Fe(OH)$_3$/ FeOOH/Fe spinels	710.47	4.44
Cr 2p$_{3/2}$	Cr^0	574.01	1.51
	Cr spinel	575.57	0.85
	C$_2$O$_3$/Cr(OH)$_3$	576.61	2.25
	CrO$_3$	578.71	1.52
Ni 2p$_{3/2}$	Ni^0	852.61	2.11
	NiO	853.88	0.95
	Ni(OH)$_2$/NiFe$_2$O$_4$	855.47	2.11
O 1s	nucleophilic oxygen	528.57	1.84
	Cr$_2$O$_3$/Fe$_2$O$_3$/Fe$_3$O$_4$/ Spinels	529.82	1.17
	Cr(OH)$_3$/Ni(OH)$_2$/ Fe hydroxides	531.16	2.39

Table 3.2: Average peak positions and FWHM values obtained for Fe 2p$_{3/2}$, Cr 2p$_{3/2}$, Ni 2p$_{3/2}$ and O 1s in unsensitised 20/25/Nb SS.

This data is similar to those of Table 3.1 and Figure 3.3. Thus, the peak assignments are alike but some differences exist and therefore the assignments of Figure 3.6 are explicitly stated. The Fe profile of unsensitised 20/25/Nb SS is shown in Figure 3.6(a). There are two peaks evident. The first peak at 706.83 eV is due to elemental iron, Fe^0. Due to the broadness of the second peak at 710.47 eV, it is likely that multiphase oxide is present consisting of iron (III) oxide (Fe$_2$O$_3$), iron (II,III) (Fe$_3$O$_4$) and spinels such as FeCr$_2$O$_4$ and NiFe$_2$O$_4$, which also have binding energies ∼710.5 eV. The Fe$_2$O$_3$ peak at ∼710.5 eV may also contain contributions from iron (III) hydroxide, Fe(OH)$_3$. The small inconsistency between the envelope and the raw data at about 709 eV may suggest a FeO peak could also be present.

The chromium profile in Figure 3.6(b) shows four peaks which can be attributed to Cr metal, 574.01 eV, chromium (III) spinel, 575.57 eV, chromium (III) oxide Cr$_2$O$_3$, 576.61 eV and chromium (IV) oxide CrO$_3$, 578.71 eV. While NiCr$_2$O$_4$ and FeCr$_2$O$_4$ both have binding energies similar to the spinel peak seen

at 575.57 eV in the Cr profile, thermodynamic calculations performed by Beverskog *et al.* indicate that it is unlikely that $NiCr_2O_4$ will form at room temperature [185]. Therefore it is possible that this peak is due to the presence of $FeCr_2O_4$. The Cr_2O_3 peak at $\sim$577.2 eV may also contain contributions from chromium (III) hydroxide, $Cr(OH)_3$.

The nickel profiles seen in Figure 3.6(c) show three peaks at 852.61 eV, 853.88 eV and 855.47 eV, which can be accredited to Ni metal Ni^0, nickel (II) oxide NiO and nickel (II) hydroxide $Ni(OH)_2$ respectively. There is the possibility that NiOOH and $NiFe_2O_4$ also contribute to the peak at 855.47 eV.
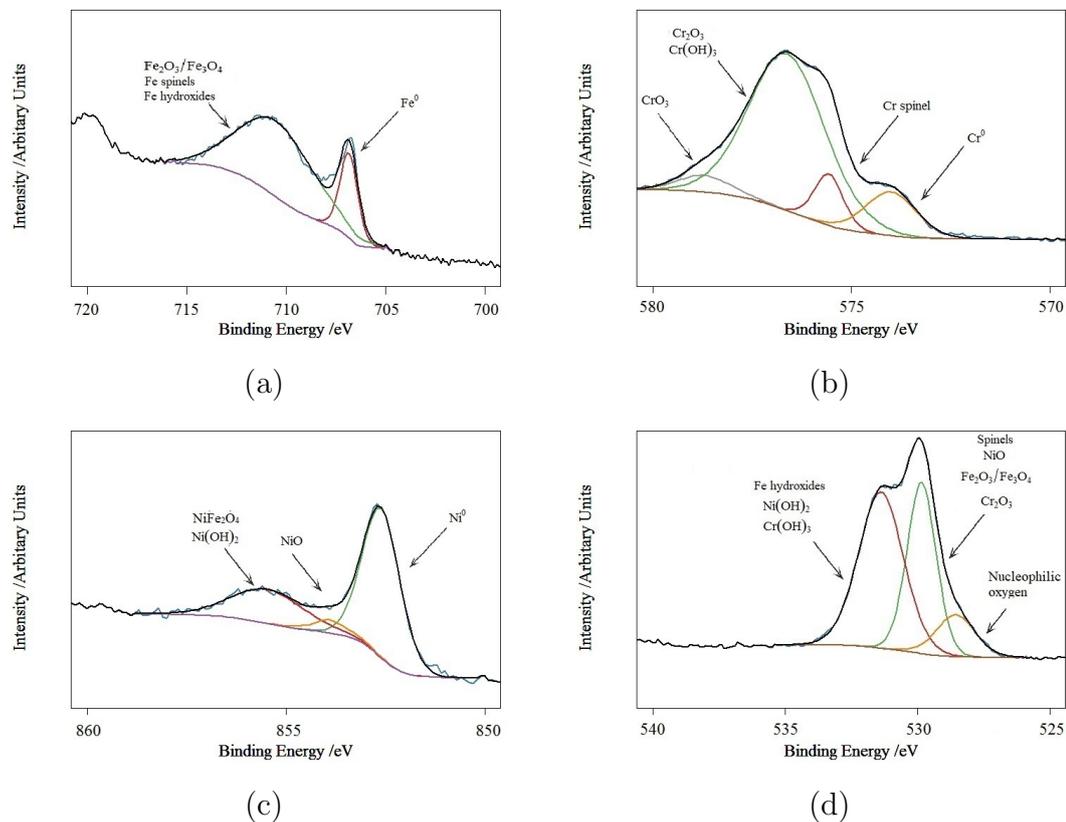
Figure 3.6: XPS profiles of (a) Fe $2p_{3/2}$, (b) Cr $2p_{3/2}$, (c) Ni $2p_{3/2}$ and (d) O 1s after week long immersion of unsensitised 20/25/Nb SS in simulant pond water, pH$\simeq$11.4 at 24 °C.

Finally, the oxygen profile is shown in Figure 3.6(d). There are three peaks, the peak at 529.82 eV can be attributed to metal oxides, the peak at 531.16 eV is consistent with the presence of metal hydroxides and defective lattice oxygens and the peak at 528.57 eV can be assigned to nucleophilic oxygen [186]. Separating the

individual components in these peaks is very challenging and beyond the scope of the work presented here, so this profile has only been used to confirm the presence of mixed Cr/Fe/Ni oxides/hydroxides on the metal surface.

As with the as-received samples the XPS data of 20/25/Nb SS post-immersion is plotted as bar charts giving the relative atomic percentages of each species observed for the main constituent metals of the steel. Accordingly, in Figure 3.7 bar A, bar B and bar C show such bar charts for the iron, chromium and nickel species observed from the steel post-immersion respectively. From Figure 3.7 bar A to bar C the contributions of the oxides formed can be compared, specifically $\sim$80 at% of the Fe contribution is an Fe oxide/hydroxide, $\sim$85 at% of Cr contributions are oxides/hydroxides and only $\sim$28 at% of Ni contributions are oxides/hydroxides.

As above, the XPS data is normalised and compiled to give a more complete picture of the passive layer. The resulting bar chart is shown in Figure 3.7 **D**. From this it can be seen that the most dominant component of the passive layer formed under open circuit conditions ($\sim$0 V) in simulant pond water is $Cr_2O_3/Cr(OH)_3$ for unsensitised 20/25/Nb SS, with Fe oxides/hydroxides being a significant secondary component of the outer oxide layer. The influence of Ni oxides in this layer is minimal ($<$1 at%). Cr spinels and CrO_3 contribute only 5 and 3 at% respectively. These results therefore suggest that the electrochemistry and thus the corrosion resistance of unsensitised 20/25/Nb SS under open circuit conditions in simulant pond water will be dominated by the electrochemistry of Cr and Fe oxide/hydroxide phases. Limited XPS data on 20/25/Nb SS has been published, however the results of Francis [187] support the findings reported here. Specifically, Francis found that for 20/25/Nb SS exposed to a high temperature CO_2 environment for 6 minutes at 600 °C a single rhombohedral oxide phase, $(Fe,Cr)_2O_3$, was growing on the surface with no evidence of any spinel.
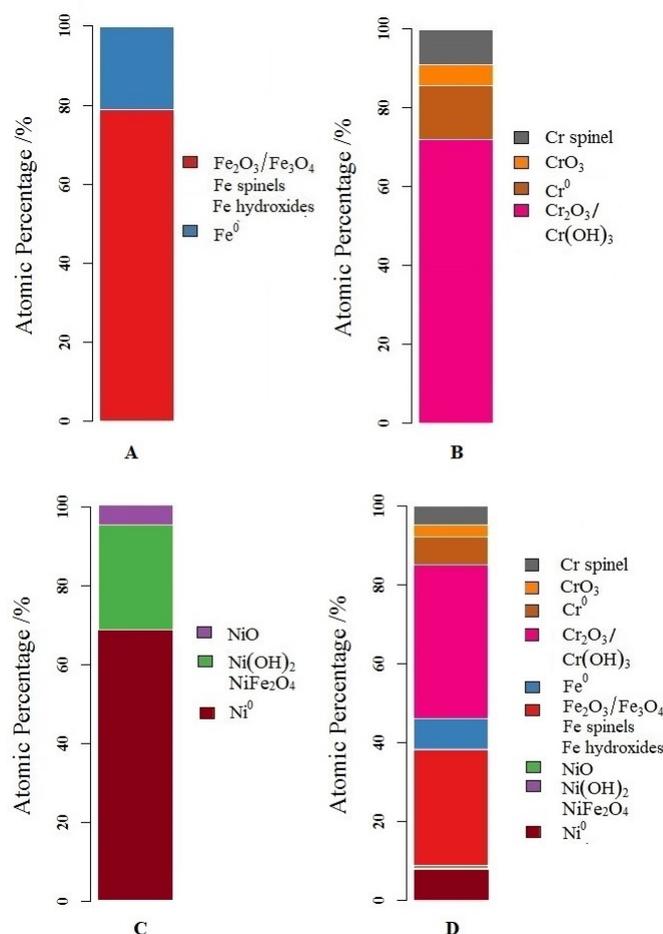
Figure 3.7: Atomic percentage data comparison of **A** Fe $2p_{3/2}$, **B** Cr $2p_{3/2}$ and **C** Ni $2p_{3/2}$ and **D** combined data extracted from XPS profiles obtained after a week long immersion of unsensitised 20/25/Nb SS in simulant pond water at 24 °C, pH$\simeq$11.4.

Finally, comparison of the two XPS datasets of Figure 3.4 **D** and Figure 3.7 **D** indicates that, while both surface layers are predominantly formed of Fe and Cr oxides/hydroxides, it is the Fe oxides/hydroxides that are most dominant in as-received samples and the Cr oxides/hydroxides that are most dominant on those 20/25/Nb SS samples that have been immersed in simulant pond water. There are no Ni oxide/hydroxide phases or Cr spinels formed on the surface of the as-received sample; however, they are present at a small at% level on the post-immersion 20/25/Nb SS samples and thus may play a role in the protection of the surface against localised attack. This point shall be returned to below.

Having now characterised the condition of the surface layer of 20/25/Nb SS

under OCP conditions in simulant pond water, the next sections explore how the condition of the surface changes in the presence of a range of oxidative stresses.

3.3　Effect of pH Variation on the Corrosion Behaviour of Unsensitised 20/25/Nb Stainless Steel

Figure 3.8 shows the polarisation curves for the unsensitised 20/25/Nb SS sample in undosed (no added NaOH) and dosed (deliberately added NaOH) simulant pond water. Potentiodynamic polarisation curves of the type shown in Figure 3.8 are usually divided into at least four clear sections in order of ascending positive potential: hydrogen evolution; active corrosion; passivity; and transpassivity. However, the polarisation curves of Figure 3.8 only exhibit three of these regions as indicated: hydrogen evolution; passivity; and transpassivity. The absence of an active region suggests that passive film growth begins or has already started at the potential where the recorded current of the polarisation curve changes from having a negative to positive value. At the very least, the potential of the sign reversal of the current corresponds to that at which passivating oxide film growth begins to dominate the electrochemistry of the system. As this point of reversal of the current sign does not then correspond to the corrosion potential, henceforth it shall be referred to simply as the potential of zero current, E_{ZC}.

From Figure 3.8 it can be seen that, for the sample exposed to undosed pH$\sim$8 simulant pond water, the formation of metastable pitting is evident, manifesting as small anodic current peaks starting at $\sim$0.4 V. In contrast to this, no such metastable pitting is observed once the pH of the water has been dosed to $\sim$11.4. The passive area of the polarisation curve is larger for the dosed pond water, indicating that dosing the water gives added corrosion protection to the 20/25/Nb SS sample. As well, the current in the passive region is larger at the higher pH,

most likely due to the kinetics of film growth under the non-steady state conditions imposed during the potential scan – a thicker passive layer being expected to be formed in the more alkaline conditions of the dosed pond water simulants [31].
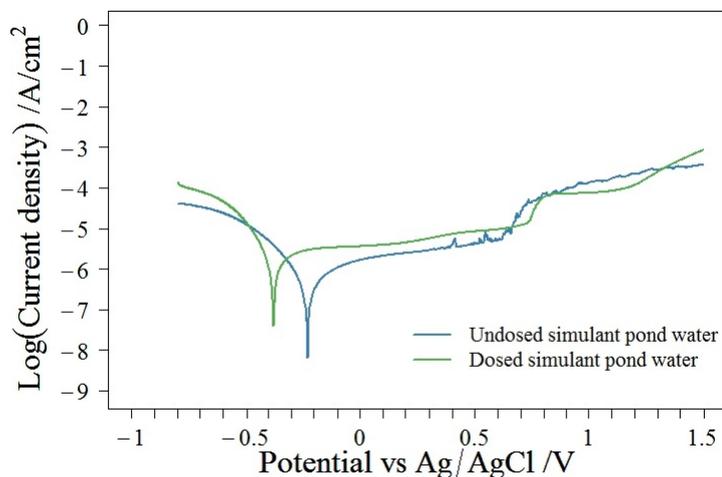
Figure 3.8: Potentiodynamic polarisation curve for unsensitised 20/25/Nb SS in NaOH-dosed, pH≃11.4, and undosed, pH≃8, water simulants at 24 °C, showing effects of dosing on corrosion behaviour. Both solutions contain 30 μmol dm^{-3} Cl$^-$.

Beverskog and Puigdomenech have previously reported Pourbaix E_h-pH diagrams for the Fe-H$_2$O, Cr-H$_2$O and Ni-H$_2$O systems that also account for the presence of the ternary Ni-Fe oxides, Cr-Fe oxides and Ni-Cr oxides [28, 30, 35, 185]. Use of these diagrams allows for the assignment of feasible associated chemistries to each of the three regions of the polarisation curves. Thus, the onset of transpassive behaviour seen at ∼0.75 V in Figure 3.8 can be reasonably attributed to the breakdown of protection derived from a Ni phase or metal spinels, NiFe$_2$O$_4$ or FeCr$_2$O$_4$ - the XPS data presented earlier contains peaks that are consistent with the presence of both of these species under open circuit conditions of Figure 3.8.

Similar analysis on a range of austenitic stainless steels [31] indicates that the protection afforded in the passive region has contributions from Fe, Ni and Cr oxides. That this is the case for 20/25/Nb SS is confirmed by Figure 3.9, where the potentiodynamic polarisation curve of 20/25/Nb SS in dosed pond water is

compared with the polarisation curves of pure Fe, Ni and Cr electrodes (the three main constituents of 20/25/Nb SS) recorded under identical solution conditions.
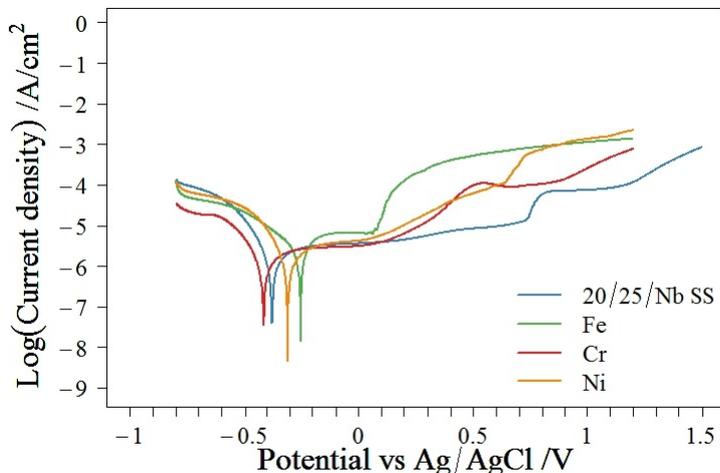
Figure 3.9: Potentiodynamic polarisation curves for 20/25/Nb SS, iron, nickel and chromium in simulant pond water, pH$\simeq$11.4 at 24 °C.

Between $\sim$0.2 and 0.06 V, all three metals are protected by their native oxides. However, passivation of the Fe metal breaks down at $\sim$0.06 V. Pure Cr starts to oxidise at a similar potential to the onset of transpasivity on Fe and it has been suggested by Betova *et al.* that this is due to the pre-transpassive oxidation of Cr(III) to Cr(VI) in the protective Cr_2O_3 film on Cr metal, with its subsequent gradual release to solution [188]. There appears to be a secondary passivation of pure Cr at higher overpotentials, $\sim$0.5 V. On pure Ni, a gradual oxidation occurs with a similar onset to Cr(III) oxidation ($\sim$0 V) and continues until the protective layer breaks down at $\sim$0.6 V. Comparison of the onset of this gradual oxidation with the thermodynamic analysis of Beverskog and Puigdomenech suggests that this transition may be assigned to the oxidation of Ni(II) to Ni(III) in the forms of β-Ni(OH)$_2$ and β-NiOOH respectively [35]. Thus, it can be seen from Figure 3.9 that the onset of transpassive behaviour occurring at $\sim$0.75 V for 20/25/Nb SS coincides with the onset of transpassive behaviour of pure Ni and the breakdown of secondary passivation on Cr – the former conclusion being consistent with that made above on the basis of the

thermodynamic data of Beverskog and Puigdomenech [28, 30, 35, 185]. Figure 3.9 also seems to suggest that the origin of the protection afforded by the passive film on 20/25/Nb SS shifts from that provided by chromium oxide films at low over potentials close to E_{ZC}, to nickel oxides at higher over potentials close to the onset of transpassivity. This will be explored further in the next section.

3.3.1 Electrochemical Impedance Spectroscopy of Unsensitised 20/25/Nb Stainless Steel in Dosed Simulant Pond Water

Electrochemical impedance spectroscopy (EIS) is a useful technique for monitoring changes at the metal solution interface such as passive film growth. Analysis of unsensitised 20/25/Nb SS in simulant pond water at pH$\simeq$11.4 was carried out over the same potential range as for the voltammetry studies. Nyquist and Bode plots for 20/25/Nb SS at several pivotal potentials can be seen in Figure 3.10.

For common stainless steels, such as 316, a generally accepted model of the surface is given in Figure 3.11(a) wherein the native alloy is protected by a duplex layer of passivating oxide. The generally accepted equivalent circuit diagram for this is shown in Figure 3.11(b) [189–194]. In the latter diagram R_s represents the solution resistance, R_1 represents the resistance of the outer oxide layer and R_2 represents the resistance of the inner oxide layer of the duplex structure shown in Figure 3.11(a). Constant phase elements (CPE) are used to represent the capacitance of these oxide layers.

(a)

(b)

(c)
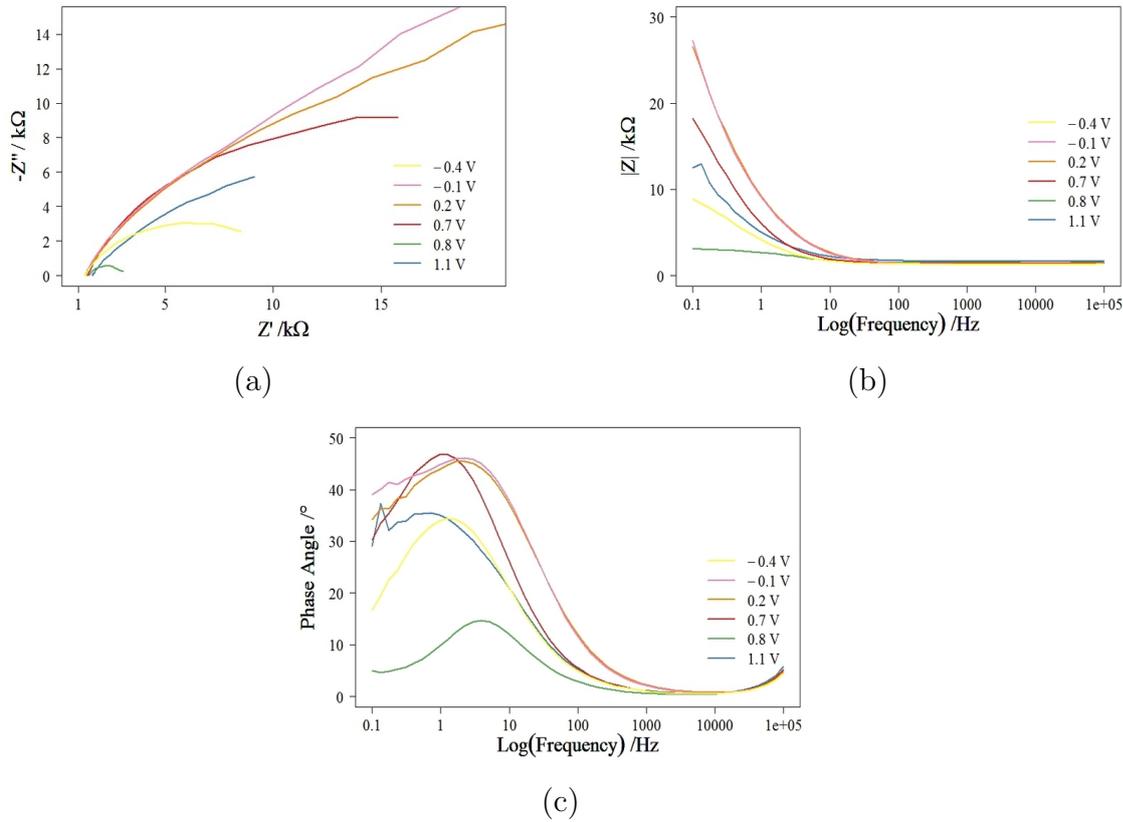
Figure 3.10: Nyquist plots (a) and (b) & (c) Bode plots at several key potentials for unsensitised 20/25/Nb SS in dosed simulant pond water, pH$\simeq$11.4 at 24 °C.

The impedance of a CPE as a function of the radial frequency, ω and the constant phase element parameter, Y_0, is given by equation 3.1.

$$Z(CPE) = Y_0^{-1}(j\omega)^{-n} \tag{3.1}$$

The CPE is equal to a capacitance when n=1, a Warburg when n=0.5 and a resistance when n=0. It is widely accepted that when n$\geq$ 0.8, the CPE is close to a capacitance. Indeed, one interpretation of the CPE is that it can be considered an imperfect capacitor. As such, is used to compensate for surface roughness, varying thickness and composition and inhomogeneous surface reaction rates.

If R_1 $\gg$ R_2 or vice versa, in Figure 3.11(b), a simple Randle circuit is appropriate. Similarly, various authors have found that for a bare oxide layer free stainless steel surface a simple Randle circuit is also suitable [195, 196].

(a)   (b)
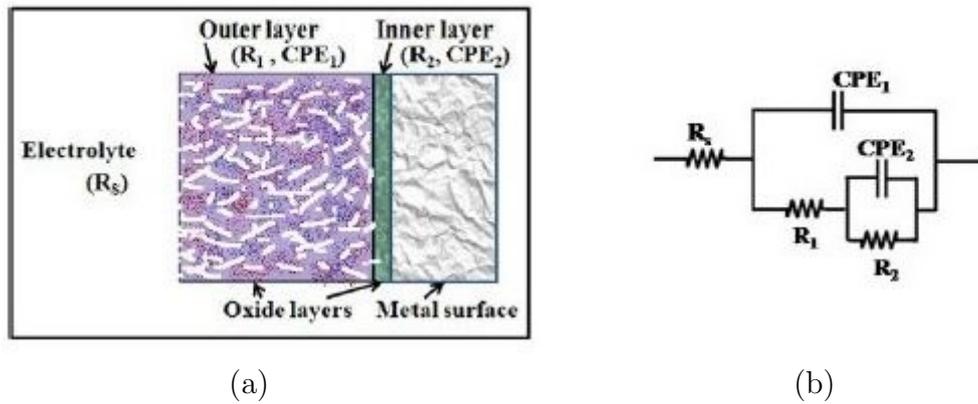
Figure 3.11: Model of the passive oxide layer on stainless steel (a) and the associated equivalent circuit model (b) [190].

The impedance spectra of Figure 3.10 exhibit a single capacitive-resistive loop across the entire potential range studied. As well, the Bode plots indicate a single time constant is present and thus validate the use of a simple Randle cell across the entire potential range. Chi-squared values in the order of 1×10^{-3} were obtained when modelled using ZView2. Under such circumstances, R_p in Figure 3.12 can be considered a lumped polarisation resistance $R_p = R_{ct} + R_{film}$ where R_{ct} is a charge transfer resistance and R_{film} is the resistance of the passive film.

The single loop in the passive region suggests that, under the experimental conditions used for the study reported here, a single R_{film} value obtains and either the two layer model of Figure 3.11 does not apply or the contribution of an inner layer to passivation is minimal in the case of as received 20/25/Nb SS and the surface structure is best described by a single oxide layer.

Figure 3.10 also shows that at the onset of transpassivity (0.8 V) there is a marked decrease in the radius of the capacitive-resistive loop and thus a reduction in the polarisation impedance, indicating a breakdown of the passive film and an accompanying low charge transfer resistance. Similar results have been observed by Blair *et al.* [197] in a study of the transpassive behaviour of steel in alkaline solutions, wherein they utilised the equivalent circuit in Figure 3.11(b) for all potentials reported. As discussed above, this can be simplified to a simple Randles cell as per Figure 3.12 and thus this latter circuit was used in the analysis of our

EIS data over the whole potential range studied in Figure 3.10. Figure 3.10 also shows that the radius of the capacitive-resistive loop at 1.1 V is greater than that at 0.8 V. This is consistent with an increase in the polarisation resistance and may attributed to the secondary passivation seen in the same potential range in the potentiodynamic polarisation curve of Figure 3.8.
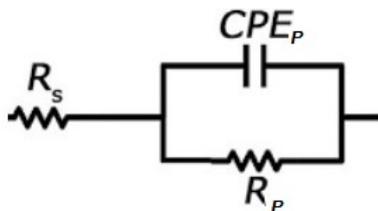
Figure 3.12: Electrical equivalent circuit model used to represent the evolution of 20/25/Nb SS surface in simulant pond water. R_s is the solution resistance, R_p is the polarisation resistance which tends to R_{ct} (the charge transfer resistance) or R_{film} depending on the applied potential and CPE_p a constant phase element (see text for relevant discussion).

Thus, the processes described by each circuit element may change when moving from the passive to transpassive regions of the potentiodynamic polarisation curve. For potentials $\geq$ 0.8 V the components of the Randles circuit represent the diffusive impedance, CPE (n<0.8) and whilst R_p is dominated by R_{ct}; since at these potentials the surface is considered to be corroding. Between -0.6 and 0.8 V the components represent the capacitance (n>0.8), CPE_p, and R_p, is dominated by R_{film}, the resistance of the passive film.

Through equivalent circuit modelling, R_p (=R_{film} or R_{ct}) and CPE may be found as a function of electrode potential, E, and the results are shown in Figure 3.13. Capacitance data is presented in the form of a (capacitance)$^{-2}$ versus E plot i.e. consistent with Mott-Schottky analysis. Since the CPE data is only considered to be representative of a capacitance when n$\geq$0.8, these plots only include the potential range over which n$\geq$0.8 for the CPE component. For materials reported here this corresponds to the following potential ranges, for 20/25/Nb SS, Cr and Ni -0.6 to 0.8 V and for Fe -0.3 to 0.4 V. In Figure 3.13, two peaks in both the corrosion resistance and capacitance are evident, with maxima at 0.1 and 0.7 V

and 0 and 0.5 V respectively.
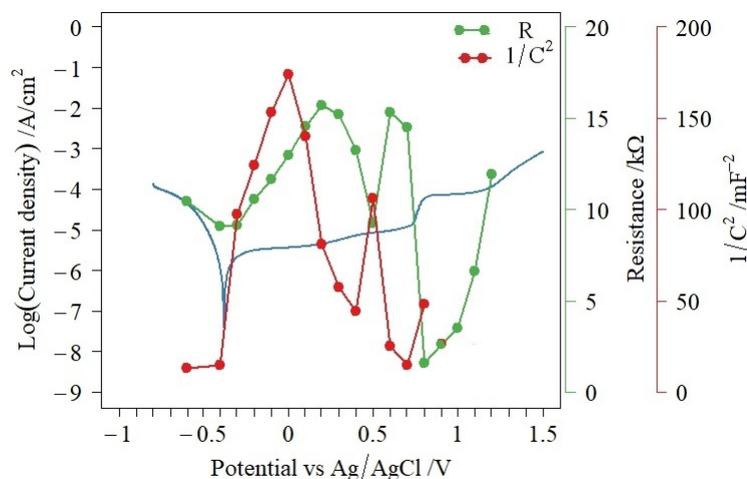
Figure 3.13: Analysis of electrochemical impedance spectroscopy unsensitised 20/25/Nb SS in dosed simulant pond water, pH≃11.4 at 24 °C. The measured potentiodynamic polarisation curve is overlaid with polarisation resistance data (green) and capacitance data (red), in the form of a Mott-Schottky-based analysis, extracted from the Nyquist plots.

In order to better understand the source of this protection, similar experiments were performed on the principal components of 20/25/Nb SS, i.e. the pure metals, Fe, Cr and Ni in simulant pond water at pH≃11.4. The same equivalent circuit as used to model the unsensitised 20/25/Nb SS was employed to model the pure metal data and the results of this analysis are shown in Figures 3.14 to 3.16 - again as (capacitance)$^{-2}$ versus E and R versus E plots - where R may be R_{ct} or R_{film} as appropriate. Comparison of these plots with those of Figure 3.13 indicate that the range over which the surface of the pure metal sample is considered to be corroding or passivated deviates from that seen for the 20/25/Nb SS sample and from metal to metal. Figure 3.14 to 3.16 now allow us to consider each component metal separately and potentially identify the component metal oxides that most influence the corrosion behaviour of the electrode surface.

(a)

(b)

(c)

(d)
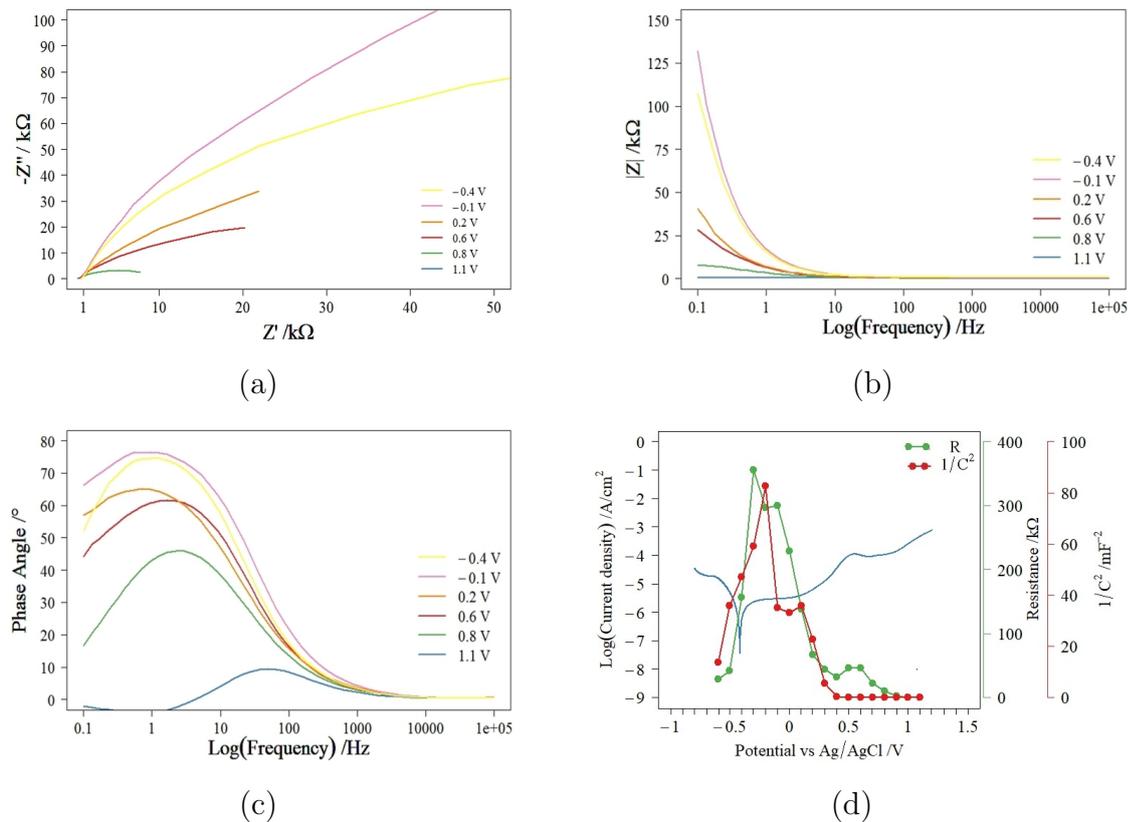
Figure 3.14: Analysis of electrochemical impedance spectroscopy data for pure chromium in dosed simulant pond water, pH$\simeq$11.4 at 24 °C. (a) Nyquist plots, (b) & (c) Bode plots and (d) the measured potentiodynamic polarisation curve is overlaid with polarisation resistance data (green) and capacitance data (red), in the form of a Mott-Schottky-based analysis, extracted from the Nyquist plots.

The change in R_p and (capacitance)$^{-2}$ with potential for chromium can be seen in Figure 3.14(d), which shows broad peak ranging from an extrapolated -0.6 to 0.5 V in the R_p versus E plot. Examination of the Cr-H$_2$O Pourbaix diagram of Figure 1.9 indicates that the cathodic onset of this peak coincides with the formation of Cr$_2$O$_3$, whilst the anodic decrease in R_p correlates with the oxidation of Cr$_2$O$_3$ to CrO$_4^{2-}$. Higher valent Cr(VI) is more soluble than Cr(III) and thus oxidation to Cr(VI) results in transpassive dissolution [188].

The associated C^{-2} versus E for pure Cr can be divided in four regions; -0.5 to -0.2 V, -0.2 to 0 V, 0 to 0.1 V and 0.1 to 0.5 V. Moffat [198] attributes the observed increase in C^{-2} with E in the region E=-0.5 to -0.2 V to the growth of the passive layer, said layer behaving like a simple dielectric where thickness increases, and so capacitance decreases, with potential. This interpretation is consistent with

both the polarisation curves and R versus E plot of Figure 3.14. In the case of the former, this potential range corresponds to the active oxide growth region (see discussion of Figure 3.9 above), whilst in the case of the latter R increases with E - as would be expected with the growth of a non-conducting oxide film.

At potentials between -0.2 and 0 V the slope of the C^{-2} vs E plot changes sign. Moffat [198] attributes this change in behaviour to the observation of p-type semiconductivity in the space charge region of the chromium oxide film, the thickness of the film now exceeding that of the space charge layer as a result of the oxide growth that occurred in the region E=-0.5 to -0.2 V. This is in agreement with the fact that the potentiodynamic polarisation curve predicts passivation of the metal surface in this region and that Cr_2O_3 is widely accepted to behave as a p-type semiconductor [198, 199].

At potentials between 0 and 0.1 V, the slope of the C^{-2} vs E plot again changes sign suggesting a switch from p to n-type character. The oxidation of Cr(III) to Cr(VI), discussed in relation to the R_p vs E plot above, results in an increase in point defects in the oxygen sublattice, causing the Cr(VI) to behave as an n-type semiconductor. Metikos-Hukovic [199] found the Cr(VI) oxide, CrO_3, to have n-type character, all of which suggests CrO_3 growth at the film/solution interface over this short potential window.

The final region from 0.1 to 0.5 V appears to manifest a p-type Mott-Schottky behaviour; however Metikos-Hukovic attributes this to the oxidation of the entire layer to a soluble Cr(VI) oxide, $Cr_2O_4^{2-}$ [199]. This behaviour corresponds to the gradual dissolution of the protective oxide layer as seen in the polarisation curve and indicated by the simultaneous drop in R_p.

(a)

(b)

(c)

(d)
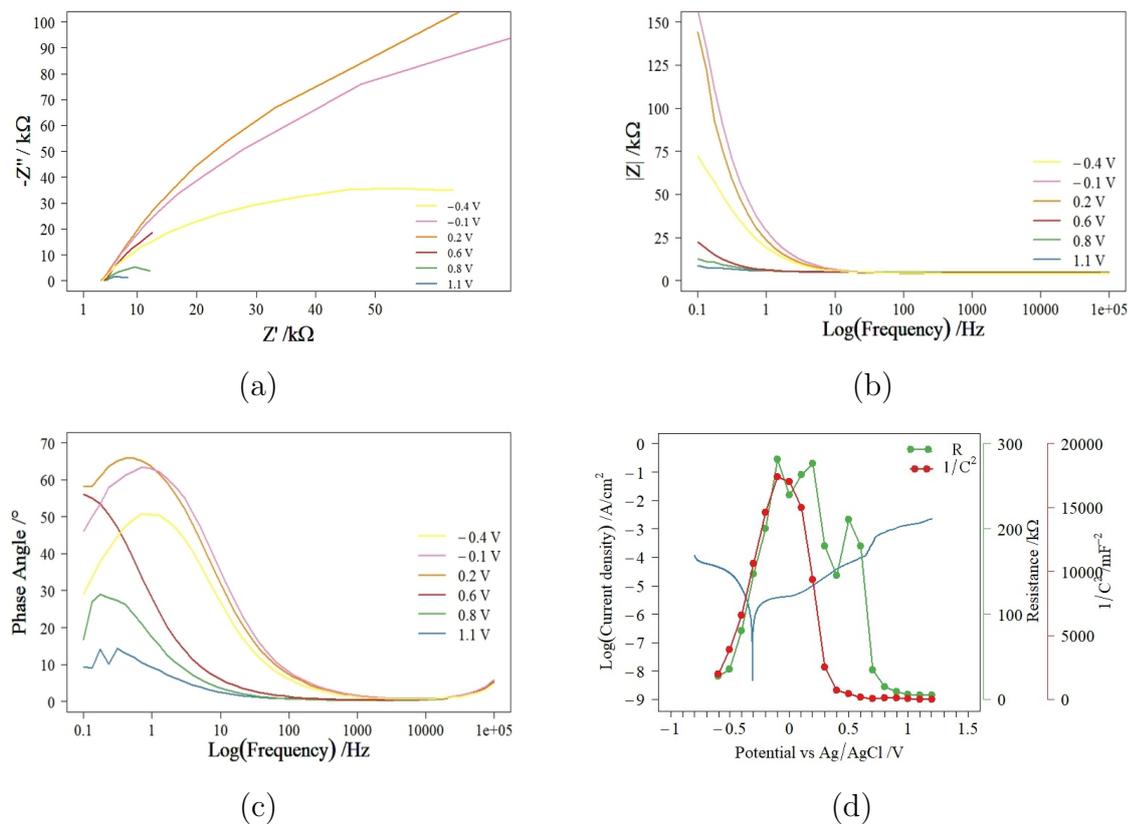
Figure 3.15: Analysis of electrochemical impedance spectroscopy data for pure nickel in dosed simulant pond water, pH$\simeq$11.4 at 24 °C. (a) Nyquist plots, (b) & (c) Bode plots and (d) the measured potentiodynamic polarisation curve is overlaid with polarisation resistance data (green) and capacitance data (red), in the form of a Mott-Schottky-based analysis, extracted from the Nyquist plots.

Figure 3.15 shows the R_p and C^{-2} vs E plots for nickel. Nickel has two significant peaks in R_p over the potential range studied, centred around E=-0.1 V and E=0.6 V. Inspection of the metastable Pourbaix diagrams, calculated by Beverskog and Puigdomenech [35] and shown in Figure 1.10, suggests that these peaks correspond to the oxidative generation of β-Ni(OH)$_2$ and β-NiOOH respectively. The final decrease in resistance starting at 0.7 V may be due to dissolution as γ-NiOOH, again assigned using the Ni-H$_2$O Pourbaix diagrams of Figure 1.10.

The C^{-2} vs E plot of pure Ni in Figure 3.15 can be divided into two distinct regions; -0.5 to 0 V, region I, and 0 to 0.5 V, region II. In region I the reciprocal capacitance increases with potential. As with pure Cr, the metal (III) oxides of Ni behave like p-type semiconductors. Thus, using Moffat's interpretation for Cr, the

decrease in capacitance observed with increasing potential for the pure Ni electrode can be considered to be a result of the simple dielectric behaviour associated with oxide layer growth. This analysis is in agreement with the nickel R_p vs E and potentiodynamic polarisation curves – the former exhibiting an increase in R_p in this region, the latter indicating the growth of a passive layer (vide supra).

In region II the now fully formed oxide layer (as inferred from the polarisation curve) appears to show p-type character. NiO and β-Ni(OH)$_2$ have been shown to behave as p-type semiconductors [200–203], reinforcing our earlier conclusion that the passivation of pure Ni can be at least in part attributed to the formation of β-Ni(OH)$_2$. Mott-Schottky analysis unfortunately does not aid in the assignment of the peak in R_p vs E at 0.5 V as there are no changes in C^{-2} at this potential. However, when p-type semiconductors are over charged they go into accumulation and display quasi-metallic behaviour. Thus, it is possible that at 0.5 V, β and γ phase NiOOH are quasi-metallic and the capacitance becomes very large (note the capacitance of a metal is infinite), explaining the observed trend in the C^{-2} vs E plot at higher potentials. Thus, it is likely that the peak in R_p vs E plot at 0.5 V is due to a resistance associated with the structural rearrangement in the Ni oxide as β and γ phase NiOOH are formed.

Figure 3.16 shows the behaviour R_p and C^{-2} vs E plot for iron. There is one distinct peak in the R_p vs E data stretching from E = -0.5 V to 0.5 V with a maximum at -0.2 V. Inspection of the Pourbaix diagrams of Figure 1.8 indicates that this peak in R_p corresponds to the transition of Fe(II) to Fe$_3$O$_4$ and/or Fe$_2$O$_3$ whilst the dominant species in the passive region of the polarisation curve is insoluble Fe$_2$O$_3$.

(a)

(b)

(c)

(d)
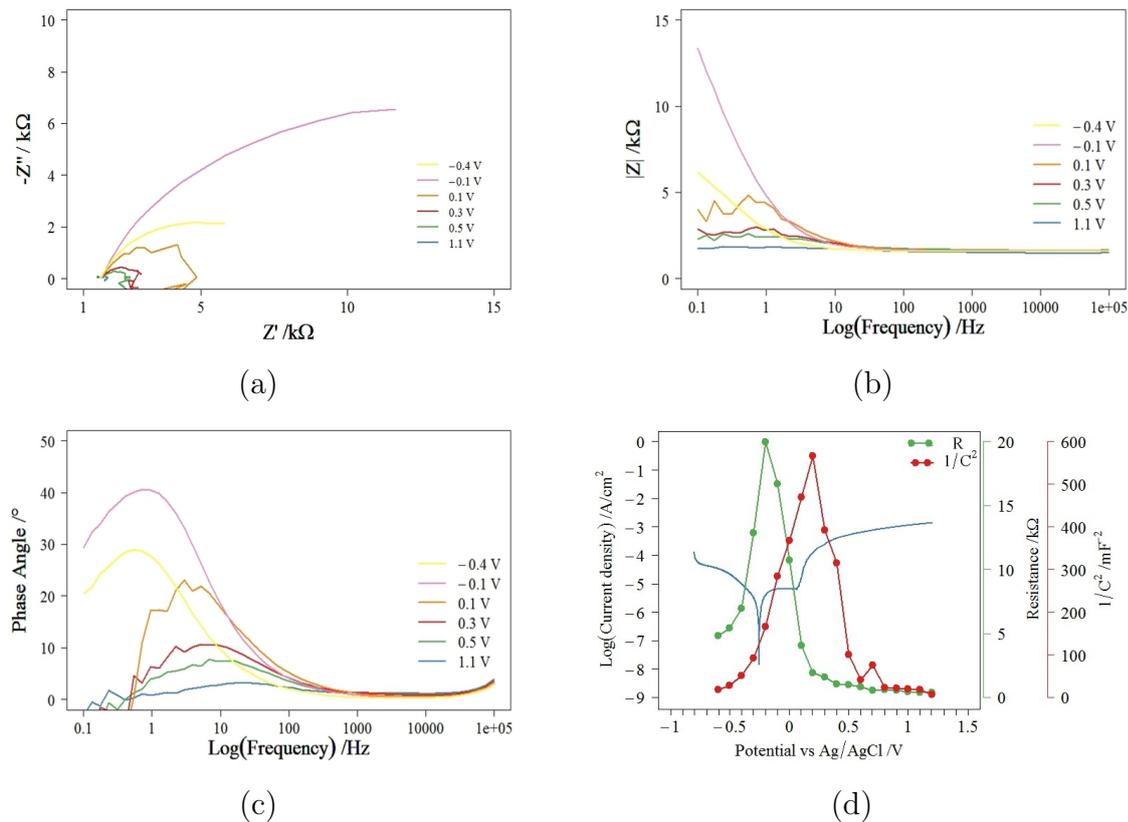
Figure 3.16: Analysis of electrochemical impedance spectroscopy data for pure iron in dosed simulant pond water, pH$\simeq$11.4 at 24 °C. (a) Nyquist plots, (b) & (c) Bode plots and (d) the measured potentiodynamic polarisation curve is overlaid with polarisation resistance data (green) and capacitance data (red), in the form of a Mott-Schottky-based analysis, extracted from the Nyquist plots.

This analysis is supported by the associated C^{-2} vs E plot. The Fe data is distinct from the Ni and Cr data in that the changes in C^{-2} with E overlap the region of the polarisation curve wherein passivation has already been observed – specifically the potential range E=-0.3 to 0.2 V. As such, the C^{-2} vs E data in this range is then reflecting the semiconducting behaviour of the metal oxide layer rather than its growth i.e the C^{-2} vs E data can be considered a true Mott-Schottky plot.

The C^{-2} vs E data can then be divided into two distinct regions, the potential ranges -0.3 to 0.2 V and 0.2 and 0.6 V showing n and p-type behaviour respectively. As discussed above, the n-type behaviour is coincident with early passive region; it is also coincident with a region of increasing polarisation resistance suggesting that the properties of a protective oxide layer are being interrogated. Fe_2O_3 is

widely accepted to behave like an n-type semiconductor [197, 204, 205], thus the surface oxide is expected to be Fe_2O_3. However, as evidenced by the increasing polarisation resistance, some oxide growth and defect elimination may still be occurring in this region and thus the n-type behaviour may be convoluted with a residual decrease in capacitance with potential behaviour as the oxide layer grows and defect density is decreased (as seen in the C^{-2} vs E plots for the pure Cr and Ni electrodes). For this reason, quantitative analysis of the layer properties using the Mott-Schottky equation was not attempted.

Behaviour switches from n to p-type at $\sim$0.2 V. Other authors have alluded to the presence of an inversion layer causing the switch to p-type behaviour [204]. However, this seems unlikely under current experimental conditions. An alternative explanation discussed by Blair *et al.* involves the oxidation of Fe(III) to Fe(IV) or Fe(V) or Fe(VI) resulting in the formation of hole type charge carriers in the oxide layer [197]. This would necessarily be a prelude to dissolution of the Fe_2O_3 layer and is not inconsistent with the data of Figure 3.16 where the potential range of p-type behaviour overlaps that of transpassivity in the potentiodynamic polarisation curve. Fe(IV)/(V)/(VI) are unstable in solution and thus most likely precipitate as Fe(III) hydroxides, these precipitates may then form the basis of secondary passivation.

In light of the electrochemical behaviour of the single metal electrodes shown in Figure 3.14-3.16, the R_p vs E and C^{-2} vs E behaviour of 20/25/Nb SS shown in Figure 3.13 can analysed as follows. The open circuit potential for 20/25/Nb SS in simulant pond water was found to be $\sim$0 V. A peak in R_p is developing at this potential in Figure 3.13. Figures 3.14-3.16 also show that that there are resistive contributions from iron, chromium and nickel oxides at 0 V. It is generally accepted that the iron and chromium oxides are the main contributors to passive layers formed on austenitic stainless steels 304 and Mo-alloyed SS in alkaline conditions [31, 206]. This is because nickel oxidises more slowly than both Fe and Cr – with the consequence that there is an enrichment of Ni in its metallic state in the

metal closest to the metal/oxide interface [31]. XPS data reported in section 3.2 indicate the same to be true for unsensitised 20/25/Nb SS. Although these Fe and Cr oxides dominate at open circuit potentials expected in the ponds, it is evident from the presence of the second peak in R_p growing at $\sim$0.5 V that an underlying nickel oxide/hydroxide, formed from the oxidation of nickel at this potential, may offer protection over a wider range of potentials. Thus, on breakdown of the iron/chromium oxide outer layer the β-Ni(OH)$_2$ or β-NiOOH (as indictated by the Pourbaix diagram) offers protection over an extended potential range at E values more positive that the open circuit potential, E_{OCP}.

The C^{-2} vs E plot of as-received 20/25/Nb SS in Figure 3.13 can be split into three regions I-III respectively: -0.5 to 0 V, 0 to 0.4 V and 0.5 to 0.7 V. Region I shows an apparent n-type character. It is tempting to attribute this to formation of n-type Fe$_2$O$_3$. However, it is important to remember that, as was observed with Cr, Ni and possibly Fe oxides in Figures 3.14 – 3.16, the capacitance associated with an oxide film decreases with increasing potential as the oxide film grows and thickens and defects are eliminated. Such growth on 20/25/Nb SS would lead to an apparent n-type behaviour in the Mott-Schottky plot consistent with that observed in region I of Figure 3.13. Supporting this interpretation, the polarisation resistance grows continuously in this potential region and growth of a passive layer is evident in the polarisation curve.

In region II a transition to p-type behaviour is observed, indicative that Cr$_2$O$_3$ is beginning to dominate the oxide layer. The resistance continues to grow in this region until $\sim$0.2 V at which point the resistance begins to decrease. From the Cr assignments this decrease is attributed to the increased oxidation of Cr(III) to Cr(VI). Region III again has p-type character, that may be correlated with the peak seen in the Ni resistance plot. However due to the lack of any distinct Mott-Schottky behaviour in the C^{-2} vs E plot for pure Ni at these potentials, the possibility of the formation of metal spinels must be considered. Although Cr, Ni and Fe spinels relevant to these experiments have not been

explicitly studied, spinels of Zn, Mn and Mg have been observed to behave like p-type semiconductors [207–209]. It therefore likely that Cr, Ni and Fe spinels also have p-type semiconductor properties.

At E>0.8 V the CPE no longer behaves like a capacitor (i.e. n<0.8) and the observed behaviour corresponds to the transpassive dissolution of the protective surface oxide layer.

3.4 Effect of Chloride Concentration in the Aqueous Phase on the Corrosion Behaviour of the 20/25/Nb Stainless Steel

To investigate the robustness of the NaOH derived protection of 20/25/Nb SS against corrosion shown in Figure 3.8, the influence of chloride concentration on the corrosion behaviour of the steel in the presence and absence of NaOH was investigated.

Firstly, the effect of chloride concentration on the corrosion behaviour of unsensitised 20/25/Nb SS in the absence of NaOH was explored. Figure 3.17 shows the resulting polarisation curves with the pH of the undosed pond water being $\sim$8 after chloride was added. From Figure 3.17, it can be seen that unsensitised 20/25/Nb SS exhibits behaviour close to the classic behaviour of all stainless steels in chloride solution, i.e. an increasingly negative shift in the onset of transpassivity with Cl^- concentration [210]. From the Pourbaix diagrams of Figure 1.10 it can be seen that at the low pH of 8 used in the experiments of Figure 3.17, there is less Ni oxide/hydroxide formation and so less protection provided by Ni against corrosion of the steel matrix [35]. Thus, the passive region observed at low $[Cl^-]$ at pH 8 is expected to be due to oxides of Fe and Cr, with the onset of transpassivity seen between $\sim$0.25 and $\sim$0.5 V being associated with the loss of this protection. Specifically, there is evidence of pitting from $\sim$0.3 V onwards. As the Cl^- concentration increases it causes the

breakdown potential of the passive layer on 20/25/Nb SS to shift in a negative direction and localised attack can proceed uninhibited at potentials as low as 0 V. These results agree with the findings of Chan *et al.* [182] who performed similar experiments on AGR cladding.
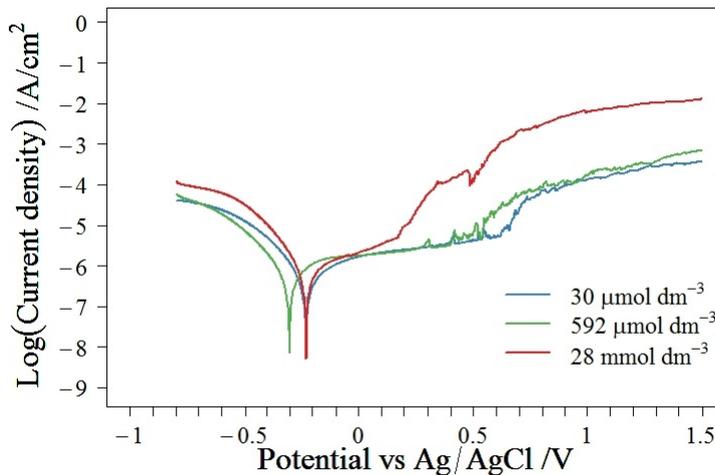
Figure 3.17: Potentiodynamic polarisation curves demonstrating the effect of increasing chloride concentration in undosed simulant pond water (pH≃8) on the corrosion behaviour of unsensitised 20/25/Nb SS at 24 °C.

Figure 3.18 shows the polarisation curves for unsensitised 20/25/Nb SS in dosed simulant pond water, pH≃11.4 (i.e. in presence of deliberately added NaOH as a corrosion inhibitor) containing increasing amounts of Cl^-. It is evident that increasing the Cl^- concentration up to 28 mmol dm^{-3} has little to no effect on the corrosion behaviour i.e. the dosing of the solution with base to pH 11.4 has almost entirely inhibited the chloride driven corrosion processes that otherwise occur at $[Cl^-]$ up to 28 mmol dm^{-3} in undosed solutions at pH 8. However, it can also be seen from Figure 3.18 that, even in dosed solutions at pH 11.4, the addition of chloride to concentrations of $[Cl^-]≃56$ mmol dm^{-3} can induce both a movement in the onset of transpassivity towards a more negative potentials and the onset of pitting corrosion at ∼0.1 V. Fortunately, chloride concentrations are not expected to reach such high concentrations in real storage environments, with values of 2-3 ppm or 0.1 mmol dm^{-3} chloride being typical. Thus, if a chloride incursion comparable to those historically experienced in the AGR spent fuel pond

were to occur in new storage ponds, it is reasonable to conclude that dosing with sodium hydroxide to pH 11.4 will suppress localised attack of the passive layer. This integrity of the 20/25/Nb SS cladding material would then be expected to be maintained, so safely preventing contact of the pond water with the underlying fuel pellets themselves.
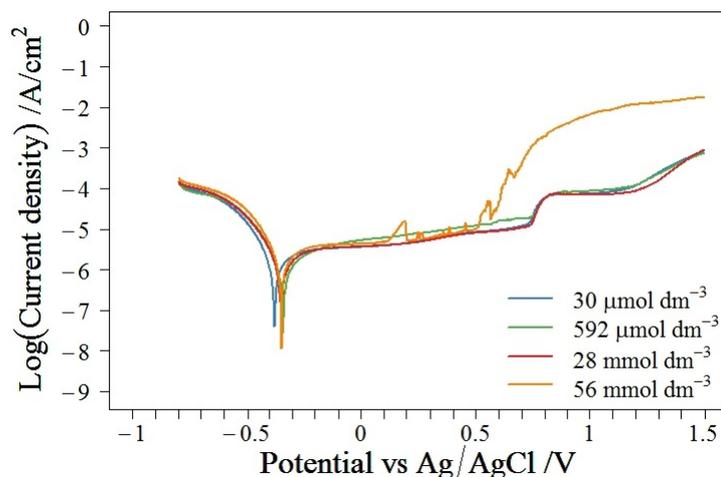
Figure 3.18: Potentiodynamic polarisation curves demonstrating the effect of increasing chloride concentration in dosed simulant pond water (pH≃11.4) on the corrosion behaviour of unsensitised 20/25/Nb SS at 24 °C.

3.5 Effect of Temperature Variation on the Corrosion Behaviour of Unsensitised 20/25/Nb Stainless Steel

Due to the expected future increase in the operating temperature of interim storage ponds at THORP, the effect of increasing the temperature of the simulant pond water on 20/25/Nb SS was investigated. Figure 3.19 shows the polarisation curves obtained at elevated temperatures in the range 45 - 90 °C. The most significant observations in the progression from 24 °C to 45 °C to 60 °C are the increase in general corrosion currents, the shift in potential of zero net current, E_{ZC}, in the anodic direction and the movement of the onset of

transpassivity to more negative potentials with increasing temperature. This means that the passive region for 20/25/Nb SS in dosed simulant pond water becomes smaller as temperature increases – most likely due to the increased solubility of the passivating oxides at higher temperatures. However, the open circuit potentials of the sample, which are measured as being $\sim$0, $\sim$ -0.07 and $\sim$ -0.1 V at 24, 45 and 60 °C respectively, still lie safely in the passive region for these operating temperatures.
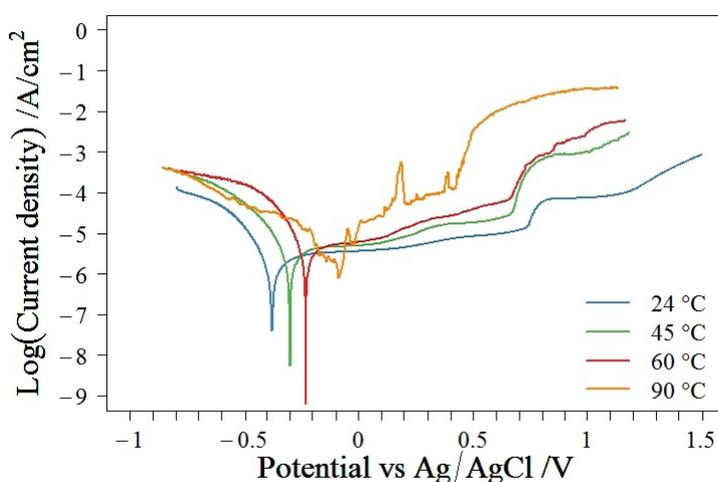
Figure 3.19: Potentiodynamic polarisation curve demonstrating the effect of increasing solution temperature on the corrosion behaviour of unsensitised 20/25/Nb SS in dosed simulant pond water, 30 μmol dm^{-3} Cl$^-$, pH$\simeq$11.4 at 24 °C.

The potentiodynamic polarization curve recorded at 90 °C is noticeably noisier than that recorded at 24, 45 and 60 °C. This is most likely due to the formation of bubbles at the electrode surface due to nucleate boiling that occurs at temperatures below the boiling point of the bulk liquid. These bubbles will be small and so cause small fluctuations in the measured current; however, these small fluctuations will be amplified by the current data being presented in logarithmic form. Despite the noisy nature of the data recorded at 90 °C, it can be seen from Figure 3.19 that there is a significant change in corrosion behaviour compared to that which is observed at the lower temperatures. Not only has the passive range contracted compared to that seen at 24-60 °C, but additionally (i) the general corrosion

current in the passive range has increased by almost an order of magnitude; and (ii) several transient current peaks are observed in the same range. It is hypothesized that this change is again associated with increased solubility of passivating oxide layers with temperature, resulting in the formation of a porous protective oxide layer at the electrode surface leading to greater corrosion currents. This hypothesis is supported by Wang *et al.* [57] in their investigation into temperature effect on AISI 304 SS. In their experiments, increases of capacitance with temperature were recorded, consistent with either film thinning or increased film porosity. As thickening of the film could be observed with the naked eye, it is likely that it is the latter explanation that obtains.

Jin and Atrens [211] found that for 18Cr-12Ni SS immersed in a 0.1 mol dm^{-3} NaCl solution, the composition and thickness of the passive layer remained relatively unchanged on increasing the solution temperature from 25 to 90 °C. Whilst there is only limited literature in the temperature range of Figure 3.19, the data of Jin and Atrens experiments and predictions from Pourbaix diagrams calculated at 100 °C [28, 30, 35] suggest that it is likely that composition of the passive film on 20/25/Nb SS will not vary significantly over the temperature range relevant to the current study.
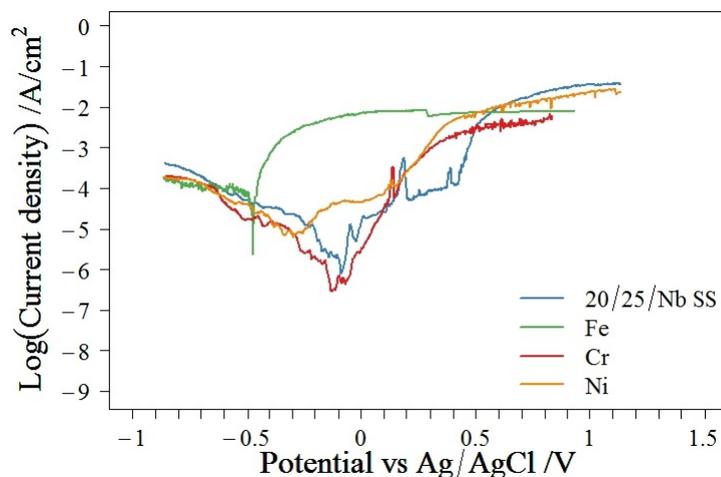
Figure 3.20: Potentiodynamic polarisation curve demonstrating the effect of increasing the temperature of the dosed simulant pond water, pH$\simeq$11.4 at 24 °C, to 90 °C on the corrosion behaviour of iron, nickel and chromium.

The peak seen at $\sim$0.2 V at 90 °C indicates the formation of a pit. Comparing this to the behaviour of chromium at the same temperature (Figure 3.20) a similar peak is observed suggesting Cr dissolution as the cause. The solubility of Cr, widely held to be a major contributor to electrode passivity, is known to increase with increasing solution temperature [212], so it is likely that residual protection at 90 °C is strongly influenced by the Ni or spinels present, as discussed at the end of section 3.2. However, it is important to note that for an increase in temperature from 24 to 90 °C there is a corresponding reduction in pH from 11.4 to 9.8. Thermodynamic data indicates that the steel may also lose some Ni protection at this lower pH (see the Pourbaix E_h-pH diagram for the Ni-H_2O system in reference [36]). Figure 3.21 shows an SEM image of the 20/25/Nb SS sample post exposure to simulant pond water at 90 °C. A pit is observed along with evidence of the presence of corrosion products. Also, the E_{OCP} is -0.18 V at 90 °C and thus lies below E_{ZC}. At potentials below E_{ZC} there is expected to be minimal passivation of the surface. Therefore, significant damage to the surface of 20/25/Nb SS would be expected if it were kept under such maloperation conditions for any extended period of time.
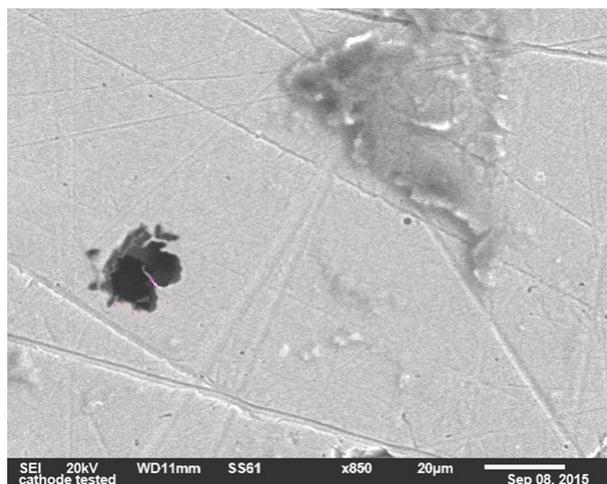
Figure 3.21: SEM image of pitting on the surface of 20/25/Nb SS post voltammetry at 90 °C in simulant pond water, pH$\simeq$11.4 at 24 °C.

3.6 Effect of the Presence of Hydrogen Peroxide in the Aqueous Phase on the Corrosion Behaviour of the 20/25/Nb Stainless Steel

As mentioned in section 1.8.4 hydrogen peroxide is a prominent oxidant that results from radiolysis. Numerous reports in the literature cite the use of H_2O_2 as a surrogate for the oxidising products of the radiolysis of water [107, 122, 142] including studies of the effect of radiolysis products on steels [74, 213]. Consistent with these reports a similar approach is adopted here in assessing the effect of radiolysis products on the corrosion behaviour of 20/25/Nb SS. Given that 20/25/Nb SS in NaOH-dosed pond water simulants has proved to be robust against corrosive attack by chloride, as with the temperature studies, H_2O_2 aqueous solutions dosed with NaOH are studied.

3.6.1 Effect of Hydrogen Peroxide Concentration in Simulant Pond Water on the Corrosion Behaviour of Unsensitised 20/25/Nb Stainless Steel

The influence of H_2O_2 concentration on the electrochemical behaviour of unsensitised 20/25/Nb SS is shown in Figure 3.22. A change in behaviour as the concentration increases above 100 μmol dm^{-3} is evident. First, an oxidative wave begins to develop with the addition of H_2O_2, starting at $\sim$0.2 V for low H_2O_2 concentration shifting to $\sim$0 V at higher H_2O_2 concentrations. Second, there is a shift in E_{ZC} to more positive potentials with increasing H_2O_2 concentration, shown in Figure 3.23.
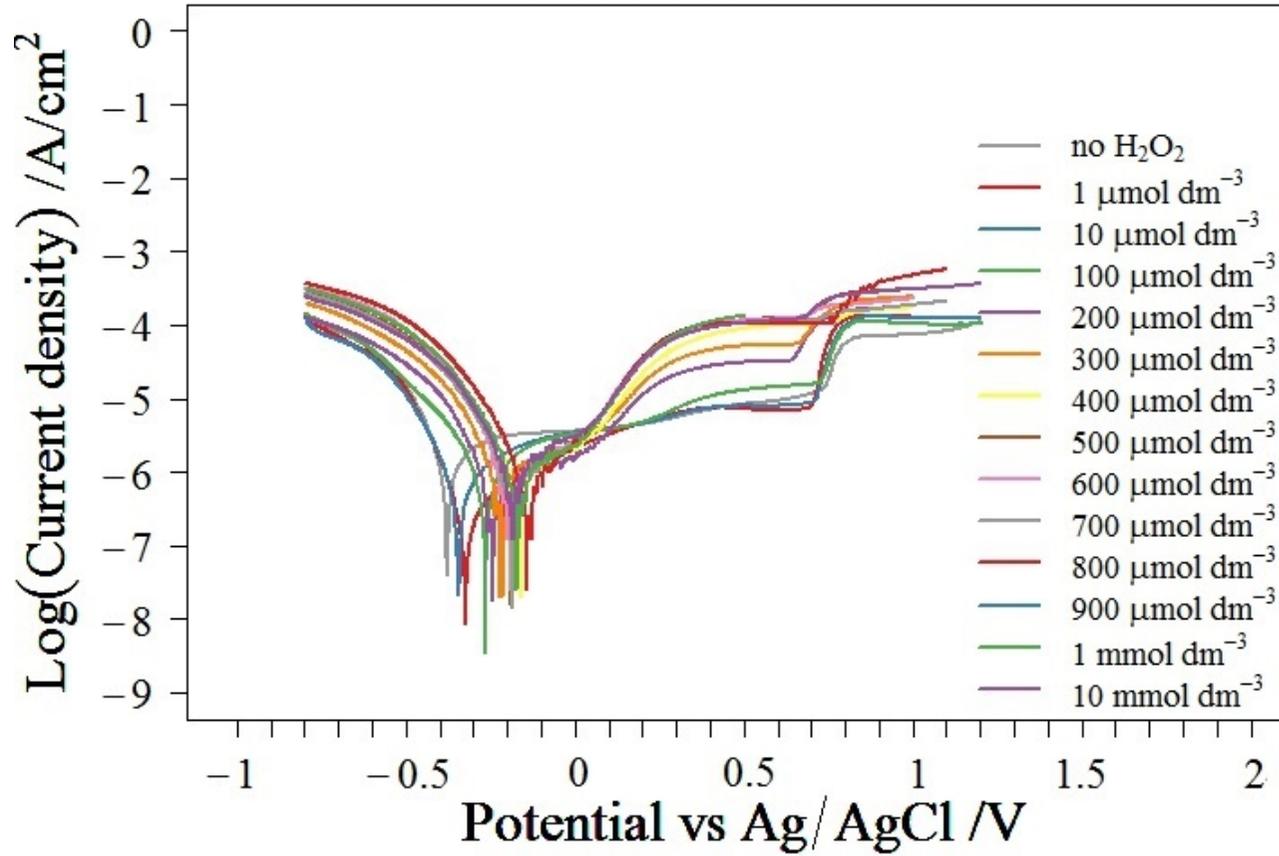
Figure 3.22: Potentiodynamic polarisation curve showing the effect of increasing H_2O_2 concentration on the corrosion behaviour of unsensitised 20/25/Nb SS in simulant pond water, 30 μmol dm^{-3} Cl$^-$, pH$\simeq$11.4 at 24 °C.

The increase in the wave current with increasing H_2O_2 concentration continues until a limiting concentration is reached and the peak current plateaus, this is shown explicitly in Figure 3.23. This behaviour is consistent with a reaction process that is controlled by a surface adsorption process - said adsorption being that of either the reactant itself or an intermediate species - under conditions where near-complete coverage or saturation has been achieved.
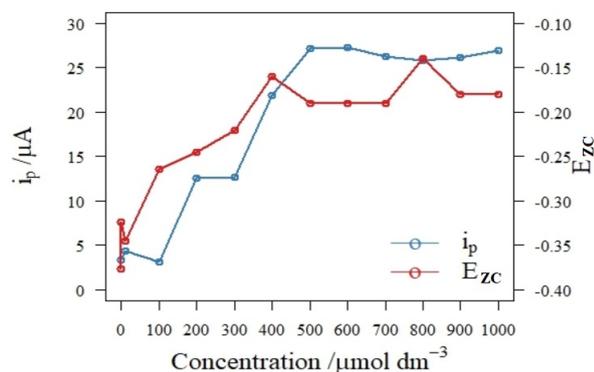
Figure 3.23: i_p and E_{ZC} vs concentration, data extracted from the potentiodynamic polarisation curve showing the effect of increasing H_2O_2 concentration on the corrosion behaviour of unsensitised 20/25/Nb SS in simulant pond water pH$\simeq$11.4 at 24 °C.

Further insight into this process can be obtained by repeating the linear sweep voltammetry experiments of Figure 3.22 as a function of scan rate, ν. According to the Randle-Sevcik equation, equation 3.2, if electrochemical reactions are diffusion-controlled the maximum peak (or in this case wave) current is linearly proportional to $\nu^{1/2}$.

$$i_p = 0.4432nFAC \left(\frac{nFD\nu}{RT} \right)^{\frac{1}{2}} \tag{3.2}$$

where i_p is the peak current, n is the number of electrons transferred in the reaction, F is the Faraday constant, A is the surface area, C is the concentration, ν is the scan rate, R is the ideal gas constant and T is the temperature.

If however, the reaction is controlled by a surface adsorption process, then the peak current is given by equation 3.3 i.e. i_p is linearly proportional to ν [214].

$$i_p = \frac{n^2 F^2 \nu \Gamma^*}{4RT} \tag{3.3}$$

where Γ^* is the surface coverage of the adsorbed species.

Thus, the relationships between peak current and potential sweep rate allows for determination of whether the associated electrochemical reaction is under diffusion control or surface/adsorption control. In the case of the former, it is the convention that the peak current is proportional to the square root of the sweep rate; in the case of the latter, the peak current is linearly proportional to potential sweep rate. However, for processes that are under diffusion control, be they reversible or irreversible, the current at any point on the associated peak / wave can be shown to be proportional to the square root of the sweep rate [215]. Based on these two relationships, Figure 3.24 shows graphs of i_p vs ν or $\nu^{1/2}$ for the data of Figure 3.22 and its wider sweep rate dependent dataset. Specifically, peak current values recorded at potentials of 0.5 V were plotted as functions of ν or $\nu^{1/2}$ – this potential having been selected on the basis that currents due to the addition of peroxide to the electrolyte solution are observed at this potential for all peroxide concentrations studied. The dependency with the largest R^2 value is deemed to control the current. R^2 values have been tabulated for the convenience of the reader in Table 3.3.

Concentration /μmol dm^{-3}	0	1	10	100	300	1000
R^2 for i_p vs ν	0.992	0.986	0.984	0.955	0.944	0.984
R^2 for i_p vs $\nu^{1/2}$	0.932	0.985	0.982	0.998	0.998	0.968

Table 3.3: R^2 values for linear regression of i_p vs ν and i_p vs $\nu^{1/2}$.

By comparison of the R^2 values for linear regression through the i_p vs ν and $\nu^{1/2}$ plots at each peroxide concentration it can be seen that, in the absence of H_2O_2 the current in the potential range of interest ($\sim$0 - 0.7 V) is linearly proportional to the scan rate (see Figure 3.24(a) and (b)). From this it can be concluded that the current is then being controlled by one or both the following; a) simple capacitive charging of the passivating oxide layer as discussed above; and/or b) oxidation of a

component of the oxide layer at the electrode surface most likely Cr(III) or Ni(II) i.e. general corrosion, again as discussed above.

The addition of 1 μmol dm^{-3} and 10 μmol dm^{-3} H$_2$O$_2$ to simulant pond water results in a linear current dependency on both ν and $\nu^{1/2}$ in the potential range of interest ($\sim$0 - 0.7 V)(see Figure 3.24(c)-(f)), suggesting the diffusion controlled electrochemistry of peroxide oxidation and the processes that occur in the absence of peroxide as previously described are in competition.

At H$_2$O$_2$ concentrations between 100 and 400 μmol dm^{-3} a linear dependence on $\nu^{1/2}$ is observed, see Figure 3.24(g)-(j). This is consistent with behaviour predicted by the Randles-Sevcik equation above i.e. the overall H$_2$O$_2$ oxidation reaction is controlled by the diffusion of H$_2$O$_2$ to the electroactive sites on the surface oxide layer.

At H$_2$O$_2$ concentration greater than $\sim$500 μmol dm^{-3} peak current is once again proportional to ν, see Figure 3.24(k) and (l). As described above, this is in accordance with a reaction that is controlled by surface adsorption of the reactant prior to its oxidation, under conditions where near-complete surface coverage or saturation has been achieved.
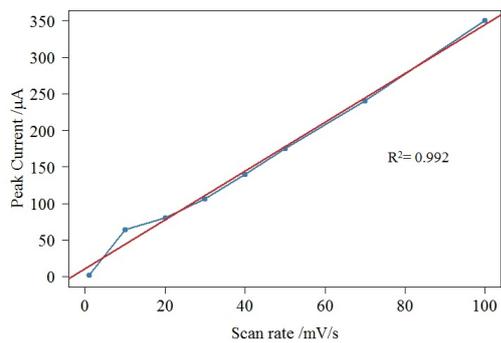
(a)
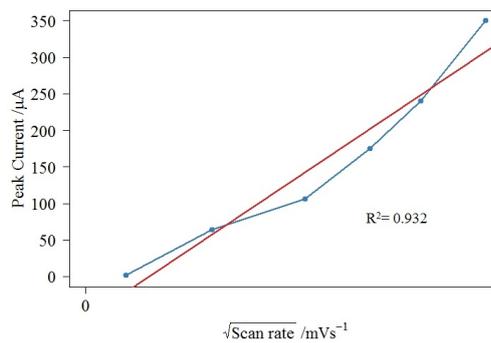
(b)
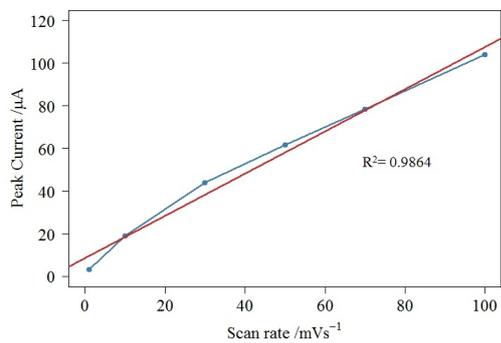
(c)
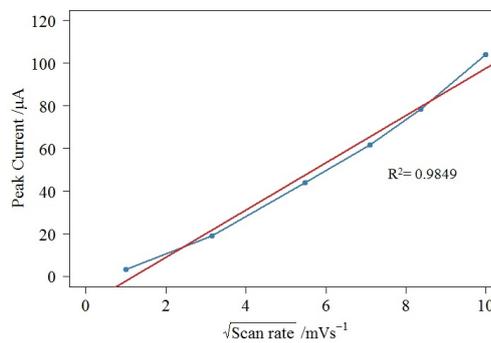
(d)
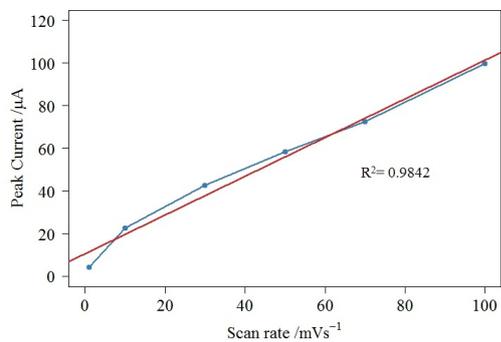
(e)
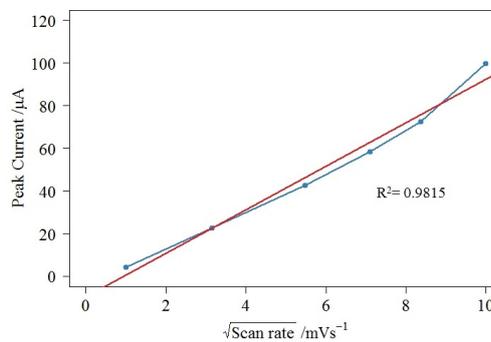
(f)
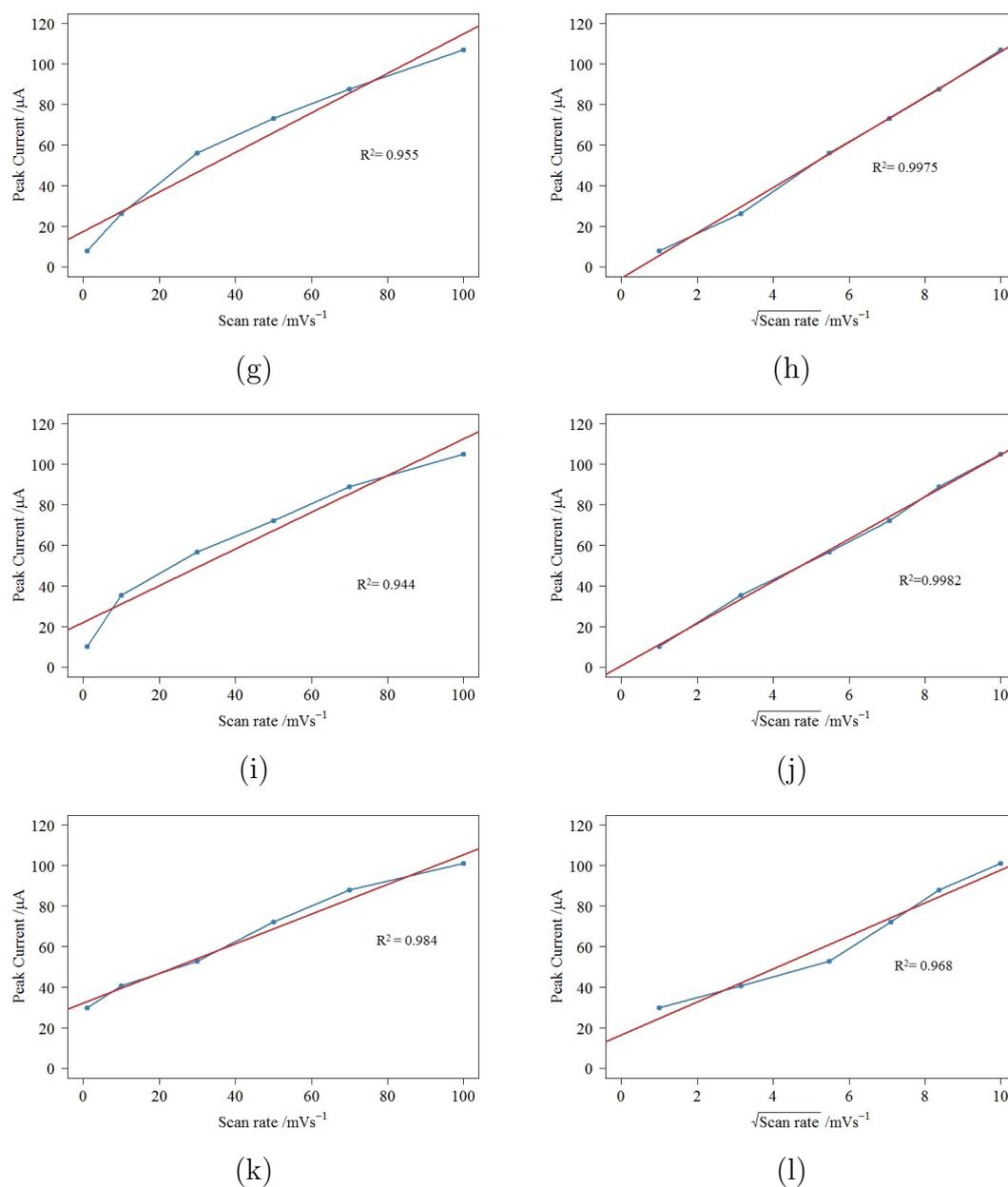
Figure 3.24: Scan rate dependency of the polarisation curves of 20/25/Nb SS in simulant pond water, pH$\simeq$11.4 at 24 °C, containing different concentrations of hydrogen peroxide (a) & (b) 0 μmol dm^{-3}, (c) & (d) 1 μmol dm^{-3}, (e) & (f) 10 μmol dm^{-3}, (g) & (h) 100 μmol dm^{-3}, (i) & (j) 300 μmol dm^{-3} and (k) & (l) 1 mmol dm^{-3}.

These findings are complimented by the data of Table 3.4, which shows the impact of H_2O_2 concentration on the open circuit potential of unsensitised 20/25/Nb SS in dosed pond water. Increasing the H_2O_2 concentration increases the OCP. OCPs of 20/25/Nb SS in solutions with H_2O_2 concentrations 100 μmol dm^{-3} and above start to become closer in value. Such a trend would be expected

if, like the passive region current data of Figure 3.22, the net anodic half reaction that defines the OCP is largely controlled by an adsorption process where surface coverage by the electroactive species saturates at these higher concentrations.

Concentration $/\mu$mol dm^{-3}	0	1	10	100	1000	10000
OCP dosed water /V	-0.01	0.01	0.09	0.17	0.2	0.22

Table 3.4: Variation in open circuit potential with increasing H_2O_2 concentration in dosed simulant pond water, pH$\simeq$11.4 at 24 °C.

Both of these findings are consistent with the general trends observed in the work of Worthington *et al.* [79] who report that, for 304H stainless steels, E_{OCP} is independent of H_2O_2 concentration above 15 μmol dm^{-3} and studies by Hall *et al.* [216] and Gorton [217] where it was reported that for the oxidation of H_2O_2 on Pt and Pd, i_p vs $[H_2O_2]$ plots begins to plateau at $[H_2O_2]>10$ mmol dm^{-3}. For both metals, this observation is explained using the following mechanism, whereby H_2O_2 first adsorbs at electrochemically generated adsorption sites before then disproportionating to H_2O and O_2. The binding sites are then regenerated electrochemically via equations 3.4-3.6:

$$M(OH)_2 + H_2O_2 \rightleftharpoons (M(OH)_2 \cdot H_2O_2)_{ads} \tag{3.4}$$

$$(M(OH)_2 \cdot H_2O_2)_{ads} \longrightarrow M + 2H_2O + O_2 \tag{3.5}$$

$$M + 2H_2O \longrightarrow M(OH)_2 + 2e^- + 2H^+ \tag{3.6}$$
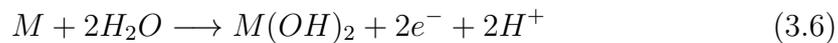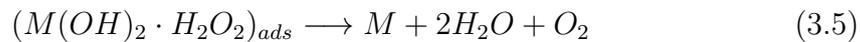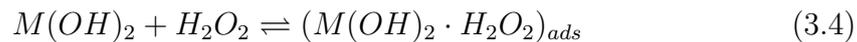
Given the results of Figure 3.22 and 3.24, it is not unreasonable to postulate a similar mechanism for the oxidation of H_2O_2 on 20/25/Nb SS. Saturation of binding sites with adsorbed H_2O_2 would then explain the increase of i_p and OCP with increasing $[H_2O_2]$ at high peroxide concentrations.

Note that of the peroxide concentrations investigated here, peroxide concentrations of 10 μmol dm^{-3} is the most realistic for the storage ponds.

3.6.2 Effect of Temperature in the Presence of Hydrogen Peroxide in Simulant Pond Water on the Corrosion Behaviour of Unsensitised 20/25/Nb Stainless Steel

Experiments in which the pond water temperature was increased in the presence of hydrogen peroxide were carried out to better simulate real storage conditions under the new packing regime as discussed in the introduction. Previous modelling work performed at the UK National Nuclear Laboratory indicates that the H_2O_2 concentration at the 20/25/Nb SS cladding surface of used AGR fuel pins will be in the region of $\sim$1 ppm (30 μmol dm^{-3}) [125]. It is well established that hydrogen peroxide is more unstable towards decomposition by disproportionation at elevated temperatures than at room temperature [2,76]. However, despite the increased decomposition rates, H_2O_2 is known to exist and be a prominent oxidant at all temperatures relevant to interim storage of spent fuel pins [67]; thus, its role in the corrosion behaviour of the cladding at high packing temperatures must be explicitly addressed.

Figure 3.25 shows the temperature dependence of the corrosion behaviour of 20/25/Nb SS with upper and lower H_2O_2 concentrations of 100 μmol dm^{-3} and 10 μmol dm^{-3} respectively in solution. Figure 3.25(a) show that, at 45 °C, currents in the passive region increase with peroxide concentration in a manner similar to that observed at 25 °C as described in section 3.5.1.

Similarly, Figure 3.25(b) shows that, at 60 °C, 20/25/Nb SS samples immersed in H_2O_2-free solution and a solution containing peroxide at $[H_2O_2]\simeq$10 μmol dm^{-3} behave in a similar manner, an observation that may be due to more rapid decomposition of the low concentration of H_2O_2 at this elevated temperature. However, samples in solutions containing 100 μmol dm^{-3} H_2O_2 exhibit more positive E_{ZC} and greater currents between 0.2 and 0.7 V, again indicating the presence of H_2O_2 electrochemistry similar to that observed at the same peroxide concentration at 24 °C.

(a)

(b)

(c)
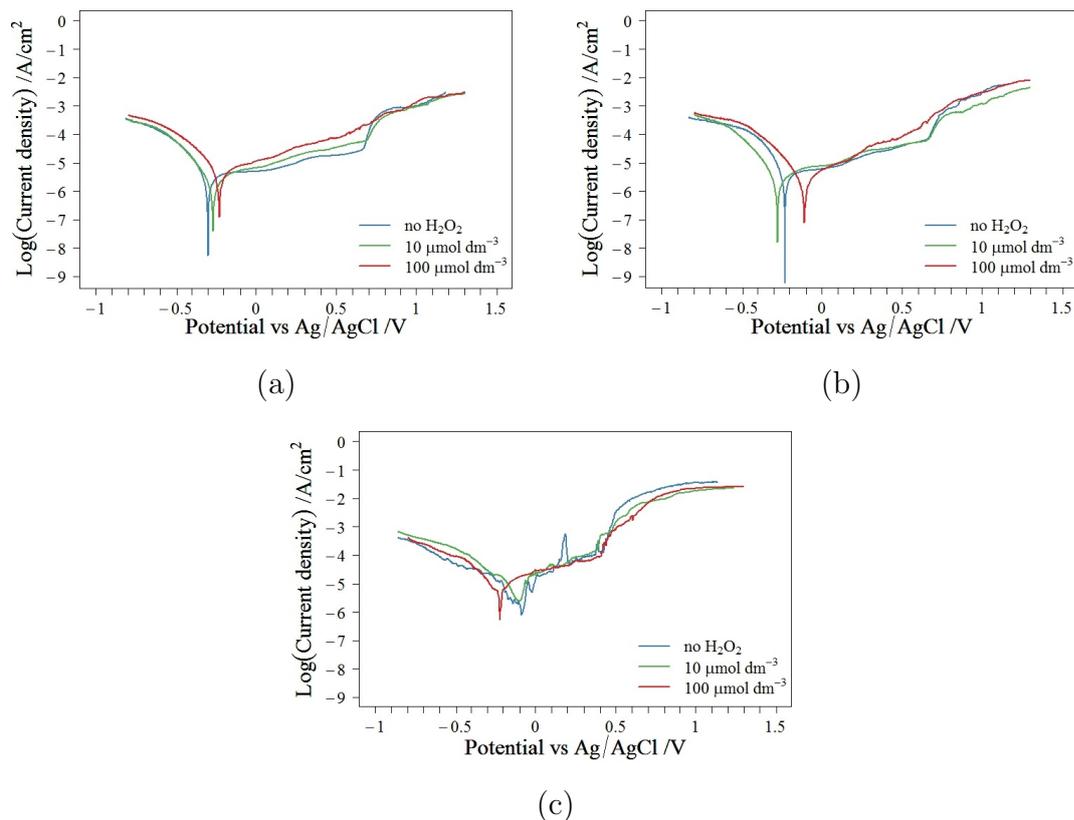
Figure 3.25: Potentiodynamic polarisation curves showing the effect of increasing temperature of the simulant pond water, 30 μmol dm^{-3} Cl$^-$, pH$\simeq$11.4 at 24 °C, containing 0, 10 and 100 μmol dm^{-3} H$_2$O$_2$, on the corrosion behaviour at (a) 45 °C, (b) 60 °C and (c) 90 °C.

From Figure 3.19 it can be seen that, for unsensitised 20/25/Nb SS in simulant pond water solution at 90 °C in the absence of H$_2$O$_2$, there is evidence of metastable pit formation - as indicated by peaks at 0.2 and 0.4 V. However, as can be seen in Figure 3.25(c), addition of as little as 10 μmol dm^{-3} H$_2$O$_2$ largely suppresses pit formation and at 100 μmol dm^{-3} metastable pit formation appears to be suppressed completely. Potential sources of this suppression are: the thermodynamically allowed reduction by H$_2$O$_2$ of soluble Cr(VI), potentially released as chromate during the pitting event, to insoluble Cr(III), most likely as Cr(OH)$_3$; or the oxidation by H$_2$O$_2$ of soluble Fe(II), also potentially released during metastable pit formation, to form a Fe(OH)$_3$ precipitate. Both mechanisms, which may lead to the repassivation of 20/25/Nb SS, may be augmented by the high temperature decomposition of H$_2$O$_2$ to OH$^-$ (equation

1.11 in Chapter 1). Irrespective of the mechanism, the presence of H_2O_2 at concentrations as low as 10 μmol dm^{-3} seems to protect against pitting corrosion at temperatures up to 90 °C – a potential safety benefit as both this temperature and [H_2O_2] are relevant to the interim wet storage of spent nuclear fuel.

3.7 Conclusions

The principal conclusions of this section regarding the electrochemical corrosion behaviour of unsensitised 20/25/Nb SS cladding under conditions relevant to the wet interim storage of AGR fuel pins are as follows.

The OCP in simulant pond water (pH$\simeq$11.4) is found to be $\sim$0 V vs Ag/AgCl. Under these conditions, XPS data indicates that the protective oxide layer formed on the surface of 20/25/Nb SS consists predominately of Fe and Cr oxides. Resistance and capacitance data from EIS experiments shows that the source of this protection changes on application of an oxidative stress i.e. as the electrode potential is increased. Through comparative analysis with single metal samples of the main constituent elements of 20/25/Nb SS, Cr, Ni and Fe, it was found that this change occurs at $\sim$0.5 V whereupon the protection provided by Cr_2O_3 is lost due to its oxidative dissolution as Cr(VI). At potentials greater than 0.5 V the surface behaviour is controlled by a Ni oxide layer with a potential contribution from spinels such as $NiFe_2O_4$. Transpassive dissolution of this (now predominantly nickel) oxide layer takes place at potentials above 0.75 V.

Voltammetric studies were used to investigate the robustness of this oxide layer. Tests under baseline conditions of pH=8 at 24 °C show a broad region of passivity from $\sim$-0.15 V vs Ag/AgCl to $\sim$0.65 V, punctuated by transient pitting events in the region of 0.4 V. However, at pH 11.4, not only are these pitting features eliminated, the window of passivity is also extended to $\sim$-0.3 V to 0.75 V – indicating that simple dosing of the system with NaOH provides significant corrosion protection on unsensitised 20/25/Nb SS samples under these conditions. This protection, derived from the reduced solubility of the constituent metals of

the alloy at higher pHs, is maintained at pH 11.4 at 45 °C in the presence of 30 μmol dm^{-3} of both Cl$^-$ and H$_2$O$_2$, i.e. under future interim storage conditions, with a separation of over a volt between E$_{ZC}$ and onset of transpassivity indicating that intergranular attack is unlikely – at least on unsensitised cladding.

The extent of the envelope of this protection was studied as a function of key solution parameters such as temperature, chloride concentration and hydrogen peroxide concentration – including conditions relevant to future wet storage scenarios and their fault conditions. Results may be summarised as follows.

With respect to chloride concentration: In the absence of hydroxide i.e. at pH 8 close to neutrality, chloride readily attacks the passive layer on 20/25/Nb SS from concentrations as low as 30 μmol dm^{-3}. Key features of this attack are a cathodic shift in the onset transpassivity and appearance of pitting corrosion in the passive range. However, when the pH is increased to 11.4, i.e. the pH of dosed simulant pond water, chloride is only seen to induce either type of corrosion behaviour (shift in onset of transpassivity, pitting corrosion) at concentrations greater than 50 mmol dm^{-3}. This is a significantly higher chloride concentration than expected under foreseen fault conditions, indicating that protection will be maintained under such.

With respect to temperature: At temperatures $\leq$60 °C, general corrosion currents increase and the onset of transpassivity moves slightly towards more negative potentials with increasing temperature. Thus, there appears to be no localised corrosion threat to fuel cladding as electrolyte / storage medium temperature is increased from 24 °C to 60 °C. However, at the higher temperature of 90 °C the potential range of passivity is attenuated by approximately 250 mV at both its cathodic and anodic limits and significant pitting activity is observed in the range of passivity that remains – suggesting that the protective oxide layer on the surface of 20/25/Nb SS is breaking down under these conditions.

With respect to hydrogen peroxide concentration: Voltammetry

indicates that H_2O_2 is simply oxidised at the surface of 20/25/Nb SS in the passive potential range. The associated oxidation current increases linearly with concentration values in the range $[H_2O_2] \simeq 10$ - 500 μmol dm^{-3}. At values higher than this, the associated current becomes invariant with concentration, indicating that the oxidation of peroxide at the steel surface is controlled by a surface adsorption process, as described in equations 3.4-3.6.

At temperatures ≤ 60 °C and at peroxide concentrations in the range 0 to 100 μmol dm^{-3}, the corrosion behaviour of 20/25/Nb SS and the dependence of peroxide oxidation current on $[H_2O_2]$ is similar to that observed at the same peroxide concentrations at 24 °C. As this $[H_2O_2]$ range embraces that expected due to the radiolysis of water in storage ponds (~ 30 μmol dm^{-3}), it is not unreasonable to conclude that radiogenic peroxide does not significantly affect cladding corrosion under these conditions. However, this is not the case at 90 °C where the presence of peroxide suppresses the pitting corrosion that is observed in the passive range at the same temperature in peroxide-free electrolytes – suggesting that peroxide actually has a protective action on 20/25/Nb SS at this temperature. As T $=$ 90 °C is one of the main fault conditions to be considered in the interim storage safety case, this peroxide-derived protection is an unexpected benefit.

Chapter 4

Heat Treated 20/25/Nb Stainless Steel

In the previous chapter the behaviour of unsensitised as-received 20/25/Nb SS was analysed. However, in section 1.9.4 radiation induced segregation (RIS) is highlighted as a source of concern for approximately 25 % of AGR fuel elements. RIS causes fuel cladding to become susceptible to intergranular corrosion. Studying irradiated cladding is problematic due to radiological and economic concerns. Therefore, the NNL have been attempting to recreate the effects of RIS using thermal ageing treatments.

The reasoning behind the heat treatments used on 20/25/Nb SS in an attempt to mimic RIS are outlined in section 2.1.4.1. Accordingly, two 20/25/Nb SS samples were subjected to two different heat treatments. One sample was solution annealed for 0.5 hours at 1050 °C and the other 0.5 hours at 1150 °C. Both were then aged for 48 hours at 600 °C. Treatment at 1050 °C attempts to minimise grain growth during the annealing stage but the free carbon concentration may not be adequate in inducing sensitisation on ageing at 600 °C. The higher temperature results in more free carbon in solid solution giving a greater probability that sensitisation will occur on subsequent ageing. The following subsections explore the electrochemical behaviour of these heat treated 20/25/Nb SS under wet interim storage conditions.

4.1   Degree of Sensitisation

Radiation induced sensitisation can cause chromium concentrations at the grain boundaries in 20/25/Nb SS to decrease to as low as 10 wt% in high burn-up fuels [82, 88]. Note that a stainless steel is considered sensitised if the chromium is ≤ 12 wt% at the grain boundaries [92]. Thus, it should be easy to demonstrate whether the heat treated 20/25/Nb SS has sufficient chromium depletion to represent RIS-affected cladding, using electrochemical etching and double loop electrochemical potentiokinetic reactivation tests. These tests are described in sections 2.2.3 (method) and 3.1 (results on unsensitised 20/25/Nb samples).

4.1.1   Electrochemical Etching of Heat Treated 20/25/Nb SS

Figures 4.1(a) and (b) show the polished surfaces of 20/25/Nb SS samples solution annealed at 1050 °C and 1150 °C respectively. Both surfaces are broadly featureless. Figure 4.1(c) shows an SEM image for the sample solution annealed at 1050 °C etched in oxalic acid for 15 seconds at 6 V. Ditching is evident but complete etch around the grains is not achieved. As no grains have been entirely encircled the level of corrosion susceptibility of the sample can not be confirmed [160]. Figure 4.1(d) shows an image of the sample solution annealed at 1150 °C post etching in oxalic acid. Complete and partial ditching around the grain boundaries is observed. This is evidence of stainless steel sensitisation according to ASTM standard A262 [160] and as summarised in section 2.2.3.1. Thus, the sample solution annealed at 1150 °C is considered to be sensitised. However, the sample solution annealed at 1050 °C is in need of further examination. Accordingly, both are subject to the DL-EPR below.

Ditching at the grain boundaries allows an average grain size to be determined. In the case of 20/25/Nb SS solution annealed at 1150 °C the average grain sizes are

~20 μm. Since only partial ditching is achieved for the sample solution annealed at 1050 °C the grain size can not be determined. However, from the image of the 20/25/Nb SS solution annealed at 1150 °C, it is clear that heat treating the stainless steel results in an increase in the grain size of the material (recalling that as-received samples have an average grain size of ~10 μm as discussed in section 3.1).

(a)

(b)

(c)

(d)
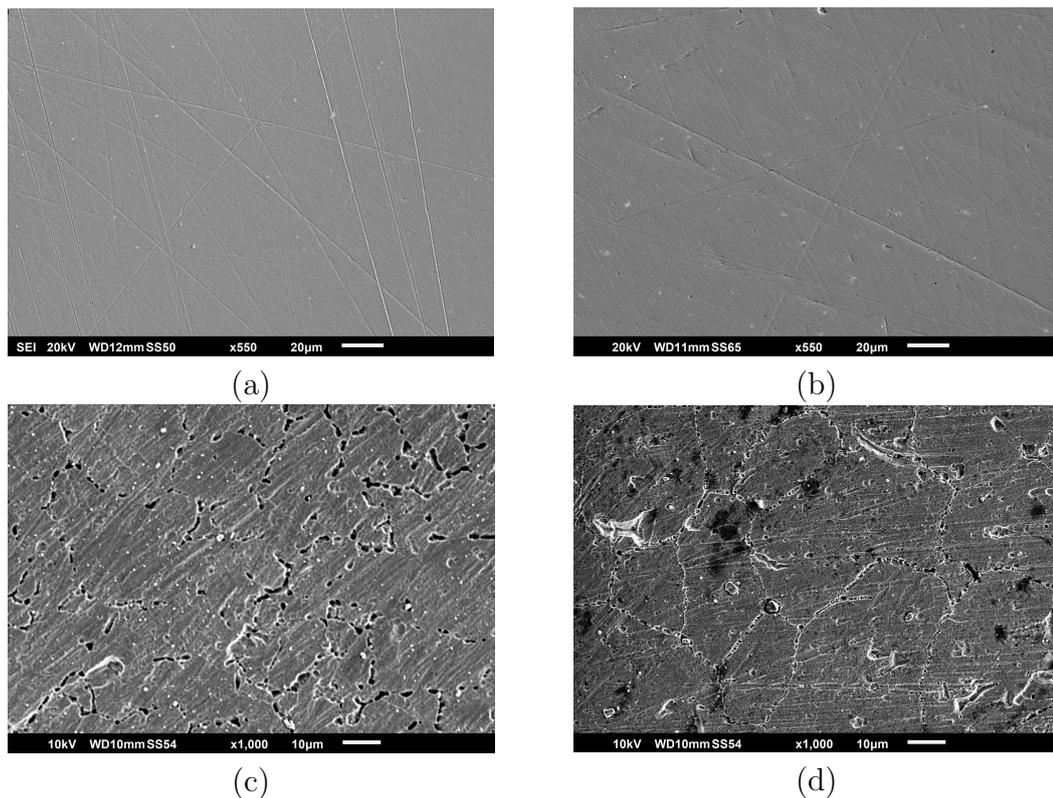
Figure 4.1: SEM images of heat treated 20/25/Nb SS pre- and post-exposure to 10% oxalic acid for 15 seconds at 6 V. Sample heat treated at (a) & (c) 1050 °C and (b) & (d) 1150 °C then both aged for 48 hours at 600 °C.

4.1.2 Double Loop Electrochemical Potentiokinetic Reactivation Tests of Heat Treated 20/25/Nb

In order to confirm and quantify the sensitisation of heat treated 20/25/Nb SS DL-EPR tests were carried out on both samples. The resultant curves are shown in Figure 4.2. The ratio of the reactivation peak current to the activation peak current for 20/25/Nb SS solution annealed at 1050 °C and aged for 48 hours at 600 °C and 20/25/Nb SS solution annealed at 1150 °C and aged for 48 hours

at 600 °C are 0.78 and 0.92 respectively. It therefore appears that both samples have been sensitised to intergranular corrosion [161, 162], with the sample solution annealed at 1150 °C showing greater corrosion susceptibility.

(a)   (b)
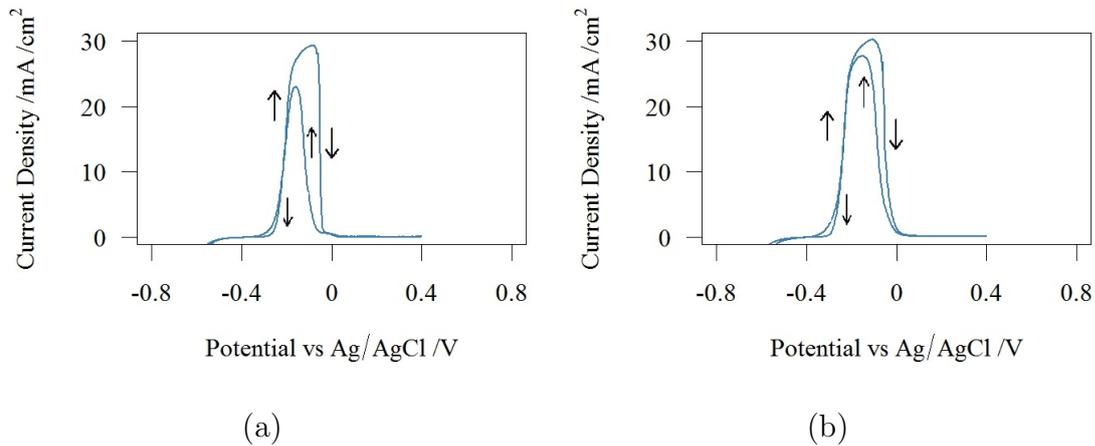
Figure 4.2: DL-EPR test on heat treated 20/25/Nb SS in solution of 0.5 mol dm^{-3} H_2SO_4 and 0.01 mol dm^{-3} KSCN with a scan rate of 1.6 mV/s. Results for samples heat treated at (a) 1050 °C and (b) 1150 °C then aged for 48 hours at 600 °C.

Despite the apparent sensitisation of the sample heated at 1050 °C for 0.5 hours and aged at 600 °C for 48 hours, this sample failed to crack during initial screening tests for RIS conducted by our collaborators at the UK National Nuclear Laboratory. Specifically, it did not crack in a C-ring test when loaded by a 316L SS bolt, tightened until the diameter of the sample was reduced by 1 mm, and immersed in acidified thiosulphate/chloride solution [82]. The sample heated at 1150 °C for 0.5 hours and aged at 600 °C for 48 hours passed this screening test. As well, elemental composition profiles recorded at sample grain boundaries using TEM showed evidence of chromium depletion, as shown in Figure 4.3 [82]. Therefore, in the sections that follow, further materials characterisation and electrochemical corrosion testing is only carried out on 20/25/Nb SS heated at 1150 °C for 0.5 hours and aged at 600 °C for 48 hours.
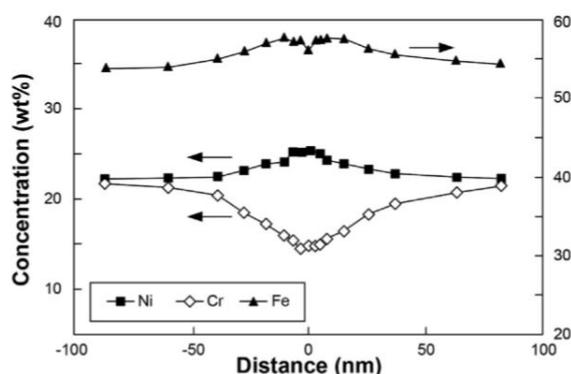
Figure 4.3: Grain boundary composition profile obtained for 20/25/Nb SS heated at 1150 °C for 0.5 hours and aged at 600 °C for 48 hours [82].

4.2 Compositional Analysis of the Passive Film Formed on Heat Treated 20/25/Nb Stainless Steel in Simulant Pond Water

Having determined the degree of sensitisation of the sample that was solution annealed at 1150 °C, it is now appropriate to determine if the composition of the surface layer under simulant pond water conditions reflects this. Thus, the composition of the passive film was examined using XPS to ascertain if any compositional differences exist in the passive film grown on heat treated compared to unsensitised 20/25/Nb SS (section 3.2) under open circuit conditions in simulant pond water.

However, before XPS measurements were performed on the immersed samples, simple electrochemical impedance spectroscopy (EIS) measurements where conducted to provide a qualitative initial assessment as to how the composition of the steel passive layer changes as a function of immersion time. Specifically, EIS measurements were conducted every 30 minutes on heat treated 20/25/Nb SS immersed in simulant pond water up to a total immersion time of 6 hours. Selected Nyquist and Bode plots from this run are shown in Figure 4.4. The Nyquist plots are somewhat noisier at the low frequency end than those

recorded during an analogous experiment on unsenitised, as-received 20/25/Nb SS. However, the Bode plots are almost invariant with time after only 30 minutes of immersion and are wholly invariant with time after 4 hours immersion. Especially in light of this latter result, it is not unreasonable to assume that the passive layer has stabilised after this relatively short immersion period. As the purpose to the data presented in Figure 4.4 was to simply provide qualitative evidence that the passive film quickly stabilises, equivalent circuit modelling of these plots was not performed. Detailed equivalent circuit modelling of the surface layer is discussed later.

(a)

(b)

(c)
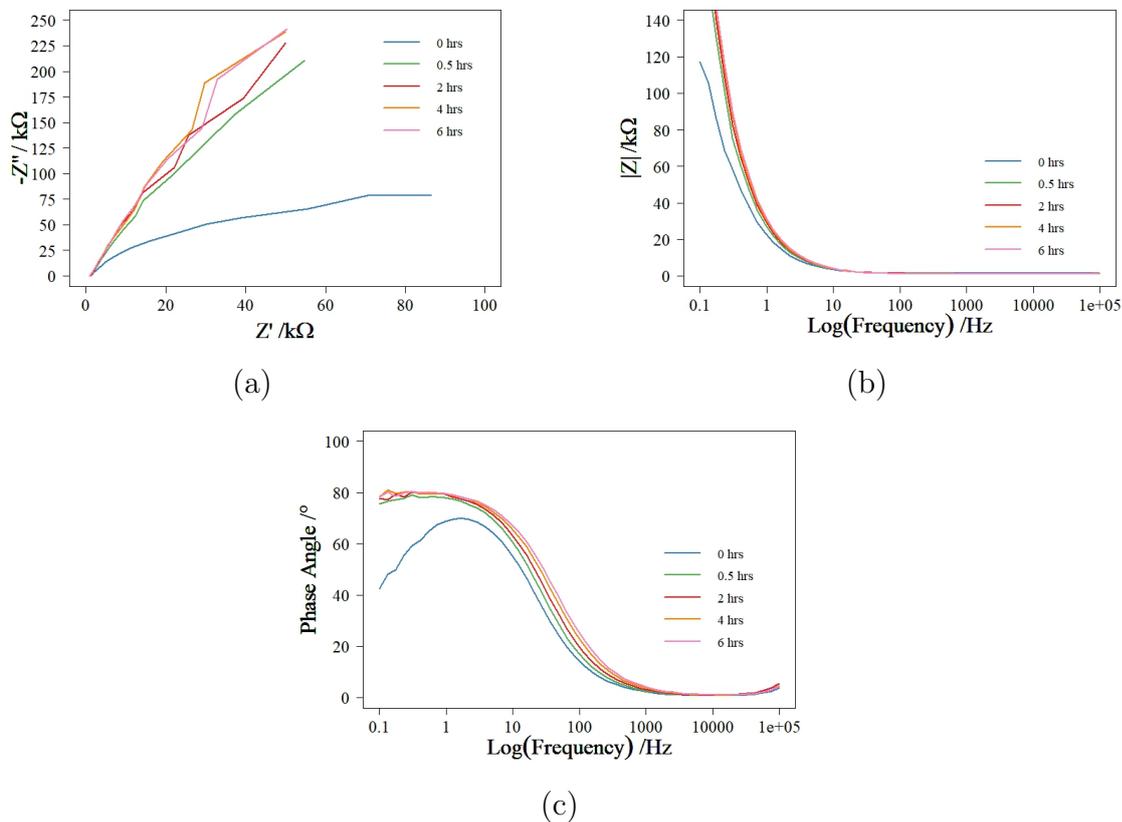
Figure 4.4: Time dependant Nyquist and Bode plots for heat treated 20/25/Nb SS in simulant pond water, pH$\simeq$11.4.

As for the unsensitised samples, XPS spectra were obtained for heat treated 20/25/Nb SS immersed in simulant pond water for one week at 24 °C. During this time the open circuit potential, E_{OCP}, was observed to obtain an equilibrium value of $\sim$-0.1 V vs Ag/AgCl. This is 100 mV negative of the value recorded on the

as-received samples and is almost certainly due to the lower Cr content observed at the surface of the heat treated sample. The spectra were analysed in the same way as for the unsensitised 20/25/Nb SS described in section 3.2. The peak positions were within ± 0.2 eV of those found for the unsensitised materials and therefore it is reasonable to assume the peak assignments hold true (see Table 3.2 and the more explicit description in section 3.2). The Fe, Cr, Ni and O profiles for heat treated 20/25/Nb SS are presented in Figure 4.5.
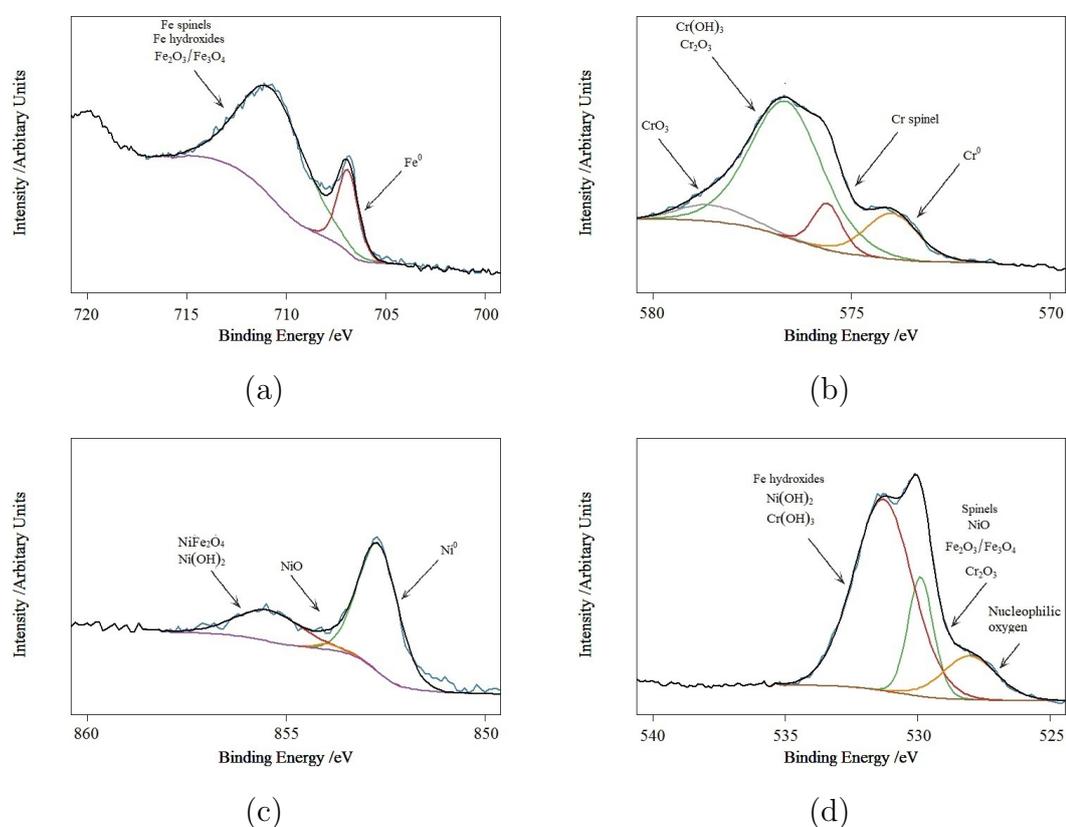
Figure 4.5: XPS profile of (a) Fe $2p_{3/2}$, (b) Cr $2p_{3/2}$, (c) Ni $2p_{3/2}$ and (d) O 1s after week long immersion of heat treated 20/25/Nb SS in simulant pond water, pH$\simeq$11.4 at 24 °C.

As discussed in section 3.2, it is difficult to determine the relative contributions of each phase to the passive layer from simple visual inspection of the XPS spectra. However, by plotting the relative atomic percentages of each species for iron, Figure 4.6(a), chromium, Figure 4.6(b) and nickel, Figure 4.6(c) the differences between the passive layer formed on unsensitised 20/25/Nb SS and heat treated 20/25/Nb SS can be more easily understood. In these figures bar A represents unsensitised

20/25/Nb SS and bar B represents heat treated 20/25/Nb SS. The data for each individual element is normalised by dividing the intensity of each component peak by its unique photoionisation cross-section and then converting to atomic percent, this allows for comparative analysis between the two samples.
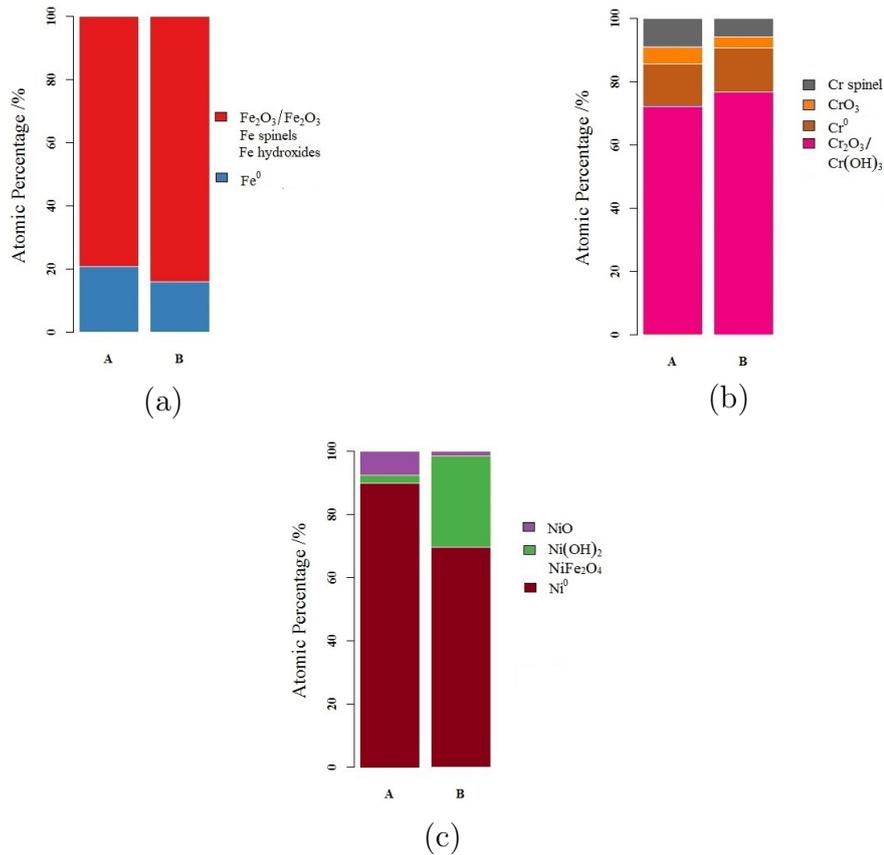
Figure 4.6: Atomic percentage data comparison of (a) Fe 2p$_{3/2}$, (b) Cr 2p$_{3/2}$ and (c) Ni 2p$_{3/2}$ extracted from XPS profiles obtained after a week long immersion of **A** unsensitised 20/25/Nb SS and **B** heat treated 20/25/Nb SS in simulant pond water at 24 °C, pH$\simeq$11.4.

Relative to the metallic Fe peak, there is a small increase in the $Fe_2O_3/Fe_3O_4/Fe(OH)_2/Fe(OH)_3/FeOOH$ peak intensity at or close to the surface of heat treated compared to unsensitised 20/25/Nb SS. This suggests that the depletion of chromium at the grain boundary in the heat treated sample causes a reduction in the Cr oxide/hydroxide in the surface layer with a consequent loss of protection against oxidation of the remaining metals and thus, leads to a larger Fe oxide/hydroxide content at the outer surface.

The relative atomic percentages for the Cr species are shown in Figure

4.6(b), the Cr metal peak has a similar intensity for both unsensitised and heat treated samples. There appears to be slightly more CrO_3 (Cr(VI)) formed on the unsensitised sample. Chromium is more soluble in its Cr(VI) oxidation state and thus greater concentrations would imply greater corrosion susceptibility. However, since the contribution is less than 10 at% for both SS samples this result maybe not be of significance. In fact this may be masked by the greater Cr spinel content in the surface layer of unsensitised 20/25/Nb SS, which were seen to offer extended corrosion protection in Chapter 3. Therefore, it is likely that heat treated 20/25/Nb SS may not be afforded this added protection. For heat treated 20/25/Nb SS Cr_2O_3/Cr(OH)$_3$ content on the surface of the samples appears to be more than 10 % greater than on the unsensitised 20/25/Nb SS. At first sight, this may appear to be a contradiction to the previous statement that Fe oxides/hydroxides may be the more dominant oxide in the outer passive film on heat treated samples. However, it is important therefore to remember that these atomic percentages only describe the relative percentage of the single element in the sample itself. To determine the relative roles played by the Cr and Fe oxides/hydroxides with respect to each other in the surface layer, it is necessary to combine relative percentage bar charts for Cr and Fe together to form a simple bar chart. Considering the high nickel content of this alloy, it would be appropriate to include nickel in such an analysis as well (as for unsensitised 20/25/Nb SS in Figure 3.7). This analysis shall be revisited below.

Contributions from Ni are largely due to Ni metal for both samples. A very small amount of $Ni(OH)_2$ is present at the unsensitised 20/25/Nb SS surface whereas $\sim$28 at% of the Ni contribution on heat treated 20/25/Nb SS is $Ni(OH)_2$. Whereas NiO is present in higher concentrations at the unsensitised 20/25/Nb SS surface. Due to the comparatively weak intensity of the NiO peak this result should be viewed with caution.

As described above, in order to achieve a true comparative analysis it is necessary to merge the three relative atomic percentage bar charts of Fe, Cr and

Ni to obtain a relative atomic percentage bar chart that considers all the dominant elements together in the passive layer. This is achieved following the same normalisation method as described in section 3.2. The resulting bar charts showing the relative atomic percentages are found in Figure 4.7.
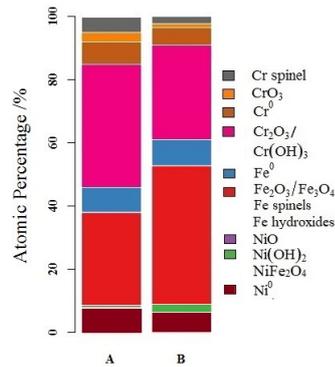
Figure 4.7: Atomic percentage data comparison of Fe, Cr and Ni in the passive layer of **A** unsensitised 20/25/Nb SS and **B** heat treated 20/25/Nb SS extracted from XPS profiles obtained after a week long immersion in simulant pond water, pH≃11.4 at 24 °C.

Firstly, considering the total contribution of each element to the surface film, the total iron concentration is higher in the surface layer formed on heat treated 20/25/Nb SS compared with unsensitised 20/25/Nb SS, the opposite is true for chromium where the total contribution is lower in the heat treated 20/25/Nb SS film and nickels total contribution stays relatively unchanged.

For heat treated 20/25/Nb SS, Fe oxides/hydroxides make up ∼44 at% of the outer passive layer and ∼30 at% consists of Cr(III) oxides/hydroxides. Comparatively, for unsensitised 20/25/Nb SS ∼29 at% of the surface film is Fe oxides/hydroxides and ∼39 at% consists of Cr(III) oxides/hydroxides. There is less available Cr at the surface of heat treated 20/25/Nb SS but a greater proportion of that Cr is in the form of $Cr_2O_3/Cr(OH)_3$ (Figure 4.6(b)). However, there is net decrease in $Cr_2O_3/Cr(OH)_3$ overall compared with unsensitised 20/25/Nb SS. The decrease in available Cr gives rise to the increase in iron oxide formation. As predicted Ni oxides offers little contribution to the outer protective oxide layer at OCP. However, $Ni(OH)_2$ is shown to be more prominent

in the oxide layer of the heat treated sample than in its unsensitised counterpart – again indicative of the greater susceptibility to oxidation of these Cr depleted surfaces. The lower percentage of Cr spinel and CrO_3 concentrations present in the film grown on heat treated 20/25/Nb SS can also be explained by the more limited amount of Cr available to partake in oxidation reactions.

In summary, from this analysis it is seen that $Cr_2O_3/Cr(OH)_3$ is the most dominant contributor for unsensitised 20/25/Nb SS. However, Fe oxides/hydroxides have the largest relative atomic percentage for heat treated 20/25/Nb SS. The lower $Cr_2O_3/Cr(OH)_3$ concentration in the heat treated oxide layer is likely due to Cr precipitation, in new or existing phases, during heat treatment preventing the Cr from forming $Cr_2O_3/Cr(OH)_3$ [19].

These precipitates are most likely chromium carbides. Chromium carbide has a binding energy coincident with that of Cr metal and therefore it would be difficult to separate their individual contributions. However, chromium carbide precipitates peaks should not be present in the XPS spectra as they reside within the metal and at the metal/oxide interface [218, 219]. Thus, their presence is obscured by formation of the oxide layer as the penetration depth of the XPS beam is between 3-10 nm and the thickness of the oxide layer is expected to be approximately 60 nm[1], this is consistent with the oxide layer thickness reported on 304 and 316 stainless steels [222].

Due to the spot size of the XPS being large compared to the mean diameter of the constituent grains of 20/25/Nb SS ($\sim$300 μm *vs.* $\sim$20 μm, see Figure 4.1(d) above), it is not possible to distinguish between the oxide layer formed at the grain boundary and that formed within the grain itself. Thus, any differences between grain and grain boundaries that may be expected in the oxide layer formed on heat treated 20/25/Nb SS are not observed.

---

[1]Estimated using the following expression: $d = \frac{\varepsilon \varepsilon_0 A}{C}$, where d is the thickness of the oxide layer, C the capacitance extracted from Figure 4.4, A is the surface area, ε is the dielectric constant of the material and ε_0 is the permittivity of free space [220], this calculation assumes a non-porous surface layer. As Fe_2O_3 is the dominant component of the surface layer at E_{OCP} the permittivity of Fe_2O_3 was used (ε=14.2 [221]).

4.3   Effect of pH Variation on the Corrosion Behaviour of Heat Treated 20/25/Nb Stainless Steel

The effect on the corrosion behaviour of heat treated 20/25/Nb SS of dosing simulant pond water with NaOH to a pH of 11.4 was investigated and the results compared to those obtained for analogous experiments on the unsensitised samples. Polarisation curves for both materials in dosed and undosed pond water simulants are shown in Figure 4.8. The surface chemistries associated with each region of the polarisation curves can be assigned using Pourbaix diagrams in a similar manner to that employed for unsensitised 20/25/Nb SS, section 3.3.

Figure 4.8(a) shows the polarisation curves for the samples immersed in undosed pond water simulants. The current at all potentials is slightly lower for heat treated 20/25/Nb SS than the unsensitised material and there is a suppression in the heat-treated sample of the pitting behaviour seen in the unsensitised sample starting at ∼0.4 V. This is a noteworthy result and a possible explanation is given in the conclusions section below.

In dosed water, Figure 4.8(b), the heat treated 20/25/Nb SS sample has lower general corrosion currents over the entire passive region compared to unsensitised 20/25/Nb SS. The XPS analyses conducted at OCP on these samples indicate that the passive layer on heat treated 20/25/Nb SS contains a greater percentage of Fe oxides/hydroxides than that of the unsensitised 20/25/Nb SS whose Cr oxide/hydroxide content is consequently greater. Fe oxides are generally recognised to be less soluble in neutral to alkaline solutions than Cr oxides (see reference [31] and references therein) – which may explain the lower general corrosion seen for heat treated 20/25/Nb SS. Transpassive currents however are greater for the heat treated sample, indicative of greater corrosion at this potential for the heat treated sample. A feasible explanation for

this is that $Cr_{23}C_6$ precipitation renders the passive layer less noble [223]. It is possible that corrosion occurs preferentially at the grain boundaries at 0.75 V (i.e. intergranular attack) due to chromium depletion at the grain boundaries adjacent to the aforementioned chromium carbide precipitates. Thus, under conditions of added stress, such as increasing applied potential, the passive layer on heat treated 20/25/Nb SS may be less resistant to corrosion than samples where no chromium depletion or carbide precipitation is evident.
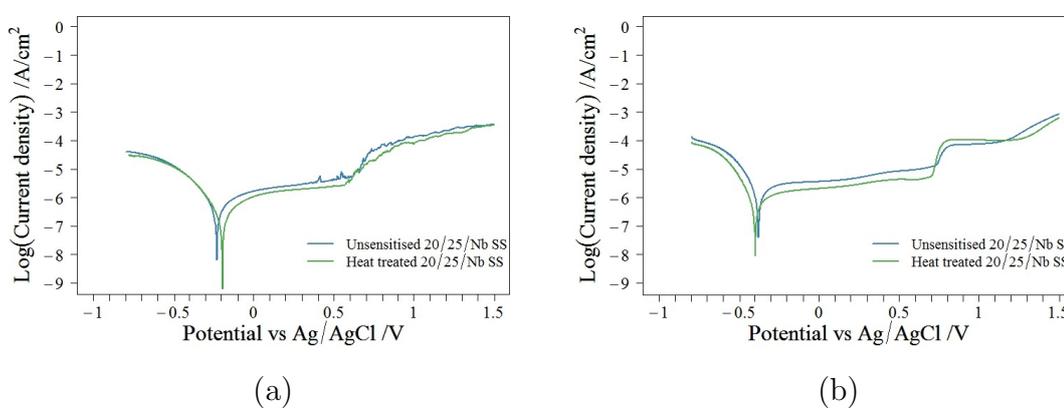
Figure 4.8: Potentiodynamic polarisation curve for heat treated and unsensitised 20/25/Nb SS in (a) undosed, pH$\simeq$8 and (b) pH$\simeq$11.4 NaOH-dosed, water simulants at 24 °C, showing effects of dosing and heat treatment on corrosion behaviour. Both solutions contain 30 μmol dm^{-3} Cl$^-$.

4.3.1 Electrochemical Impedance Spectroscopy of Heat treated 20/25/Nb Stainless Steel in Dosed Simulant Pond Water

EIS studies were carried out on heat treated 20/25/Nb SS in pond water simulants dosed to pH$\simeq$11.4 and over the same potential range as the voltammetry studies of Figure 4.8. EIS allows for surface compositional changes at the metal-solution interface to be observed. Consequently, Figure 4.9 shows Nyquist and Bode plots obtained at several key potentials. The largest impedance values are observed at -0.1 V and the smallest seen at 0.8 V.

(a)

(b)

(c)
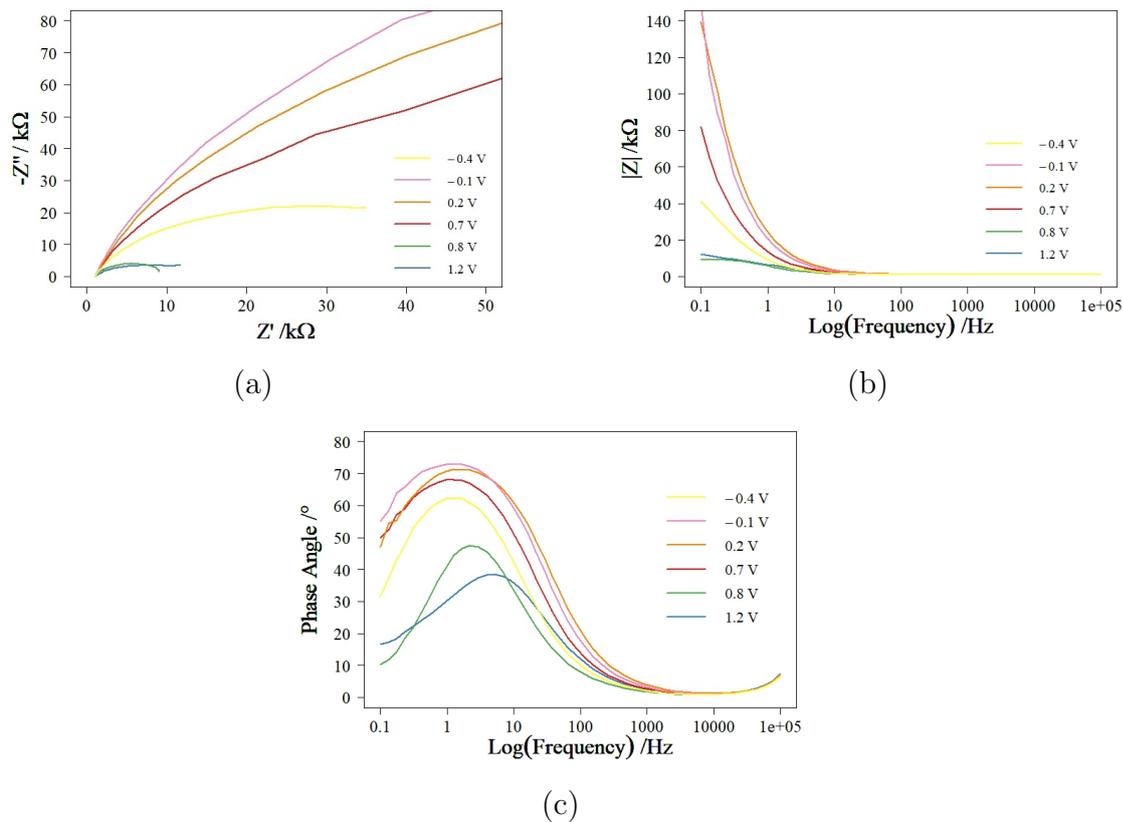
Figure 4.9: Nyquist (a) and (b) & (c) Bode plots at several key potentials for heat treated 20/25/Nb SS in dosed simulant pond water, pH≃11.4 at 24 °C.

Due to the single resistance-capacitive loop and time constant observed over the entire potential range studied, the same equivalent circuit system (i.e. a simple Randle circuit, see Figure 4.10) as used for unsensitised 20/25/Nb SS was found to be applicable for the analysis of the data in Figure 4.9 – the rationale for this and the meaning of the circuit elements over the separate potential ranges studied are discussed in detail in section 3.3.1. The polarisation resistance and capacitance values (whose interpretation change according the potential range under study – again, see section 3.3.1) were extracted from these equivalent circuits and plotted as a function of potential in Figure 4.11.
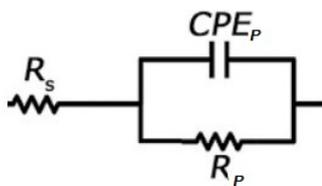
Figure 4.10: Electrical equivalent circuit model used to represent the evolution of 20/25/Nb SS surface in simulant pond water. R_s is the solution resistance, R_p is the polarisation resistance which tends to R_{ct} (the charge transfer resistance) or R_{film} depending on the applied potential and CPE_p a constant phase element (see section 3.3.1 for relevant discussion).

The form of the R_p vs E plot of Figure 4.11(a) is consistent with the surface of the SS corroding at potentials $\leq$-0.4 V and $\geq$0.8 V. The development of the passive layer between -0.3 and 0.7 V is evident through the increased R_p values in this potential region. If the data of Figure 4.11(a) is compared with the results shown in Figures 3.14 to 3.16 of the single metal EIS studies conducted on Cr, Fe and Ni, it can be seen that the passive region once again has contributions from all three metals. From the pure metal analyses, at lower potentials the trend in increasing R_p values is consistent with that of pure Fe (Figure 3.16) i.e. R_p is increasing between -0.5 and -0.2 V for both samples. However, since pure Cr (Figure 3.14) shows a rapid increase in R_p values between -0.5 and -0.3 V contributions from Cr oxides are likely to play a significant role due to Cr oxide formation being more thermodynamically favourable than Fe oxide formation at low potentials [30]. Notably, there is a drop in resistance at E>0 V; this is coincident with the potential at which Cr_2O_3 starts to oxidise to CrO_4^- and with the oxidation of Fe(III) to higher, more soluble oxidation states, as determined from the Pourbaix diagrams of Figure 1.8 to 1.10.

Comparing the R_p vs E plots of Figure 4.11(a) (heat treated 20/25/Nb SS) to that of Figure 4.11(b) (unsensitised 20/25/Nb SS), it can be seen that the first peak is more pronounced in the former, with R_p rising quickly at lower potentials in the range $\sim$0.5 to -0.2 V and stabilising in the range -0.2 to 0 V. The more pronounced nature of this peak is consistent with the lower general corrosion currents observed from the heat treated sample vs the unsensitised sample i.e. an increase in R_p

results in a decrease in current density. As stated above Fe oxides are less soluble in alkaline solution and from the XPS analysis Fe oxides/hydroxides are the most dominant species at E_{OCP} for heat treated 20/25/Nb SS. Thus, it is reasonable to assume that the -0.2 to 0 V plateau in R_p is a result of a surface layer with a high iron concentration and for the unsensitised sample the lower Fe oxide content of the layer is the cause of the difference in shape and size of this feature in Figure 4.11(b) i.e. R_p rises at a slower rate with potential than for the heat treated sample and there is no potential region where R_p is invariant.

A second peak occurs at ~0.6 V for the heat treated material; this is similar to the unsensitised material and so may be similarly attributed to Ni oxide phases or spinels offering a wider passive potential range.

(a)   (b)
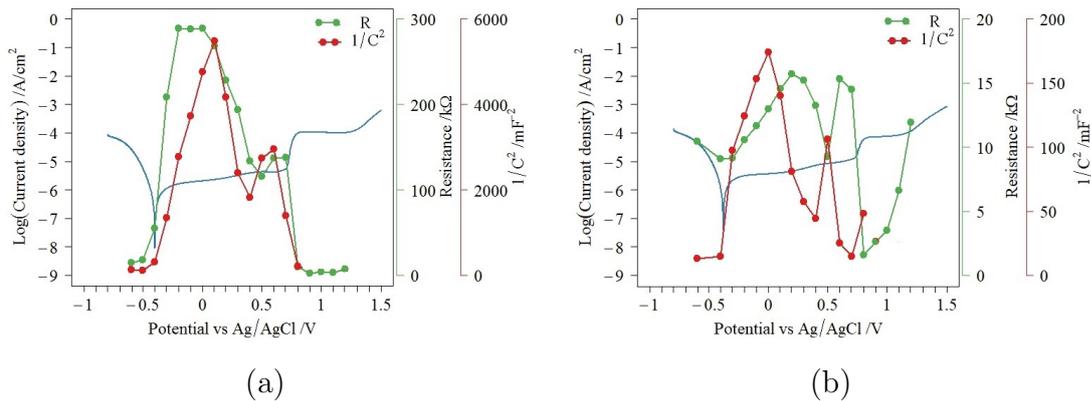
Figure 4.11: Electrochemical impedance spectroscopy analysis of (a) heat treated 20/25/Nb SS and (b) unsensitised 20/25/Nb SS in dosed simulant pond water, pH≃11.4 at 24 °C, specifically potentiodynamic polarisation curve overlaid with polarisation resistance data (green) and capacitance data (red), in the form of a Mott-Schottky plot, extracted from the Nyquist plots.

Again, similar to unsensitised 20/25/Nb SS, the C^{-2} vs E behaviour of heat treated 20/25/Nb SS (Figure 4.11(a)) can be divided into a number of distinct regions, in this case five, designated as region I to V as follows; -0.6 to -0.2 V, -0.2 to 0.1 V, 0.1 to 0.4 V, 0.4 to 0.6 V and 0.6 to 0.8 V. Since the CPE data is only considered to be representative of a capacitance when n≥0.8, these plots only consider the potential range over which n≥0.8 for the CPE component, i.e. in this case -0.6 to 0.8 V.

Region I shows n-type behaviour that may be attributed to the growth of a protective oxide layer based on the accompanying increase in R_p in this region, as Fe_2O_3 has n-type characteristics it is tempting to assign this behaviour to Fe_2O_3. However, as stated previously, other oxides such as Cr_2O_3 may be growing and defect elimination may still be occurring in this region and thus the n-type behaviour may be convoluted with a residual decrease in capacitance with potential behaviour as the oxide layer grows and defect density is decreased.

Layer growth has ceased in region II (as evidenced by the invariance of R_p with E) and thus the form of the C^{-2} vs E plot can be attributed to Mott-Schottky behaviour of the n-type semiconductor Fe_2O_3 layer. The presence of this iron oxide layer is confirmed by the XPS analysis at OCP ($\sim$-0.1 V) which show the main contributors ($\sim$44 at%) to the passive layer are Fe oxides at this potential.

The C^{-2} vs E behaviour in region III has p-type characteristics - suggesting, as in the case of region II of the analogous plot for the unsensitised steel (see section 3.2 above) - that the Cr_2O_3 contribution to the passive layer dominates. This coincides with a decrease in R_p, suggesting that dissolution of the iron oxide layer is occurring (consistent with Figure 3.16) leaving a chromium oxide film to dominate and so provide protection. As long as this Cr_2O_3 layer is still thicker than the space charge layer, then it is still possible to characterise its semiconducting nature. Thus, despite the loss in corrosion resistance in this region, it appears Cr_2O_3 is still present at the SS surface and offers corrosion protection evidenced by the behaviour of the polarisation curve in this potential range. In region IV, the peak starting at 0.4 V then corresponds to the oxidation of Cr(III) to Cr(VI) and its subsequent dissolution in region V corresponding with the transpassive behaviour of the polarisation curve.

Despite these similarities, direct comparison of Figure 4.11 (a) and (b) reveals some noteworthy differences between the behaviour of heat treated and unsensitised 20/25/Nb SS. The low voltage region of apparent n-type behaviour is extended in heat treated 20/25/Nb SS compared to the unsensitised sample.

The switch in behaviour to p-type character occurs at 0.1 V for heat treated 20/25/Nb SS and 0 V for unsensitised 20/25/Nb SS. The change in the dominant oxide at E_{OCP} from chromium oxide to iron oxide on heat treatment of the 20/25/Nb SS is evident from the XPS of section 4.2 and thus the switch from n- to p-type characteristics in the C^{-2} vs E plots of Figure 4.11 can be attributed to the change in principal oxide in the surface layer. Both samples change character again at 0.4 V. This shortening of the potential region in which Cr_2O_3 is dominant may suggest a depletion in the contribution of Cr to the passive layer behaviour for heat treated 20/25/Nb SS.

Finally, the p-type region 0.5 to 0.7 V in the C^{-2} vs E plot for unsensitised 20/25/Nb SS does not coincide with transpassivity and this peak was attributed to spinels at the surface of the unsensitised steel. There is no p-type behaviour in the same range for heat treated 20/25/Nb SS, considering the lower Cr spinel content at OCP for heat treated 20/25/Nb SS (Figure 4.7) it is not unreasonable to assume spinels play a lesser role the passive protection of the heat treated SS. However, there is a p-type region at ∼0.8 V for the heat treated sample that coincides with transpassivity and thus, dissolution of the surface oxide/hydroxide layer.

4.4 Effect of Chloride Concentration in the Aqueous Phase on the Corrosion Behaviour of the Heat treated 20/25/Nb Stainless Steel

To investigate the stability and robustness of the passive protection observed for the heat treated 20/25/Nb SS, the effect of chloride concentration on the corrosion behaviour of the SS in the absence and presence of sodium hydroxide was investigated.

Figure 4.12(a) shows the polarisation curves obtained with increasing Cl^-

concentration in the absence of a corrosion inhibitor (NaOH). No evidence of pitting corrosion is seen in the potential range -0.2 to 0.5 V at 30 μmol dm^{-3} chloride, with passive film breakdown occurring at $\sim$0.6 V. Upon increasing the Cl$^-$ concentration to 592 μmol dm^{-3}, two sets of pitting peaks occur - a single peak at $\sim$0.2 V and a closely bunched group of peaks at E>0.4 V. These extend up to $\sim$0.6 V at which point passive film breakdown again occurs. Increasing the Cl$^-$ concentration further to 28 mmol dm^{-3} causes a negative shift in the breakdown potential from $\sim$0.6 V to $\sim$0.3 V with continuous pitting commencing at $\sim$0.2 V. This behaviour is comparable to that of unsensitised 20/25/Nb SS under the same conditions (reprinted here as Figure 4.12(b) for the convenience of the reader). Therefore, the same data interpretation is relevant i.e. Ni oxide/hydroxide formation at this pH (pH$\simeq$8) is limited and loss of protection is associated with the breakdown of the Fe and Cr oxides formed on the surface of the SS.

(a)   (b)
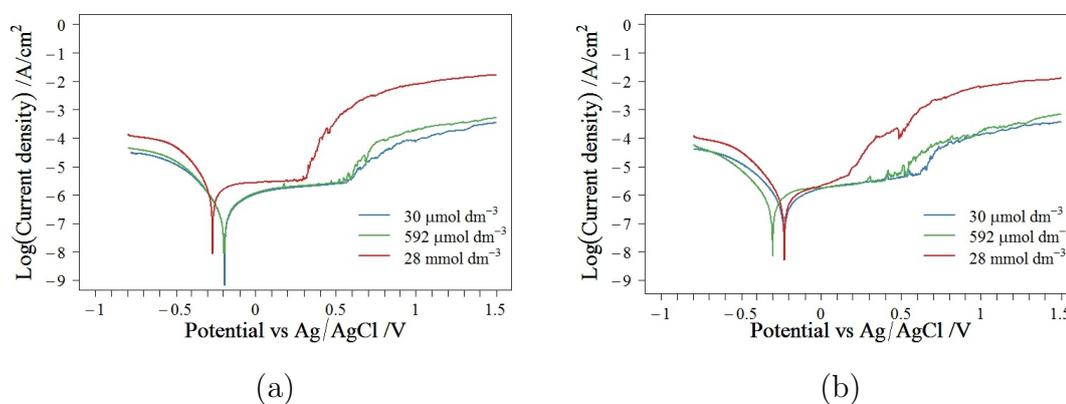
Figure 4.12: Potentiodynamic polarisation curves demonstrating the effect of increasing chloride concentration in undosed simulant pond water (pH$\simeq$8 at 24 °C) on the corrosion behaviour of (a) heat treated 20/25/Nb SS and (b) unsensitised 20/25/Nb SS.

Linear sweep voltammetry was then performed on heat treated 20/25/Nb SS in simulant pond water dosed to pH$\simeq$11.4 with sodium hydroxide corrosion inhibitor at increasing chloride concentrations. The resulting polarisation curves are shown in Figure 4.13(a). As in the case of the unsensitised material (Figure 4.13(b)) the introduction of hydroxide extends the passive potential range at low [Cl$^-$] from $\sim$-0.2 to $\sim$0.6 V in the absence of hydroxide to $\sim$-0.4 to $\sim$0.7 V in its

presence, evidencing the corrosion protection afforded by OH^- to this system. Increasing the Cl^- concentration results in several changes to the corrosion behaviour of this system. The onset potential for transpassivity stays almost constant until very high chloride concentrations of 560 mmol dm^{-3} are present. However, transpassive currents increase with increasing $[Cl^-]$. High transpassive currents suggest the presence of significant intergranular attack. Electrochemical quartz crystal microbalance studies by Woodhouse *et al.* [224] show that such currents are usually associated with significant mass loss from the steel surface.
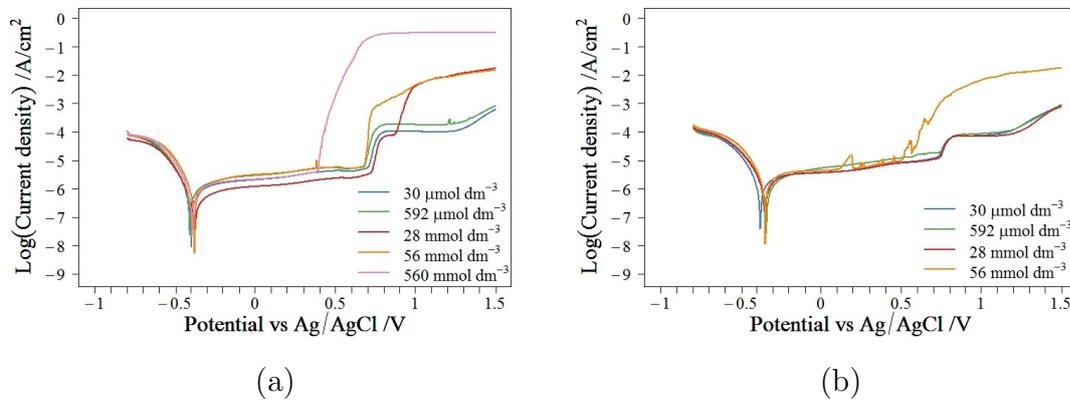
Figure 4.13: Potentiodynamic polarisation curves demonstrating the effect of increasing chloride concentration in dosed simulant pond water (pH$\simeq$11.4 at 24 °C) on the corrosion behaviour of (a) heat treated 20/25/Nb SS and (b) unsensitised 20/25/Nb SS.

At potentials greater than that of transpassive dissolution the system is repassivated before dissolution occurs again around 1.2 V. A secondary process is observed in this potential region ($\sim$0.75 - 1.2 V), most obviously at $[Cl^-]\simeq$28 mmol dm^{-3}. This secondary process shifts towards more negative potentials with increasing $[Cl^-]$ specifically $\sim$350 mV per decadic change in $[Cl^-]$. If the Nernst equation is assumed to hold for this process, the value of the decadic shift in the onset potential with increasing chloride concentration is consistent with the participation of 6 Cl^- ions in a one electron oxidation. This may be explained as follows. The Nernst equation is given by equation 4.1:

$$E = E^0 - \frac{RT}{nF}lnQ \qquad (4.1)$$

where E^0 is the standard potential for the reaction, Q is the reactant quotient, n is the number of electrons transferred in the reaction and the other symbols have their usual meanings.

In general for stainless steels, the majority contribution to secondary passivation is derived from iron oxides due to surface depletion of Cr as a result of dissolution of Cr(VI) in the transpassive region [225]. It is well known that chloride interferes with the formation of such Fe oxide layers [226–228]. In contrast, chloride does not participate with Cr in complex formation at high pH [225]. Both of these observations suggest that this movement in the onset potential of this secondary transpassive process observed in Figure 4.13(a) is associated with formation of chloride complexes of Fe(III) – specifically complexes that involve the participation of six chlorides per ferric ion given the shift of ∼350 mV per 10 fold increase in chloride concentration reported above. One such complex is the hexachloroferric complex, $FeCl_6^{3-}$.

Transpassive dissolution of the alloyed surface involves the dissolution of Cr, Fe, Ni and spinel components of the surface film in parallel reactions. In light of the shift in the onset potential of the secondary process of Figure 4.13(a) with [Cl^-], and the conclusions of section 4.3 that protection in this potential region is at least in part derived from spinels such as $FeCr_2O_4$, the reaction associated with this secondary process is hypothesised to be given by equation 4.2, with the associated Nernst equation given by equations 4.4 to 4.5 rationalising the ∼350 mV shift in the onset potential for transpassivity with each decadic increase in chloride concentration.

$$6Cl^- + FeCr_2O_4 \longrightarrow Cr_2O_4^{2-} + FeCl_6^{3-} \tag{4.2}$$
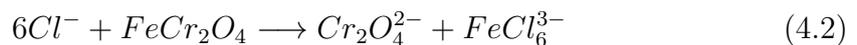
$$E = E^0 + \frac{RT}{F}\frac{ln[Cr_2O_4^{2-}][FeCl_6^{3-}]}{[Cl^-]^6} \tag{4.3}$$

$$E = E^0 + \frac{RT}{F}ln[Cr_2O_4^{2-}][FeCl_6^{3-}] - \frac{6RT}{F}ln[Cl^-] \tag{4.4}$$

$$E = E^0 + \frac{RT}{F}ln[Cr_2O_4^{2-}][FeCl_6^{3-}] - (6 \times 0.059)log_{10}[Cl^-] \tag{4.5}$$

Comparing the polarisation curves obtained from heat treated and unsensitised samples at $[Cl^-] \simeq 56$ mmol dm^{-3} in Figure 4.13(a) and Figure 4.13(b) respectively, it can be seen that the corrosion behaviour preceding the breakdown of the passive layer is different. For the unsensitised sample, continuous pitting corrosion is evident from ~ 0.2 V until the transpassive onset at ~ 0.5 V; whereas for the heat treated sample only one or two small peaks are seen at ~ 0.4 V before the sudden loss of passivity at ~ 0.7 V. This would seem to indicate a greater corrosion resistance to pitting for the heat treated sample – an apparently counter-intuitive deduction as heat treatment should result in increased corrosion susceptibility. This point will be returned to below. It is important to remember that concentrations of this magnitude are not expected and this would only represent the worst case scenario.

4.5 Effect of Temperature Variation on the Corrosion Behaviour of Heat treated 20/25/Nb Stainless Steel

The corrosion behaviour of heat treated 20/25/Nb SS at elevated temperatures (24 - 90 °C) was examined using linear sweep voltammetry. The resulting polarisation curves are shown in Figure 4.14(a). As the temperature of the solution increases from 24 °C to 45 °C there is a marked increase in general corrosion currents in the passive region but as the temperature rises further to 60 and 90 °C these currents do not alter significantly. However, E_{ZC} and the onset of transpassivity shift in anodic and cathodic directions respectively across the entire temperature range, with the net effect of decreasing the passive potential window with increasing temperature.

At 90 °C a peak at ~ 0.2 V is observed comparable to that seen for the unsensitised sample and the pure chromium sample under otherwise identical conditions (see Figure 4.14(b) and Figure 3.20 respectively). Using the same

explanation as described in section **??**, the peak is caused by oxidative dissolution of Cr(III) oxides. Unlike the unsensitised sample, the heat treated SS does not regain any passivity at higher potentials at this temperature. Breakdown of the passive layer occurs immediately after this peak.

At 45 °C, 60 °C and 90 °C the heat treated sample shows greater corrosion susceptibility than the unsensitised sample as evidenced by larger general corrosion currents and more negative potentials for the onset of transpassivity. As stated in section 4.3 chromium depletion causes a less noble formation of the passive film [223]. Thus, when an external stress such as increasing temperature is applied, the heat treated sample exhibits greater susceptibility to corrosion at any one elevated temperature than the non-heat treated steel.
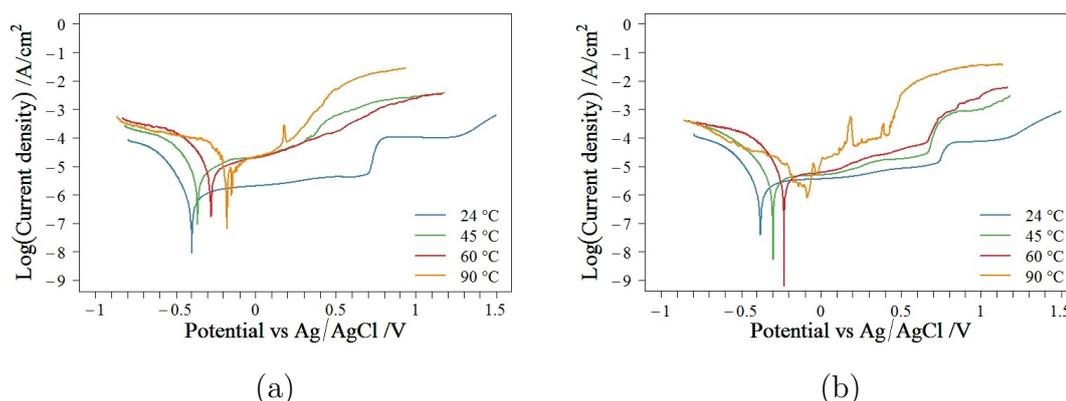
Figure 4.14: Potentiodynamic polarisation curve demonstrating the effect of increasing simulant pond water,30 μmol dm^{-3} Cl$^-$, pH$\simeq$11.4 at 24 °C, temperature on the corrosion behaviour of (a) heat treated 20/25/Nb SS and (b) unsensitised 20/25/Nb SS.

The open circuit potentials of heat treated samples at 24 °C, 45 °C and 60 °C are -0.1, 0.04 and 0.1 respectively. Thus, at each of these temperatures the surface of the SS should remain passivated, albeit with enhanced general corrosion rates compared to unsensitised samples. However, at 90 °C the open circuit potential is found to be -0.13 V and sits within the potential range where minimal protective oxide formation is likely to occur and thus corrosion rates at this temperature will be significantly enhanced compare to the other temperatures studied. Thus it is concluded that, under open circuit conditions, the heat treated 20/25/Nb SS

corrodes freely. This conclusion was supported by visual inspection of the surface after exposure to simulant pond water at 90 °C which showed rust beginning to form on the surface of the electrode, there was no evidence of this at 24, 45 and 60 °C. Hence, in the event of a loss of coolant accident, re-establishing normal operating temperatures will be integral to limiting the corrosion of the cladding.

4.6   Effect of the Presence of Hydrogen Peroxide in the Aqueous Phase on the Corrosion Behaviour of the Heat Treated Stainless Steel

As with the unsensitised 20/25/Nb SS, an assessment of the corrosion behaviour of heat treated 20/25/Nb SS in the presence of H_2O_2 in simulant pond water dosed with NaOH was carried out in an attempt to mimic the effect of radiolysis.

4.6.1   Effect of Hydrogen Peroxide Concentration in Simulant Pond Water on the Corrosion Behaviour of Heat Treated 20/25/Nb Stainless Steel

The effect of H_2O_2 concentration on the electrochemical behaviour of heat treated 20/25/Nb SS is illustrated by potentiodynamic polarisation curves in Figure 4.15. The addition of H_2O_2 results in the movement of the E_{ZC} to more positive potentials, an increase in the general corrosion currents and growth of a wave starting ∼0.2 V.

This behaviour is almost identical to that of unsensitised 20/25/Nb SS, Figure 3.22. Thus, the analysis of section 3.5.1 is also appropriate here for heat treated 20/25/Nb SS. The in-growth of the peak can be attributed to the electroxidation

of the adsorbed H_2O_2 on the stainless steel surface.
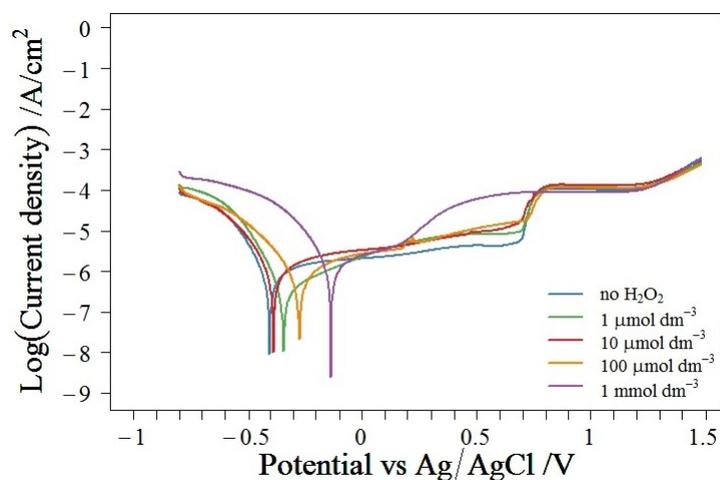
Figure 4.15: Potentiodynamic polarisation curve showing the effect of increasing H_2O_2 concentration on the corrosion behaviour of heat treated 20/25/Nb SS in simulant pond water pH$\simeq$11.4, 30 μmol dm^{-3} Cl$^-$.

4.6.2 Effect of Temperature in the Presence of Hydrogen Peroxide in Simulant Pond Water on the Corrosion Behaviour of Heat Treated 20/25/Nb Stainless Steel

Figure 4.16(a) shows the effect of increasing the temperature of simulant pond water containing 10 μmol dm^{-3} H_2O_2 on the corrosion susceptibility of heat treated 20/25/Nb SS. As the temperature increases there is a rise in the general corrosion currents and a shift in the onset of transpassivity towards lower potentials. From 24 to 60 °C E_{ZC} becomes more positive effectively decreasing the passive potential range. However, at 90 °C E_{ZC} unexpectedly is more negative than at the other temperatures of interest.

(a)   (b)
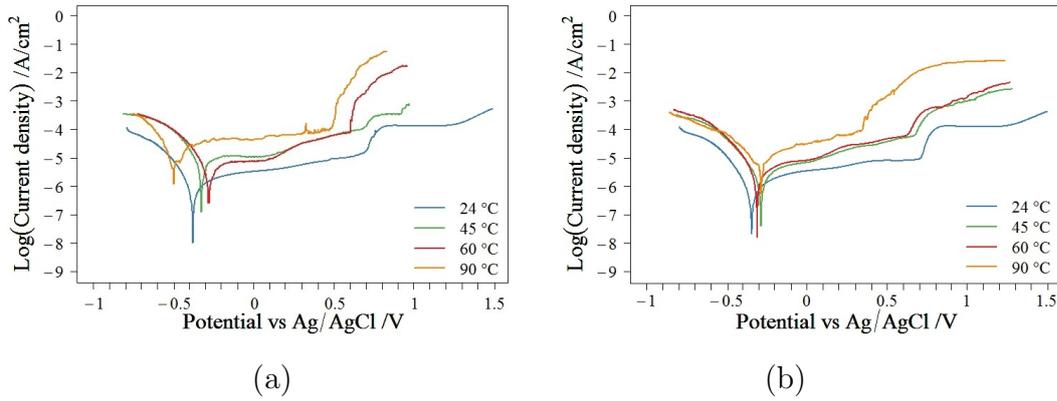
Figure 4.16: Potentiodynamic polarisation curves showing the effect of increasing temperature of the simulant pond water, 30 μmol dm^{-3} Cl$^-$, pH$\simeq$11.4 at 24 °C, containing 10 μmol dm^{-3} H$_2$O$_2$ on the corrosion behaviour of (a) heat treated 20/25/Nb SS and (b) unsensitised 20/25/Nb SS.

Comparing Figure 4.16(a) to Figure 4.14(a) - which show the effect of increasing temperature with and without H$_2$O$_2$ present respectively - some interesting observations can be made. Firstly, there is a reduction in the general corrosion currents in the presence of H$_2$O$_2$ at 45 and 60 °C. Secondly, at 45 and 60 °C the onset of transpassivity occurs at higher potentials when the surface is exposed to H$_2$O$_2$. Under accident conditions, i.e. a temperature of 90 °C, the metastable pit seen at $\sim$0.2 V is no longer present, however a metastable pit is evident at $\sim$0.3 V. In the absence of H$_2$O$_2$ the surface does not repassivate and breakdown of the film occurs immediately after pit formation. When H$_2$O$_2$ is present the surface repassivates after the pit, although the surface may be interspersed with small pitting events between $\sim$0.3 and $\sim$0.5 V. Breakdown does not occur until $\sim$0.5 V compared with $\sim$0.2 V in the absence of peroxide. On top of this, E$_{ZC}$ is significantly more negative in the presence of H$_2$O$_2$ and therefore the passive region is much larger. These results suggest that the addition of H$_2$O$_2$ at elevated temperatures gives rise to a more protective oxide layer. There are a couple of possible explanations for this as described in section 3.5.2. The augmented protection may be a result of reduction by H$_2$O$_2$ of soluble Cr(VI) to insoluble Cr(III), most likely as Cr(OH)$_3$; or the oxidation by H$_2$O$_2$ of soluble Fe(II), to form a Fe(OH)$_3$ precipitate. Also, the decrease in pH with

increasing temperature is compensated for by the decomposition of H_2O_2 to OH^- (equation 1.11, Chapter 1) which in turn would aid in precipitation of Cr or Fe hydroxides onto the surface of the SS.

Lastly, the behaviour of heat treated 20/25/Nb SS must be compared to that of its unsensitised counterpart, Figure 4.16(b). At 45 °C the general corrosion currents of the heat treated sample are slightly higher than that of the unsensitised sample and the onset of transpassivity takes place at the same potential, $\sim$0.7 V. At 60 °C general corrosion currents are similar and passive film breakdown occurs at almost the same potential, $\sim$0.6 V. The transpassive currents are greater for the heat treated 20/25/Nb SS sample. At 90 °C, the extra protection identified by the disappearance of the metastable pit at $\sim$0.2 V for unsensistised 20/25/Nb SS is once again present for heat treated 20/25/Nb SS. In the case of the heat treated sample, there is a metastable pit formed at the same potential ($\sim$0.3 V) as film breakdown occurs in unsensitised 20/25/Nb SS. From this observation, and the conclusions drawn with respect to the protection afforded by peroxide above, it is not unreasonable to conclude that, in the case of the heat treated sample, the peroxide is again able to protect the surface against corrosion by repassivation of the metastable pit. However, in the case of the unsensitised sample, the so-formed pit appears to be more stable – so much so that the peroxide present is now insufficient to induce repassivation, the pit therefore propagates and transpassivity obtains. The apparent differences in pitting susceptibility between the unsensitised and heat treated samples are returned to immediately below.

4.7 Conclusions

The principal conclusions of this section regarding the electrochemical corrosion behaviour of heat treated 20/25/Nb SS cladding under conditions relevant to the wet interim storage of AGR fuel pins are as follows.

The OCP in simulant pond water (pH$\simeq$11.4) is found to be $\sim$-0.1 V vs Ag/AgCl. Under these conditions, XPS data indicates that the protective oxide

layer formed on the surface of 20/25/Nb SS consists predominately of Fe and Cr oxides, with Fe oxide being the more dominant of the two. Resistance and capacitance data from EIS experiments shows that the source of this protection changes on application of an oxidative stress i.e. as the electrode potential is increased. Through Mott-Schottky analysis it was found that this change occurs at ~0.1 V whereupon the protection provided by Fe oxides is lost due its oxidative dissolution and Cr oxides dominate until 0.6 V.

Voltammetric studies were used to determine the robustness of this oxide layer. Studies under baseline conditions of pH=8 at 24 °C show a wide region of passivity from ~-0.15 V to ~0.6 V vs Ag/AgCl. However, at pH 11.4 the window of passivity is extended to ~-0.3 V to 0.75 V – indicating that simple dosing of the system with NaOH provides significant added corrosion protection for heat treated 20/25/Nb SS samples under these conditions. This protection is maintained at pH 11.4 at 45 °C in the presence of 30 μmol dm^{-3} of both Cl$^-$ and H$_2$O$_2$, i.e. under future interim storage conditions, with a separation of approximately a volt between the E$_{ZC}$ and onset of transpassivity and as E$_{OCP}$ lies within this passive range intergranular attack is unlikely.

The extent of the envelope of this protection was studied as a function of key solution parameters such as temperature, chloride concentration and hydrogen peroxide concentration – including conditions relevant to future wet storage scenarios and their fault conditions. Results may be summarised as follows.

With respect to chloride concentration:
In the absence of hydroxide i.e. at pH 8 close to neutrality, chloride readily attacks the passive layer on 20/25/Nb SS from concentrations of 592 μmol dm^{-3}. Key features of this attack are a cathodic shift in the onset transpassivity and appearance of pitting corrosion in the passive range. However, when the pH is increased to 11.4, i.e. the pH of dosed simulant pond water, chloride is only seen to induce a shift in the onset of transpassivity at concentrations greater than 56 mmol dm^{-3}. This is a significantly higher chloride concentration than expected

under foreseen fault conditions, indicating that protection will be maintained under such.

With respect to temperature:

The general corrosion currents significantly increase as the temperature increases from 24 °C to 45 °C but do not noticeably change as the temperatures increases further. However, the onset of transpassivity moves towards more negative potentials with increasing temperature. However, passivation of the surface is expected to occur at the OCP potentials for pond water temperature ≤60 °C, despite the changes in behaviour with temperature. Therefore, there seems to be no localised corrosion threat to fuel cladding as electrolyte / storage medium temperature is increased from 24 °C to 60 °C. However, at 90 °C the OCP of the heat treated 20/25/Nb SS lies in the region where surface passivation will be minimal and if any protective oxide layer does exist on the surface of 20/25/Nb SS it will most likely dissolve under these conditions.

With respect to hydrogen peroxide concentration:

Voltammetry suggest that, as is the case for unsensitised 20/25/Nb SS, H_2O_2 is simply oxidised at the surface of heat treated 20/25/Nb SS in the passive potential range. Oxidation of peroxide at the steel surface is controlled by a surface adsorption process. At simulant pond water temperatures between 45-90 °C the presence of peroxide (10 μmol dm^{-3}) extends the potential passive window. At 90 °C the presence of peroxide suppresses the pitting corrosion that is observed at 0.2 V in the passive range at the same temperature in peroxide-free electrolytes, but pitting is observed from ∼0.4 V. This suggests that peroxide offers some protective action on heat treated 20/25/Nb SS at this temperature. As T≃90 °C is one of the major fault conditions to be considered in the interim storage safety case, this peroxide-derived protection is a bonus.

Comparison of heat treated and unsensitised 20/25/Nb SS

Comparing the behaviour of heat treated 20/25/Nb SS to its unsensitised counterpart some further conclusions can be drawn. In general, under the

conditions studied heat treated 20/25/Nb SS appears to be marginally more susceptible to transpassive corrosion and thus intergranular attack. This observation is consistent with Figure 4.1 and 4.2 (oxalic etch and DL-EPR tests) which show a greater susceptibility to intergranular attack and with XPS studies which showed reduced Cr(III) oxide and Cr spinel content in the passive layer at OCP. EIS studies also show a decrease in contributions of chromium to the passive layer, all suggesting heat treatment results in net depletion of Cr at the grain boundaries. Interestingly heat treatment does not seem to increase susceptibility to pitting or general corrosion, in fact the unsensitised sample appears more vulnerable. As discussed in section 4.3, in neutral to alkaline conditions Fe oxides are less soluble than Cr oxides. During heat treatment some Cr is immobilised by the formation of chromium carbides and therefore unavailable to participate in oxide layer growth resulting in an Fe rich protective layer. Hence, general corrosion of heat treated 20/25/Nb SS occurs at a slower rate than for unsensitised 20/25/Nb SS.

With regards to pitting susceptibility, it is possible that during heat treatment NbC inclusions, which provide pitting centres, are dissolved and Nb dispersed throughout the steel matrix. Therefore, there are fewer pitting centres on the SS surface and heat treated 20/25/Nb SS becomes less prone to pitting corrosion than unsensitised 20/25/Nb SS. This difference in behaviour is evident for the SS samples in simulant pond water containing peroxide at 90 °C. Unsensitised samples exhibit transpassive behaviour at 0.2 V likely initiated through pit formation whereas due to the dissolution of NbC pitting centres in the heat treated sample H_2O_2 is able to shut down the metastable pit and maintain some passivity. More in-depth analysis of NbC pitting centres and there effects on pitting of 20/25/Nb SS in chloride environments can be found these references [19, 229].

Chapter 5

AGR Fuel Cladding Analogue - 304H Stainless Steel

The previous two chapters have presented an analysis of the corrosion behaviour of unsensitised and heat treated 20/25/Nb SS under conditions relevant to interim storage. However, although heat treated 20/25/Nb SS has passed initial screening tests for use as an analogue for RIS-affected cladding, tests conducted by the NNL show that the material has failed to meet all the criteria laid out in section 1.9.6 [82]. Therefore, other possible analogues have been sought.

Stainless steel 304H (304H SS) was selected as a possible analogue for 20/25/Nb SS due to its similar chromium and carbon content (see Table 2.2). The lack of a Nb stabiliser means the carbon is free to react with chromium when heat treated resulting in chromium carbide precipitation and chromium loss at the grain boundaries. Thus, 304H SS should theoretically be more easily sensitised than 20/25/Nb SS, potentially yielding a good simulant for irradiated cladding.

5.1 Unsensitised 304H Stainless Steel

This chapter presents a study of the effect of heat treatment of 304H SS as a simulant for the radiation sensitisation of 20/25/Nb SS. As such, it begins with a study of the baseline corrosion behaviour of as-received 304H SS before

heat treatment. This will allow for qualitative and quantitative comparisons to be made regarding the effect that heat treatment has on the corrosion susceptibility of 304H SS. It also allows comparisons between 20/25/Nb SS and 304H SS corrosion behaviour to be made.

5.1.1   Degree of Sensitisation

In order to establish its inherent susceptibility towards various modes of corrosion, the as-received 304H SS was subjected to both qualitative and quantitative degree of sensitisation tests in accordance with the methods described in Section 2.2.3.   Results of these tests are presented in the next section, beginning with the qualitative oxalic acid etch test.

5.1.1.1   Electrochemical Etching

Firstly, an oxalic acid etch test was carried out on 304H SS. Figure 5.1 shows the 304H SS pre- and post-exposure to oxalic acid.   Figure 5.1(a) is broadly featureless. Post exposure to the etchant, pitting at the grain boundary is observed, Figure 5.1(b). As no grains have been completely encircled it would appear that the inherent susceptibility towards corrosion of the as-received samples is limited.   However, a definite conclusion cannot be drawn as to the absolute level of corrosion susceptibility based on this simple visual inspection [160].
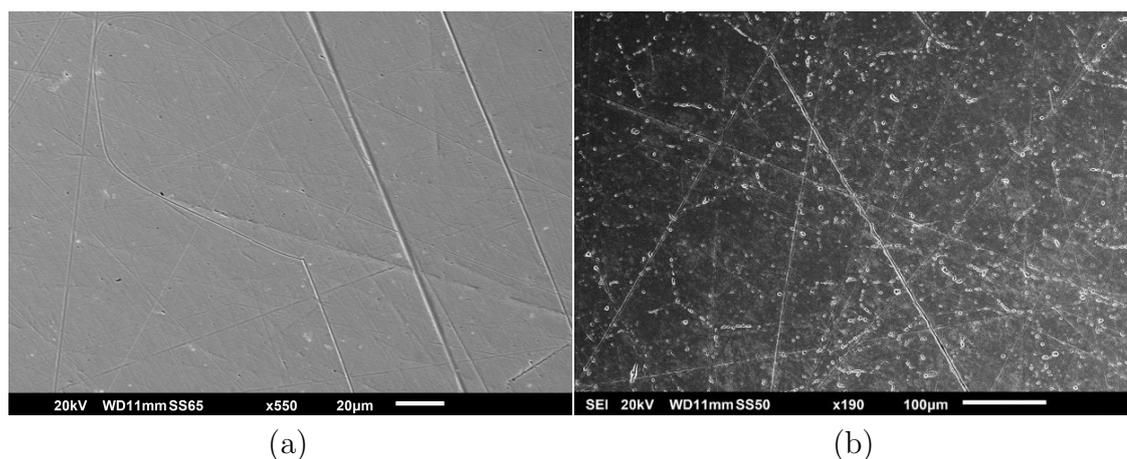
Figure 5.1: SEM image of as received 304H SS (a) pre- and (b) post-immersion in 10% oxalic acid for 15 seconds with an applied potential of 6 V.

5.1.1.2 Double Loop Electrochemical Potentiokinetic Reactivation Tests

Since visual inspection of the results of the oxalic acid test was inconclusive, DL-EPR tests were performed on the 304H SS sample. Figure 5.2 shows the resulting voltammograms. Data can be interpreted in accordance with the procedure described in section 2.2.3.2, with the ratio of the reactivation peak, I_r to the activation peak, I_a, then being found to be 0.165. Consistent with the diagnostic criteria described in section 2.2.3.2, the sample is therefore considered to be unsensitised [161, 162]. However, on comparison with the analogous test on unsensitised 20/25/Nb, whose I_r/I_a ratio is found to be 0.015, it can be seen that as-received 304H SS has a greater inherent corrosion susceptibility to as received 20/25/Nb SS.
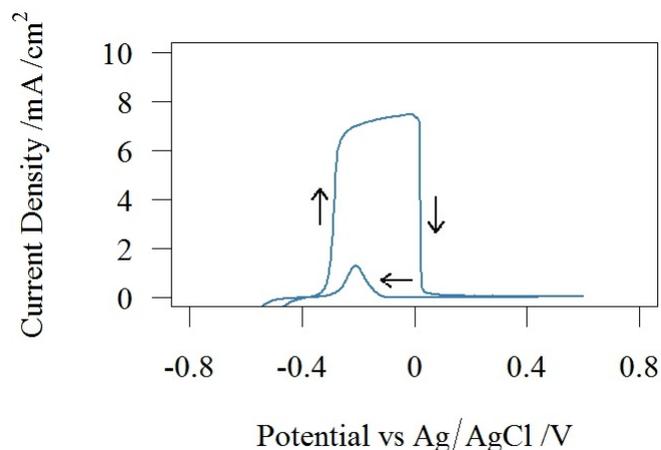
Figure 5.2: DL-EPR curve of as received 304H SS in a solution of 0.5 mol dm^{-3} H_2SO_4 and 0.01 mol dm^{-3} KSCN with a scan rate of 1.6 mV/s.

5.1.2   Compositional Analysis of the Passive Film formed on Unsensitised 304H Stainless Steel in Simulant Pond Water

Having determined the limited susceptibility towards intergranular corrosion of the unsensitised as-received 304H SS samples, this section describes XPS experiments designed to determine analytically the composition of the passive film grown on the samples in simulant pond water under open circuit conditions at 24 °C. These experiments also seek to determine if any compositional differences exist in the passive film grown on unsensitised 304H SS compared to unsensitised 20/25/Nb SS. The XPS data can then be used to inform the analysis of polarisation curves later in this chapter.

However, before XPS measurements were performed on the immersed samples, simple electrochemical impedance spectroscopy (EIS) measurements where conducted to provide a qualitative initial assessment as to how the composition of the surface layer changes as a function of immersion time. Specifically, EIS measurements were conducted every 30 minutes on unsensitised 304H SS immersed in simulant pond water up to a total immersion time of 6

hours. Selected Nyquist and Bode plots from this run are shown in Figure 5.3 from which it can be seen that these plots begin to stabilise with time after only 30 minutes of immersion.   There are moderate increases in phase at low frequencies and decreases in imaginary impedance at immersion times from 30 minutes up until 6 hours, indicating an increase in resistance and therefore a slight thickening of the oxide/hydroxide surface layer in this period. However, given the very slight nature of these changes, it is not unreasonable to assume that the passive layer is relatively stable after the immersion period of 30 minutes.   As the purpose of the data presented in Figure 5.3 was to simply provide qualitative evidence of passive film stabilisation, equivalent circuit modelling of these plots was not performed. Detailed equivalent circuit modelling of the surface layer is discussed later.

(a)

(b)

(c)
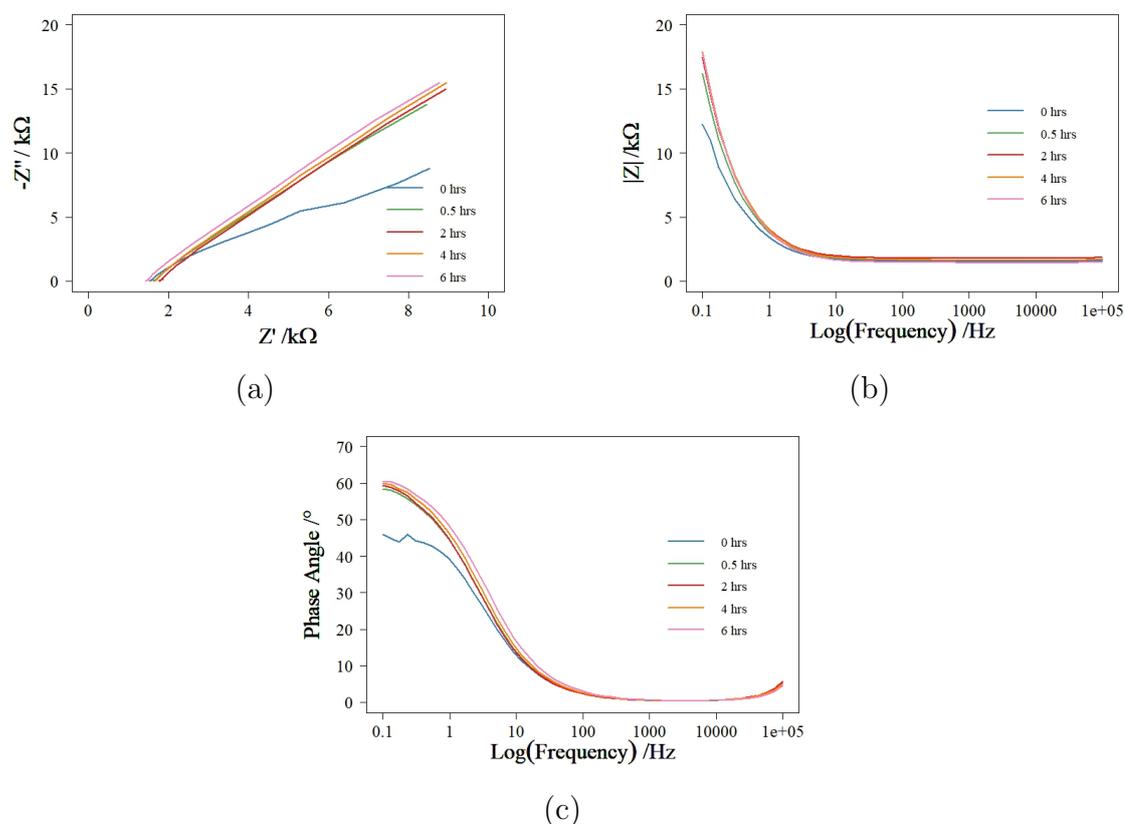
Figure 5.3: Time dependant Nyquist and Bode plots for unsensitised 304H SS in simulant pond water, pH≃11.4.

XPS spectra were then obtained for unsensitised 304H SS immersed in

simulant pond water for one week at 24 °C. During this time the open circuit potential, E_{OCP}, was observed to obtain an equilibrium value of $\sim$-0.19 V vs Ag/AgCl. The same analysis procedure was undertaken as that described in section 3.2 for data obtained from 20/25/Nb SS. Curves are fitted to the averaged XPS spectra obtained for unsensitised 304H SS and the results are shown in Figure 5.4. The average binding energy and full width half maximum (FWHM) of the spectra for each of the dominant elements, Fe, Cr, Ni and O are shown in Table 5.1.

Just as for the 20/25/Nb SS data of Figure 3.3, the iron profiles for 304H SS shown in Figure 5.4(a) show two distinct peaks. The first, lower energy peak at 706.83 eV is due to elemental iron, Fe^0. Due to the broadness of the second peak at 710.47 eV, it is likely that multiphase oxide is present consisting of iron (III) oxide (Fe_2O_3), iron (II,III) (Fe_3O_4) and spinels such as $FeCr_2O_4$ and $NiFe_2O_4$, which also have binding energies $\sim$710.5 eV. It may also contain contributions from iron hydroxides, $Fe(OH)_2$, $Fe(OH)_3$ and $FeOOH$, which are also known to present spectral features at $\sim$710.5 eV.
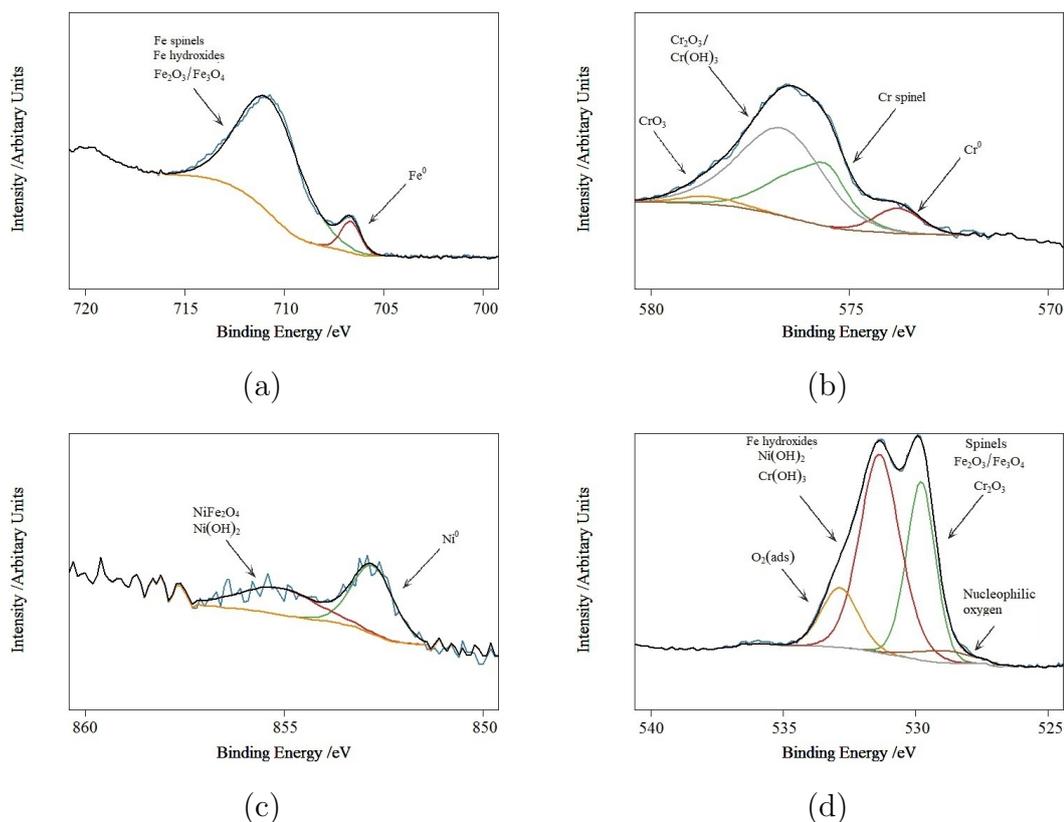
Figure 5.4: XPS profile of (a) Fe $2p_{3/2}$, (b) Cr $2p_{3/2}$, (c) Ni $2p_{3/2}$ and (d) O 1s after week long immersion of unsensitised 304H SS in simulant pond water, pH$\simeq$11.4 at 24 °C.

The chromium profile in Figure 5.4(b) shows four peaks which are due to elemental Cr, 573.78 eV, Cr spinels, 575.7 eV, C_2O_3, 576.5 eV and CrO_3 at 578.56 eV. As mentioned previously, $NiCr_2O_4$ and $FeCr_2O_4$ both have binding energies similar to the spinel peak seen at 575.57 eV in the Cr profile, however, it is unlikely $NiCr_2O_4$ will form at room temperature [185]. Therefore, it is possible that this peak is due to the presence of $FeCr_2O_4$. The broadness of the Cr_2O_3 suggest that there may be another phase contributing to the peak. It is likely that this is $Cr(OH)_3$ which is known to have a binding energy $\sim$577.2 eV [183].

Only weak Ni peaks are recorded, one peak due to Ni metal, Ni^0 at 852.73 eV and a very low intensity peak at 854.92 eV caused by $Ni(OH)_2$ or possibly $NiFe_2O_4$. Due to the low intensity of these peaks it is suspected that Ni is not a major contributor to the passive oxide layer formed on unsensitised 304H SS.

The oxygen profiles are shown in Figure 5.4(d). There are four peaks, the

peak at ~529.78 eV can be attributed to metal oxides, the peak at 531.3 eV is consistent with the presence of metal hydroxides and defective lattice oxygens, the peak at 532.85 eV is associated with adsorbed oxygen and the peak at 528.89 eV is associated with nucleophilic oxygen. Although these peaks cannot be deconvolved into their individual contributors it is beneficial in confirming the presence of metal oxides and hydroxides on the stainless steel surface.

Component	Assignment	Average Peak Position	FWHM
Fe 2p$_{3/2}$	Fe^0	706.63	1.17
	Fe$_2$O$_3$/Fe$_3$O$_4$	710.71	3.67
	Fe(OH)$_2$/Fe(OH)$_3$		
	FeOOH/Fe Spinels		
Cr 2p$_{3/2}$	Cr^0	573.78	1.33
	Cr spinel	575.7	1.892
	C$_2$O$_3$/Cr(OH)$_3$	576.5	1.999
	CrO$_3$	578.56	1.65
Ni 2p$_{3/2}$	Ni^0	852.73	1.123
	Ni(OH)$_2$/NiFe$_2$O$_4$	854.92	0.65
O 1s	nucleophilic oxygen	528.89	2.55
	Cr$_2$O$_3$/Fe$_2$O$_3$/Fe$_3$O$_4$/ Spinels	529.78	1.25
	Cr(OH)$_3$/Ni(OH)$_2$ Fe hydroxides	531.3	1.88
	O$_2$(ads)	532.85	1.63

Table 5.1: Average peak positions and FWHM values obtained for Fe 2p$_{3/2}$, Cr 2p$_{3/2}$, Ni 2p$_{3/2}$ and O 1s in unsensitised 304H SS.

From visual inspection of the XPS spectra it is difficult to ascertain the relative contributions of each phase to the passive layer. However, by plotting the relative atomic percentages of each species on a bar chart, the nature of each of these metal components in the passive layer formed on unsensitised 304H SS may be more readily determined. To obtain a detailed understanding of the extent of oxidation of each of the individual metal components the relative atomic percentages of each species for iron, chromium, and nickel are presented in separate bar charts in Figure 5.5. This approach is similar to that used for analogous data obtained from 20/25/Nb SS samples, as shown in Figures 3.7. Thus 5.5(a), (b) and (c) show

the relative at% of each species present in the surface layer for iron, chromium and nickel respectively. Figure 5.5 also allows for a direct comparison to be made between the compositions of the surface layer formed on as-received 304H and 20/25/Nb SS; in each of Figures 5.5(a), (b) and (c) bar A represents unsensitised 304H SS data and bar B represents unsensitised 20/25/Nb SS data.
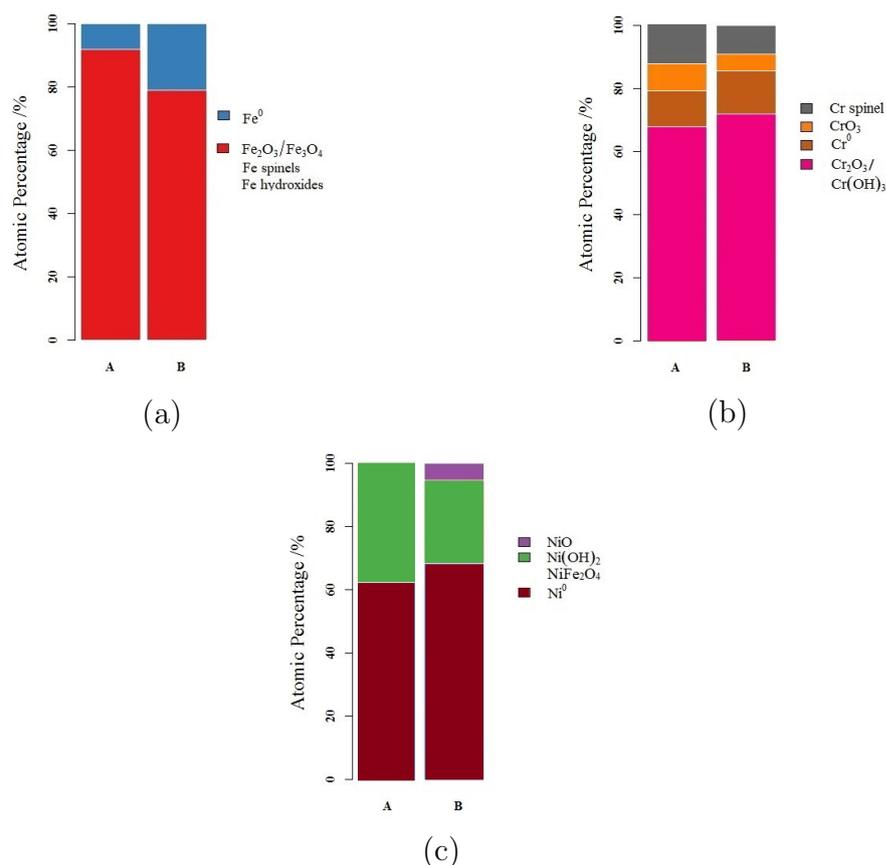
Figure 5.5: Atomic percentage data comparison of (a) Fe $2p_{3/2}$, (b) Cr $2p_{3/2}$ and (c) Ni $2p_{3/2}$ extracted from XPS profiles obtained after a week long immersion of **A** unsensitised 304H SS and **B** unsensitised 20/25/Nb SS in simulant pond water, pH$\simeq$11.4 at 24 °C.

Considering the bar A data from Figures 5.5(a) to 5.5(c), the contributions of the oxides/hydroxides formed on 304H SS can be compared, specifically $\sim$90 at% of the Fe contribution is an Fe oxides/hydroxides/spinel, $\sim$90 at% of Cr contributions are oxides/hydroxides and $\sim$38 at% of Ni contributions are hydroxide/spinel.

As described above, some comparisons can be made between 304H and 20/25/Nb SSs using Figure 5.5. Overall, it is clear that there is greater oxidation of each of the component metals on surface of the 304H SS sample than on the

surface of the 20/25/Nb SS sample. This would suggest an enhanced corrosion susceptibility for 304H SS compared with 20/25/Nb SS.

More specifically, considering Figure 5.5(a), the relative atomic percentage contribution of the Fe oxides/hydroxides/spinels in the case unsensitised 304H SS is ~90 at% and ~80 at% in the case of unsensitised 20/25/Nb SS.

From the Cr data of Figure 5.5(b), there are some obvious differences between these unsensitised SS samples. The relative atomic percentage contribution of $Cr_2O_3/Cr(OH)_3$ is approximately 5 at% less for the unsensitised 304H SS sample. It is possible that some chromium carbide precipitates formed during the casting of the 304H sample due to the lack of Nb stabiliser in this steel and that an associated proportion of the Cr would therefore not be free to form $Cr_2O_3/Cr(OH)_3$ – which may explain the apparent greater corrosion susceptibility of this material compared to 20/25/Nb SS. Alternatively, some of the Cr(III) oxide/hydroxide may have oxidised to Cr(VI) oxide, so accounting for the greater at% CrO_3 on the 304H SS surface compared to the 20/25/Nb SS surface. The presence of the CrO_3 would again suggest an enhanced corrosion susceptibility for 304H compared to 20/25/Nb SS. In contrast, the apparent increases in the Cr spinel content in the case of unsensitised 304H SS may mask any potential enhanced corrosion susceptibility associated with this surface layer, as noted in section 4.2 for unsensitised 20/25/Nb SS.

Looking at the relative atomic percentage contribution of Ni to the passive film, Figure 5.5(c), there is no evidence of NiO formation on 304H SS and the contribution of $Ni(OH)_2$ has increased compared with the passive layer of unsensitised 20/25/Nb SS. Considering that (i) Ni concentrations in 304H SS are ~15 wt% less than in 20/25/Nb SS and (ii) the weak intensity of the Ni peaks for unsensitised 304H SS, it is sensible to be cautious in the interpretation of any Ni passivation that may be associated with these results.

In order to achieve a true comparative analysis, the relative atomic percentages of the species of all three elements in the oxide/hydroxide layer

considered simultaneously. This is achieved by normalising the individual component $2p_{3/2}$ peaks and plotting the results on a single bar chart (full details are given in section 3.2). Figure 5.6 shows the relative atomic percentages of the dominant components of the surface layer. Figure 5.6 also allows for a direct comparison to be made between the compositions of the surface layer formed on as-received 304H and 20/25/Nb steels, with bar A representing unsensitised 304H SS data and bar B representing unsensitised 20/25/Nb SS data.
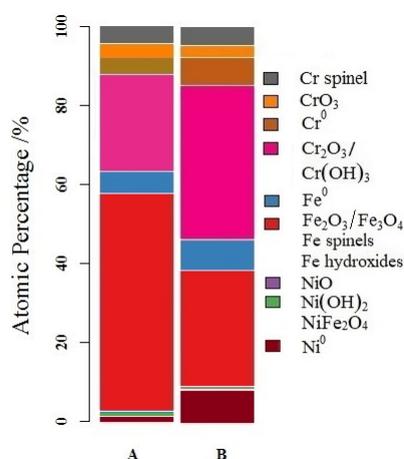
Figure 5.6: Atomic percentage data comparison of Fe, Cr and Ni phases in the passive layer of **A** unsensitised 304H SS and **B** unsensitised 20/25/Nb SS extracted from XPS profiles obtained after a week long immersion in simulant pond water, pH$\simeq$11.4 at 24 °C.

It can be seen from Figure 5.6 that the most dominant components of the surface layer formed on unsensitised 304H SS under open circuit conditions ($E_{OCP} \simeq$-0.19 V) in simulant pond water are the Fe oxides/hydroxides, with Cr (III) oxides/hydroxides being significant secondary components of the outer oxide layer. The influence of metallic Ni in this layer is minimal at <1 at%, in contrast to the analogous layer on 20/25/Nb SS where nickel comprises just less than 10 at% of the surface. Cr spinels and CrO_3 contribute $\sim$5 at% in each steel. Note that $FeCr_2O_4$ will have contributions to the Fe oxide/hydroxide portion of the bar chart and the Cr spinel portion. However, since the Cr spinel contribution is $\sim$5 at%, the percentage of the Fe oxide/hydroxide portion of the bar chart attributed to $FeCr_2O_4$ is likely to be <5 at%. Likewise, the $NiFe_2O_4$

spinel will also have contributions to the Fe oxide/hydroxide portion of the bar chart and the Ni oxide/hydroxide/spinel portion. The contribution of the Ni oxide/hydroxide/spinel portion of the overall bar chart contribution is <1 at% - therefore any $NiFe_2O_4$ contribution to the Fe portion will be minimal. These results therefore suggest that the electrochemistry and thus the corrosion resistance of unsensitised 304H SS under open circuit conditions in simulant pond water will be dominated by the electrochemistry of Fe and Cr oxide/hydroxide phases.

Comparing unsensitised 304H and 20/25/Nb SSs (bar A with bar B), the passive layer formed unsensitised 304H SS contains more Fe oxide/hydroxide ($\sim$50 at% compared to $\sim$30 at%) and less Cr_2O_3 ($\sim$22 at% compared to $\sim$38 at%) than in the surface layer of unsensitised 20/25/Nb SS. Cr spinels, CrO_3 and Ni oxide/hydroxide contributions to the surface layer differ by only 1 or 2 at% between the unsensitised SS samples.

Having now characterised the condition of the surface of 304H SS under OCP conditions in simulant pond water and compared this with the surface composition of 20/25/Nb SS, the next sections explore how the condition of the surface changes in the presence of a range of oxidative stresses. As a result of the above observed differences in surface oxide composition it is likely the electrochemical behaviour of 304H SS will differ for that of 20/25/Nb SS. Any such differences are highlighted and explored in the following sections. In this discussion, it will become clear that despite enhanced oxidation of the 304H SS surface compared to 20/25/Nb SS it is still resistant to localised corrosion under conditions where the integrity of the passive film is not challenged e.g. in simulant pond water at pH$\simeq$11.4 at 24 °C.

5.1.3   Effect of pH Variation on the Corrosion Behaviour of Unsensitised 304H Stainless Steel

Linear sweep voltammetry was performed on unsensitised 304H SS in simulant pond water at pH$\simeq$8 and at pH$\simeq$11.4. The resulting polarisation curves are shown

in Figure 5.7(a). In undosed simulant pond water 304H SS begins to pit at $\sim$0.1 V, indicated by the presence of small peaks, and transpassive dissolution occurs approximately 0.1 V after this at $\sim$0.2 V. Once the simulant pond water has been dosed with NaOH to a pH$\simeq$11.4 there is no evidence of pitting and the breakdown potential shifts to $\sim$0.8 V. The merits of increasing the pH are clear from this extended region of passivity and the absence of pitting behaviour.

(a)   (b)
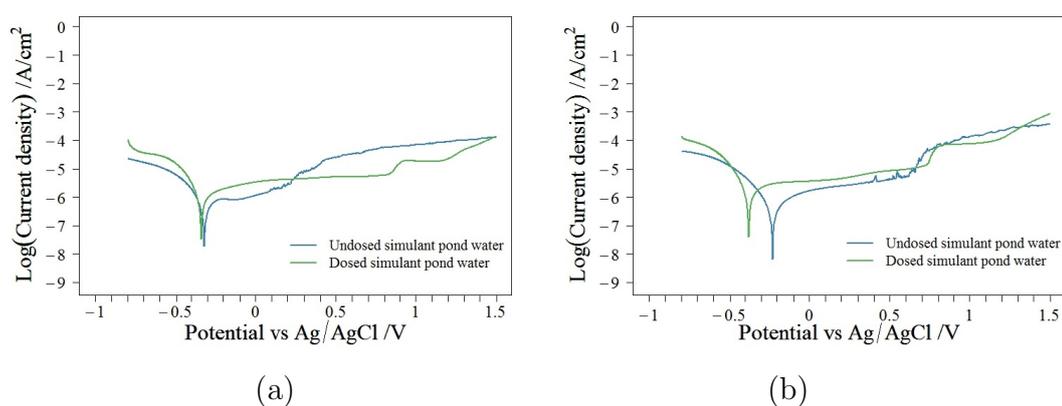
Figure 5.7: Potentiodynamic polarisation curve for (a) unsensitised 304H SS and (b) unsensitised 20/25/Nb SS in undosed (pH$\simeq$8) and NaOH dosed (pH$\simeq$11.4) pond water simulants at 24 °C, showing the effects of dosing on corrosion behaviour. Both solutions contain 30 μmol dm^{-3} Cl$^-$.

These polarisation curves for unsensitised 304H SS are compared to those of unsensitised 20/25/Nb SS in Figure 5.7(b). For the undosed solution, 20/25/Nb SS offers a wider potential range of passive protection (-0.15 to 0.4 V) before pitting corrosion occurs and subsequent transpassive dissolution. Considering the Ni content is significantly higher in 20/25/Nb SS than in 304H SS and that Ni is known to passivate in neutral to alkaline solutions [230–233], it is likely to be the cause of this added protection in 20/25/Nb SS.

In relation to dosed simulant pond water, three observations can be made: (i) 20/25/Nb and 304 SS have similar general corrosion currents, (ii) 20/25/Nb SS has higher transpassive currents than 304H SS and (iii) the onset of transpassivity of 304H SS is $\sim$0.05 V more positive than that of 20/25/Nb SS. Taking into account the results of the XPS study in section 5.1.2 the latter two observations are explained as follows. The higher transpassive currents of 20/25/Nb SS are

due to the higher $Cr_2O_3/Cr(OH)_3$ content in the passive layer of unsensitised 20/25/Nb SS and the higher Ni concentration in the same layer. With more $Cr_2O_3/Cr(OH)_3$ transforming to Cr(VI) greater transpassive currents are observed as Cr(VI) dissolves. This is also evidenced by the slight rise in the current density between 0.3 and 0.75 V on the 20/25/Nb SS that is associated with the oxidation of Cr(III) to Cr(VI) oxides in the film and that is not observed on the 304H SS polarisation curve. The Ni content of 20/25/Nb SS is more than three times that of 304H SS so it is reasonable to assume the underlying Ni oxide/hydroxide layer, expected to develop for passivated stainless steels, is thicker on 20/25/Nb SS than on 304H SS. Thus, in the transpassive region, where Ni is leaching from the surface, there would be a greater oxidation of a protective Ni oxide/hydroxide phase to a more soluble Ni oxyhydroxide species such as the γ-NiOOH phase for the 20/25/Nb SS sample (see section 3.3 for further detail).

The onset of transpassivity occurs at lower potentials for the unsensitised 20/25/Nb SS than for unsensitised 304H SS, the difference being approximately 50 mV. A possible explanation for this is that, again, the surface film on 20/25/Nb SS contains a higher proportion of the oxidisable Cr and Ni species, $Cr_2O_3/Cr(OH)_3$ and $Ni(OH)_2$; literature and the pure metal studies of section 3.3 suggest that transpassive dissolution of stainless steels is largely due to the dissolution of chromium as a Cr(VI) oxide [188, 234]. The film on 304H SS will be comprised of a greater proportion of non-oxidisable Fe(III) oxide species and thus, counter-intuitively, less susceptible to further oxidation.

5.1.3.1   Electrochemical Impedance Spectroscopy of Unsensitised 304H Stainless Steel in Dosed Simulant Pond Water

Electrochemical impedance spectroscopy was used to attain insight into the nature of passive layer formation on unsensitised 304H SS. Figure 5.8 shows the Nyquist and Bode plots obtained at several key potentials in simulant pond water, pH$\simeq$11.4 at 24 °C. A single resistance-capacitance loop and time constant

is observed at all potentials studied – thus the same simple Randle cell equivalent circuit was used as for 20/25/Nb SS found in Figure 3.12, see section 3.3.1 for relevant discussion. R_p and CPE values were found by fitting an equivalent circuit model to the plots of Figure 5.8. As discussed in section 3.3.1, the CPE can be equated to a capacitor for n≥0.8. For the data of Figure 5.8, this condition is found to be satisfied in the potential range -0.4 to 1 V. Consequently the CPE can be taken to be equal to a capacitance over the same range and, as such, only this potential range is considered for Mott-Schottky analysis.

(a)

(b)

(c)
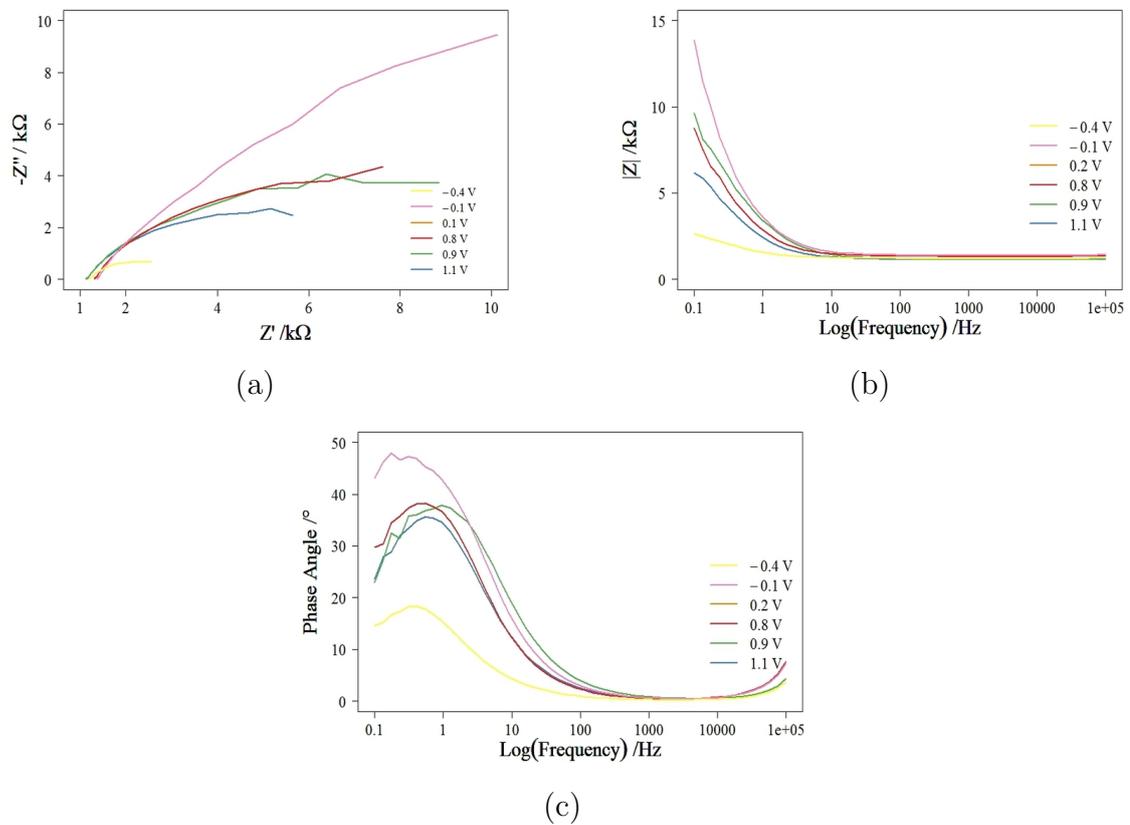
Figure 5.8: Nyquist (a) and Bode (b) & (c) plots at several key potentials for unsensitised 304H SS in dosed simulant pond water, pH≃11.4 at 24 °C.

Figure 5.9(a) shows the polarisation resistances and inverse squared capacitances extracted from the Nyquist and Bode plots of Figure 5.8 as a function of potential overlaid on the relevant polarisation curve. Data for unsensitised 20/25/Nb SS under the same conditions is presented alongside for ease of comparison, Figure 5.9(b).

From the R_p vs E plots of Figure 5.9(a), 304H SS can be considered to be either corroding or exhibiting hydrogen evolution at E≤-0.4 V and corroding at E≥1 V due to the low R_p values observed in these ranges; similarly, due to the high R_p values observed for potentials -0.3 to 0.9 V, the steel can be considered to be well passivated in this range.

(a)   (b)
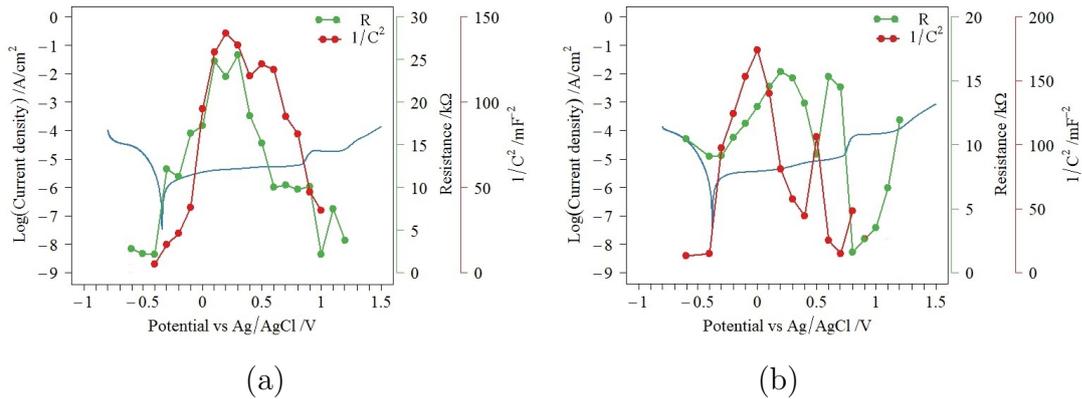
Figure 5.9: Electrochemical impedance spectroscopy analysis of (a) unsensitised 304H SS and (b) unsensitised 20/25/Nb SS in dosed simulant pond water, pH≃11.4 at 24 °C, specifically potentiodynamic polarisation curve overlaid with polarisation resistance data (green) and capacitance data (red), in the form of a Mott-Schottky plot, extracted from the Nyquist plots.

Direct comparison of Figure 5.9(a) and Figure 5.9(b) shows that for potentials less than 0.5 V the change in polarisation resistance is similar for unsensitised 304H SS and unsensitised 20/25/Nb SS i.e. increases in polarisation resistance are observed between -0.5 and 0.1 V and decreases in resistance between 0.3 and 0.5 V for both stainless steel types under these conditions. In section 3.3.1, for 20/25/Nb SS, this peak was seen to have contributions from Fe and Cr oxides/hydroxides. Due to the general similarity in the trend in resistance at these potentials it is reasonable to assume that this is the case for 304H SS also. This assignment will be revisited in the Mott-Schottky analysis below. However, at potentials positive of this peak, it can be seen that the R_p vs E behaviour for 304H SS is significantly different to that observed earlier for 20/25/Nb SS. Specifically, the peak seen for unsensitised 20/25/Nb SS at 0.6 V is not seen for the 304H SS sample. The reader is reminded that, in the case of 20/25/Nb SS, this peak was assigned to the

formation of Ni hydroxide. Thus, it is not unreasonable to attribute the absence of this peak in 304H SS to the fact that 304H has a substantially lower Ni content than 20/25/Nb SS and that Ni will thus play a similarly diminished role in the surface resistive behaviour of this SS. In other words, Ni offers an underlying protection beneath the chrome/iron oxide/hydroxide layer in 20/25/Nb SS; thus, lower Ni content would mean lower corrosion resistance at higher potentials. Interestingly, despite the lack of this peak in resistance, the resistance does not decrease in this region, it remains relatively constant over this potential range (0.6-0.9 V) i.e. it is not seen to decrease substantially. As discussed in section 3.3.1, the iron and chromium oxide contribution to passivation is presumed to be minimal at these potentials, thus the presence of spinels could be the cause of this plateau in resistance as spinels are also presumed to extend the passive range in our discussion of the corresponding potential range for 20/25/Nb SS above.

Now considering the capacitance data of Figure 5.9(a), the C^{-2} vs E behaviour of unsensitised 304H SS can be divided into four regions; -0.4 to 0.2 V, 0.2 to 0.4 V, 0.4 to 0.5 V and 0.5 to 1 V. As with 20/25/Nb SS, Region I is of apparent n-type character with an positive slope in the C^{-2} vs E plot; however, as in the case of 20/25/Nb SS, this behaviour can actually be attributed to the growing passive layer, defect elimination and the formation of Fe_2O_3 at the 304H SS surface. The presence of this iron oxide layer is confirmed by the XPS analysis at OCP ($\sim$-0.19 V) which show the main contributor to the passive layer is Fe oxides/hydroxides at this potential.

Region II is of apparent p-type character with an negative slope in the C^{-2} vs E plot. As with unsensitised 20/25/Nb SS, the behaviour of the passive layer is expected to be dominated by the semiconducting properties of Cr_2O_3 in this potential range. It is likely that there is some oxidative dissolution of the Fe_2O_3 beginning in this region evidenced in the pure Fe Mott-Schottky plot of Figure 3.16. There are indications of n-type behaviour over the short Region III between 0.4 and 0.5 V; this is most likely due to the oxidation of Cr(III) to a Cr(VI) oxide

phase as previously discussed for 20/25/Nb SS in section 3.3.1 above.

The apparent p-type behaviour observed indicated by a negative slope in the C^{-2} vs E plot in region IV (0.5 - 1 V) is coincident with the transpassive behaviour seen in the polarisation curve i.e. in this region the passive layer is in-part dissolving. It is possible to further sub-divide region IV into two regions on the basis of the potential of the onset of transpassivity i.e. 0.5 to 0.8 V and 0.8 to 1 V. As such, the p-type characteristics observed in the potential range 0.5 to 0.8 V may be dominated by the spinels discussed in section 3.3.1. The negative slope of 0.8 to 1 V is then most likely associated with the dissolution of passive oxides from the surface of the 304H SS.

Comparing the C^{-2} vs E plots of unsensitised 304H (Figure 5.9(a)) and 20/25/Nb (Figure 5.9(b)) SSs, the apparent n-type behaviour is prevalent over a wider potential for the 304H SS sample. This is probably a result of the greater iron content in 304H SS. This hypothesis is supported by the XPS data of the previous section which showed greater amounts of Fe_2O_3 on the surface of 304H SS compared to the surface of 20/25/Nb SS under open circuit conditions. The interpretation of the C^{-2} vs E plots of the two stainless steels is the same between 0.2 and 0.7 V where chromium oxide and spinel electrochemistry dominates the capacitive behaviour. At higher potentials CPE$\neq$C for unsensitised 20/25/Nb SS, therefore Mott-Schottky analysis was not performed above 0.8 V for 20/25/Nb SS and comparisons of capacitive behaviour above 0.8 V are beyond the scope of this thesis.

5.1.4 Effect of Chloride Concentration in the Aqueous Phase on the Corrosion Behaviour of Unsensitised 304H Stainless Steel

To investigate the stability and robustness of the passive protection observed for the 304H SS, samples were immersed in solutions containing chloride. Firstly, the effect of chloride concentration on the corrosion behaviour of unsensitised 304H

SS in the absence of sodium hydroxide was investigated. Figure 5.10(a) shows the resulting polarisation curves. As the chloride concentration increases the onset on transpassivity shifts towards more negative potentials. Once Cl^- concentrations reach 28 mmol dm^{-3} any passivity seen for lower concentrations of chloride has disappeared and the SS corrodes at all potentials. In order to provide further insight into this observed behaviour Figure 5.10(b) shows the effects of increasing Cl^- concentration on pure iron. From comparison of these figures it is seen that the behaviour of 304H SS in the presence of chloride is almost identical to that of pure iron. Thus, it is clear that iron electrochemistry dominates the behaviour of 304H SS in undosed pond water with increases in chloride concentrations.

(a)   (b)
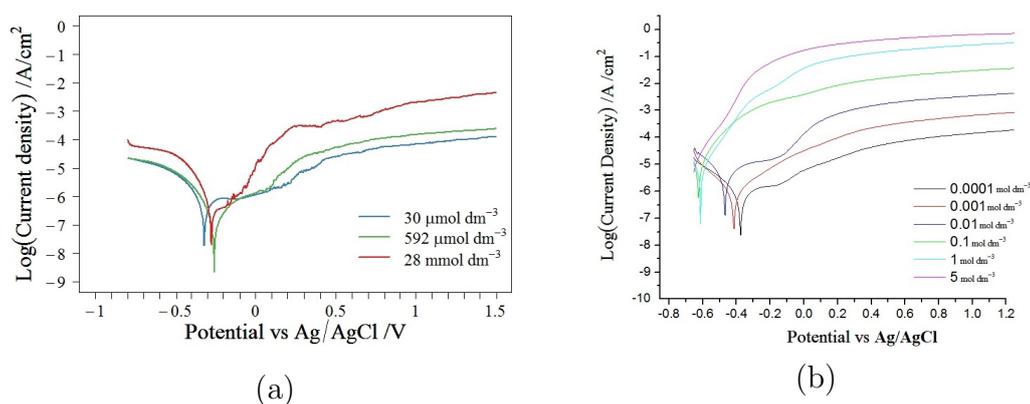
Figure 5.10: Potentiodynamic polarisation curves demonstrating the effect of increasing chloride concentration (a) on the corrosion behaviour of unsensitised 304H SS in undosed simulant pond water, pH$\simeq$8 at 24 °C and (b) on pure iron, pH$\simeq$5.5 at 24 °C (Plot courtesy of Christopher Anwyl, Lancaster University).

Figure 5.11(a) shows, for 304H SS, the influence of NaOH addition on passive film breakdown due to the presence of chloride. From Figure 5.11(a), it can be seen that on addition of NaOH the observable passive range extends to -0.4 to 0.8 V for all chloride concentrations up to $\sim$56 mmol dm^{-3} - at which concentration the onset potential for transpassivity exhibits a negative shift of $\sim$750 mV to 0.05 V vs Ag/AgCl, so considerably reducing the width of the passive range. It is of note that, at $[Cl^-]\simeq$28 mmol dm^{-3}, a secondary transpassive process appears at $\sim$1.1 V in the potential range corresponding to secondary passivation. This is similar to the behaviour observed for heat treated 20/25/Nb SS (Figure 4.12(a)) which

was attributed to the formation of $FeCl_6^{3-}$, see section 4.4 for relevant discussion.
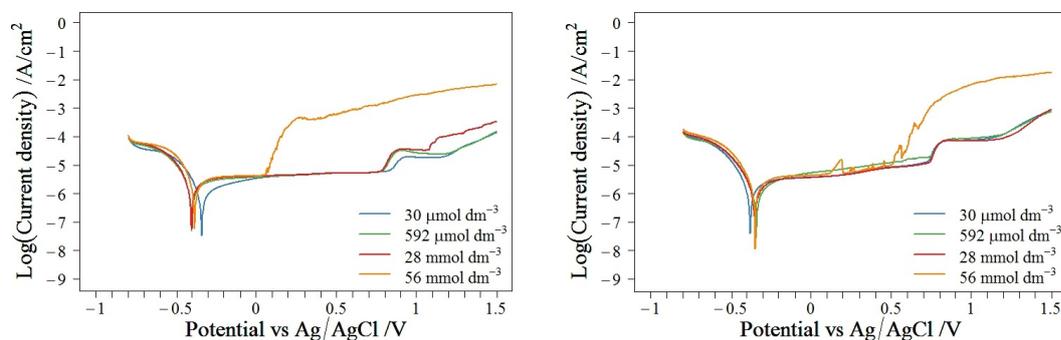
Figure 5.11:   Potentiodynamic polarisation curve demonstrating the effect of increasing chloride concentration in dosed simulant pond water, pH$\simeq$11.4 at 24 °C, on the corrosion behaviour of (a) unsensitised 304H SS and (b) unsensitised 20/25/Nb SS.

Both 20/25/Nb SS and 304H SS are generally unaffected by the Cl^- concentrations investigated below 56 mmol dm^{-3} (see Figure 5.11(b)) and exhibit similar electrochemistries in this concentration range. Above this concentration value the two steels behave differently.   304H SS exhibits large transpassive currents at low potentials whereas 20/25/Nb SS exhibits continuous pitting corrosion until the eventual collapse of the protective film. The difference here could be attributed to the lower Ni content in 304H SS leading to less protection of the stainless steel in corrosive environments. Also, the higher Cr oxide content in the passive layer of 20/25/Nb SS (seen from the XPS data) may allow this SS type to close down pits on their formation whereas the passive film on 304H SS breaks down completely. NbC pitting centres found in 20/25/Nb SS are not present in 304H SS and therefore it is not unreasonable to conclude that 304H SS may be less susceptible to pitting corrosion. However the fact that, at $[Cl^-]\simeq$56 mmol dm^{-3}, the potential of the onset of transpassivity on 304H SS is coincident with a pitting peak at the same potential on 20/25/Nb SS suggests that not all pit nucleation centres are due to the presence of NbC and are due to other impurities/non-metallic inclusions in the SS such as sulphides [235, 236].

5.1.5 Effect of Temperature Variation on the Corrosion Behaviour of Unsensitised 304H Stainless Steel

LSV studies were carried out in simulant pond water at 45, 60 and 90 °C. The polarisation curves obtained are presented in Figure 5.12(a). As the temperature increases from 24 °C to 60 °C it can be seen that there is an increase in the general corrosion currents and greater transpassive currents are observed as well. As in the case of similar results obtained from analogous experiments conducted on 20/25/Nb SS in Chapter 3 (see Figure 3.19, reprinted below as Figure 5.12(b) for the convenience of the reader), both of these changes are most likely due to the formation of a disordered inhomogeneous porous oxide film [237] and the increased solubility of the passivating oxides at higher temperatures.

Separate measurement of the OCPs at each temperature indicate that these are -0.19, -0.14 and -0.09 V for unsensistised 304H SS in simulant pond water at 24, 45 and 60 °C respectively. Comparison of these OCP values with the data of Figure 5.12(a) indicate that they all sit squarely within the observable passive range allowing us to conclude that, under normal operating conditions, a passive film will be maintained on the surface of 304H SS.

At 90 °C there is a major shift in the onset of transpassivity to ∼0 V from the value of ∼0.6 V observed at 60 °C. However, the OCP of unsensitised 304H SS in simulant pond water at 90 °C is -0.15 V which, surprisingly, still sits squarely within this truncated passive range. Thus, despite the reduced passive region at this temperature a passive layer may still be expected to be maintained at the surface of 304H SS, albeit at a greater uniform corrosion rate.
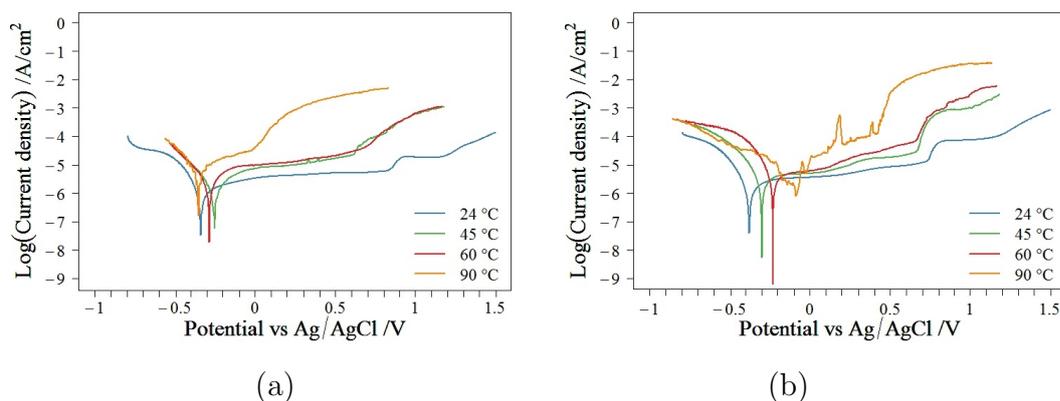
Figure 5.12: Potentiodynamic polarisation curves demonstrating the effect of increasing simulant pond water, 30 μmol dm^{-3} Cl$^-$, pH$\simeq$11.4 at 24 °C, temperature on the corrosion behaviour of (a) unsensitised 304H SS and (b) unsensitised 20/25/Nb SS.

Comparing Figure 5.12(a) and Figure 5.12(b) the trend in behaviour with increasing temperature from 24 – 60 °C is similar for both SSs. However, at 90 °C some differences are observed. Firstly, the noisiness of the polarisation curve of 20/25/Nb SS at potentials around E$_{ZC}$ is not present in the polarisation curve of 304H SS. A possible explanation for this is the difference in the exposed surface areas of the samples. The tube from which the 304H SS sample was prepared has a thicker wall than the cladding tube from which the 20/25/Nb SS sample was fabricated – and since bubble formation, the source of the noise, occurs mainly at the metal-epoxy interface the interaction of 304H SS with solution is proportionately less obscured by bubble nucleation than in the case of 20/25/Nb SS (see Figure 2.2 for images of the electrodes). Secondly, compared to unsensitised 20/25/Nb SS where pitting is evident at 90 °C, there are no peaks associated with pitting corrosion in the polarisation curve for 304H SS at this temperature. This is comparable to the behaviour seen for increases in Cl$^-$ concentration and may once again be a result of the lower population of pit initiation/nucleation centres due to the lack of NbC inclusions in 304H SS and the higher Cr oxide content in the passive layer of 20/25/Nb SS (seen from the XPS data) may be allowing the shut down of pits on their formation whereas the passive film on 304H SS breaks down completely.

5.1.6 Effect of Hydrogen Peroxide Concentration in the Aqueous Phase on the Corrosion Behaviour of the 304H Stainless Steel Samples

As with the 20/25/Nb SS samples, an assessment of the corrosion behaviour of 304H SS in the presence of H_2O_2 in simulant pond water dosed with NaOH was carried out in an attempt to mimic the effect of radiolysis.

5.1.6.1 Effect of Hydrogen Peroxide Concentration in Simulant Pond Water on the Corrosion Behaviour of Unsensitised 304H Stainless Steel

The influence of H_2O_2 concentration on the electrochemical behaviour of unsensitised 304H SS is shown in Figure 5.13(a). There are several noticeable changes in the electrochemical behaviour of 304H SS with increased H_2O_2 concentration. Firstly, there is a shift in E_{ZC} towards more positive potentials with increasing H_2O_2 concentration. Secondly, the onset of transpassivity shifts in the cathodic direction with increasing H_2O_2 concentration; this point is returned to below using comparative analysis to explain this phenomenon. These changes indicate a decrease in the passive potential range and thus an increased corrosion susceptibility. Finally, a wave begins to grow between ∼0.2 and ∼0.75 V. This peak is attributed to H_2O_2 adsorption chemistry. An in depth analysis of this peak was presented in section 3.5.1 and it is reasonably assumed that this analysis holds for the case of 304H SS.

(a)   (b)
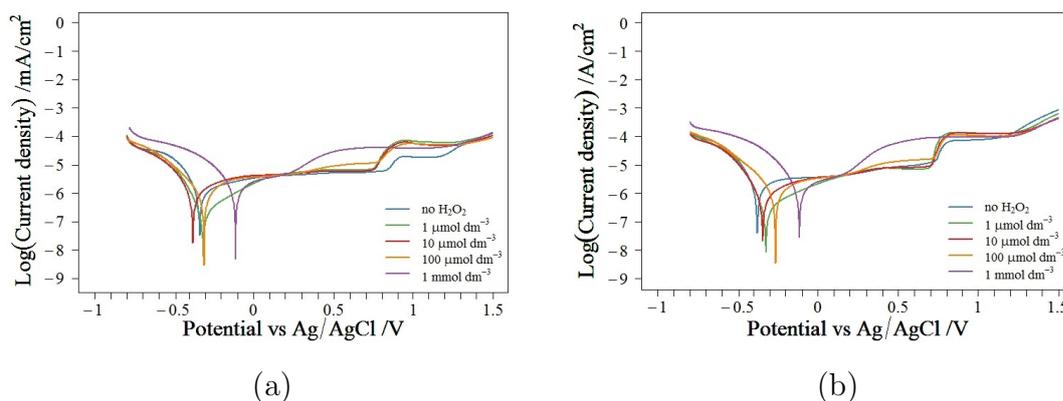
Figure 5.13: Effect of hydrogen peroxide concentration on the corrosion behaviour of (a) unsensitised 304H SS and (b) unsensitised 20/25/Nb SS in simulant pond water, 30 μmol dm^{-3} Cl$^-$, pH$\simeq$11.4 at 24 °C.

Once again the behaviour of 304H SS must be compared to that of 20/25/Nb SS, Figure 5.13(b). Both types of stainless steels experience the in-growth of the H$_2$O$_2$ oxidation wave and an anodic shift in E$_{ZC}$ with increases in H$_2$O$_2$ concentration. However, the cathodic shift, from $\sim$0.85 to $\sim$0.75 V, in the transpassive onset observed for 304H SS is not seen for 20/25/Nb SS under the same conditions. This is a result similar to that observed by Song *et al.* [74] who investigated the effects of peroxide on 304H SS. Song attributes this shift to changes in the metal oxide layer via oxidation, however they do not expand on the exact nature of this change. Using the results of the previous sections, an attempt to provide some insight into the cause of this change can be made.

From the studies above, the passive protection in the region 0.6 to 0.8 V on 304H SS is attributed to spinels, these is most likely to be predominantly FeCr$_2$O$_4$, due to low Ni content of this SS type, and non-oxidisable Fe oxides. From the data analysis of chapter 3 it is concluded that for 20/25/Nb SS, in the same potential range, the surface layer will be dominated by Ni hydroxide with a secondary contribution from spinels, both NiFe$_2$O$_4$ and FeCr$_2$O$_4$. There is limited literature on the corrosion behaviour of spinels in peroxide solutions but from the available information a hypothesis can be made as to the source of the cathodic shift in the onset potential for transpassivity.

FeCr$_2$O$_4$ is less susceptible to oxidation by peroxide than Cr oxide/hydroxide

[238] and thus it allows the stainless steel to remain passive across a wide potential window. However, $FeCr_2O_4$ is more susceptible to oxidation in the presence of peroxide than in its absence [239] and therefore the passive window would be expected to narrow in the presence of added H_2O_2 - something that is seen here with the addition of as little at 1 μmol dm^{-3} H_2O_2. The addition of H_2O_2 results in an initial oxidation of Cr(III) to soluble Cr(VI) in $FeCr_2O_4$, so compromising the integrity of the film and resulting in the shift in the transpassive onset. Cr(III) oxide/hydroxide will also oxidise to soluble Cr(VI) in the presence of peroxide [238]. Thus, the bulk of the remaining protection will then be provided by the Fe(III) oxides/hydroxides and Ni phases across the passive range -0.35 to 0.75 V. The onset of transpassivity on 304H does not then continue to shift with increasing in H_2O_2 concentrations above 1 μmol dm^{-3} H_2O_2 as the protection is provided by non-oxidisable Fe and Ni oxide/hydroxide phases and Ni-Fe spinels, as in the case of 20/25/Nb SS.

Ni is more noble than Cr and Fe and is therefore more slowly oxidised. Experiments by PNNL show Ni chromite is even less susceptible to peroxide driven oxidation than $FeCr_2O_4$ [238]. It would follow that $NiFe_2O_4$ is also more resistant to oxidation by H_2O_2, although comparative experiments on these spinels have not been reported in the literature various sources report that $NiFe_2O_4$ is less soluble than Ni oxide/hydroxide [240, 241]. Due to Ni phases being more resistant to oxidation than Cr phases, the 20/25/Nb SS does not experience this shift in transpassivity as any dissolution of $FeCr_2O_4$ may be compensated for by the Ni phases.

5.1.6.2 Effect of Temperature in the Presence of Hydrogen Peroxide in Simulant Pond Water on the Corrosion Behaviour of Unsensitised 304H Stainless Steel

Experiments where the pond water temperature is increased in the presence of hydrogen peroxide were performed with the intention of better simulating real

storage conditions under the new packing regime. Figure 5.14(a) shows the polarization curves at 24, 45, 60 and 90 °C in simulant pond water containing 10 μmol dm^{-3} H$_2$O$_2$, as current predictions estimate the radiolytically generated peroxide concentration in pond water to be close to this value. Increasing the temperature of the simulant pond water containing H$_2$O$_2$ causes movement of E$_{ZC}$ to more positive potentials, a rise of the general corrosion currents and a shift in the onset of transpassivity to lower potentials.

(a)   (b)
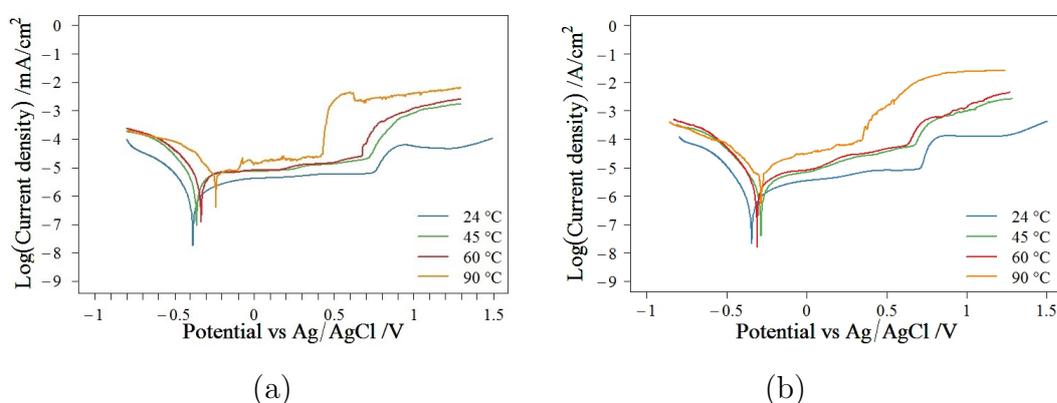
Figure 5.14: Effect of increasing temperature on the corrosion behaviour of (a) unsensitised 304H SS and (b) unsensitised 20/25/Nb SS in simulant pond water, pH$\simeq$11.4 at 24 °C, containing [H$_2$O$_2$]$\simeq$10 μmol dm^{-3} and 30 μmol dm^{-3} Cl$^-$.

In order to understand the impact of H$_2$O$_2$ at elevated temperatures it is necessary to compare these results to those in Figure 5.12(a). In Figure 5.12(a) the effect of increasing temperature in the absence of H$_2$O$_2$ was presented - it was noted that both general corrosion and transpassive currents increase with temperature – phenomena partly attributed to the increased solubility of the passivating oxides at higher temperatures. On increasing the temperature of the simulant pond water containing H$_2$O$_2$ to 45 °C a wider passive region is established in the presence of peroxide than in its absence; however the general corrosion currents are similar. The same is true at 60 °C, although to a reduced extent. At 90 °C the influence of H$_2$O$_2$ is most prominent, with the width of the passive range being considerably increased in the presence of H$_2$O$_2$ compared to the range recorded in its absence. There is however, evidence of pitting in the extended passive region. As discussed above, the addition of H$_2$O$_2$ at room

temperature resulted in a cathodic shift in the potential associated with the onset of transpassivity – a phenomenon attributed to increased solubility of $FeCr_2O_4$ in the presence of peroxide. However, the opposite is true for T$\geq$45 °C, at these temperatures the presence of peroxide appears to promote the growth of the passive layer – with these most likely being a large contribution from $Fe(OH)_3$ to this growth as from the above discussion Fe oxide/hydroxide will dominate if Cr oxides/hydroxides/spinels are dissolved in peroxide.

The impact of raising the simulant pond water temperature containing H_2O_2 on 304H SS is akin to that on 20/25/Nb SS under the same conditions, Figure 5.14(b). Specifically, for both stainless steel types the addition of peroxide to simulant pond water at elevated temperatures extends the passive potential window resulting in an enhanced protection of the SS surfaces compared to in peroxide free solutions.

5.1.7   Conclusions

Thus far the principal aim of this chapter has been to provide an outline of the corrosion behaviour of unsensitised 304H SS under conditions relevant to the wet interim storage of AGR fuel pins. The purpose of this section is twofold. Firstly, heat treated 304H SS has been proposed as a RIS-affected AGR cladding analogue, therefore it is essential to understand the baseline behaviour of unsensitised 304H SS before analysis of its heat treated counterparts can be undertaken. Secondly, the experiments described in this section are identical to those reported in Chapter 3 on unsensitised 20/25/Nb SS, as such direct comparisons between the two steel types can be made and inherent behavioural differences elucidated.

The key conclusions of this section regarding the electrochemical corrosion behaviour of unsensitised 304H SS are as follows.

The OCP in simulant pond water (pH$\simeq$11.4) is found to be $\sim$-0.19 V vs Ag/AgCl. Under these conditions, XPS data indicates that the protective oxide layer formed on the surface of 304H SS consists predominately of Fe and Cr

oxides/hydroxides, with Fe oxide/hydroxide being the more dominant of the two. Resistance and capacitance data from EIS experiments shows that the source of this protection changes on application of an oxidative stress i.e. as the electrode potential is increased. Through Mott-Schottky analysis it was found that this change occurs at ∼0.2 V whereupon the protection provided by Fe oxides decreases due to its oxidative dissolution and Cr oxides dominate until ∼0.8 V.

Voltammetric studies were used to determine the robustness of this oxide layer. Studies under baseline conditions of pH=8 at 24 °C show a region of passivity from ∼-0.25 V vs Ag/AgCl to ∼0.2 V. However, at pH 11.4 the window of passivity is extended to ∼-0.25 V to 0.8 V – indicating that simple dosing of the system with NaOH provides significant added corrosion protection for 304H SS samples under these conditions. This protection is maintained at pH 11.4 at 45 °C in the presence of 30 μmol dm^{-3} of both Cl$^-$ and H$_2$O$_2$, i.e. under future interim storage conditions, with a separation of approximately a volt between E$_{ZC}$ and onset of transpassivity. Since the measured E$_{OCP}$ for this steel lies in this passive region, it is unlikely that intergranular attack will occur under these pond/solution conditions.

The extent of the envelope of this protection was studied as a function of key solution parameters such as chloride concentration, temperature and hydrogen peroxide concentration – including conditions relevant to future wet storage scenarios and their fault conditions. Results may be summarised as follows.

With respect to chloride concentration:

In the absence of hydroxide i.e. at pH 8 - close to neutrality, chloride readily attacks the passive layer on 304H SS. Key features of this attack are a cathodic shift in the onset transpassivity and appearance of pitting corrosion in the passive range from [Cl$^-$]≥30 μmol dm^{-3}. At [Cl$^-$]≥28 mmol dm^{-3} 304H SS corrodes freely. However, increasing the pH to ∼11.4, through the addition of NaOH, leads to the protection of the surface from localised attack for [Cl$^-$]≤28 mmol dm^{-3}. At [Cl$^-$]≃56 mmol dm^{-3} there is a significant cathodic shift in the onset of transpassivity, however

passive behaviour is still observed at lower potentials ($\sim$-0.4 to $\sim$0 V).

With respect to temperature:

The general corrosion currents increase as the temperature increases from 24 °C to 90 °C and the onset of transpassivity moves towards more negative potentials with increasing temperature thus reducing the passive potential range. However, at all temperatures of interest a passive layer is expected to grow on 304H SS in simulant pond water.

With respect to hydrogen peroxide concentration:

Voltammetry suggests that, as is the case for unsensitised 20/25/Nb SS, the most dominant electrochemical behaviour observed is the simple electrooxidation of H_2O_2 at the surface of heat treated 304H SS in the passive potential range. By analogy with 20/25/Nb SS, it is expected that the oxidation of peroxide at the steel surface is controlled by a surface adsorption process. At low peroxide additions of $\sim$1 μmol dm^{-3}, there is an initial cathodic shift in the onset of transpassivity associated with H_2O_2-driven dissolution of Cr spinel. At simulant pond water temperatures between 45-90 °C the presence of peroxide promotes growth of a protective layer thus extending the potential passive window. This effect is most prominent at 90 °C, however pitting corrosion is observed throughout this region at this temperature.

Comparison of unsensitised 304H SS and unsensitised 20/25/Nb SS:

Comparing the behaviour of unsensitised 304H SS to unsensitised 20/25/Nb SS some further conclusions can be drawn. Generally, under the conditions studied, unsensitised 304H SS appears to be slightly more susceptible to transpassive corrosion and thus intergranular attack. This observation is consistent with Figure 5.1 and 5.2 (oxalic etch and DL-EPR tests for 304H SS) which show a greater susceptibility to intergranular attack compared to 20/25/Nb SS, Figure 3.1 and Figure 3.2. This is also in agreement with the XPS and EIS studies which showed reduced Cr(III) oxide content in the passive layer at OCP on 304H

SS. This vulnerability to transpassive corrosion may also be due to the reduced nickel content in 304H SS which would presumably offer a thinner inner protective oxide/hydroxide layer compared to that formed on 20/25/Nb SS. This behaviour is most evident at elevated temperatures and in solutions containing high chloride concentrations. With regards to pitting susceptibility, one could speculate that since the NbC inclusions present in 20/25/Nb SS, which provide pitting centres, are not present in 304H SS this leaves 304H SS less vulnerable to this form of localised attack. This difference in behaviour is evident for the SS samples in simulant pond water containing $[Cl^-] \simeq 28$ mmol dm^{-3} and in simulant pond water at 90 °C. Uniform corrosion in the passive range occurs at almost the same rate for all studies at pH 11.4. This indicates that despite some compositional differences in the passive layers on 20/25/Nb and 304H SSs the mechanism for uniform loss of Fe and Cr oxides from the outer surface are concurrent and if the loss of the one oxide is more preferable to the other the residual oxide is able to compensate for this loss effectively in alkaline solutions.

5.2 Heat Treated 304H Stainless Steel

So far, this chapter has focused on the corrosion behaviour of unsensitised as-received 304H SS with the aim of establishing the baseline behaviour of 304H SS under conditions relevant to interim storage and to highlight fundamental differences between the corrosion behaviour of 304H SS and 20/25/Nb SS. As stated above, heat treated 304H SS was selected to be used as an analogue for irradiated AGR cladding due to its chromium and carbon content being similar to 20/25/Nb SS and because the lack of Nb stabiliser, making this SS type more readily sensitised.

Whillock *et al.* [82] investigated suitable heat treatments regimes in order to create 304H SS samples that are representative of irradiated RIS-affected AGR fuel cladding. The sample preparation is described in section 2.1.4.2 and the criteria for such analogues is presented in section 1.9.6. Two promising heat treatments were identified as ageing the stainless steel at 600 °C for (i) 48 hours or for (ii) 72 hours. The electrochemical corrosion testing results for 304H SS samples for both heat treatments, under conditions relevant to wet interim storage, are given in the following subsections.

5.2.1 Degree of Sensitisation

Grain boundary profiling of these two samples (304H SS aged at 600 °C for (i) 48 hours or for (ii) 72 hours) was carried out by Whillock *et al.* [82]. The sample aged for 48 hours showed chromium depleting to ∼15 wt% at the grain boundary and the grain boundary chromium concentration in the sample aged for 72 hours dropped to ∼10 wt%. Theses grain boundary profiles are shown in Figure 5.15. This decrease in chromium can be also clearly seen in the two sensitisation tests performed here, the results of which are as follows.

(a)

(b)
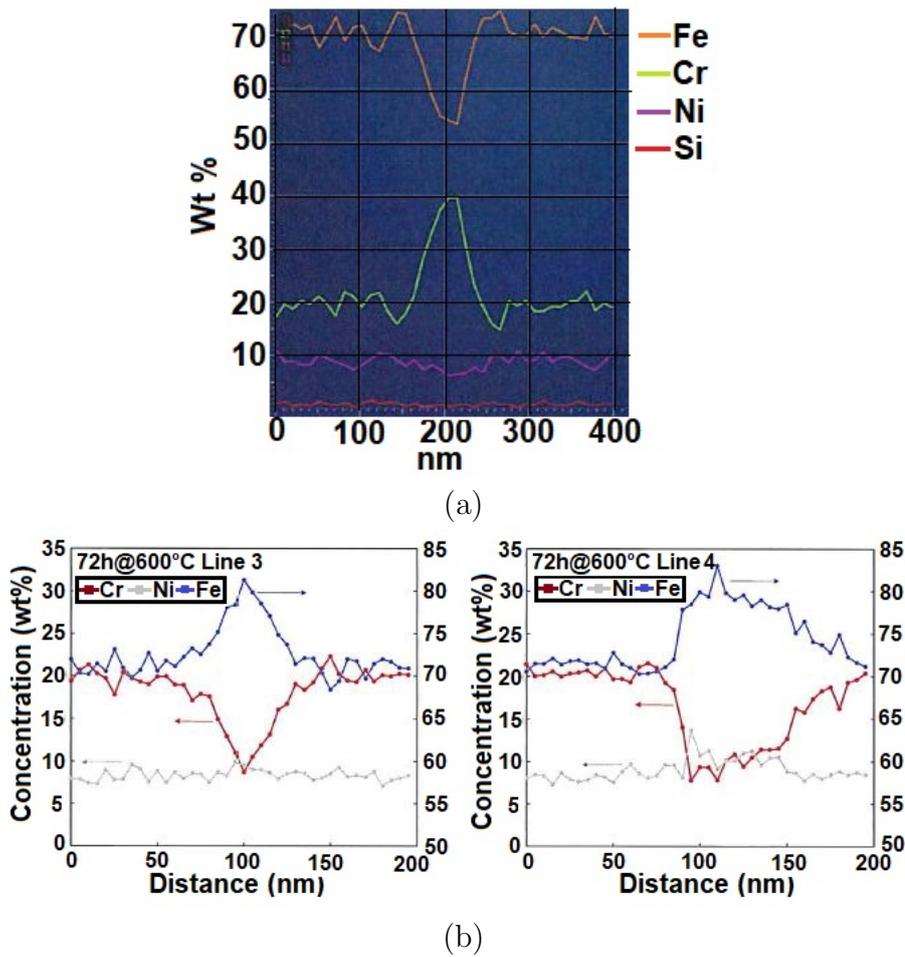
Figure 5.15: Grain boundary composition profile obtained for 304H SS heated at 600 °C for (a) 48 hours and (b) 72 hours [125].

5.2.1.1   Electrochemical Etching

A qualitative assessment of the degree of sensitisation was performed on the two heat treated 304H SS samples using the oxalic acid etch test. Figure 5.16 shows the heat treated 304H SS samples pre and post-exposure to oxalic acid. Figure 5.16 (a) and (b) are broadly featureless. Post exposure to the etchant, complete etching of the grain boundaries is observed for both heat treated samples, as can be seen in Figure 5.16 (c) and (d). This is a clear indication of the depletion of chromium at the grain boundary according to ASTM Standard A262 [160]. 304H SS aged at 600 °C for 48 or 72 hours should therefore be susceptible to localised corrosion. This is consistent with the grain boundary profiles obtained by Whillock *et al.* on 304H SS samples which had undergone the same heat treatment, as shown in

Figure 5.15 [82].

Ditching at the grain boundaries allows an average grain size to be determined. Both heat treated samples have an average grain size of ~ 75 μm.
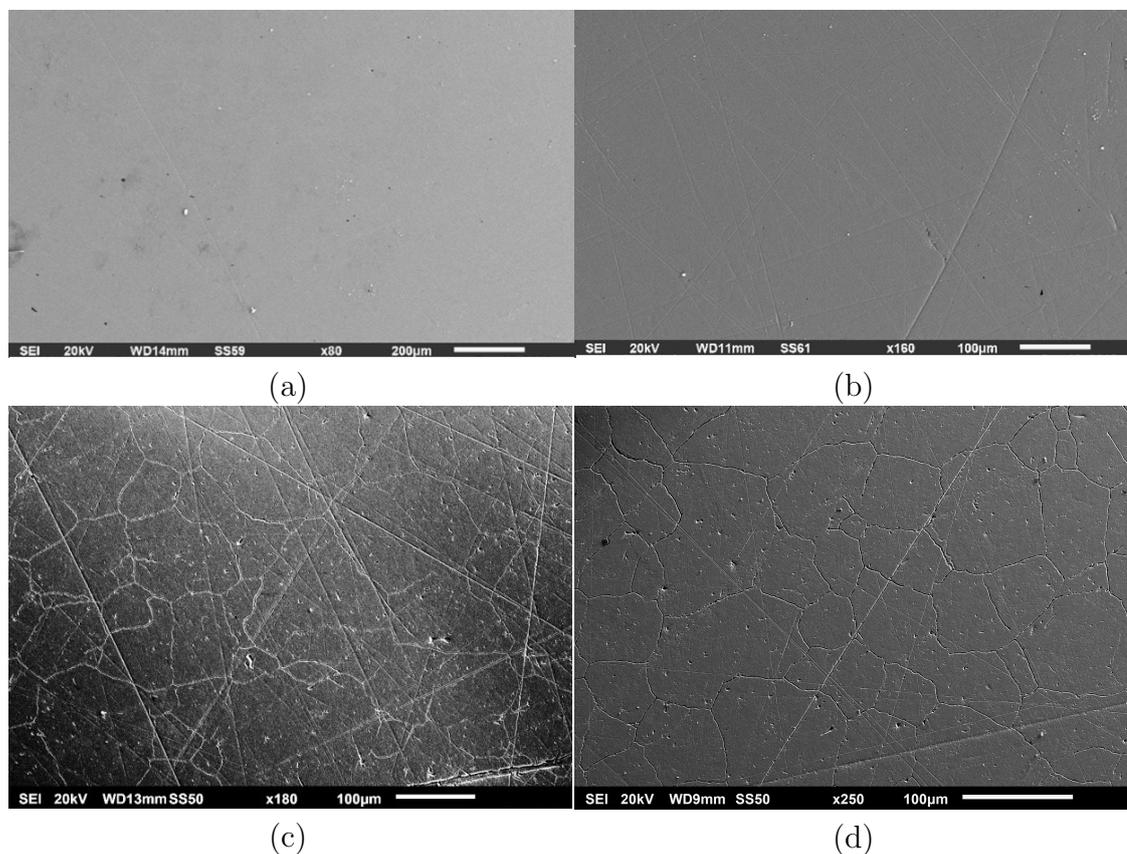
Figure 5.16: SEM images of heat treated 304H SS pre- and post-exposure to 10% oxalic acid for 15 seconds with an applied potential of 6 V, (a) & (c) sample aged for 48 hours at 600 °C and (b) & (d) sample aged for 72 hours at 600 °C.

5.2.1.2 Double Loop Electrochemical Potentiokinetic Reactivation Tests

The degree of sensitisation of heat treated 304H SS was quantitatively evaluated using the DL-EPR testing method. The DL-EPR voltammetric behaviour of the heat treated 304H SSs is shown in Figure 5.17. The 304H SS samples, one aged for 48 hours and one for 72 hours at 600 °C have peak current ratios of 0.92 and 0.91 respectively. Evidently both heat treatment regimes have caused the 304H SS to become significantly sensitised. This confirms the grain boundary and oxalic acid etch assessments and therefore, it is reasonable to

predict that these samples are vulnerable to intergranular attack.

(a)   (b)
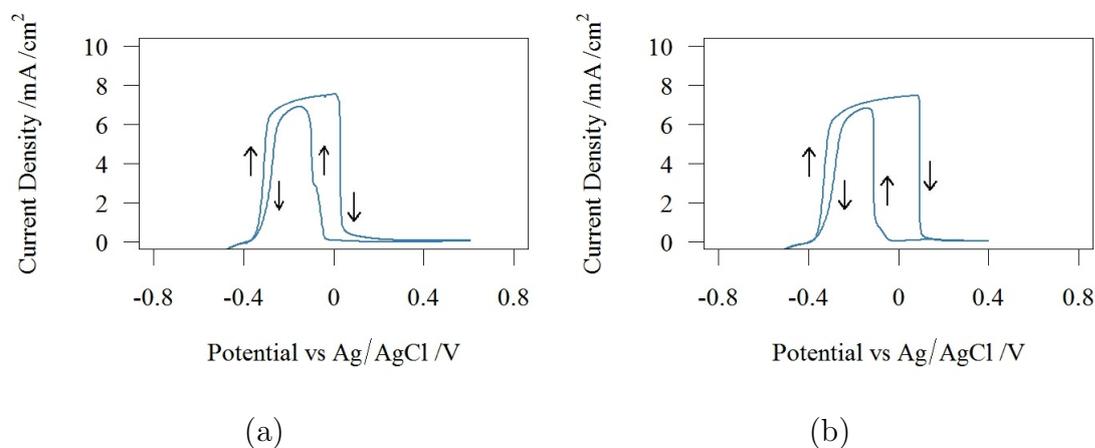
Figure 5.17: DL-EPR test on heat treated 304H SS in a solution of 0.5 mol dm^{-3} H$_2$SO$_4$ and 0.01 mol dm^{-3} KSCN with scan rate of 1.6 mV/s, (a) sample aged for 48 hours at 600 °C and (b) sample aged for 72 hours at 600 °C.

5.2.2   Compositional Analysis of the Passive Film Formed on Heat Treated 304H Stainless Steel in Simulant Pond Water

Having demonstrated the susceptibility towards intergranular corrosion of the heat treated 304H SS samples, this section describes XPS experiments designed to determine analytically the composition of the passive film grown on the samples in simulant pond water under open circuit conditions at 24 °C. Due to time and access restrictions XPS analysis was performed on the 304H SS sample aged for 48 hours at 600 °C only. These experiments also seek to determine if any compositional differences exist in the passive film grown on 304H SS aged for 48 hours at 600 °C compared to that of unsensitised 304H SS and heat treated 20/25/Nb SS samples. The XPS data can then be used to inform the analysis of polarisation curves later in this chapter.

However, before XPS measurements were performed on the immersed samples, simple electrochemical impedance spectroscopy (EIS) measurements were conducted to provide a qualitative initial assessment as to how the

composition of the steel passive layer changes as a function of immersion time. Specifically, EIS measurements were conducted every 30 minutes on heat treated 304H SS immersed in simulant pond water up to a total immersion time of 6 hours. Selected Nyquist and Bode plots from this run are shown in Figure 5.18. From which it can be seen that these plots do not stabilise in the 6 hour period. There is a increase in the magnitude of the imaginary impedance from 0 to 2 hrs consistent with a passive layer growth. However, from 2 to 6 hrs the magnitude of the imaginary impedance decreases. The phase angle (Figure 5.18(c)) shows a similar result at low frequencies where the angle increases for first 2 hours and then drops with longer immersion times. However, |Z| shows no obvious changes after 30 mins of immersion. This shows an instability in the passive layer that was not observed for unsensitised 304H SS or either 20/25/Nb SS sample.

Despite this apparent instability, in a separate experiment, a stable OCP was eventually attained after 16 hours immersion. In light of this latter result, it is not unreasonable to assume that the passive layer will stabilise after a longer immersion period. As the purpose to the data presented in Figure 5.18 was to simply provide qualitative evidence of the passive film formation and possible stabilisation, equivalent circuit modelling of these plots was not performed. Detailed equivalent circuit modelling of the surface layer is discussed later.

(a)

(b)

(c)
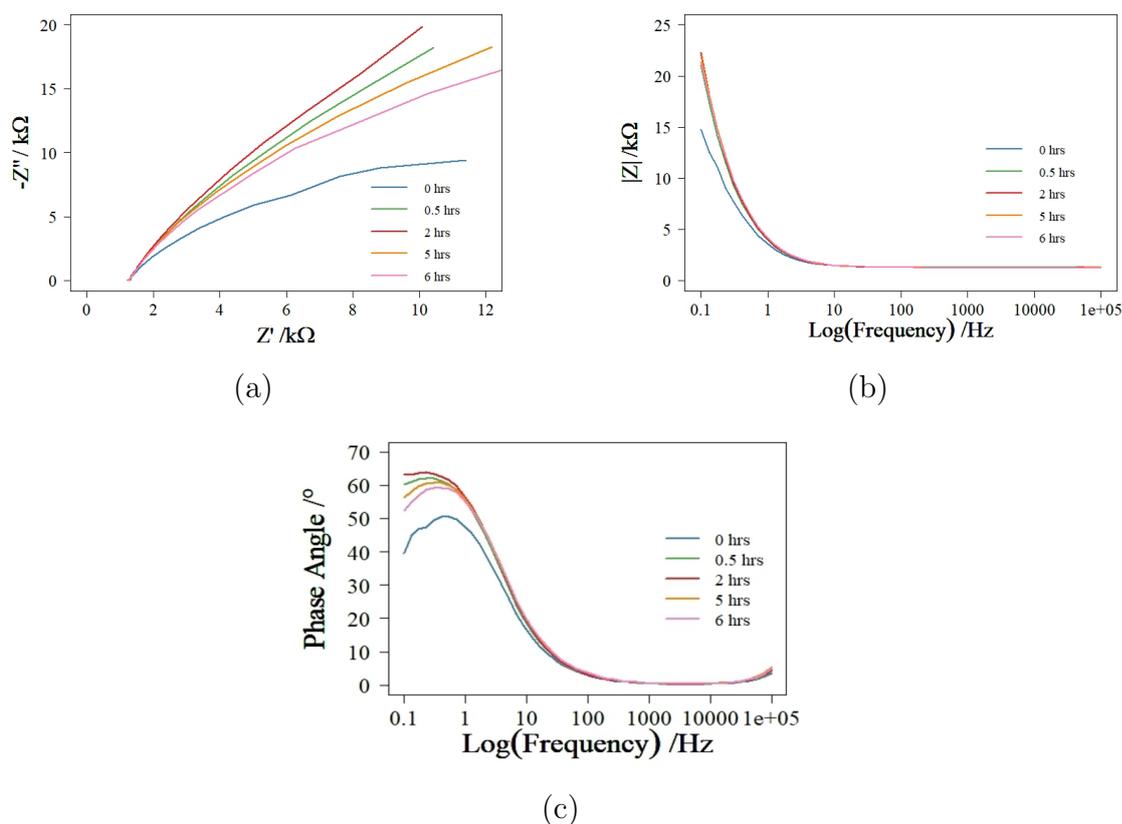
Figure 5.18: Time dependant Nyquist and Bode plots for heat treated 304H SS aged for 48 hours at 600 °C in simulant pond water, pH≃11.4.

XPS spectra were then obtained for 304H SS aged for 48 hours at 600 °C immersed in simulant pond water for one week at 24 °C. During this time the open circuit potential, E_{OCP}, was observed to obtain an equilibrium value of ∼-0.16 V vs Ag/AgCl. The same analysis procedure was undertaken as that described in section 3.2 for data obtained from 20/25/Nb SS. Curves are fitted to the averaged XPS spectra obtained for 304H SS aged for 48 hours at 600 °C and the results are shown in Figure 5.19. The average binding energy and full width half maximum (FWHM) of the spectra for each of the dominant elements, Fe, Cr, Ni and O were within ±0.2 eV of those found for the unsensitised sample and thus it is sensible to assume the peak assignments are the same are those presented in Table 5.1. The exception is the O 1s profile which has been deconvolved to just two peaks, a peak at 529.91 eV attributed to metal oxides and one at 531.5 eV representing metal hydroxides.
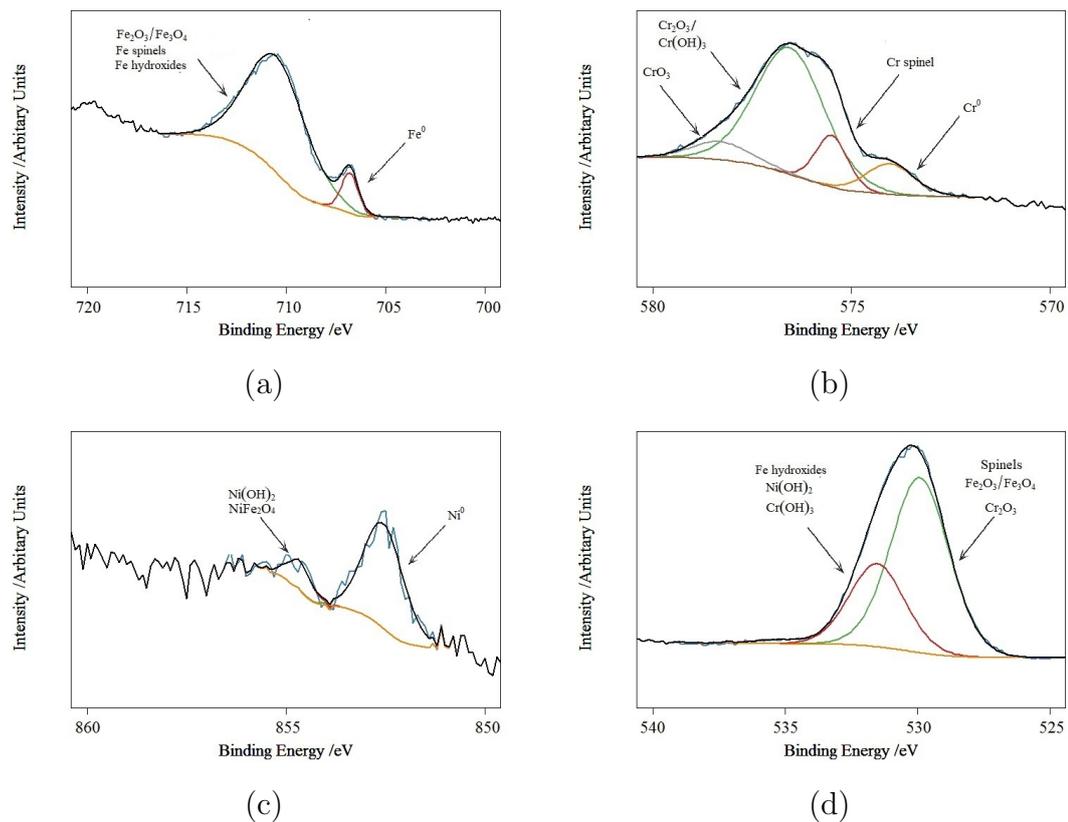
Figure 5.19: XPS profile of (a) Fe 2p$_{3/2}$, (b) Cr 2p$_{3/2}$, (c) Ni 2p$_{3/2}$ and (d) O 1s after week long immersion of heat treated 304H SS (aged for 48 hours at 600 °C) in simulant pond water.

As discussed in section 3.2, it is difficult to determine the relative contributions of each phase to the passive layer from simple visual inspection of the XPS spectra. However, by plotting the relative atomic percentages of each species for iron, Figure 5.20(a), chromium, Figure 5.20(b) and nickel, Figure 5.20(c) the differences between the passive layer formed on unsensitised 304H SS and heat treated 304H SS can be more easily understood. In these figures bar A represents unsensitised 304H SS and bar B represents heat treated 304H SS. As with the analysis of the 20/25/Nb SS samples, it is important to remember to be careful not to make assumptions as to the nature of the passive layer as a whole from these figures alone.

(a)

(b)

(c)
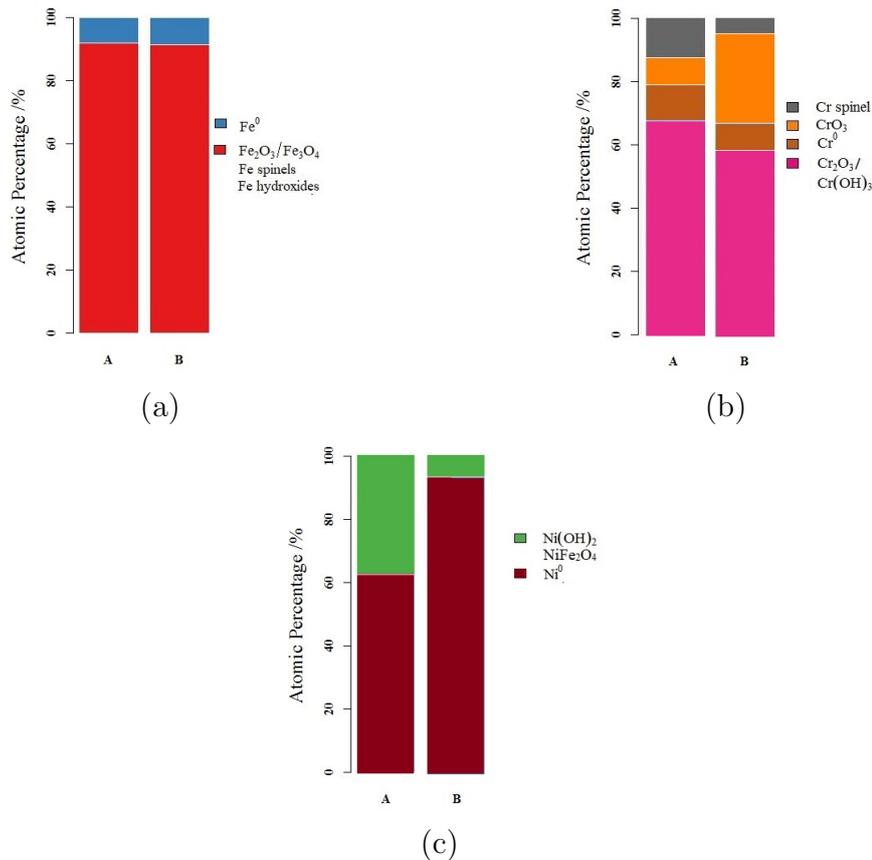
Figure 5.20: Atomic percentage data comparison of (a) Fe $2p_{3/2}$, (b) Cr $2p_{3/2}$ and (c) Ni $2p_{3/2}$ extracted from XPS profiles obtained after a week long immersion of **A** unsensitised 304H SS and **B** heat treated 304H SS (aged for 48 hours at 600 °C) in simulant pond water, pH$\simeq$11.4 at 24 °C.

From Figure 5.20(a) the relative atomic percentages of the Fe phases are seen to be almost identical for both unsensitised and heat treated 304H SS samples. Over 90 at% of the iron contribution to the passive layer is in the form of iron oxide/hydroxide/spinel compared to less than 10 at% from metallic Fe for both 304H samples. Any contribution from Fe spinels will be low using the same argument made in the XPS sections of previous chapters, this is clearer in Figure 5.21 where the surface is present as a whole. This suggests Fe oxides/hydroxides are likely to be a major contributor to the outer surface layer formed on heat treated 304H SS.

The relative atomic percentages for Cr species presented in Figure 5.20(b) show that the most obvious differences between thermally aged 304H SS and unsensitised 304H SS are the lower percentage of Cr_2O_3/$Cr(OH)_3$ and Cr spinels

and higher percentage of CrO_3 in the passive layer formed on the aged 304H SS compared to the unsensitised 304H SS.

Figure 5.20(c) shows that there is a clear decrease in the intensity of $Ni(OH)_2$/ $NiFe_2O_4$ peak in the oxide film grown on thermally aged 304H SS compared with that grown on unsensitised 304H SS. However, due the weak intensity of the Ni peaks these results should be viewed with caution.

In order to achieve a true comparative analysis it is necessary to merge the three relative atomic percentage bar charts of Fe, Cr and Ni to obtain a relative atomic percentage bar chart that considers all the dominant elements together in the passive layer. This is achieved following the same normalisation method as described in section 3.2. The resulting bar chart showing the relative atomic percentages are found in Figure 5.21. Data for 20/25/Nb SS is displayed along side the 304H SS data for ease of comparison of the stainless steel types.
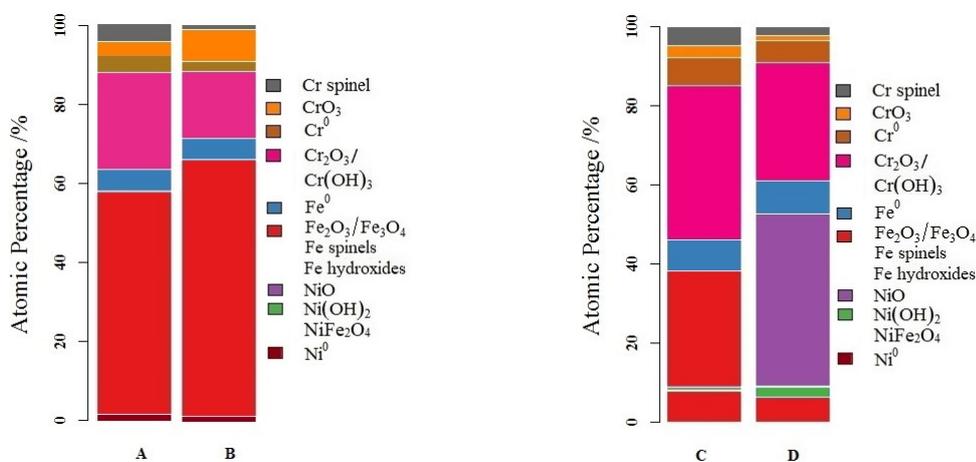
Figure 5.21: Atomic percentage data comparison of Fe, Cr and Ni in the passive layer of **A** unsensitised 304H SS, **B** heat treated 304H SS, **C** unsensitised 20/25/Nb SS and **D** heat treated 20/25/Nb SS extracted from XPS profiles obtained after a week long immersion in simulant pond water, pH$\simeq$11.4 at 24 °C.

Comparing unsensitised and heat treated 304H SS, it is clear that the heat treated sample has a lower contribution from Cr species to the surface layer than in the surface layer of the unsensitised sample. This is most likely due to chromium being consumed in the formation of chromium carbides during the heat treatment of the SS, leaving less chromium available for oxidation. As

stated in Chapter 4, chromium carbides will not be detected by XPS as they lie below the oxide/hydroxide layer [218, 219]. Thus, protective $Cr_2O_3/Cr(OH)_3$ is present in lower concentrations on the surface of heat treated 304H SS compared with unsensitised 304H SS, rendering the former more vulnerable to corrosion than the latter. This greater susceptibility to surface oxidation also manifests itself in a higher concentration of the more soluble Cr(VI) oxide, CrO_3, being present on the heat treated sample. The presence of the soluble CrO_3 and the lower at% of Cr(III) oxide/hydroxide together indicate an increased vulnerability to corrosion. In unsensitised 304H SS, Cr spinels have a higher relative atomic percentage than in heat treated 304H SS. In the absence of peroxide (either deliberately added or radiogenically generated) $FeCr_2O_4$ is known to have low solubility [242] and in previous chapters has been shown to extend the passive window. Therefore, it being present at lower concentrations generally weakens a materials resistance to corrosion. Thus, heat treated 304H would be expected to be more susceptible to corrosion.

Fe oxides/hydroxides are more dominant in the surface layer of heat treated 304H SS than on unsensitised 304H SS. This most likely manifests from there being less oxidisable Cr in the heat treated sample. There are no noteworthy differences in the contribution of Ni and its oxides/hydroxides to the passive film on both samples.

Comparisons between heat treated 304H and heat treated 20/25/Nb SS are also be made. The contribution of $Cr_2O_3/Cr(OH)_3$ to the surface layer is lower for both heat treated 304H SS and 20/25/Nb SS compared with their unsensitised counterparts. Interestingly despite the similar Cr composition of the two stainless steel types the outer passive layer of heat treated 304H SS contains less $Cr_2O_3/Cr(OH)_3$ than heat treated 20/25/Nb SS. $Cr_2O_3/Cr(OH)_3$ content is $\sim$30 at% for heat treated 20/25/Nb SS and $\sim$17 at% for heat treated 304H SS. This could be indicative of heat treated 304H SS being more sensitised than heat treated 20/25/Nb SS.

If there is less Cr free to oxidise, it follows that Fe oxides/hydroxides are more dominant in the heat treated 304H SS surface layer than in heat treated 20/25/Nb SS surface layer, as shown in Figure 5.21. Also, Fe is present in a greater concentration in the bare 304H SS and thus there is more Fe to oxidise at the metal surface.

Since 304H SS contains ∼15 wt% less Ni than 20/25/Nb SS, it is expected that the Ni components of the passive layer would be considerably smaller than for 20/25/Nb SS and as shown in Figure 5.21 this holds true.

Having now characterised the condition of the surface of heat treated 304H SS (aged for 48 hours at 600 °C) under OCP conditions in simulant pond water and compared this with the surface composition of heat treated 20/25/Nb SS, the next sections explore how the condition of the surface condition changes in the presence of a range of oxidative stresses. As a result of the above observed differences in surface oxide composition it is likely the electrochemical behaviour of heat treated 304H SS will differ for that of heat treated 20/25/Nb SS, any differences are highlighted and discussed in the following sections.

5.2.3 Effect of pH Variation on the Corrosion Behaviour of Heat Treated 304H Stainless Steel Samples

The electrochemical corrosion behaviour of heat treated 304H SS (sample aged for 48 hours at 600 °C and sample aged for 72 hours at 600 °C) in undosed and dosed simulant pond water at 24 °C was characterised using LSV experiments and compared to that of unsensitised 304H SS and heat treated 20/25/Nb SS. The polarisation curves obtained are shown in Figure 5.22.

Figure 5.22(a) shows the behaviour of the three 304H SS samples in undosed simulant pond water. E_{ZC} is observed to shift in the anodic direction for heat treated samples compared to unsensitised 304H SS. The sample aged for 48 hours and the unsensitised 304H SS sample have comparable general corrosion currents in the passive region. However, the sample aged for 72 hours has greater general

corrosion currents than the other electrodes. The onset of transpassivity occurs at almost the same potential for all three 304H SS samples. Generally, it is observed that the sensitised samples exhibit a decreased passive potential region and experience an increase in corrosion susceptibility relative to their unsensitised counterpart. If the behaviour of the heat treated samples is compared to that of pure iron at pH$\simeq$5.8 in Figure 5.10(b) (specifically the behaviour at [Cl$^-$]=0.0001 mol dm^{-3}) the similarities in the polarisation curves is clear. Thus, indicating that the surface oxidation is predominantly dictated by iron electrochemistry, this is consistent with the depletion of chromium in the surface film observed in the XPS results of section 5.2.2.

(a)   (b)
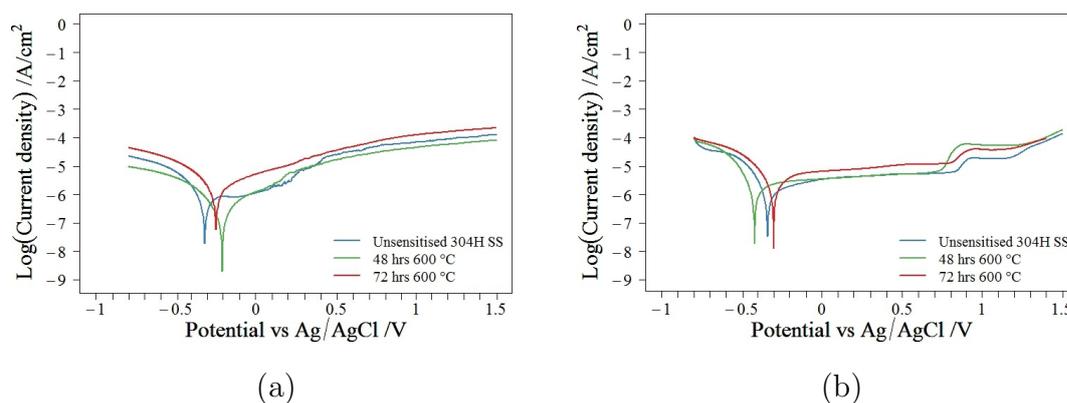
Figure 5.22: Potentiodynamic polarisation curves for heat treated 304H SS in (a) undosed (pH$\simeq$8) and (b) NaOH dosed (pH$\simeq$11.4) pond water simulants at 24 °C, showing the effects of dosing on the corrosion behaviour. Both solutions contain 30 μmol dm^{-3} Cl$^-$.

Figure 5.22(b) shows the effect of dosing the pond water to a pH$\simeq$11.4 on the electrochemical behaviour of unsensitised and sensitised 304H SS. It is clear that dosing with NaOH results in a wider protective region of passivity for all samples, from approximately a 0.4 volt protective window at pH 8 to greater than 1 volt at pH 11.4.

Comparing the behaviour of the sample heated for 48 hours and that of the unsensitised 304H SS, the breakdown potential of the passive film is lower and the transpassive currents are greater for the former sample. Considering the XPS data presented in section 5.2.2, which describes the surface layer formed at OCP on 304H

SS samples aged at 600 °C for 48 hours immersed in simulant pond water, some observations can be made. The transpassive onset for 304H SS is considered to be due the oxidation of Cr(III) to Cr(VI). Since the heat treated sample has greater Cr(VI) oxide content, there is less work required to oxidise Cr(III) to Cr(VI) - leading to a lower onset for transpassivity and greater transpassive currents. The shift in the onset of transpassivity to more negative potentials for the heat treated sample can also be attributed to the decrease in Cr spinel content in the passive layer compared to the unsensitised 304H SS; recall that Cr spinels are predicted to extend the passive potential range. It is important to remember the exact composition of the underlying oxide layer is unknown, so only the outer passive layer is considered in this interpretation.

304H SS aged for 72 hrs has the greatest general corrosion currents of the three samples. However, E_{ZC} and breakdown potentials of 304H SS heated for 72 hours are close to those of unsensitised 304H SS. The increased general corrosion rates may be due to enhanced chromium carbide precipitation in this stainless steel compared with the other two samples (this would be consistent with the grain boundary profiles of Figure 5.15); this would lead to a less homogeneous formation of the passive layer on the sensitised stainless steel, thus leaving the sample aged for 72 hours more susceptible to corrosion.

Referring to Figure 4.8 where the behaviour of heat treated 20/25/Nb SS is presented, some comparisons between heat treated 304H SS and heat treated 20/25/Nb SS can be made. The uniform corrosion currents are higher for the heat treated 304H SS. This may be due to the lower Ni content of 304H SS as the lower general corrosion currents of heat treated 20/25/Nb SS can be attributed to added protection derived from the underlying Ni hydroxide rich layer, vide supra. This inner oxide/hydroxide layer may be the cause of the larger transpassive currents observed in 20/25/Nb SS compared with the 304H SS samples as there is more Ni being oxidised to a soluble Ni phase in the former. As well, comparing the XPS results of heat treated 304H SS and heat treated 20/25/Nb SS, the difference in

transpassive currents can also be attributed to the greater percentage of (ultimately oxidisable) $Cr_2O_3/Cr(OH)_3$ in the passive layer of heat treated 20/25/Nb SS.

5.2.3.1   Electrochemical Impedance Spectroscopy of Heat Treated 304H Stainless Steel in Dosed Simulant Pond Water

EIS was shown to be a useful technique when investigating the changes in the passive film on the electrode surface in previous sections. Here, 304H SS samples aged for 48 hours and 72 hours at 600 °C and exposed to simulant pond water were analysed in the same potential region as the polarisation studies of Figure 5.22(b). Figure 5.23 and Figure 5.24 show the resulting Nyquist and Bode plots. Once again a single capacitive loop and time constant is observed over the entire potential range studied and thus, the same sequence of equivalent circuits were used as for 20/25/Nb SS found in Figure 3.12. R_p and CPE values were found by fitting an equivalent circuit model to the obtained Nyquist and Bode plots. As mentioned previously, CPE can be equated to a capacitor for n≥0.8. As such, in the case of the heat treated 304H SS CPE=C in the potential ranges -0.5 to 1 V and -0.4 to 1 V for 304H SS aged for 48 hours and 72 hours respectively. Figure 5.25 show the resulting polarisation resistances and capacitances as a function of potential.

(a)

(b)

(c)
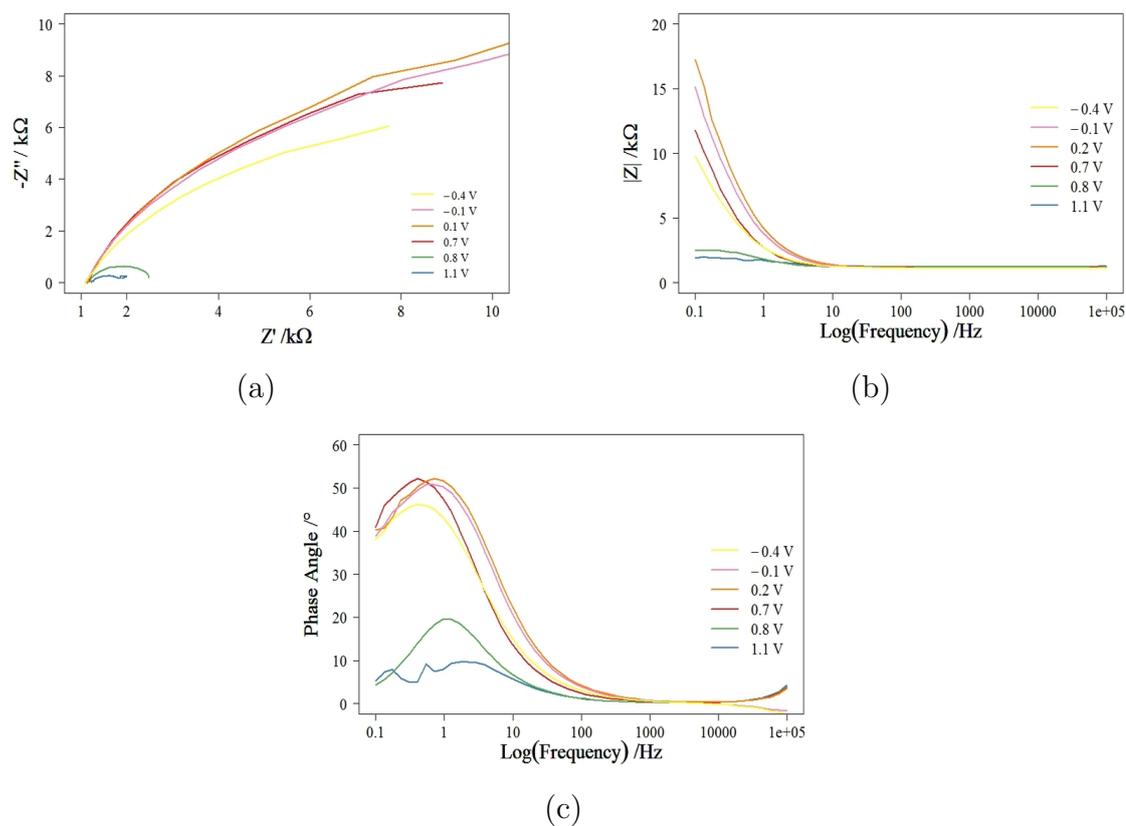
Figure 5.23: Nyquist (a) and Bode plots (b) & (c) at several key potentials for heat treated 304H SS in dosed simulant pond water, pH≃11.4 at 24 °C, for 304H SS aged for 48 hours at 600 °C.

(a)

(b)

(c)
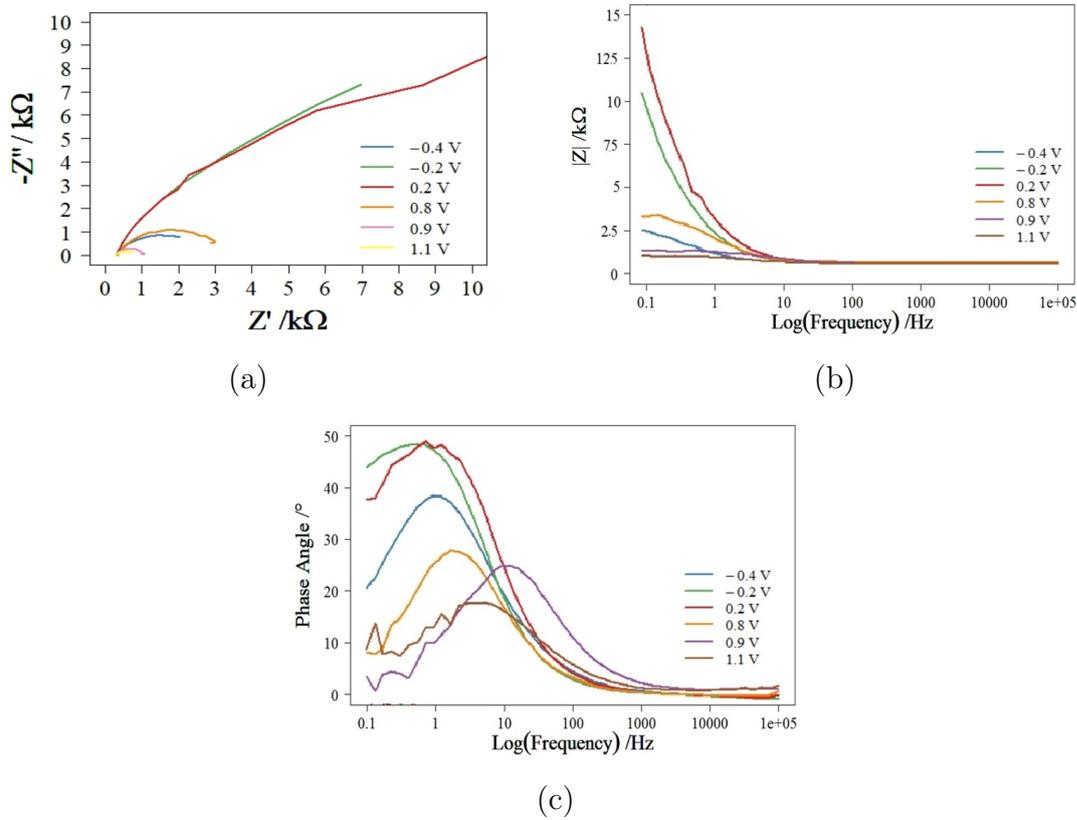
Figure 5.24: Nyquist (a) and Bode plots (b) & (c) at several key potentials for heat treated 304H SS in dosed simulant pond water, pH$\simeq$11.4 at 24 °C, for 304H SS aged for 72 hours at 600 °C.

From inspection of Figure 5.25(a), 304H SS aged for 48 hours is considered to be corroding at potentials $\leq$-0.5 and $\geq$0.8 V due to the low R_p values and passivated for potentials -0.4 to 0.7 V due to increased R_p values. For 304H SS aged for 48 hours R_p does not vary widely between -0.3 and 0.7 V.

The C^{-2} vs E plot of Figure 5.25(a) can be divided into four regions with the interpretation of the observed behaviour in each of these regions being exactly analogous to that for unsensitised 20/25/Nb SS in section 3.2. The four regions and their behaviours are: -0.5 to 0.1 V (apparent n-type), 0.1 to 0.4 V (p-type), 0.4 to 0.6 V (n-type) and 0.6 to 1 V (p-type). Again, in analogy to unsensitised 20/25/Nb stainless steel, the apparent n-type behaviour in region I is observed due to simple dielectric behaviour, defect elimination and the growth of a Fe_2O_3 passive layer. In region II genuine p-type behaviour derived from Cr_2O_3 dominates the passive layer and in region III Cr(III) oxidises to Cr(VI) causing the switch in

semiconducting behaviour. The apparent p-type behaviour in region IV coincides with the transpassive behaviour in the polarisation curve and loss of polarisation resistance i.e. dissolution of the passive layer.
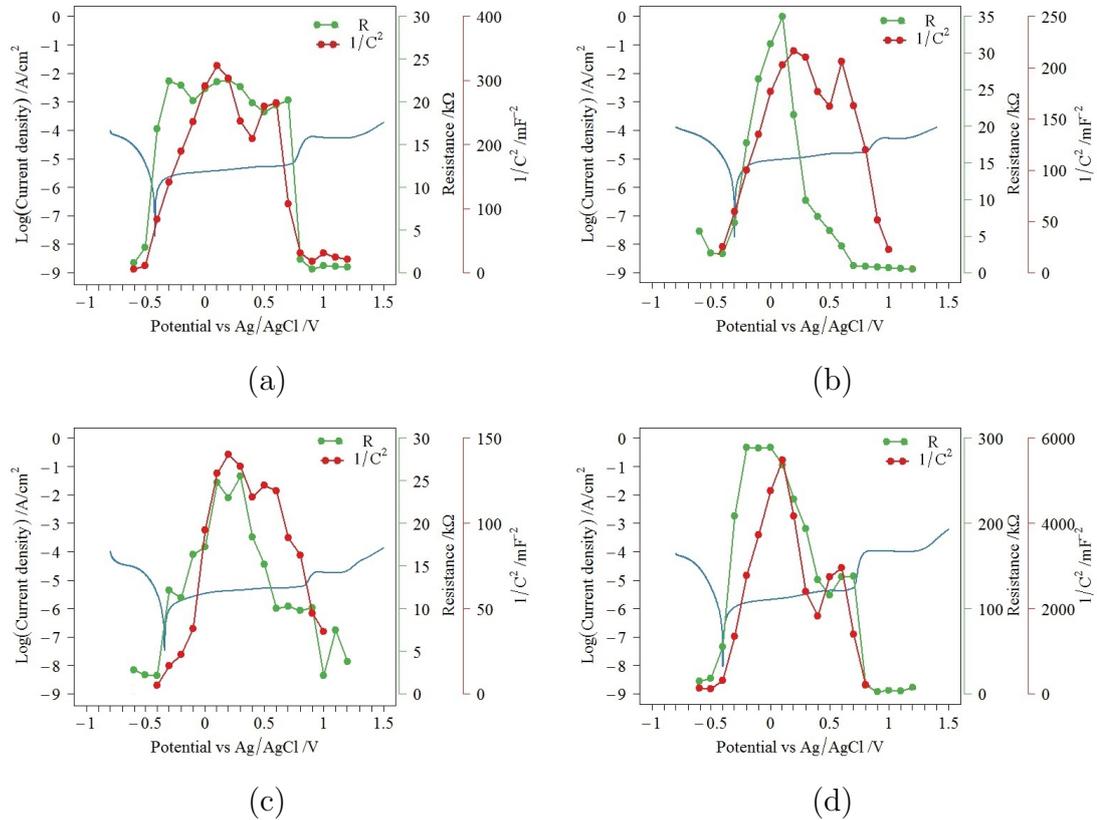
Figure 5.25: Electrochemical impedance spectroscopy analysis of (a) 304H SS aged for 48 hours at 600 °C, (b) 304H SS aged for 72 hours at 600 °C, (c) unsensitised 304H SS and (d) heat treated 20/25/Nb SS in dosed simulant pond water, pH≃11.4 at 24 °C, specifically potentiodynamic polarisation curve overlaid with polarisation resistance data (green) and capacitance data (red), in the form of a Mott-Schottky plot, extracted from the Nyquist plots.

From inspection of Figure 5.25(b), 304H SS aged for 72 hours can be considered to be corroding at potentials ≤-0.4 and ≥0.6 V due to the low R_p values and passivated for potentials -0.4 to 0.3 V due to increased R_p values. The behaviour is reminiscent of the resistance of pure iron as shown in Figure 3.16. Therefore, a substantial portion of the passive layer is expected to be formed of iron oxide for this sample. This point will be returned to below.

Considering the C^{-2} vs E plot for the 304H SS aged for 72 hours shown in Figure 5.25(b), the plot can again be split into four regions; -0.5 to 0.2 V (apparent

n-type), 0.2 to 0.5 V (p-type), 0.5 to 0.6 V (n-type) and 0.6 to 1 V (apparent p-type). Once again, the apparent n-type character of region I corresponds to the growth of a passive layer dominated by Fe_2O_3 and/or the elimination defect therein. This is consistent with the R_p data which shows region I to coincide with the increases in R_p. The p-type behaviour observed in region II is indicative of the protection afforded by Cr_2O_3. In region III the oxidation of Cr(III) to Cr(VI) occurs indicated by n-type semiconductor behaviour. In region IV the capacitive behaviour shows p-type character, this corresponds to the dissolution of the passive layer. This is in agreement with the R_p data which shows a gradual drop in resistance over this range and the polarisation curve which exhibits transpassive behaviour.

To obtain a clearer picture of the effects of the heat treatment of SS on passive layer formation, it is necessary to compare Figure 5.25(a) and 5.25(b) to Figure 5.25(c), where the R_p values of unsensitised 304H SS are shown.

Beginning with the data for the unsensitised steel shown in Figure 5.25(c), two main features are seen in the R_p vs E plot – a broad peak centred at $\sim$0.2 V and a low R_p plateau extending from 0.5 to 0.8 V. These have previously attributed these to the presence of a mixture iron and chromium oxide/oxyhydroxides and an iron-chromium spinel respectively in section 5.1.2.

Turning now to Figure 5.25(b), the data for the sample that has experienced the longest heat treatment of 72 hours at 600 °C it can be seen, as noted above, that the R_p vs E plot now strongly resembles that of the analogous plot for pure iron – an observation consistent with the expectation that this heat treatment will result in chromium depletion from the steel surface. More specifically there is a loss of protection at potentials <-0.2 V and >0.3 V compared with the unsensitised sample.

In the context of these two extremes, the data of Figure 5.25(a), recorded from the sample that has undergone a shorter period of heat treatment (i.e. 48 hours), can now be regarded as being an intermediate case wherein the chromium oxide

component of the compound peak has diminished leaving the iron component to dominate. As well, the spinel feature at 0.5 to 0.8 V, absent in Figure 5.25(b) can still be seen – suggesting that the heat treatment of 5.25(a) is not strong enough to deplete this i.e. Cr in the spinel phase is more stable than chromium in the oxide/hydroxide phase. This is consistent with the relative placement of the chromium oxide and spinel oxidation features in the voltammetry.

Consider the trend in R_p with potential for heat treated 20/25/Nb SS and for heat treated 304H SS (Figure 5.25 (d) compared to 5.25 (a) and (b)). 304H aged for 48 hours and heat treated 20/25/Nb SS have the same passive range. However, the peak centred at 0 V is a more dominant feature for heat treated 20/25/Nb SS perhaps this is due to the greater Cr oxide concentration of the 20/25/Nb SS sample (seen in the XPS results of Figure 5.21). The passive range of 304H SS aged for 72 hours is 0.3 V shorter than for the other two heat treated samples. This suggests that of the three analogues for RIS-affected cladding the 304H SS sample aged for 72 hours is the most susceptible to corrosion.

Comparing the capacitance data for the three 304H SS samples, the explanations for regions I to III are the same for each sample. The potentials at which they switch semiconductor type is however altered slightly. The apparent n-type behaviour of region I occurs between -0.5 and 0.2 V for unsensitised 304H SS and the sample aged for 72 hours but this region is 0.1 V shorter for the sample ages for 48 hours (i.e. -0.5 – 0.1 V). Unfortunately, this does not reveal much about the effect of heat treatment on corrosion behaviour other than for the sample aged for 72 hours the potential range over which Fe oxide (n-type behaviour) is slightly extended compared to the other heat treated sample. This once again confirms the greater depletion of Cr from the grain boundaries of this sample.

The trend in capacitance of heat treated 20/25/Nb SS and that of the 304H SS aged for 48 hours and 72 hours are the similar and thus offers no real comparative insight.

5.2.4 Effect of Chloride Concentration on the Corrosion Behaviour of Heat Treated 304H Stainless Steel Samples

In order to investigate the durability of the passive oxide layer formed on heat treated 304H SS the effect of increasing the concentration of chloride in the absence and presence of the NaOH corrosion inhibitor is examined. Figure 5.26 shows the resultant polarisation curves for the two heat treated 304H SS samples.

(a)   (b)

(c)   (d)
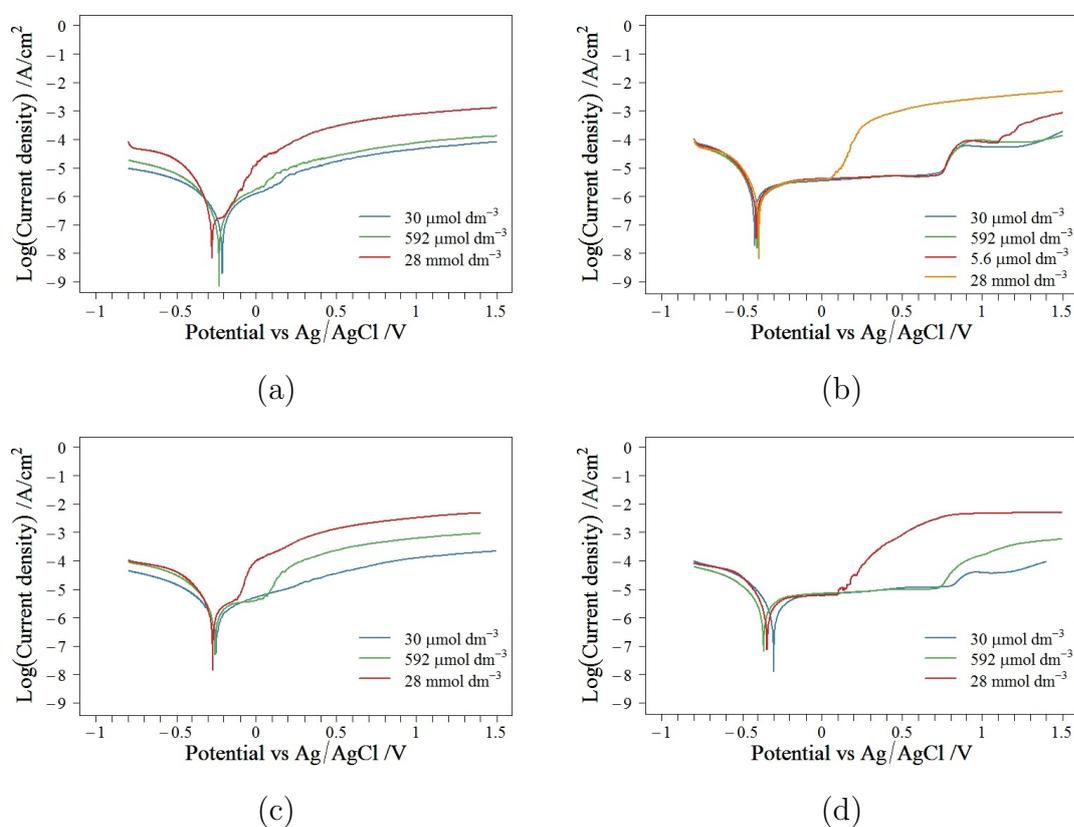
Figure 5.26: Potentiodynamic polarisation curves demonstrating the effect of increasing chloride concentration at 24 °C on the corrosion behaviour of heat treated 304H SS. The sample aged for 48 hours at 600 °C (a) in undosed simulant pond water pH$\simeq$8 and (b) in dosed pond water pH$\simeq$11.4. The sample aged for 72 hours at 600 °C (c) in undosed simulant pond water pH$\simeq$8 and (d) in dosed simulant pond water pH$\simeq$11.4.

Figure 5.26(a) shows polarisation curves for 304H SS aged for 48 hours in undosed simulant pond water with increasing Cl$^-$ concentrations. The behaviour seen is comparable to the behaviour of pure iron in chloride solutions, as shown in

Figure 5.10(b) where there is a cathodic shift in the onset of transpassivity and an increase in transpassive corrosion currents with increasing chloride concentration. There is almost no evidence for the presence of a protective layer at the electrode surface in the polarisation curve recorded at chloride concentrations greater than 592 μmol dm^{-3} and corrosion of the surface is likely to proceed uninhibited.

Figure 5.26(c) shows polarisation curves for 304H SS aged for 72 hours in undosed simulant pond water with increasing Cl$^-$ concentrations. There is a similar trend with increasing Cl$^-$ concentration to that observed for the sample aged for 48 hours with shifting transpassive onset and increased transpassive currents. However, there is still some protection evident over a very limited potential range at 28 mmol $^{-3}$ Cl$^-$ but due to the size of the passive potential window it is unlikely that the surface will be adequately protected.

Both heat treated 304H SS samples behave similarly to unsensistised 304H SS in undosed simulant pond water containing increasing amount of chloride. For all three samples a cathodic shift in the onset of transpassivity and an increase in transpassive currents with increasing chloride concentration is observed, see Figure 5.10 for comparison.

The polarisation curves of both heat treated 304H SS samples show that they offer less corrosion protection than the heat treated 20/25/Nb SS sample in undosed pond water containing increased Cl$^-$ concentrations, Figure 4.12. This is presumably due to the lower Ni content of 304H SS and/or more enhanced Cr depletion at the grain boundaries.

The effect of Cl$^-$ concentration in simulant pond water dosed to pH$\simeq$11.4 on the corrosion behaviour of heat treated 304H SS is shown in Figure 5.26(b) and Figure 5.26(d). A Cl$^-$ concentration of 28 mmol dm^{-3} is necessary to cause a significant cathodic shift in the onset of transpassivity for both samples. Even at this concentration passivation is possible over a short potential range which is not the case for samples in undosed water. The passive window extends from <0.1 V and $\sim$0.2 V to 0.5 V and 0.4 V respectively for the sample aged for 48 hours and

that aged for 72 hours. The corrosion inhibition offered by NaOH is clear.

For heat treated 304H SS samples only half the Cl^- concentration is required to cause a similar cathodic shift in the breakdown potential as that seen for unsensitised 304H SS (Figure 5.11). Evidently heat treatment of 304H SS causes changes to the passive layer resulting in an increased susceptibility to corrosion, leaving these samples more vulnerable to localised corrosion than their unsensitised counterpart.

Again, heat treated 304H SS is compared with heat treated 20/25/Nb SS in dosed pond water containing Cl^-, Figure 4.13. From this it can be seen that, to produce the same magnitude cathodic shift in breakdown potential, it takes twenty times as much chloride for heat treated 20/25/Nb SS ($[Cl^-]{\simeq}560$ mmol dm^{-3}) than heat treated 304H SS ($[Cl^-]{\simeq}28$ mmol dm^{-3}). In comparison with unsensitised 20/25/Nb SS, none of these three heat treated samples exhibit a continuous sequence of small pitting features as the potential applied to the electrode is increased; rather, they all exhibit the same abrupt onset of a large increase in current density previously associated with significant mass loss from the surface, indicating an inability of these samples to shut down pitting and/or other localised corrosion events. At $[Cl^-]{\simeq}28$ mmol dm^{-3} the three samples have similar transpassive currents. There are also indications that the secondary process seen for heat treated 20/25/Nb SS is also occurring for the heat treated 304H SS. This secondary process is attributed to the formation of hexochloroferic ions (see section 4.4 for relevant discussion).

5.2.5   Effect of Temperature Variation on the Corrosion Behaviour of Heat Treated 304H Stainless Steel Samples

Due to the future expected increase of operating temperature of interim storage ponds, the effect of temperature variation on the corrosion behaviour of heat treated 304H SS was investigated. Figure 5.27 shows the polarisation curves

obtained for the four temperatures of interest, 24, 45, 60 and 90 °C.

(a)

(b)

(c)

(d)
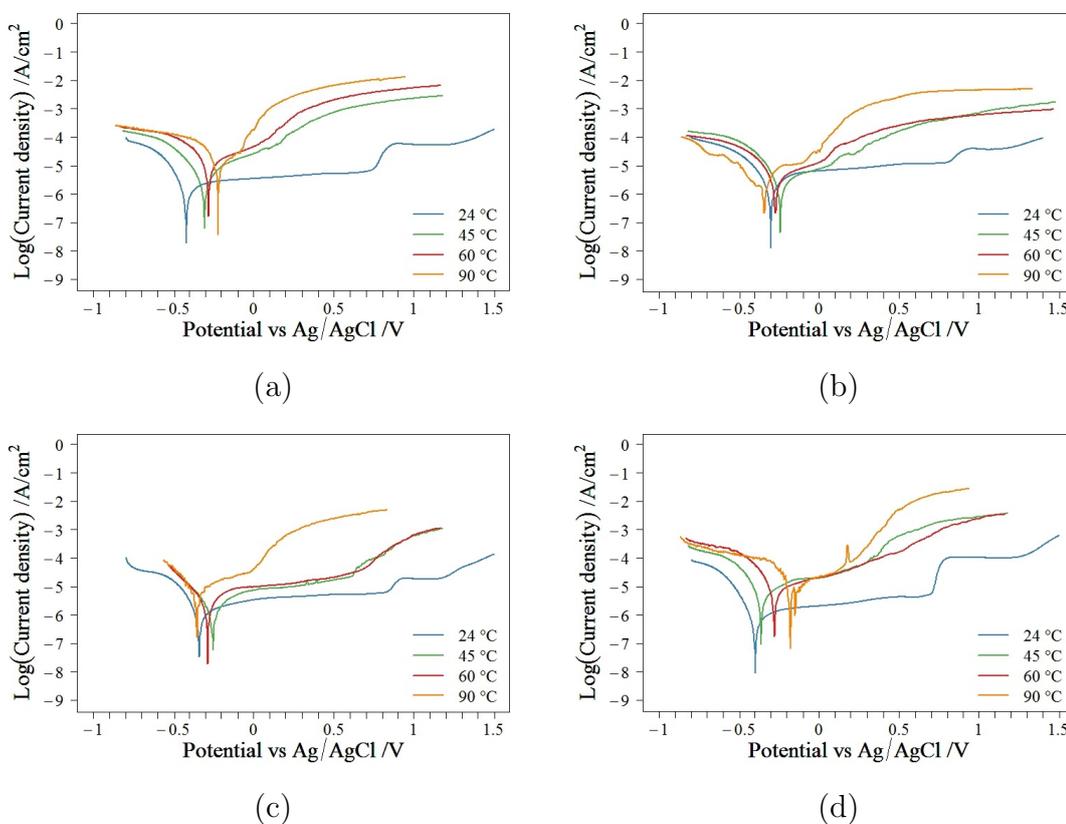
Figure 5.27: Potentiodynamic polarisation curves demonstrating the effect of increasing simulant pond water, 30 μmol dm^{-3} Cl$^-$, pH$\simeq$11.4 at 24 °C, temperature on the corrosion behaviour of 304H SS, (a) sample aged for 48 hours at 600 °C, (b) sample aged for 72 hours at 600 °C and (c) unsensitised, and (d) heat treated 20/25/Nb SS.

For the sample aged for 48 hours there are several noticeable trends with increasing temperature. E$_{ZC}$ increases with increasing temperature. The general corrosion currents increase as the temperature rises from 24 to 60 °C. There is also a movement in the onset of transpassivity in the cathodic direction as the temperature rises.

For 304H SS aged for 72 hours, there is a less significant increase in general corrosion current with increasing temperature compared with the 304H SS sample aged for 48 hours. E$_{ZC}$ does not show a clear trend with rising temperatures. However, there is a marked decrease in the breakdown potential as the temperature of the simulant pond water goes from 24 to 90 °C.

The reduction in corrosion resistance for temperatures $\geq$45 °C is undeniable

for both heat treatments, with the passive potential range being considerably diminished. As stated before in section **??**, this is due to the formation of a porous surface layer most likely of similar composition to that observed in the XPS analysis at 24 °C [28, 30, 35, 211] and the increased solubility of the stainless steel oxidation products at elevated temperatures.

The OCPs for all 304H SS samples are presented in Table 5.2. The heated treated 20/25/Nb SS OCPs are presented here also for the interest of the reader, see section 4.5 for relevant discussion. Despite the significantly diminished passive range, the OCPs at ≤60 °C lie at potentials where a passive layer is expected to grow on the surface for all 304H SS samples. However, at 90 °C, whilst the OCP for the unsensitised 304H sample lies at a potential where a passive layer is expected to grow, the same is not true for the both of the heat treated 304H samples, with the OCPs lying in the transpassive region where the uninhibited dissolution of the samples can proceed. Thus, heat treated 304H immersed in dosed pond water at this temperature would be expected to corrode freely – a finding that may have implications for the stability of RIS-affected steels under this accident condition.

Sample	**24 °C**	**45 °C**	**60 °C**	**90 °C**
Unsensitised 304H SS	-0.19	-0.14	-0.09	-0.15
304H SS heat treated for 48 hours at 600 °C	-0.16	-0.13	-0.12	-0.1
304H SS heat treated for 72 hours at 600 °C	-0.2	-0.18	-0.15	-0.12
Heat treated 20/25/Nb SS	-0.1	0.04	0.1	-0.13

Table 5.2: Open circuit potentials for 304H SS samples and heat treated 20/25/Nb SS in simulant pond water at the four temperatures of interest, 24, 45, 60 and 90 °C. All potentials are quoted as V vs Ag/AgCl.

The impact of heat treatment on corrosion susceptibility is explored by examining the differences between the effect of solution temperature increases on unsensitised 304H SS (Figure 5.12) and thermally aged 304H SS. For temperatures ≥45 °C there is a large shift in the breakdown potential towards more negative values for the heat treated samples compared with the unsensitised stainless steel. Therefore, there is a greatly reduced region of

passivity in the polarisation curves of heat treated stainless steels. At 45 and 60 °C the general corrosion currents of 304H SS aged for 48 hours at 600 °C are greater than those of the unsensitised stainless steel. An increased susceptibility to corrosion at elevated temperatures for thermally aged 304H SS compared to its unsensitised counterpart is evident.

Figure 5.27(d) shows the effect of increasing simulant pond water temperature on the corrosion behaviour of heat treated 20/25/Nb SS. It is possible to compare both of the heat treated 304H SS samples with heat treated 20/25/Nb SS. The general corrosion currents are similar for the heat treated 304H SS and heat treated 20/25/Nb SS samples. However, the passivation of heat treated 20/25/Nb SS occurs over a wider potential range. The metastable pit evident at 90 °C for heated treated 20/25/Nb SS, attributed to chromium electrochemistry, is not present in the polarisation curves of the heat treated 304H SS electrodes. This may be because the breakdown of the passive film on heat treated 304H SS at this temperature is $\sim$0 V and therefore, the chromium oxide in the protective layer never experiences the high potentials associated with pitting behaviour.

5.2.6 Effect of Hydrogen Peroxide Concentration in the Aqueous Phase on the Corrosion Behaviour of the Heat Treated 304H Stainless Steel Samples

As stated previously the addition of H_2O_2 to simulant pond water can be used to mimic the effects of radiolysis on the corrosion behaviour of stainless steels. As such, this section discusses the influence of H_2O_2 on heat treated 304H SS under storage conditions.

5.2.6.1   Effect of Hydrogen Peroxide Concentration in Simulant Pond Water on the Corrosion Behaviour of Heat Treated 304H Stainless Steel

The impact of H_2O_2 concentration on the electrochemical behaviour of heat treated 304H SS (aged for 48 hours at 600 °C) is shown in Figure 5.28. Increases in H_2O_2 concentration causes the following changes to the polarisation curves of heat treated 304H SS. As the H_2O_2 concentration rises there is an increase in E_{ZC}, an increase in general corrosion currents, an initial increase in transpassive currents and a shift in the onset of transpassivity, and an in-growth of a wave from ~ 0.2 V. As with the previously analysed SS samples the peak can be attributed to the oxidation H_2O_2 at the surface of the stainless steel via an absorption process (see section 3.5.1). The initial shift in the onset of transpassivity is also observed for unsensitised 304H SS, which has previously been attributed to changes in the metal oxide layer via oxidation - more specifically the enhanced oxidation rate of spinels in the presence of peroxide compared with their oxidation rate in the absence of peroxide, see section 5.1.6.1 for relevant discussion.
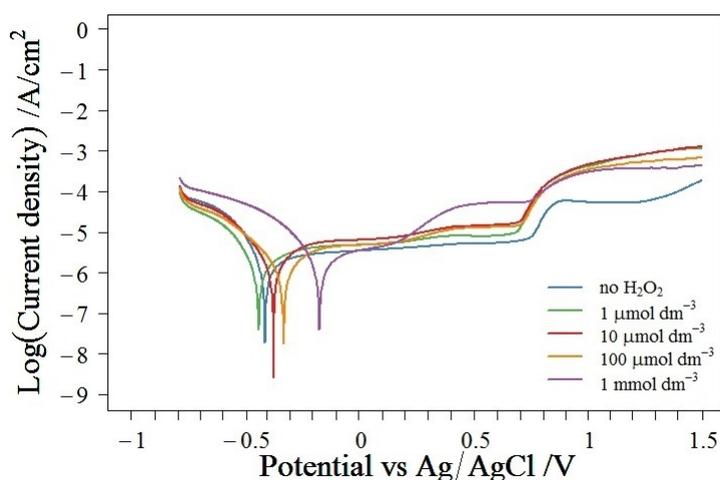
Figure 5.28: Effect of hydrogen peroxide concentration on the corrosion behaviour of heat treated 304H SS (aged for 48 hours at 600 °C) in simulant pond water, 30 μmol dm^{-3} Cl$^-$, pH$\simeq$11.4 at 24 °C.

5.2.6.2 Effect of Temperature in the Presence of Hydrogen Peroxide in Simulant Pond Water on the Corrosion Behaviour of Heat Treated 304H Stainless Steel

Figure 5.29 shows the polarization curves of heat treated 304H SS (Figure 5.29(a) aged for 48 hours at 600 °C and Figure 5.29(b) aged for 72 hours at 600 °C) at 24, 45, 60 and 90 °C in hydroxide dosed simulant pond water containing 10 μmol dm^{-3} H$_2$O$_2$. For both samples, E$_{ZC}$ shifts in the anodic direction as the pond water temperature increases. Above 45 °C the breakdown potential moves in the cathodic direction. Hence, the width of the passive range decreases with increasing temperature. At 90 °C pitting corrosion occurs throughout the passive region of both heat treated steels and samples are vulnerable to localised attack across the entire potential range.

(a)   (b)
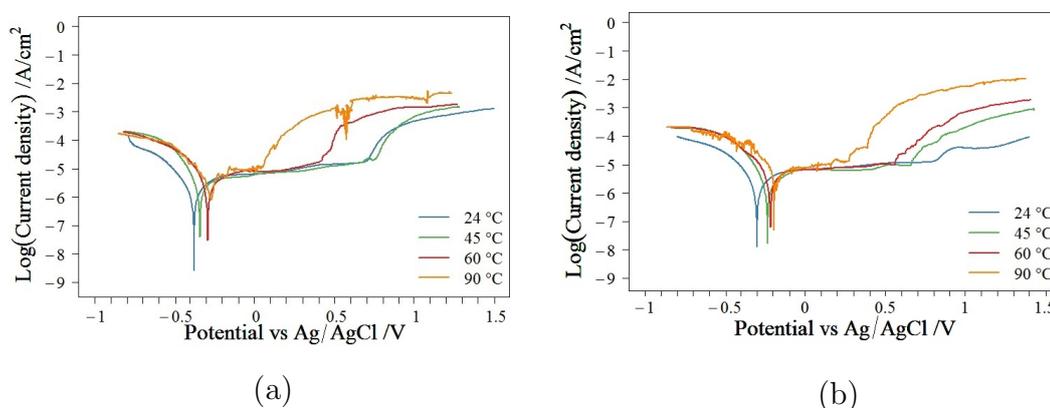
Figure 5.29: Effect of increasing temperature on the corrosion behaviour of heat treated 304H SS ((a) aged for 48 hours at 600 °C and (b) aged for 72 hours at 600 °C) in simulant pond water, pH$\simeq$11.4 at 24 °C, containing [H$_2$O$_2$]$\simeq$10 μmol dm^{-3} and 30 μmol dm^{-3} Cl$^-$.

Differences and similarities in corrosion behaviour in the presence and absence of H$_2$O$_2$ at elevated temperatures can be seen by comparing Figure 5.27(a) and Figure 5.29(a), and Figure 5.27(b) and Figure 5.29(b). First considering 304H SS aged for 48 hours, the general corrosion currents are significantly reduced in the presence of H$_2$O$_2$. However for 304H SS aged for 72 hours, the general corrosion currents are similar in the presence and absence of peroxide. For both samples, the

onset of transpassive behaviour occurs at higher potentials when H_2O_2 is present and in both the absence and presence of H_2O_2 E_{ZC} becomes more positive with increasing temperature.

As with 20/25/Nb SS samples and unsensitised 304H SS samples, there are obvious benefits from H_2O_2 production on the corrosion susceptibility of heat treated 304H SS. The increased corrosion resistance at elevated temperatures in the presence of peroxide is unmistakeable. The improved protection observed in the peroxide environment may be a result of reduction by H_2O_2 of soluble $Cr(VI)$ to insoluble $Cr(III)$, most likely as $Cr(OH)_3$; or the oxidation by H_2O_2 of soluble $Fe(II)$, to form a $Fe(OH)_3$ precipitate. Also, the decrease in pH with increasing temperature is compensated for by the decomposition of H_2O_2 to OH^- which in turn would aid in precipitation of Cr or Fe hydroxides onto the surface of the SS.

Comparisons between the corrosion behaviour of heat treated 304H SS and heat treated 20/25/Nb SS, Figure 4.16(a), in the presence of peroxide at elevated temperatures can be made. Firstly, there is no increase in the general corrosion currents of heat treated 304H SS with temperature, however uniform corrosion rates are temperature dependent for heat treated 20/25/Nb SS. The shift in the onset of transpassivity with temperature is more prominent on the heat treated 304H SS sample, this may be due to greater precipitation of $Fe(OH)_3$ on the surface of 304H SS due to its higher Fe content.

5.2.7   Conclusions

Heat treated 304H SS was used as an analogue for RIS-affected AGR fuel cladding. The corrosion behaviour of two heat treated 304H SS samples under possible storage pond conditions was examined in this section, one sample heated for 48 hours at 600 °C and one heated for 72 hours at 600 °C. The principal conclusions of this section are as follows.

The OCP in simulant pond water (pH$\simeq$11.4) is found to be $\sim$-0.16 V vs Ag/AgCl and $\sim$-0.2 V vs Ag/AgCl for the sample heated for 48 hours at 600 °C

and the sample heated for 72 hours at 600 °C respectively. Under these conditions, XPS data for the sample aged for 48 hours indicates that the protective oxide layer formed on the surface of heat treated 304H SS consists predominately of Fe and Cr oxides/hydroxides, with Fe oxide/hydroxides being the far more dominant of the two. Resistance and capacitance data from EIS experiments shows that the source of this protection changes on application of an oxidative stress i.e. as the electrode potential is increased. Through Mott-Schottky analysis it was found that this change occurs at $\sim$0.1 V and 0.2 V for the sample aged for 48 hours and the sample aged 72 hours respectively, whereupon the protection provided by Fe oxides decreases due to its oxidative dissolution and Cr oxides dominate until 0.6 V.

Voltammetric studies were used to determine the robustness of this oxide layer. Studies under baseline conditions of pH=8 at 24 °C show a short region of passivity from $\sim$-0.2 V vs Ag/AgCl to $\sim$0.2 V for both heat treated sample. However, at pH 11.4 the window of passivity is extended to $\sim$-0.4 V to 0.75 V and $\sim$-0.3 V to 0.85 V for the sample aged for 48 hours and the sample aged 72 hours respectively – indicating that simple dosing of the system with NaOH provides significant added corrosion protection for heat treated 304H SS samples under these conditions. This protection is maintained at pH 11.4 at 45 °C in the presence of 30 μmol dm^{-3} of both Cl$^-$ and H$_2$O$_2$, i.e. under future interim storage conditions, with a separation of approximately a volt between the E$_{ZC}$ and onset of transpassivity and as E$_{OCP}$ lies within this passive range intergranular attack is unlikely.

The extent of the envelope of this protection was studied as a function of key solution parameters such as chloride concentration, temperature and hydrogen peroxide concentration – including conditions relevant to future wet storage scenarios and their fault conditions. Results may be summarised as follows.

With respect to chloride concentration:
In the absence of hydroxide, pH$\simeq$8, there is minimal passive protection from

chloride ions from concentrations as low as 30 μmol dm^{-3}. At [Cl$^-$]$\geq$28 mmol dm^{-3} there is no evidence of passivation thus the surface is expected to corrode freely. Dosing the simulant pond water to pH$\simeq$11.4 increases both heat treated samples resistance against localised corrosion. Chloride concentrations of $\sim$28 mmol dm^{-3} are necessary to cause a cathodic shift in the breakdown potential. This is a significantly higher chloride concentration than expected under foreseen fault conditions, indicating that protection will be maintained under such.

With respect to temperature:

Increases in the simulant pond water temperature result in heat treated 304H SS becoming less corrosion resistant. The passive range of both heat treated 304H SS samples is significantly reduced at temperatures $\geq$45 °C. Despite the reduction in passivity at temperatures $\leq$60 °C the OCPs values lie in the passive region. Thus, leading to the belief that under the anticipated operating conditions no localised corrosion would be expected. At 90 °C the OCPs lie in the transpassive region where the uninhibited dissolution of the samples can proceed.

With respect to hydrogen peroxide concentration:

Voltammetry suggests that, as is the case for 20/25/Nb SS and unsensitised 304H SS, H_2O_2 is simply oxidised by the surface of heat treated 304H SS in the passive potential range. Oxidation of peroxide at the steel surface is controlled by a surface adsorption process. The addition of hydrogen peroxide to simulant pond water at between 45 - 90 °C causes the passive range to extend. Evidently the stainless steel has been afforded protection by the peroxide. However, at 90 °C pitting corrosion is observed in the passive region and therefore the SS surface will vulnerable to localised attack under this accident condition.

Comparison to unsensitised 304H SS:

Heat treated 304H SS is more susceptible to general corrosion, pitting and transpassive corrosion than its unsensitised counterpart. This is suspected to be largely due to the depletion of chromium from the grain boundaries during heat treatment, this results in the formation of an inhomogeneous passive layer with

reduced Cr oxide/hydroxide content leaving the heat treated samples more vulnerable to corrosion.

Comparison to heat treated 20/25/Nb SS:

Comparing the behaviour of heat treated 304H SS to heat treated 20/25/Nb SS some further conclusions can be drawn. Generally, although heat treated 20/25/Nb SS exhibited less pitting susceptibility than unsensitised 20/25/Nb SS it is still more susceptible to this type of corrosion than heat treated 304H SS. This could indicate that perhaps not all of the NbC pitting centres were dissolved during heat treatment as previously alluded.

Heat treated 304H SS was more susceptible, than heat treated 20/25/Nb SS, to transpassive dissolution under the same experimental conditions. This indicates an inability of heat treated 304H samples to shut down pitting and/or other localised corrosion events compared with heat treated 20/25/Nb SS. This is possibly a result of the much lower Ni content of 304H SS and/or the lower contribution of Cr(III) oxide/hydroxide to the passive layer observed via XPS analysis.

Chapter 6

Uranium Dioxide and Simulated AGR Spent Nuclear Fuel

Chapters 3 to 5 have focused on the corrosion behaviour of AGR fuel cladding and cladding analogues. Cladding is the primary means of containment for radioactive release and thus is of high importance when considering the integrity of the fuel pins. However, in the unlikely event that the fuel cladding is perforated during interim storage the spent fuel itself will become exposed to the pond water. This chapter aims to establish a comprehensive understanding of the surface evolution of UO_2 spent fuel to support the fuel storage safety case. This is achieved by investigating the electrochemical corrosion behaviour of uranium dioxide and simulated AGR spent nuclear fuel, SIMFuels, under various conditions relevant to wet interim storage. Two SIMFuels have been used in this study, one with a simulated burn-up of 25 GWd/tU and one with a simulant burn-up of 43 GWd/tU. The composition and properties of these SIMFuels can be found in section 2.1.3.

6.1   Raman Spectroscopy of Uranium Dioxide and AGR SIMFuels

Firstly, raman spectroscopy has been used to characterise the composition and structure of UO_2 and AGR SIMFuels. Raman spectra of the three polished samples, UO_2 and two SIMFuels, can be seen in Figure 6.1. These spectra are an average of 20 spectra taken randomly across the surface of each sample, taking care to avoid precipitates. Pure UO_2 has two peaks, one prominent peak at 445 cm^{-1} and one weaker peak at ~1200 cm^{-1}. The former is due to the fundamental U-O stretch and the later to the first overtone of a longitudinal optical phonon at 575 cm^{-1}. The 575 cm^{-1} peak is barely visible since it is selection rule forbidden under the lattice symmetry of pure UO_2. The 445 cm^{-1} peak decreases within increased simulated burn-up indicating a departure from the perfect fluorite lattice structure due to either non-stoichiometry or dopant defects [106]. A broad peak between 500 and 700 cm^{-1} is evident in the spectra of the two SIMFuel samples. This peak is asymmetric and therefore likely to be a set of contiguous bands.
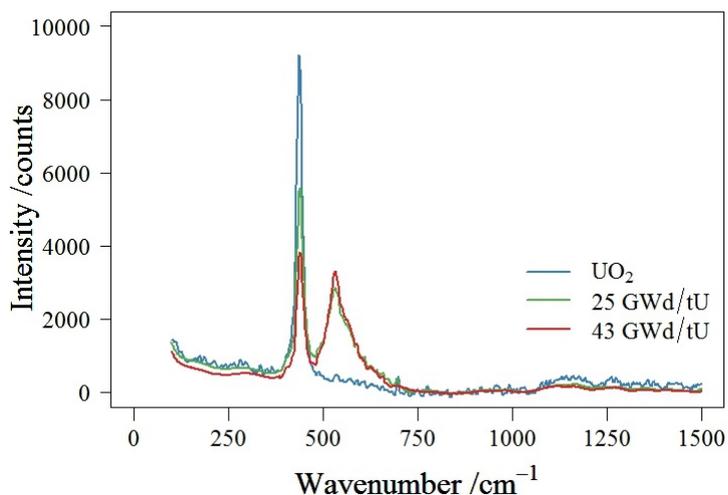
Figure 6.1: Raman spectra for UO_2, 25 GWd/tU and 43 GWd/tU SIMFuel, laser wavelength 633 nm.

Using Lorentzian peak fitting it is possible to deconvolve the second peak of the Raman spectra of the SIMFuel samples into three separate peaks at 530, 570

and 630 cm^{-1}. Firstly, an initial linear baseline correction over the range 350-700 cm^{-1} was performed, the wavelength limits of the correction chosen as being those closest to the peak whilst still exhibiting no associated change in absorbance with increasing simulated burn-up.

Following the baseline correction, peak wavenumbers were found by finding the first derivative of the data and plotting the first derivative as a function of increasing wavenumber. A peak in the original spectrum has a downward-going zero-crossing at the peak maximum. Then, an iterative least-squares fit of a multiple unconstrained Lorentzian fit was carried out at the obtained wavenumbers. Figure 6.2 shows the deconvolved bands. Interpretation of these peaks through literature and experimental analysis was carried out by Wilbraham [243]. A brief explanation for the presence of each of these peaks is given here:

1. The 530 cm^{-1} peak: Raman measurements of lanthanide doped UO_2 show a peak between 530 and 540 cm^{-1} and this peak grows with increasing lanthanide content [138, 244–246]. Therefore, this peak is attributed to a local phonon mode related to oxygen-vacancy induced lattice distortion [244–246]. These oxygen vacancies are generated to charge compensate for the presence of 3+ lanthanide dopants [138]. As seen from Table 2.3, which reports the composition of these SIMFuels, as the simulated burn-up increases there is a marked increase in lanthanide concentration. As expected this peak is larger for the 43 GWd/tU than for the 25 GWd/tU.

2. The 570 cm^{-1} peak: Oxygen-vacancy sites, defect clustering and hyperstochiometry cause the structure of UO_2 to deviate from the perfect fluorite structure [101, 106]. This results in the breakdown of selection rules and the formation of a peak at 570 cm^{-1}. As the structure becomes more hyperstoichiometric and transformation to a tetragonal structure begins there is an associated decrease in this peak. Figure 6.2 shows a small

increase in this peak with increased simulated burn-up of the SIMFuels. This is attributed to the introduction of lanthanides resulting in an increased number of oxygen-vacancy sites [246]. Hyperstochiometry is unlikely to be the cause for reasons highlighted in the following point.

3. The 630 cm^{-1} peak: This peak exists due to the presence of hyperstoichiometry in the UO$_2$ lattice and the formation of U$_4$O$_9$ [101, 106, 246, 247]. Increases in hyperstochiometry should result in growth of this peak. Curiously, for the SIMFuel samples examined here, the 630 cm^{-1} peak decreases slightly with increased burn-up. A possible explanation for this is that at high dopant levels the number of oxygen vacancies is diminished and these vacancies are needed for the incorporation of oxygen interstitials [138]. However, due to its weak intensity, interpretation of this peak should be considered with caution.
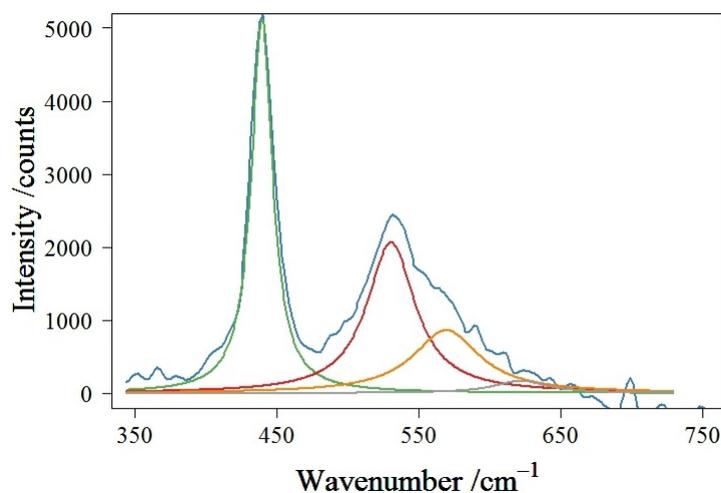
(a)
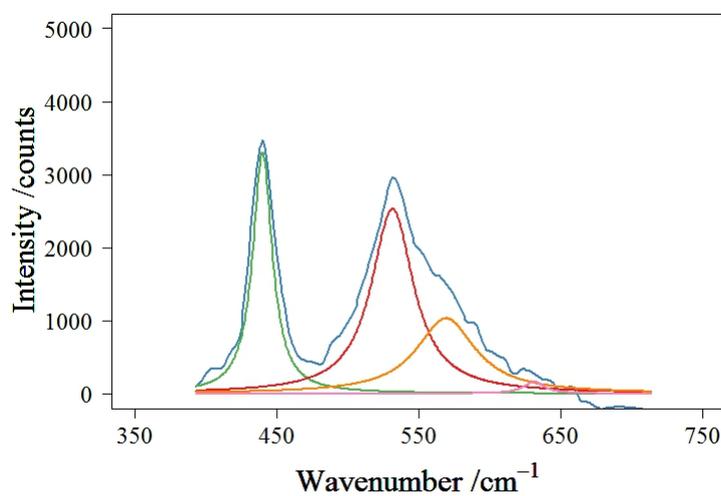
(b)

Figure 6.2: Lorentzian peak fit of Raman spectra for 25 GWd/tU and 43 GWd/tU SIMFuel.

6.2 Behaviour of Uranium Dioxide and AGR SIMFuels in 0.5 mol dm^{-3} Sodium Sulphate

To establish the baseline electrochemical behaviour of these samples, CV experiments were carried out on the UO$_2$ and the two SIMFuel samples in 0.5 mol dm^{-3} Na$_2$SO$_4$, pH$\simeq$5.6. The resulting CVs are shown in Figure 6.3 from which it can be seen that the forward scans of each sample have three common peaks/regions. From the literature [248, 249] the origin of these peaks, designated

as peaks I to III with increasing applied potential, can be assigned as follows:

- Peak I: oxidation of UO$_2$ to UO$_{2+x}$ at the grain boundaries;

- Peak II: oxidation of the bulk UO$_2$ matrix to UO$_{2+x}$ with incorporation of O$_2^-$ ions into the lattice until a limiting stoichiometry of UO$_{2.33}$ is attained;

- Peak III: oxidation of UO$_{2+x}$ to a U(VI) species such as soluble UO$_2^{2+}$ or insoluble UO$_3 \cdot$yH$_2$O [62].
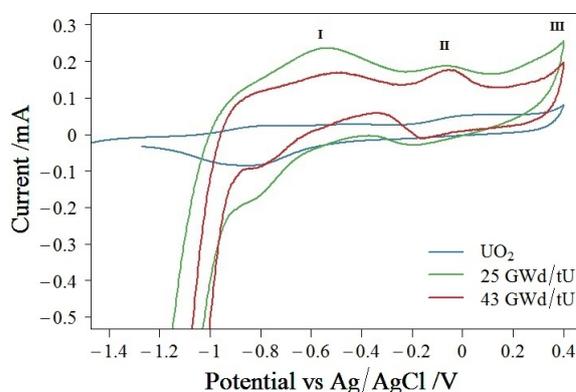
Figure 6.3: Cyclic Voltammetry of UO$_2$, 25 and 43 GWd/tU SIMFuels in 0.5 mol dm^{-3} Na$_2$SO$_4$, pH$\simeq$5.6.

It has been previously reported in work on LWR SIMFuels that the addition of lower valence species, such as trivalent rare earths, causes an increase in the conductivity of the UO$_2$ bulk matrix allowing for the passage of higher electrochemical currents though LWR SIMFuels than pure UO$_2$ [99]. It can be seen from the CV results of Figure 6.3 that AGR SIMFuels behave in a similar fashion.

However, the currents associated with the higher burn-up SIMFuel, 43 GWd/tU, are unexpectedly lower than those of the 25 GWd/tU sample. It has been suggested by He *et al.* that doping at higher lanthanide levels may stabilize the fluorite lattice against anodic oxidation and dissolution by decreasing the amount of vacancy sites free for O$_2^-$ incorporation [135] and it may be this stabilization that is responsible for the suppressed oxidation currents observed from the 43 GWd/tU sample compared to the 25 GWd/tU sample in Figure 6.3.

At potentials lower than $\sim$-1 V, there is a distinct change in behaviour between the UO$_2$ and SIMFuel samples. There is a clear enhancement of the hydrogen evolution process on the SIMFuels compared to the undoped UO$_2$ sample. This results from hydrogen dissociation being catalysed by the noble metals present in the SIMFuels [142, 250].
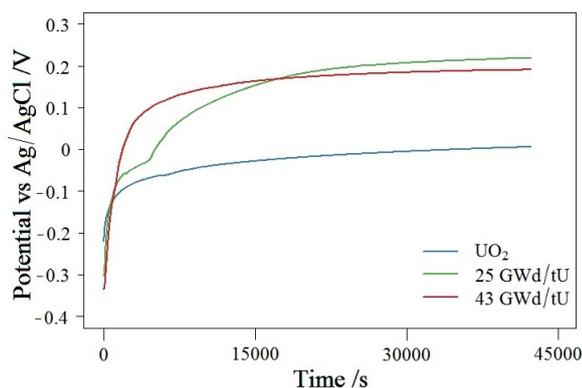
Figure 6.4: Open Circuit Potential measurements of UO$_2$, 25 and 43 GWd/tU SIMFuels in 0.5 mol dm^{-3} Na$_2$SO$_4$, pH$\simeq$5.6.

The OCPs for the UO$_2$, 25 GWd/tU and 43 GWd/tU samples in 0.5 mol dm^{-3} Na$_2$SO$_4$ are observed to be 0.01 V, 0.22 V and 0.19 V respectively as shown in Figure 6.4. If these values are compared to their positions on their respective CV in Figure 6.3, it is seen that the OCP of pure UO$_2$ sits on the anodic side of the current-voltage peak associated with the onset of the UO$_2$ to UO$_{2+x}$ oxidation process. However, the OCPs of both SIMFuel samples are situated at the onset of the third peak/region where a U(VI) species is developing. Inspection of Pourbaix diagrams for the uranium-H$_2$O system (Figure 6.5) reveals that the OCPs of the SIMFuels in the pH$\simeq$5.6 Na$_2$SO$_4$ solution used in the experiments of Figures 6.3 lie in the potential region where the dissolution as UO$_2^{2+}$ is expected to begin [29]. This indicates that under neutral broadly non-corrosive, non-complexing conditions SIMFuels have a greater susceptibility to corrosion than pure UO$_2$.
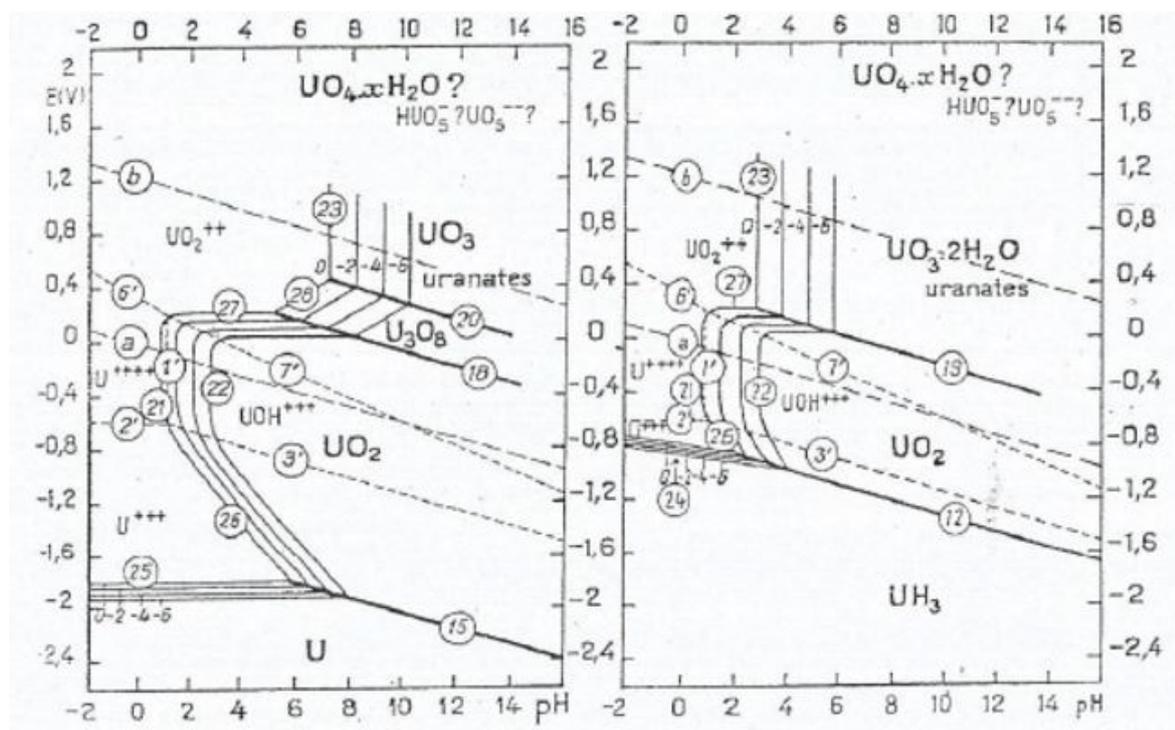
Figure 6.5: Pourbaix diagrams for uranium-water at 25 °C, E vs NHE [29].

6.2.1   Effect of Sodium Sulphate Concentration on the Electrochemical Behaviour of Uranium Dioxide and AGR SIMFuels

Later in this chapter Na_2SO_4 is proposed as a possible supporting electrolyte for simulant pond water, necessary due the large solution resistance of pond water. The work is presented here as baseline CVs were carried out in Na_2SO_4 and thus, it is in line with the solutions used for experimental results presented in this section of the chapter. In an attempt to show that Na_2SO_4 does not complex with UO_2 and disrupt formation of a passive layer or enhance dissolution of UO_2, CV experiments were carried out at increments of Na_2SO_4 concentration. The effect of Na_2SO_4 concentration on the cyclic voltammetry of UO_2, 25 GWd/tU and 43 GWd/tU samples is seen in Figure 6.6.
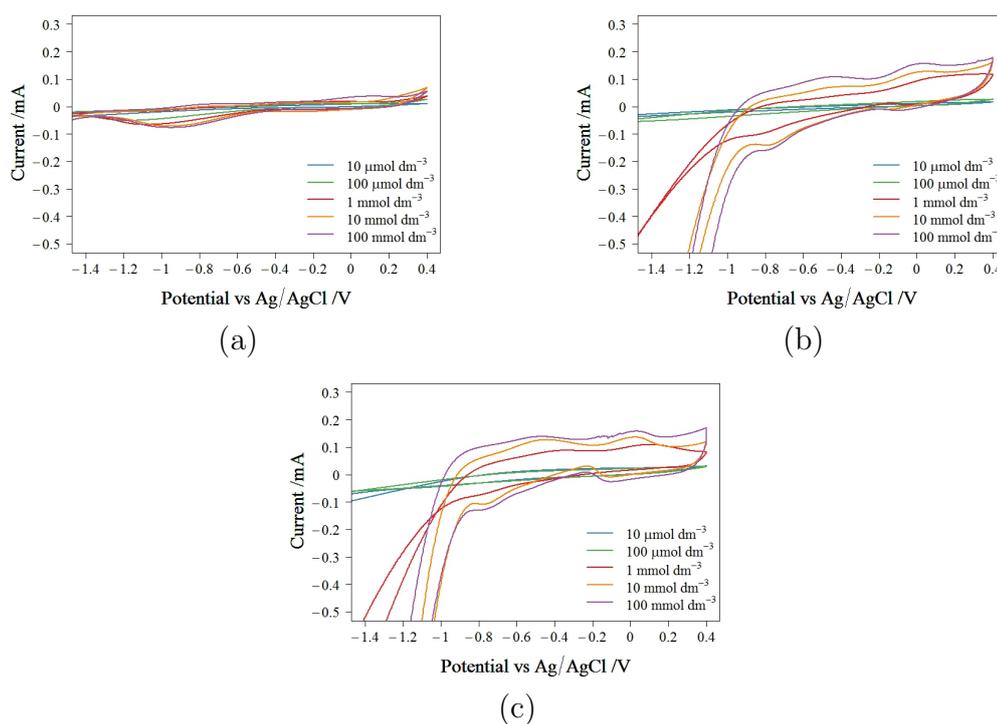
Figure 6.6: Effect of Na_2SO_4 concentration on the cyclic voltammetry of (a) UO_2, (b) 25 GWd/tU and (c) 43 GWd/tU.

The same three peaks described in section 6.2 are present at all concentrations. Increases in concentration result in increased peak current and broadening of the peaks. These features are consistent with the increase in ionic strength rather than the enhanced dissolution of UO_2.

Figure 6.7 shows Pourbaix diagrams for the U-H_2O system that have been especially computed in the presence of a range of concentrations of solution phase sulphate using Medusa software in order to assist in the interpretation of Figure 6.6. This also includes thermodynamic information for U_4O_9 that was previously inaccessible to or deliberately omitted by Pourbaix at the time of computation of Figure 6.29. The inclusion of this phase is advantageous in that it is likely to be the first of the hyperstoichiometric oxides that may be generated upon oxidation of UO_2 to uranyl and so provides an indirect means to interrogate the formation of UO_{2+x}. Note that U_4O_9 forms as cuboctahedral clusters but retains the cubic fluorite lattice structure however further oxidation results in transformation of the lattice to orthorhombic U_3O_8. This is kinetically more difficult to form.

From these diagrams, it is seen that for a solution with pH$\lesssim$6 and Na$_2$SO$_4$ concentration > 0.8 mmol dm^{-3}, the oxidation of uranium oxide can result in the formation of a uranyl sulphate complex, UO$_2$SO$_4$, at potentials greater than approximately +0.4 vs SHE and +0.2 V vs Ag/AgCl. As the concentration of solution phase sulphate increases (Figure 6.7 (c)) the uranium-sulphate complex formed at potentials greater than approximately +0.4 vs SHE and +0.2 V vs Ag/AgCl is UO$_2$(SO$_4$)$_2^{2-}$. At potentials > 0.2 V vs Ag/AgCl in Figure 6.6, the height of the oxidation wave can be seen to increases with increasing concentration of Na$_2$SO$_4$. In light of the computed speciation diagrams of Figure 6.7, it is possible that this is due to uranium sulphate complex formation facilitating the oxidative dissolution of the electrode surface.

However, under alkaline conditions, these uranyl-sulphate complexes do not form at oxidising potentials more than $\sim$+0 V vs Ag/AgCl, even at Na$_2$SO$_4$ concentrations as high as 0.5 mol dm^{-3}, see Figure 6.7(c). This point will be returned to below in section 6.3.1.
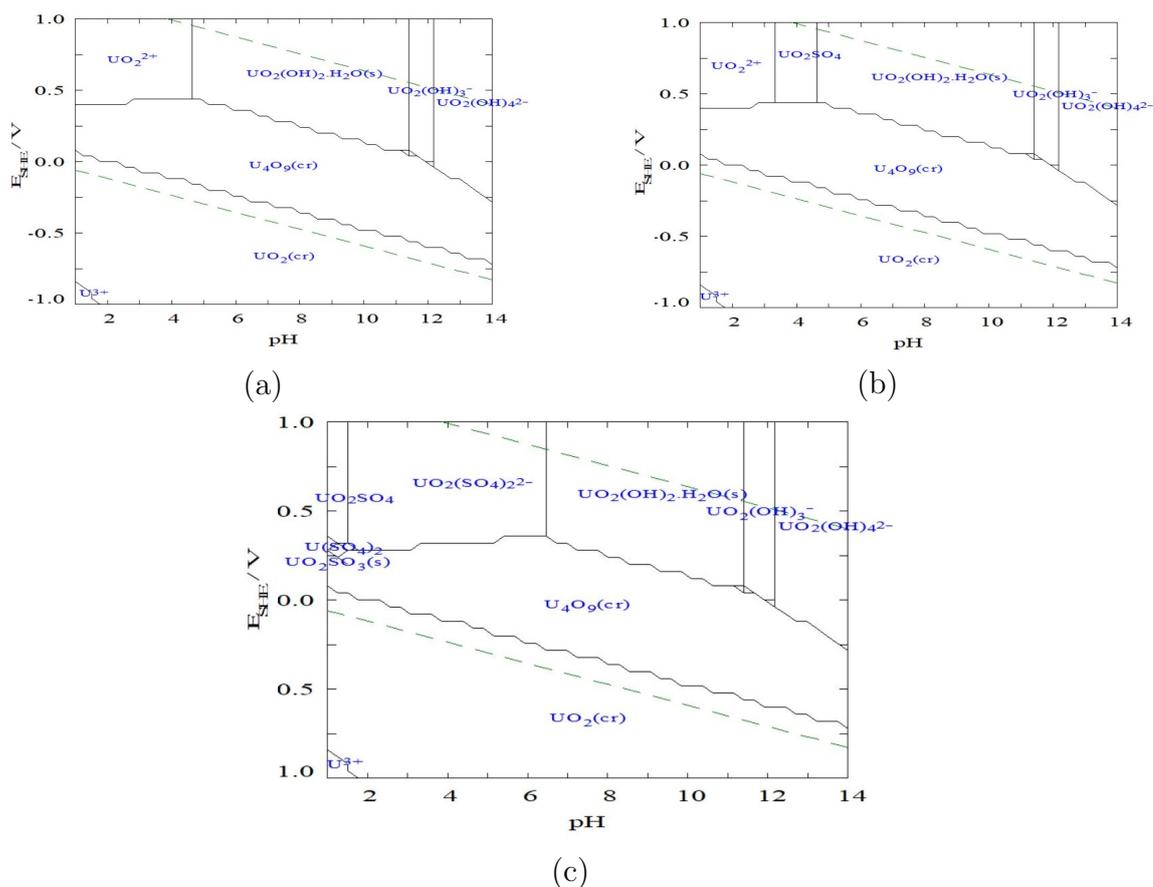
Figure 6.7: Pourbaix diagrams of uranium-water containing (a) 0.75 mmol dm^{-3}, (b) 0.8 mmol dm^{-3} and (c) 0.5 mol dm^{-3} Na$_2$SO$_4$ at 25 °C, produced using Medusa software [251].

6.2.2 Electrochemical Impedance Spectroscopy of Uranium Dioxide and AGR SIMFuels in 0.5 mol dm^{-3} Sodium Sulphate

In Chapters 3 to 5 EIS proved to be a useful tool for interrogating changes to stainless steel electrode surfaces that may be indicative of passive film growth. Thus, EIS studies were conducted on UO$_2$ and the two SIMFuel samples in the same way as for the stainless steel samples in the hopes of determining potential regions where changes to the surface occur. The potential was scanned from -1.5 to 0.4 V in 0.5 mol dm^{-3} Na$_2$SO$_4$ and impedance data taken every 0.1 V. The Nyquist and Bode plots recorded are seen in Figure 6.8, Figure 6.9 and Figure 6.10, only the data recorded at 0.2 V intervals is displayed for clarity; the full data

is available on request.

There are clear differences between the Nyquist plots for the three samples. UO$_2$ has two distinct features indicating the presence of two time constants in the system - an analysis confirmed by the form of the Bode plots that are also consistent with the presence of two time constants. The first feature in the Nyquist plot occurs at Z$'$ < 1.5 kΩ and is a well-formed semicircle, whilst a second feature at Z$'$ > 1.5 kΩ is either a second semicircle of much larger radius or a Warburg feature. For 25 GWd/tU SIMFuel the radius of the first semicircle at low Z$'$ in the Nyquist plot is substantially smaller than that obtained for the UO$_2$ electrode, whilst the second feature seen at larger values of Z$'$ is now clearly observed to be a second semicircle. The decrease in resistance that can be inferred from the decrease in the radius of the first semicircle with increasing simulated burn-up is consistent with the expectation that the doped SIMFuel samples will exhibit higher conductivities than the unadulterated UO$_2$ sample. The semicircle at lower Z$'$ values appears to vanish entirely in the Nyquist plot obtained from the 43 GWd/tU SIMFuel, with only the semicircle at higher value Z$'$ values now being readily observed.

(a)

(b)

(c)
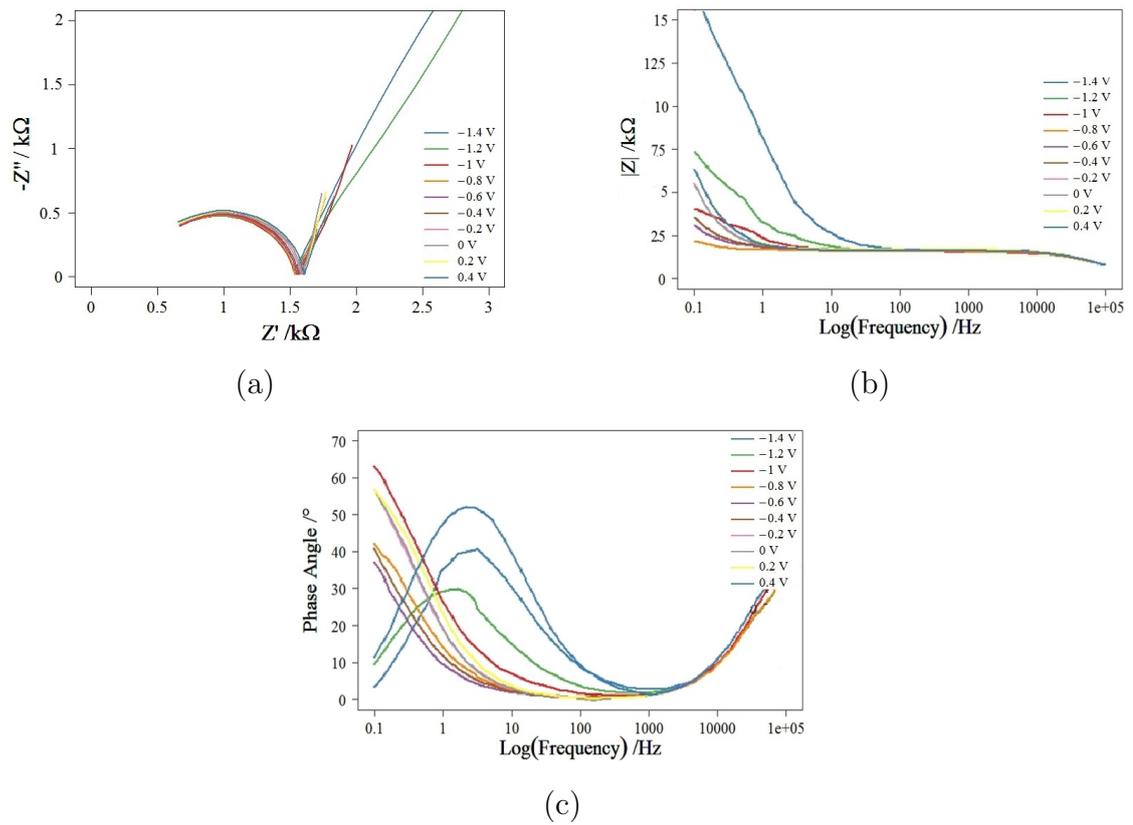
Figure 6.8: Nyquist (a) and Bode (b) & (c) plots of a UO$_2$ sample immersed in 0.5 mol dm^{-3} Na$_2$SO$_4$, pH$\simeq$5.6.

(a)

(b)

(c)
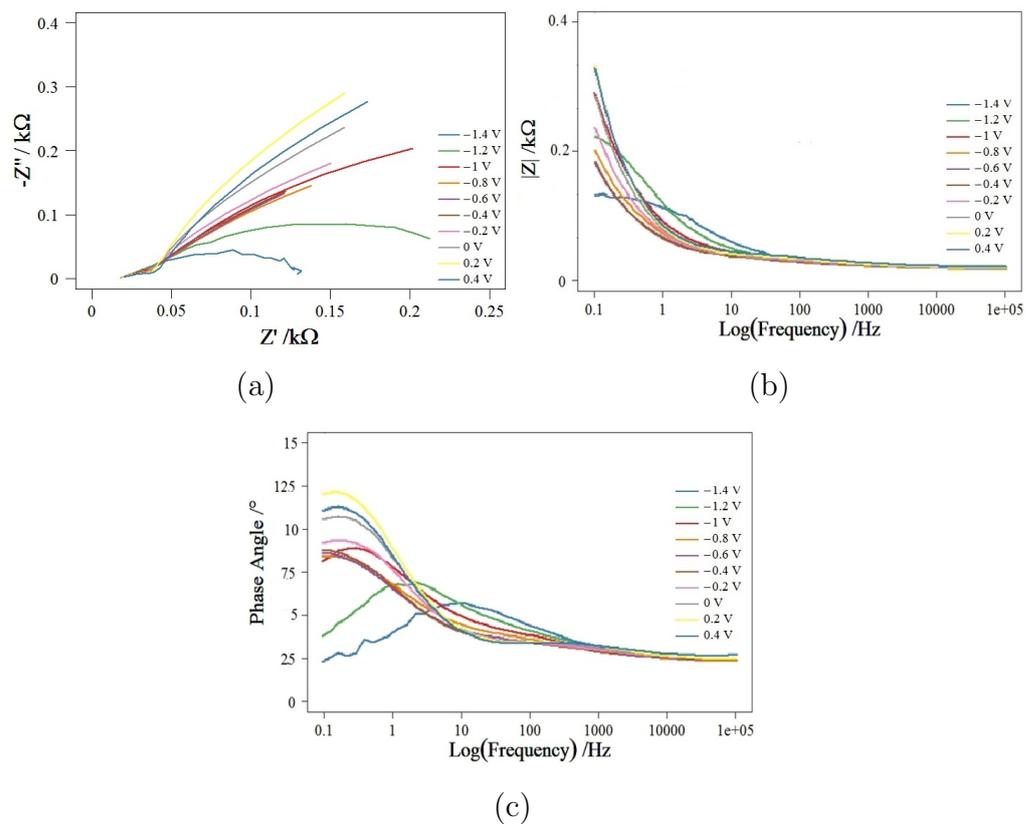
Figure 6.9: Nyquist (a) and Bode (b) & (c) plots of a 25 GWd/tU sample immersed in 0.5 mol dm^{-3} Na$_2$SO$_4$, pH$\simeq$5.6.

(a)

(b)

(c)
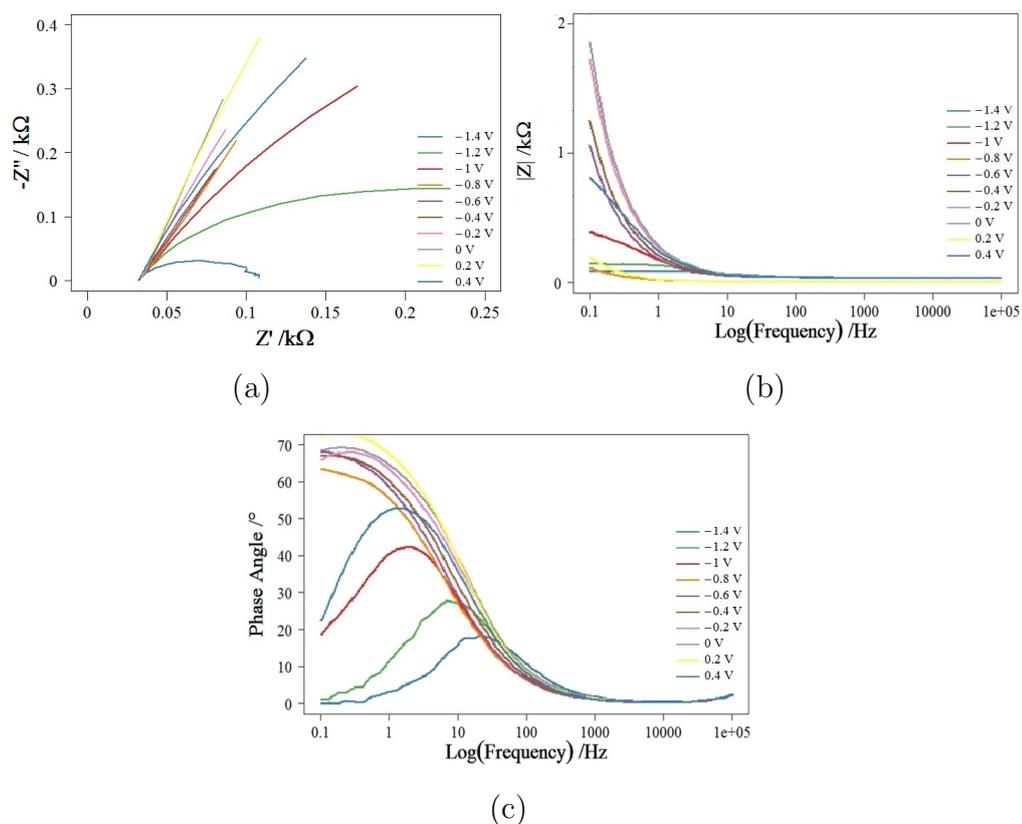
Figure 6.10: Nyquist (a) and Bode (b) & (c) plots of a 43 GWd/tU sample immersed in 0.5 mol dm^{-3} Na$_2$SO$_4$, pH$\simeq$5.6.

As in the case of the steel EIS data earlier, the Nyquist and Bode plots in Figure 6.8 were modelled using equivalent circuits. For all three samples one equivalent circuit was sufficient for the entire potential range of interest. For UO$_2$ this range is -1.5 to 0.4 V however for SIMFuels only potentials between -0.9 and 0.4 V are considered. This is because, for the SIMFuels, significant hydrogen evolution is observed at potentials more negative than -0.9 V, presumably promoted by the electrocatalytic action of the noble metal ε-particles present on the SIMFuel surface but absent on that of the pure UO$_2$ electrodes. This hydrogen evolution dominates the impedance response at low potentials and it would be difficult to determine any intrinsic electrochemistry of the SIMFuel bulk or surface in these results. Thus, analysis of the EIS data is only conducted outside the potential range of hydrogen evolution i.e. at E>-0.9V.

The equivalent circuit model used here was based on those proposed by Bottomley *et al.* [131] and Shoesmith [99] for UO$_2$ systems. These models are

shown in Figure 6.11 and are comprised of two modified Randles circuits in series with a resistor. Consistent with the models of Bottomley *et al.* and Shoesmith, one Randles circuit describes the bulk electrical properties of the electrode, whilst the other describes behaviour at the electrode/electrolyte interface. The series resistor is related to the solution and/or contact resistances of the system. For the work reported in this thesis two amendments to their circuits were made:

1. Constant phase elements were used instead of ideal capacitors;

2. The resistance-capacitance pair, R$_{ads}$ and C$_{ads}$, in the Shoesmith circuit was eliminated. These were introduced by Shoesmith to account for the adsorption of deliberately added carbonate ions at the electrode surface. In keeping with Bottomley *et al.*, there is no deliberately added carbonate and so this feature was eliminated in the circuit model for the work presented here. However, it must be noted that in real pond water conditions, dissolved CO$_2$ from the atmosphere will be present.

3. Shoesmith breaks down the capacitance of the second Randles circuit, i.e. that related to behaviour at the electrode/electrolyte interface, into two: a contribution from the Helmholtz/double layer and a contribution from the surface layer of the electrode. In the work presented here, the capacitance associated with the Helmholtz/double layer is not used in the case of UO$_2$ as the material is so resistive that the voltage drop occurs across the space charge layer in the electrode itself. As such there is no variation in voltage across the Helmholtz layer and C$_{H/dl}$ is effectively infinite, leaving the reciprocal of the total capacitance to be approximately equal to the reciprocal of the capacitance of the space charge capacitance [170]. For related reasons, a similar argument can be advanced regarding the value of C$_{H/dl}$ at the SIMFuel surface at potentials of interest i.e. E > -0.4 V. However, the situation with the SIMFuels has some additional complexities and these will be discussed in detail later in this section.

Thus, a model circuit consisting of two simple Randle cells was deemed appropriate, as shown in Figure 6.12. This is consistent with the two RC loops of the Nyquist plots and the two time constant features evidenced in the Bode plots, although the first loop/time constant is not very clear in the case of the 43 GWd/tU.
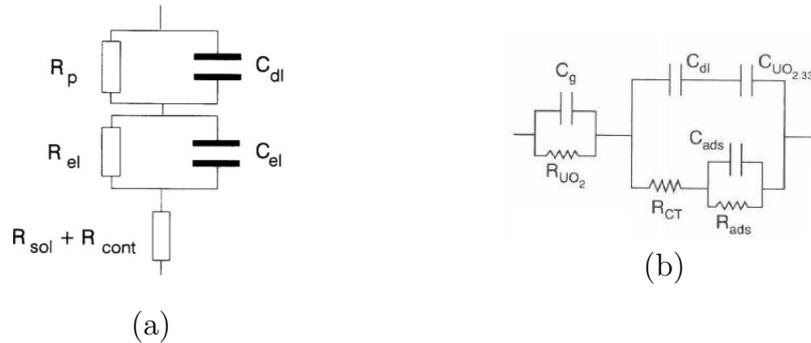
Figure 6.11: Equivalent circuit models proposed by (a) Bottomley *et al.* [131] and (b) Shoesmith [99] for UO$_2$ systems.

In line with the approached of Bottomley and Shoesmith the components in the circuit employed here (Figure 6.12) have the following meanings:

- R$_s$ is the combined contact and solution resistance;

- R$_{el}$ is the resistance associated with the bulk electrode material, be that UO$_2$ or either of the SIMFuels;

- R$_p$ is the polarisation resistance;

- CPE$_{el}$ is a constant phase element related to the geometric capacitance of the electrode; and

- CPE$_{SC/UO_{2+x}}$ is the space charge capacitance of either the bulk electrode material (UO$_2$ in practice) or any UO$_{2+x}$-based surface layer formed on the electrode.
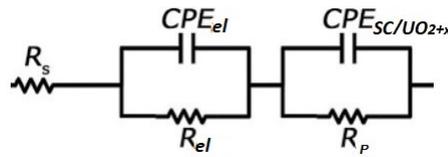
Figure 6.12: Electrical equivalent circuit model used to represent the behaviour of UO$_2$ and SIMFuels in 0.5 mol dm^{-3} Na$_2$SO$_4$. R$_s$ is the combined contact and solution resistance, R$_{el}$ is the resistance associated with the bulk electrode material, R$_p$ is the polarisation resistance, CPE$_{el}$ is a constant phase element related to the capacitance the bulk electrode, CPE$_{SC/UO_{2+x}}$ is the space charge capacitance of the bulk UO$_2$ or the surface layer dependent on potential.

As will be described later, the formation of said layer is dependent upon potential. At low potentials where no UO$_{2+x}$ is being generated (see Figure 6.3 and its interpretation above) the capacitance in the second Randle cell is associated with the space charge layer of the bulk UO$_2$ material. At higher potentials where UO$_{2+x}$ forms the capacitance in the second Randle cell may be the space charge layer associated with UO$_{2+x}$. This point shall be returned to shortly.

For any one electrode material, the R$_s$ value, determined by a combination of solution and contact resistance, should not be expected to vary much with potential. The R and CPE values associated with the bulk electrode material, be that UO$_2$ or either of the SIMFuels, should also be invariant with applied potential for each electrode material. This indeed seems to be the case as the first arc in the Nyquist plots do not change significantly across the potential range for either material. For each electrode system, the R$_s$ and R$_{el}$ values can be estimated by where the first, low Z$'$ value loop intersects the x-axis (real impedance axis). From Table 6.1 it can be seen that R$_{el}$ changes in a similar way to reflect the change in conductivity of the materials i.e. the values for R$_{el}$ are of the following order: UO$_2$ >25 GWd/tU>43 GWd/tU. It can also be seen from Table 6.1 that R$_s$ decreases with increased simulated burnup i.e. UO$_2$ >25 GWd/tU>43 GWd/tU. This is most likely due to the differences in work functions (and Fermi levels) of the materials as the doping level is changed and is sympathetic to the change in conductivity of the materials. These values can be used to assist the fitting software, Zview2, with fitting; specifically, the two resistances can be fixed and all

other parameters left to float.

	UO$_2$	25 GWd/tU	43 GWd/tU
R$_s$	330 Ω	16.77 Ω	38 Ω
R$_{el}$	1233 Ω	24 Ω	0.87 Ω

Table 6.1: Average R$_s$ and R$_{el}$ values for UO$_2$ and SIMFuels immersed in 0.5 mol dm$^-$3 Na$_2$SO$_4$.

Values for each component at each potential can be found in the Appendices. Chi-squared values of the order of 1×10^{-3} were obtained for all three electrode materials across the potential ranges of interest when the relevant EIS data was modelled using ZView2.

Thus, through equivalent circuit modelling, values of CPE$_{el}$, R$_p$ and CPE$_{SC/UO_{2+x}}$ as a function of applied electrode potential, E, are found. Taking each in turn, the Z(CPE) values for CPE$_{el}$ are, when compared to the other circuit elements R$_p$, and CPE$_{SC/UO_{2+x}}$, found to be relatively invariant with applied potential with values of Z(CPE)= 1.3×10^{-8} – 2.99×10^{-8} F, 1.5×10^{-3} - 6×10^{-3} F and 4.24×10^{-5} - 5.89×10^{-5} F for UO$_2$, 25 GWd/tU burnup SIMFuel and 43 GWd/tU burnup SIMFuel respectively. The relative invariance with potential for these values is in line with the expectation for CPE$_{el}$ behaviour outlined above.

The results for R$_p$ vs E are seen in Figure 6.13. Areas of increased corrosion resistance are evident for all three samples. For UO$_2$ there is an increase in resistance between -1.3 to -1 V and between -0.4 to 0.1 V. The peak in resistance at low potentials is due to the polarisation resistance of the bare UO$_2$ surface, most likely due to the oxidation of UO$_2$ to UO$_{2+x}$ at grain boundaries. The peak in resistance at higher potentials corresponds to the oxidation of UO$_2$ to UO$_{2+x}$ on the CVs. Hence, the UO$_{2+x}$ surface layer must have protective qualities. For 25 GWd/tU and 43 GWd/tU samples there is an increase in resistance between -0.9 to -0.4 V corresponding to the oxidation of UO$_2$ to UO$_{2+x}$ at the grain boundaries. A second peak in resistance between -0.1 to 0.3 V occurs for the

25GWd/tU sample and between 0 and 0.3 V for the 43 GWd/tU sample again corresponding to the oxidation of UO$_2$ to UO$_{2+x}$.

As stated in section 6.2, the OCPs of UO$_2$, 25 GWd/tU and 43 GWd/tU SIMFuels are 0.01, 0.22 and 0.19 V respectively. The OCP for UO$_2$ and SIMFuels lies in the region of increased resistance in Figure 6.13, indicating that the surface has some enhanced resilience against corrosion. However, for all three samples, the OCP falls on the higher potential, falling side of the resistance peak, suggesting that this resilience may be easily compromised by e.g. imposition of a small adventitious oxidative stress. Under such circumstances, and as discussed in section 6.2, the SIMFuel samples would be expected to corrode more readily than the UO$_2$ samples due to the closer proximity of the OCP of the SIMFuels to onset of the wave for U(VI) generation in the corresponding CVs.

Finding the x value in the UO$_{2+x}$ phase at the OCP is therefore of interest and the following subsection describes the estimation of the x value using Mott-Schottky analysis.
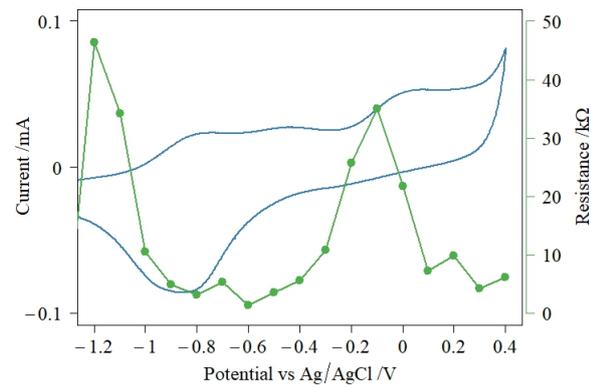
(a)
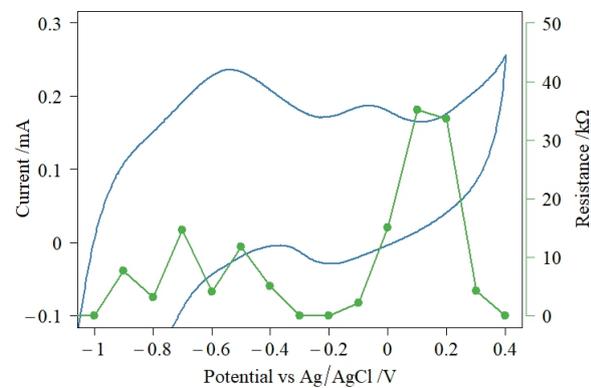
(b)
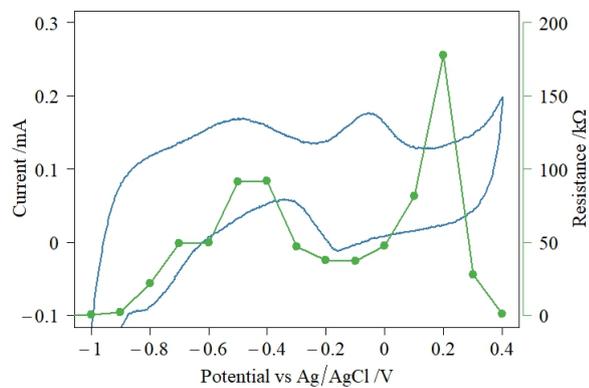
(c)

Figure 6.13: Potentiodynamic polarisation curves overlaid with polarisation resistance data extracted from the Nyquist plots of (a) UO$_2$, (b) 25 GWd/tU SIMFuel and (c) 43 GWd/tU SIMFuel in 0.5 mol dm^{-3} Na$_2$SO$_4$.

**6.2.2.1   Mott-Schottky Analysis using data obtained through
Electrochemical Impedance Spectroscopy for 0.5 mol dm^{-3}
Sodium Sulphate**

In section 2.2.4.2 the reasoning and simplified theory behind the use of Mott-Schottky analysis was discussed. Due to the semiconductor properties of metal oxides formed on stainless steel it is used in Chapters 3-5 to determine the dominant oxides present on the surface of AGR fuel cladding. Uranium dioxide is also known to have semiconductor properties and therefore can be analysed using Mott-Schottky analysis.

C^{-2} vs E plots for UO$_2$, 25 GWd/tU and 43 GWd/tU SIMFuels in 0.5 mol dm^{-3} Na$_2$SO$_4$ are seen in Figure 6.14. Note that n>0.8 for CPE$_{SC/UO_{2+x}}$ over the entire potential range of interest and it can therefore be treated as an ideal capacitor. Two distinct trends can be seen in these C^{-2} vs E plots. A linear relationship with a negative slope (p-type character) is present at low potentials e.g. E<-1 V for UO$_2$ and a linear relationship with a positive slope (n-type character) is present at higher potentials e.g. E>-0.4 V, again for UO$_2$. Therefore, there is a clear transition for p-type to n-type semiconductor behaviour as the applied potential is increased. Comparing these results to those of CV experiments, Figure 6.3, the region of n-type character lies at potentials where UO$_{2+x}$ species are being formed i.e. where the x-value may be considered to be increasing. The presence of p-type and n-type characteristics is explained as follows.

Slightly hyper-stoichiometric UO$_2$ is generally accepted to have p-type semiconductor properties [99]. This is due to the incorporation of O^{2-} at interstitial sites in the fluorite lattice. The U^{IV} is oxidised to U^{V} to maintain the charge balance, creating mobile holes in the U 5f band and thus giving the UO$_{2+x}$ p-type semiconductor properties. It is unlikely that the UO$_2$ samples used in the experiments reported in this thesis are entirely stoichiometric (i.e. x>0), therefore the samples are likely to display p-type semiconductor characteristics

even at low potentials where a bare surface is expected.

In the Raman spectra of the SIMFuels (Figure 6.2) deviations from the perfect fluorite lattice are observed. These defects can be used to predict the semiconductor properties of the material. As discussed in section 6.1, the defect peak observed at 530 cm^{-1} is due to the addition of lower valent dopants, Ln^{3+} (530 cm^{-1} peak), where U(IV) is substituted with Ln^{3+} causing U(IV) to oxidise to U(VI) to maintain charge balance, so creating mobile holes. The peak at 630 cm^{-1} has been attributed to hyperstoichiometry in the UO$_2$ lattice i.e. an increase in x value. As discussed above, this also leads to the oxidation of U(IV) to maintain the charge balance, creating mobile holes in the U 5f band. Thus, both of these defects create mobile holes, which are the majority charge carrier for p-type semiconductors.

As x increases O^{2-} is incorporated into the vacant sites at the centre of the unit cell of the face centred cubic fluorite structure of uranium dioxide, ultimately forming cuboctrahedral clusters [101, 106]. For pure UO$_2$, oxidation results in a high concentration of oxygen interstitial defect clusters causing a tetragonal distortion in the cubic lattice. Thomas *et al.* [252] have shown that the phase associated with and resulting from this tetragonal distortion is U$_3$O$_7$ [135, 138].

For SIMFuels, the presence of dopants disrupts the ordering of defect clusters, the concentration of clusters not being intrinsically high enough to cause deformation of the cubic lattice. Thomas *et al.* [252] have shown that under these circumstances the oxidation of the bulk UO$_2$ lattice results in the formation of U$_4$O$_9$ [135, 138].

In the case of both U$_4$O$_9$ and U$_3$O$_7$, Willardson *et al.* has shown that these phases are metal excess semiconductors. Waber *et al.* [253] have shown that U$_3$O$_8$ is an metal excess semiconductor due to the presence of oxygen vacancies (i.e. anion vacancies) and it is therefore not unreasonable to assume U$_4$O$_9$ and U$_3$O$_7$ are metal excess semiconductors for the same reason. Oxygen vacancy clusters lead to an excess of unpaired electrons and as electrons are the majority charge

carriers in n-type semiconductors, U_4O_9 and U_3O_7 would be expected to behave as such. This has indeed been shown to be the case by Morrell *et al.* and Willardson *et al.* [254, 255].

Thus, at potentials -0.4≤E≤-0.1 the surface composition is expected to be U_3O_7 for UO_2 and U_4O_9 for SIMFuel samples, with both phases exhibiting n-type conductivity.

At potentials ≥ 0 V there is a flattening or decrease in C^{-2} this is most likely due to the oxidation of U(IV/V) to U(VI) and dissolution of the U_4O_9/U_3O_7 surface as UO_2^{2+}. Flattening in C^{-2} may be due to the formation of a deep depletion layer (as might be expected at high positive overpotentials for n-type semiconductors or high reverse bias) whereas decreases in C^{-2} could be a result of thinning of the surface film and/or formation of an inversion layer (as might be expected at very high reverse bias) [256].
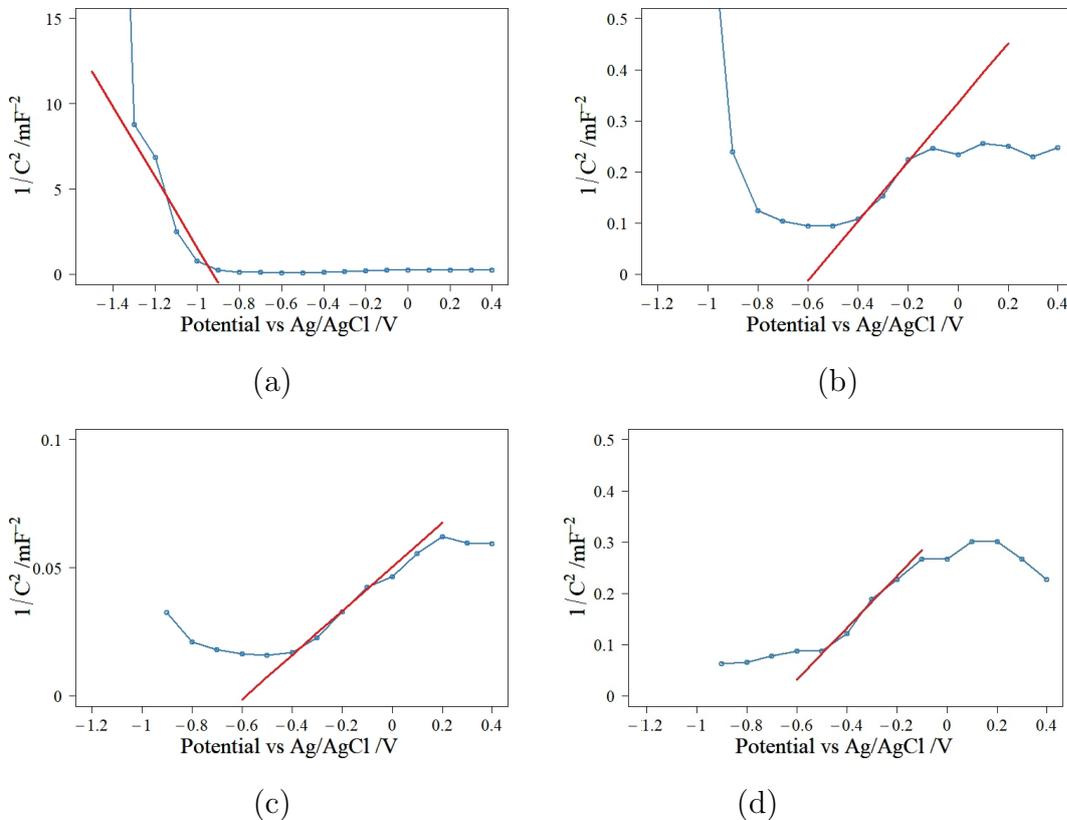
Figure 6.14: Mott-Schottky plots of (a) UO_2, (b) UO_2 with altered x and y-axis for clarity, (c) 25 GWd/tU sample and (d) 43 GWd/tU sample immersed in 0.5 mol dm^{-3} Na_2SO_4, pH≃5.6.

By calculating the slope of the linear portion of the C^{-2} vs E plots, the donor density and the flat band potential can be determined using the Mott-Schottky equation, equation 6.1. Table 6.2 shows the calculated values for UO$_2$, 25 GWd/tU and 43 GWd/tU SIMFuels in 0.5 mol dm^{-3} Na$_2$SO$_4$.

$$\frac{1}{C^2} = \frac{2}{\epsilon\epsilon_0 A^2 q N_D}(-E + E_{FB} + \frac{k_B T}{q}) \tag{6.1}$$

E$_{FB}$ for UO$_2$ is found to be -1.17 V. This is similar to the value of -1.25 V found by Hocking *et al.* for UO$_2$ in 0.2 mol dm^{-3} Na$_2$SO$_4$ at pH$\simeq$10 [257, 258].

E$_{FB}$ for the n-type oxide layer formed on UO$_2$ at E$>$-0.4 V is -0.6 V. N$_D$ for the n-type oxide layer is three orders of magnitude larger than that for the base p-type oxide, this is most likely a reflection of the level of incorporation of oxygen defects into the surface layer upon oxidation.

E$_{FB}$ values for the n-type material on the SIMFuels are $\sim$-0.59 V and $\sim$-0.61 V respectively for the 25 GWd/tU sample and the 43 GWd/tU and is very similar to that formed on UO$_2$.

For the n-type surface layer the order of N$_D$ is 25 GWd/tU > 43 GWd/tU > UO$_2$. This reflects the magnitude of the currents seen in the CVs of each material under applied voltage conditions where this n-type material is generated, Figure 6.3. The reasons for this specific sample-to-sample hierarchy of current magnitudes are discussed in reference to Figure 6.3. More generally, however, increased conductivity as a result of larger N$_D$ is indicative of the surface being less corrosion resistant [259]. Lower N$_D$ values have been observed with increases in the applied potential on steel electrodes. Such increases in applied voltage also lead to an increase in the thickness of the passive film at the electrode surface. These two phenomena have been linked by a suggestion by Lu *et al.* [260] that thicker passive layers allow the constituent atoms to have more space to rearrange themselves into a more stable structure so leading to a decrease in defects associated with displaced atoms (interstitials, vacancies etc). It is not unreasonable to speculate that a similar correlation may exist in the case of UO$_2$ based materials, and that

the passive layer is therefore thicker on UO$_2$ than on either of the SIMFuels – thus rendering it more resistant to further corrosion.

Sample	N$_D$ /m^{-3}	E$_{FB}$ /V vs Ag/AgCl
	p-type	
UO$_2$	5.65$\times$10^{28}	-1.17
	n-type	
UO$_2$	1.79$\times$10^{31}	-0.6
25 GWd/tU	1.36$\times$10^{32}	-0.59
43 GWd/tU	3.74$\times$10^{31}	-0.61

Table 6.2: Dopant densities and flat-band potentials for UO$_2$, 25 GWd/tU and 43 GWd/tU SIMFuels immersed in 0.5 mol dm^{-3} Na$_2$SO$_4$, pH$\simeq$5.6.

Comparing the OCP values for UO$_2$ and SIMFuels to the Mott-Schottky plots the surface phase, in the absence of external oxidative stresses, can be predicted. For the UO$_2$ and SIMFuel samples, the OCPs lie outside the potential region where U$_3$O$_7$ or U$_4$O$_9$ is expected to form. This is likely due to the creation of a soluble U(VI) species, UO$_2^{2+}$. This is consistent with observations made from the CV experiments.

6.3   Behaviour of Uranium Dioxide and AGR SIMFuels in Simulant Pond Water

CV experiments were then carried out on the three samples in simulant pond water solutions of pH$\simeq$11.4. The results of these CV experiments are seen in Figure 6.15. Similar to the results seen in sodium sulphate solution, three common peaks/regions were observed in the forward-going sweeps of each voltammogram. These can be attributed to the oxidation and dissolution of the surface with the same peak assignments as per Figure 6.3. However the currents observed in Figure 6.15 are suppressed compared to those observed in Figure 6.3. Based on Figure 1.26 of Chapter 1 which shows the solubility of UO$_2$ to be almost invariant with pH between pH 2 and pH 11, dissolutions rate should not vary significantly between

these two solutions. However, it is possible that the corrosion currents are greater in Na$_2$SO$_4$ due in part to the development of local acidity as a result of hydrolysis of the UO$_2^{2+}$ generated at positive potentials [135].

$$nUO_2^{2+} + yH_2O \rightarrow ((UO_2)n(OH)y)(2n-y) + yH^+ \qquad (6.2)$$
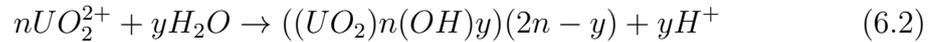
In the simulant pond water, this acidity may be neutralized by the presence of the NaOH. In alkaline solution UO$_2^{2+}$ has limited solubility and from inspection of the relevant Pourbaix diagrams, Figure 6.5, the U(VI) generated at higher potentials takes the form of insoluble UO$_3$·yH$_2$O [135], which itself would be expected to precipitate as a current suppressing surface layer.

At potentials lower than $\sim$1 V, the reduction of water is catalysed by noble metals in the SIMFuels. The observed difference in this potential region between the samples in Na$_2$SO$_4$ is a pH effect, with hydrogen evolution occurring at lower potentials in alkaline solutions.
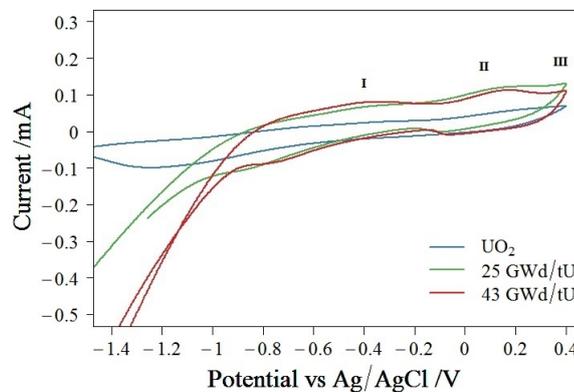
Figure 6.15: Cyclic Voltammetry of UO$_2$, 25 and 43 GWd/tU SIMFuels in simulant pond water, pH$\simeq$11.4.

A reduction in the OCPs is also observed under pond water conditions. The values recorded for pure UO$_2$, 25 GWd/tU and 43 GWd/tU being -0.01, 0.05 and 0.06 V respectively, as shown in Figure 6.16. On inspection of the CVs of these samples in simulant pond water shown in Figure 6.15, it can be seen that the OCP of pure UO$_2$ again sits at the onset of the current peak associated with the onset of the UO$_2$ to UO$_{2+x}$ oxidation process. In contrast the OCPs of both

SIMFuel samples sit on anodic side of this same wave, i.e. towards potentials where the oxidation to UO_{2+x} will be more advanced. Therefore, the OCPs for both SIMFuels in pond water lie at potentials negative of those seen in near-neutral Na_2SO_4 solutions (see Figure 6.4) and in the region where a potentially protective UO_{2+x}–type oxide layer is growing on the surface of the sample.
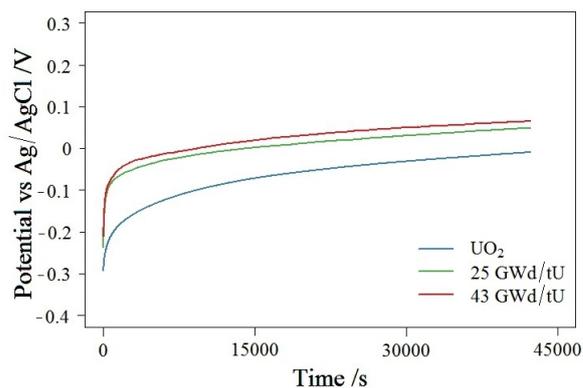
Figure 6.16: Open Circuit Potential measurements of UO$_2$, 25 and 43 GWd/tU SIMFuels in simulant pond water, pH≃11.4.

In order to show the direct implications of the effect of NaOH and pH, the OCPs were measured for a 0.5 mol dm^{-3} Na_2SO_4 solution dosed with NaOH to pH≃11.4 see Figure 6.17 from which it can be seen that the equilibrium OCPs for pure UO$_2$, 25 and 43 GWd/tU samples are -0.06 , 0.04 and 0.06 V respectively. These values are almost identical to those found for simulant pond water at the same pH as shown in Figure 6.16. These values for UO$_2$, 25 and 43 GWd/tU samples are all more negative than the analogous readings recorded in neutral electrolyte, Figure 6.4, illustrating how increasing the pH decreases the OCPs of all three samples. The equilibrium OCPs recorded from the 25 and 43 GWdtU samples in neutral media in Figure 2 lie on the wave associated with matrix oxidation to UO_2^{2+} in Figure 6.3. In contrast, the analogous OCPs recorded in pH≃11.4 media in Figures 6.16 and 6.17 lie at potentials more negative than those where dissolution as UO_2^{2+} would be expected in Figure 6.15, suggesting that the presence of NaOH at pH≃11.4 suppresses the dissolution as UO_2^{2+}.
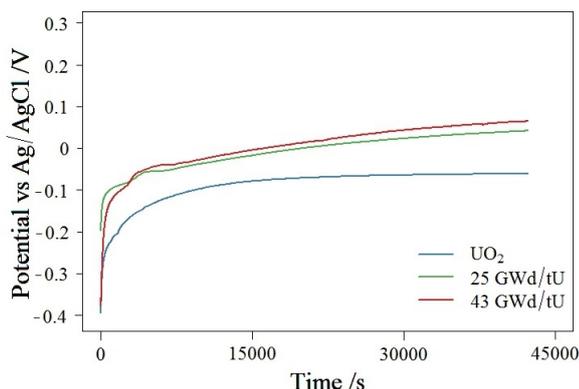
Figure 6.17: Open Circuit Potential measurements of UO$_2$, 25 and 43 GWd/tU SIMFuels in 0.5 mol dm^{-3} Na$_2$SO$_4$ dosed with NaOH to a pH$\simeq$11.4.

6.3.1 Electrochemical Impedance Spectroscopy of Uranium Dioxide and AGR SIMFuels in Simulant Pond Water

Once again EIS was employed to interrogate the surface of the UO$_2$ and SIMFuel samples to elucidate any changes to the surface phases. Figures 6.18 to 6.20 show the resulting Nyquist and Bode plots for UO$_2$ and SIMFuels in simulant pond water. Compared to the data recorded in sulphate electrolytes, section 6.2.2, there are some major irregularities with these data, irregularities that are most apparent in the Nyquist plots. For UO$_2$ at low potentials and high frequencies the imaginary impedance has a positive value and thus goes below the x-axis. This feature is often associated with inductance in the literature [261]. As for the SIMFuels the Nyquists shift along the x-axis with potential and values of real impedance increase at high frequency. Both of these features are abnormal for Nyquist plots and cannot be fitted using equivalent circuit modelling.

(a)

(b)

(c)
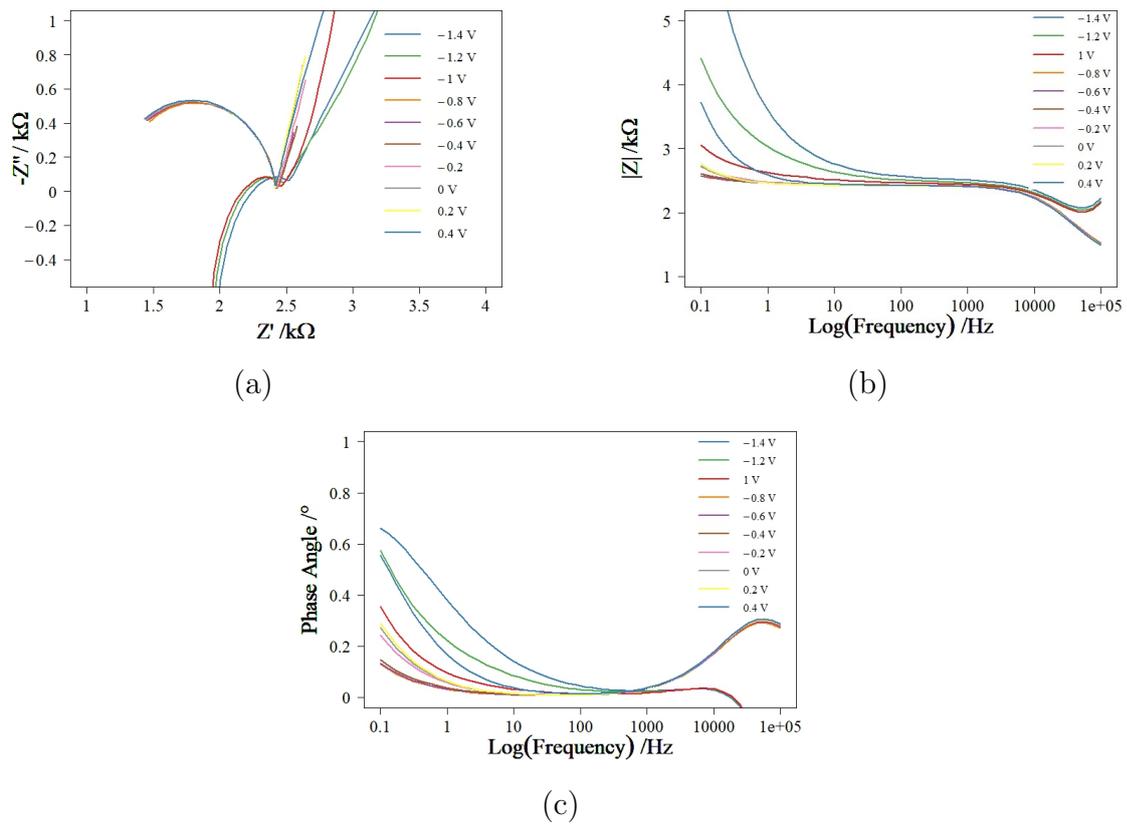
Figure 6.18: Nyquist (a) and Bode (b) & (c) plots of a UO$_2$ sample immersed in simulant pond water pH$\simeq$11.4.

(a)

(b)

(c)
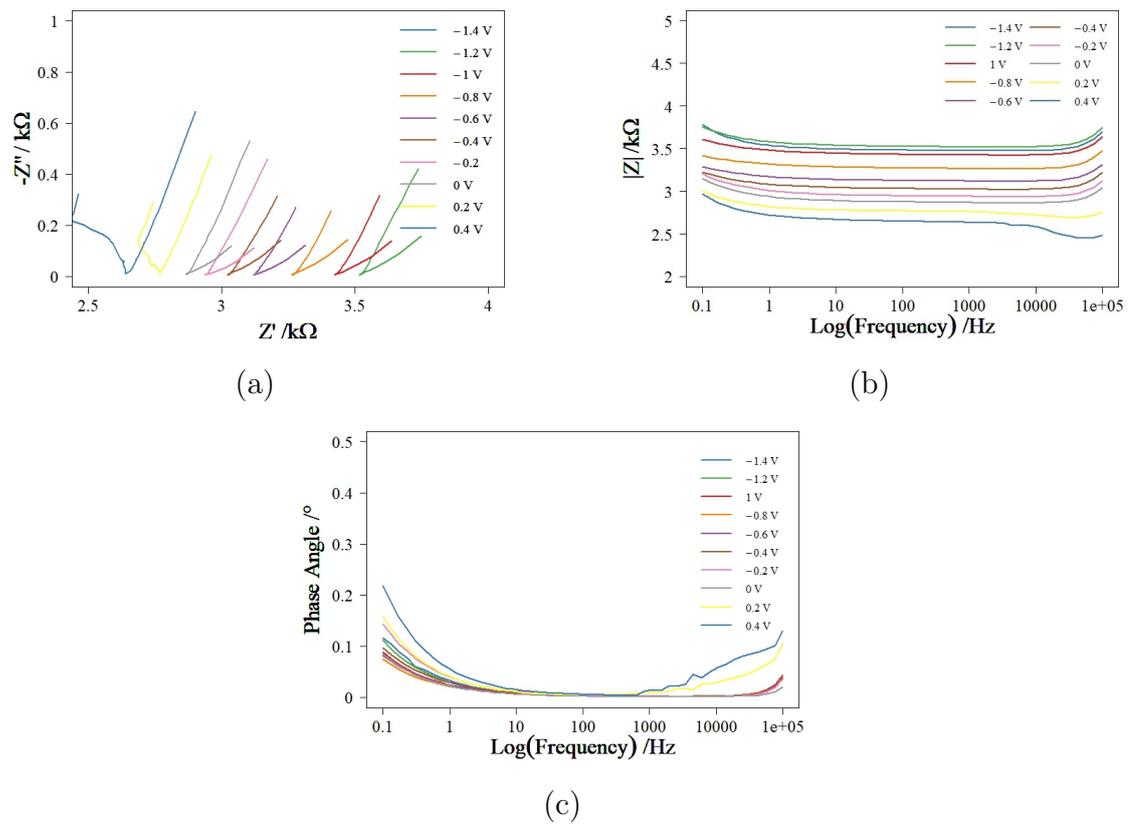
Figure 6.19: Nyquist (a) and Bode (b) & (c) plots of a 25 GWd/tU SIMFuel sample immersed in simulant pond water pH≃11.4.

(a)

(b)

(c)
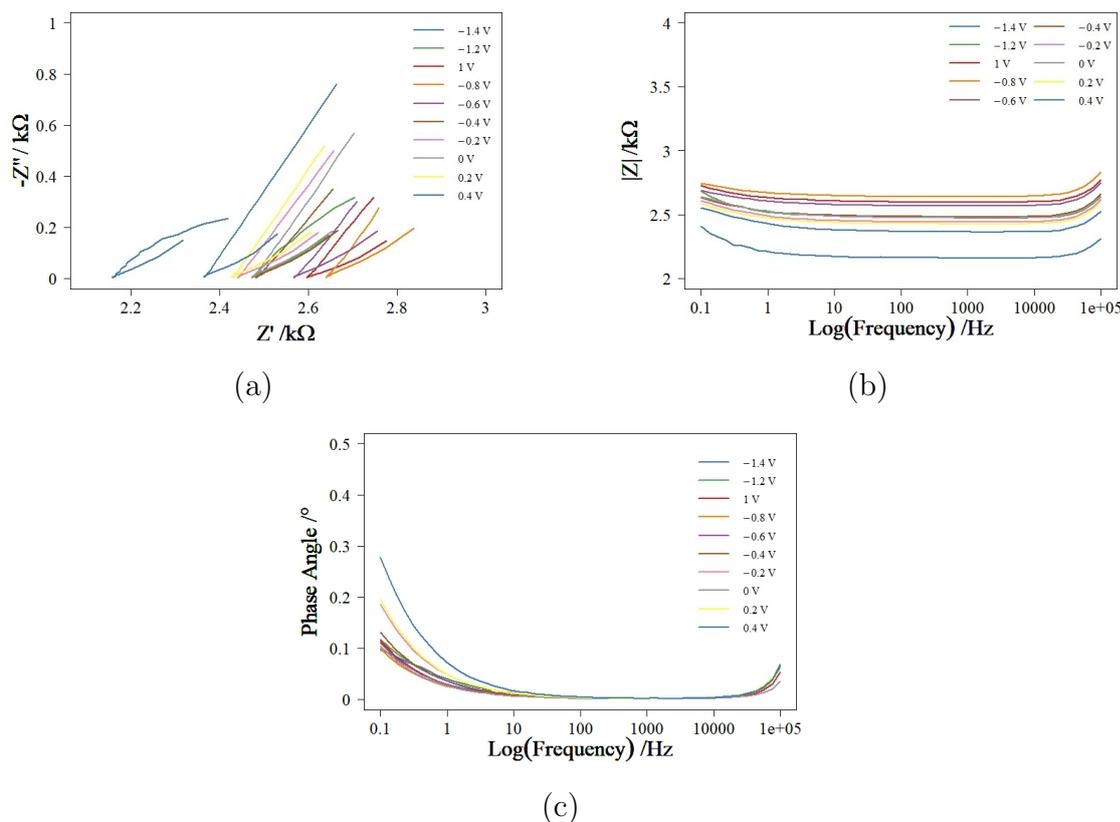
Figure 6.20: Nyquist (a) and Bode (b) & (c) plots of a 43 GWd/tU SIMFuel sample immersed in simulant pond water pH≃11.4.

The irregularities in the plots are most likely associated with the large solution resistance. To adjust the experiment to compensate for the effect of solution resistance, a high concentration of fully dissociated electrolytes is added to the solution, a concentration approximately 100 times that of the analyte is used. It is also important that the selected electrolyte does not interfere with the surface reactions. Sodium sulphate was chosen as the electrolyte as sulphate only reacts with uranium at low pH values (seen through Pourbaix diagrams produced using Medusa software [251] and shown in Figure 6.7) and proven through the CV experiments of section 6.2.1.

6.3.1.1   Electrochemical Impedance Spectroscopy in Simulant Pond Water containing a Supporting Electrolyte

EIS experiments were then repeated in simulant pond water in the presence of 0.5 mol dm^{-3} Na$_2$SO$_4$. Once sodium sulphate is present, the Nyquist plots behave

in a manner more consistent with work by previous authors on UO_2 analogous systems [99,131]. Therefore, all EIS experiments preformed in simulant pond water containing 0.5 mol dm^{-3} Na_2SO_4 in the solution. The resulting Nyquist plots for UO_2, 25 GWd/tU and 43 GWd/tU SIMFuel samples immersed in simulant pond water containing 0.5 mol dm^{-3} Na_2SO_4 are presented in Figure 6.21, Figure 6.22 and Figure 6.23.
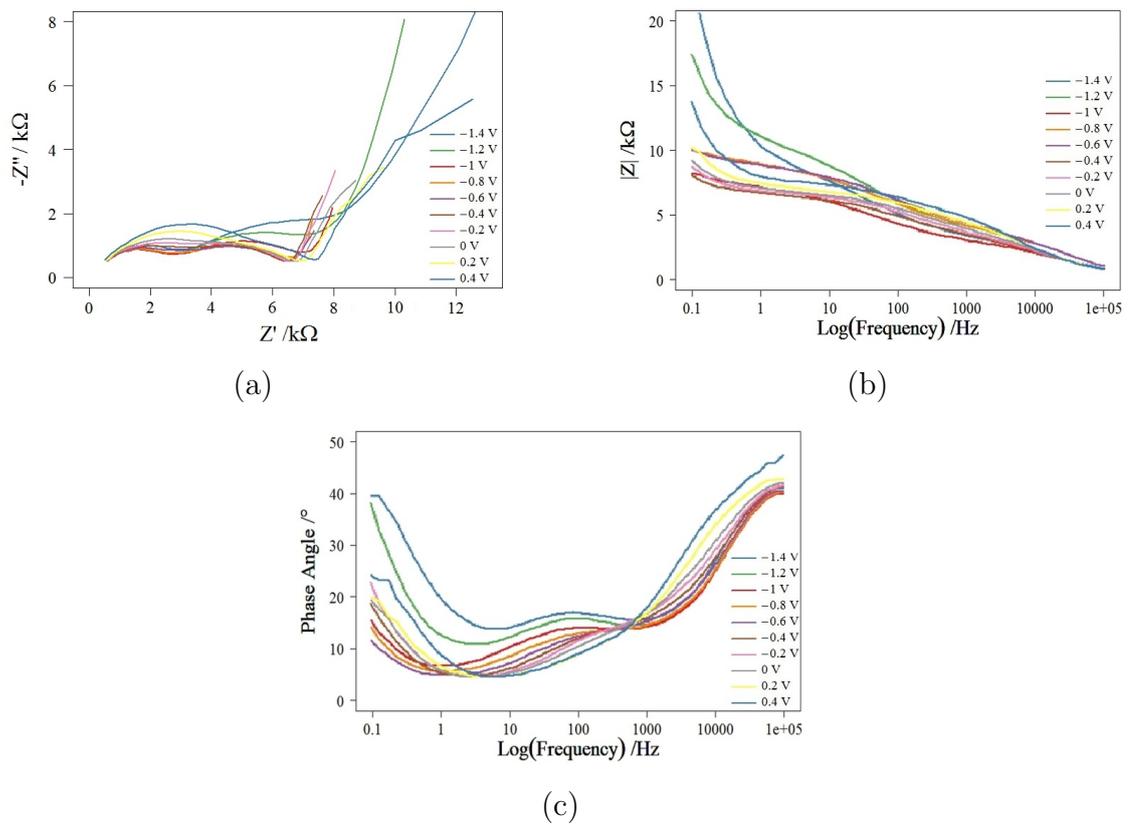
Figure 6.21: Nyquist (a) and Bode (b) & (c) plots of a UO_2 sample immersed in simulant pond water with 0.5 mol dm^{-3} Na_2SO_4 added as a supporting electrolyte, pH≃11.4.

(a)

(b)

(c)
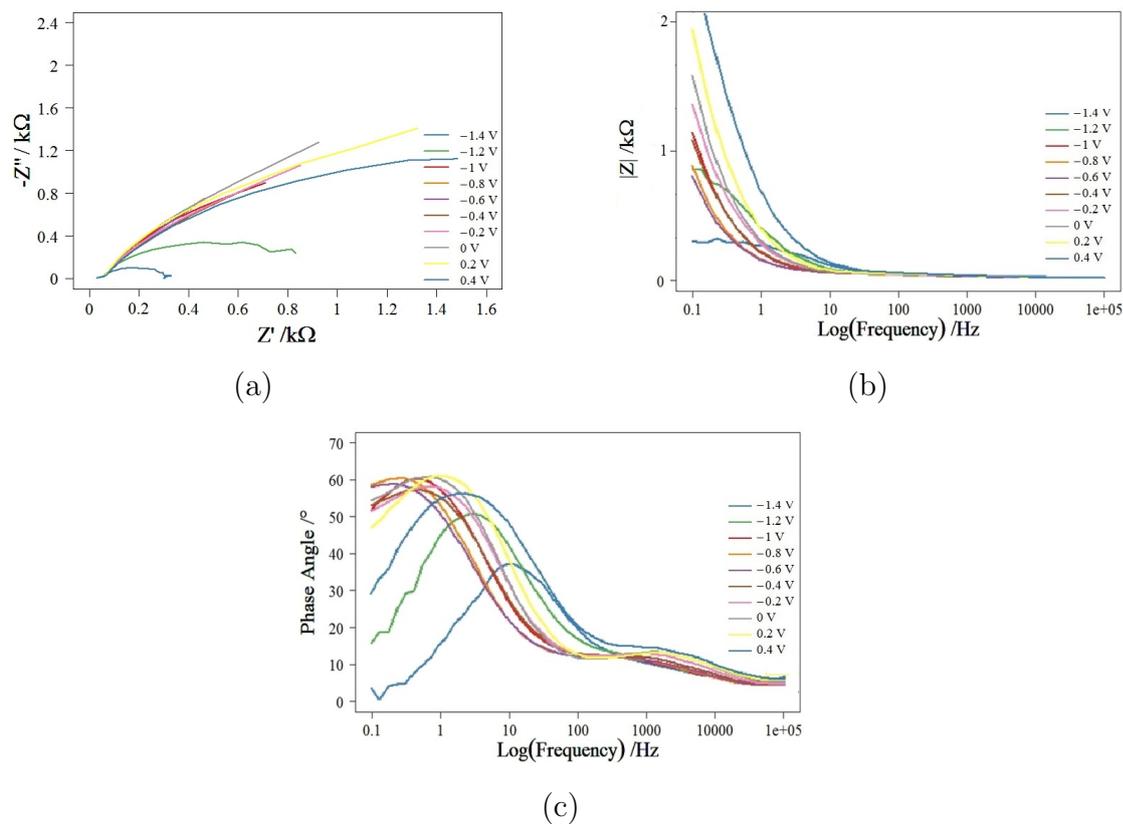
Figure 6.22: Nyquist (a) and Bode (b) & (c) plots of a 25 GWd/tU sample immersed in simulant pond water with 0.5 mol dm^{-3} Na$_2$SO$_4$ added as a supporting electrolyte, pH$\simeq$11.4.

(a)

(b)

(c)
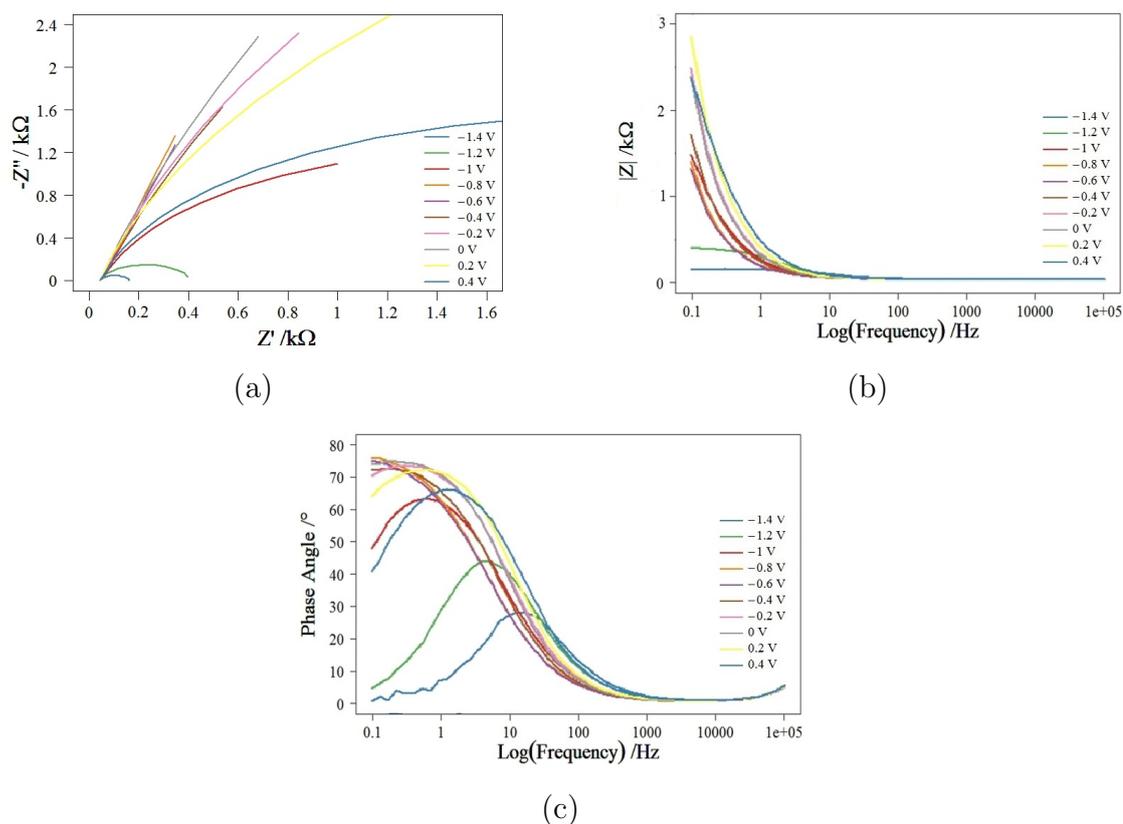
Figure 6.23: Nyquist (a) and Bode (b) & (c) plots of a UO$_2$ sample immersed in simulant pond water with 0.5 mol dm^{-3} Na$_2$SO$_4$ added as a supporting electrolyte, pH$\simeq$11.4.

The Nyquist plots were again modelled using equivalent circuits. For UO$_2$ one equivalent circuit composed of three Randle cells was considered appropriate, as seen in Figure 6.24. This is consistent with the three loops observed in the Nyquist plots of Figure 6.21(a) and the three times constant-related features seen in the Bode plots of Figure 6.21(b) and (c).
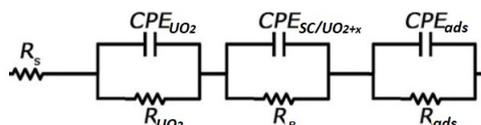
Figure 6.24: Electrical equivalent circuit model used to represent the behaviour of UO$_2$ in simulant pond water containing 0.5 mol dm^{-3} Na$_2$SO$_4$.

In line with the equivalent circuit presented in section 6.2.2 R$_s$ is the combined contact and solution resistance, R$_{UO_2}$ is the resistance associated with the bulk UO$_2$ lattice, R$_p$ is the polarisation resistance, CPE$_{UO_2}$ is a constant

phase element representing the capacitance associated with the bulk UO$_2$ lattice, CPE$_{SC/UO_{2+x}}$ is the space charge capacitance of the bulk UO$_2$ or the surface layer dependent on potential. As described above, the formation of said layer is dependent upon potential. At low potentials where no UO$_{2+x}$ is being generated (see Figure 6.15 and its interpretation above) the capacitance in the second Randle cell is associated with the space charge layer of the bulk UO$_2$ material. At higher potentials where UO$_{2+x}$ forms, the capacitance in the second Randle cell may be the space charge layer associated with UO$_{2+x}$ surface layer. The resistance and capacitance of the third Randle cell is tentatively assigned to the relaxation of an adsorbed intermediate as has been previously suggested by Shoesmith [99] and was discussed in detail above with respect to Figure 6.11.

A similar approach to fitting was employed as in section 6.2.2. The R$_s$ value was estimated using the intersection at the x-axis. The other parameters were left to float as there are clear changes in the Nyquist plots over the potential range for these parameters. Assignments for the other components of the Randle cells are made based on their comparative behaviour to those measured in 0.5 Na$_2$SO$_4$ mol dm^{-3}. The Randle cell representing the bulk electrode was assigned due to CPE having values in the order of 10^{-8} and the R values being between 2000 and 3000 i.e. in the range of the measured resistance of the UO$_2$ material. The second Randle cell is assigned to the polarisation resistance and the capacitance of the space charge layer as the capacitance is in the order of 10^{-5}-10^{-4} and because the trend in R and CPE values is akin to those seen in pure 0.5 mol dm^{-3} Na$_2$SO$_4$ solution. By elimination, the remaining R and CPE data set - wherein CPE has values in the order of 10^{-6} F and R in the range 2397- 6878 Ω - were assigned to the R$_{ads}$/CPE$_{ads}$ Randles circuit. All R and CPE values can be found in Appendix B. Chi-squared values of the order of 1$\times$10^{-3} were obtained when modelled using ZView2.

For the 25 GWd/tU and 43GW d/tU SIMFuels, as in the case of the solution containing only 0.5 mol dm^{-3} Na$_2$SO$_4$, one equivalent circuit consisting

of two Randle cells was considered appropriate, as seen in Figure 6.25, with the resistance and capacitances holding the same meanings as before. This is consistent with the RC loops of the Nyquist and time constant-features seen in Bode plots. Chi-squared values in the order of 1×10^{-3} were obtained for all three electrode materials across the potential ranges of interest when the relevant EIS data was modelled using ZView2.
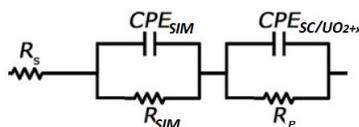
Figure 6.25: Electrical equivalent circuit model used to represent the behaviour of 25 GWd/tU and 43 GWd/tU SIMFuels in simulant pond water containing 0.5 mol dm^{-3} Na$_2$SO$_4$.

The nature of the adsorption process associated with the constant phase element CPE$_{ads}$ and the resistance R$_{ads}$ in the third Randles circuit of Figure 6.24 will be revisited below – as will the reasons for its absence in the EIS measurements conducted on UO$_2$ electrodes in sulphate-only containing electrolytes (Figure 6.8) and its absence in the EIS measurements conducted on the SIMFuel samples under all solution conditions studied here.

Through equivalent circuit modelling R$_p$ values as a function of electrode potential are found, the results are seen in Figure 6.26. The resistances are plotted on a log scale for clarity. Regions of increased resistance are evident for all three samples.

For UO$_2$ there is an increase in resistance -1.3$\geq$E$<$-0.9 V, -0.9$<$E$\leq$-0.6 V and from -0.3 to 0 V. At E$>$0 V the resistance value plateaus. The peak in polarisation resistance at low potentials is due to the resistance of the bare UO$_2$ surface, most likely due to the oxidation of UO$_2$ to UO$_{2+x}$ at grain boundaries. The peak in resistance at higher potentials corresponds to the oxidation of UO$_2$ to UO$_{2+x}$ on the CVs. Hence, the UO$_{2+x}$ surface layer must have protective qualities. The plateauing of the resistance at E$>$0 V can be attributed to the precipitation of UO$_3 \cdot$yH$_2$O onto the surface. Such precipitation was not observed

during the analogous experiments conducted using sulphate-only bearing electrolytes in section 6.2.2 as the pH of those solutions was 5.6 whilst that of the solutions employed in the experiments described in this section was 11.4.

For the 25 GWd/tU sample there is an increase in resistance between -0.9 and -0.5 V and from -0.2 to 0 V. Again at lower potentials the increased resistance corresponds to the oxidation of UO$_2$ to UO$_{2+x}$ at the grain boundaries and the peak at higher potentials corresponds to the bulk oxidation of UO$_2$ to UO$_{2+x}$. At E>0.1 V the resistance almost plateaus which can be attributed to the precipitation of UO$_3$·yH$_2$O onto the surface.

For the 43 GWd/tU sample there is an increase in resistance between -0.9 to -0.3 V and from -0.3 to 0.2 V. Similar to the other samples, at lower potentials the increased resistance corresponds to the oxidation of UO$_2$ to UO$_{2+x}$ at the grain boundaries and the peak at higher potentials corresponds to the bulk oxidation of UO$_2$ to UO$_{2+x}$. At E>0.2 V the resistance almost plateaus which can be attributed to the precipitation of UO$_3$·yH$_2$O onto the surface.

As stated in section 6.3, the OCPs of UO$_2$, 25 GWd/tU and 43 GWd/tU SIMFuels are -0.01, 0.05 and 0.06 V respectively. The OCP for UO$_2$ and SIMFuels lies in the region of increased resistance indicating that the surface has an enhanced resistance against corrosion.
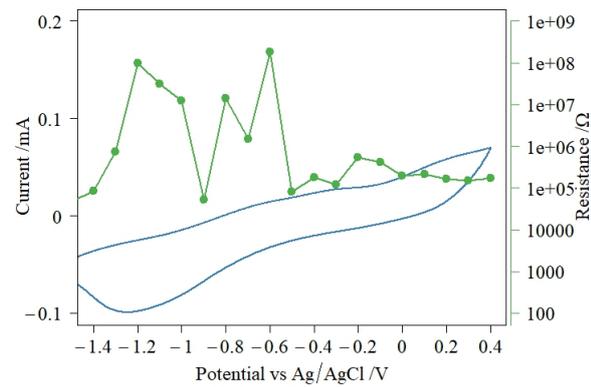
(a)
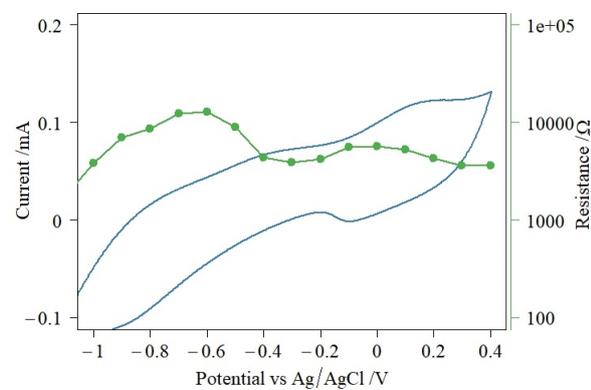
(b)
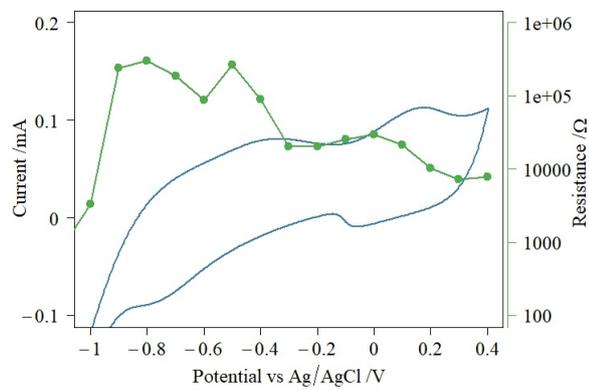
(c)

Figure 6.26: Potentiodynamic polarisation curves overlaid with polarisation resistance data extracted from the Nyquist plots of (a) UO$_2$, (b) 25 GWd/tU SIMFuel and (c) 43 GWd/tU SIMFuel in simulant pond water.

6.3.1.2   Mott-Schottky Analysis using data obtained through Electrochemical Impedance Spectroscopy for Simulant Pond Water containing 0.5 mol dm^{-3} Na$_2$SO$_4$

The same approach as described above in section 6.2.2.1 was used to perform Mott-Schottky analysis on samples immersed in simulant pond water containing a supporting electrolyte of 0.5 mol dm^{-3} Na$_2$SO$_4$. Figure 6.27 shows C^{-2} vs E plots for UO$_2$, 25 GWd/tU and 43 GWd/tU SIMFuels immersed in simulant pond water containing a supporting electrolyte of 0.5 mol dm^{-3} Na$_2$SO$_4$. Note that the value of n for CPE$_{SC/UO_{2+x}}$ was greater than 0.8 over the entire potential range of interest and therefore this CPE can be treated as an ideal capacitor. There is a similar trend to that seen for the samples immersed in 0.5 mol dm^{-3} Na$_2$SO$_4$ with the samples behaving like p-type semiconductors at low potentials and n-type semiconductors at more positive potentials. Once again, the n-type region is expected to be due to the formation of a U$_3$O$_7$ layer for the UO$_2$ sample and a U$_4$O$_9$ film for the SIMFuel samples. However, for the UO$_2$ and SIMFuel samples in simulant pond water there is an increase in C^{-2} at $\sim$0 V. By inspection of the CVs (Figure 6.15) and Pourbaix diagrams (Figure 6.5), this corresponds to the oxidation of U$_4$O$_9$/U$_3$O$_7$ to UO$_3$·yH$_2$O, which can re-precipitate on the sample surface.
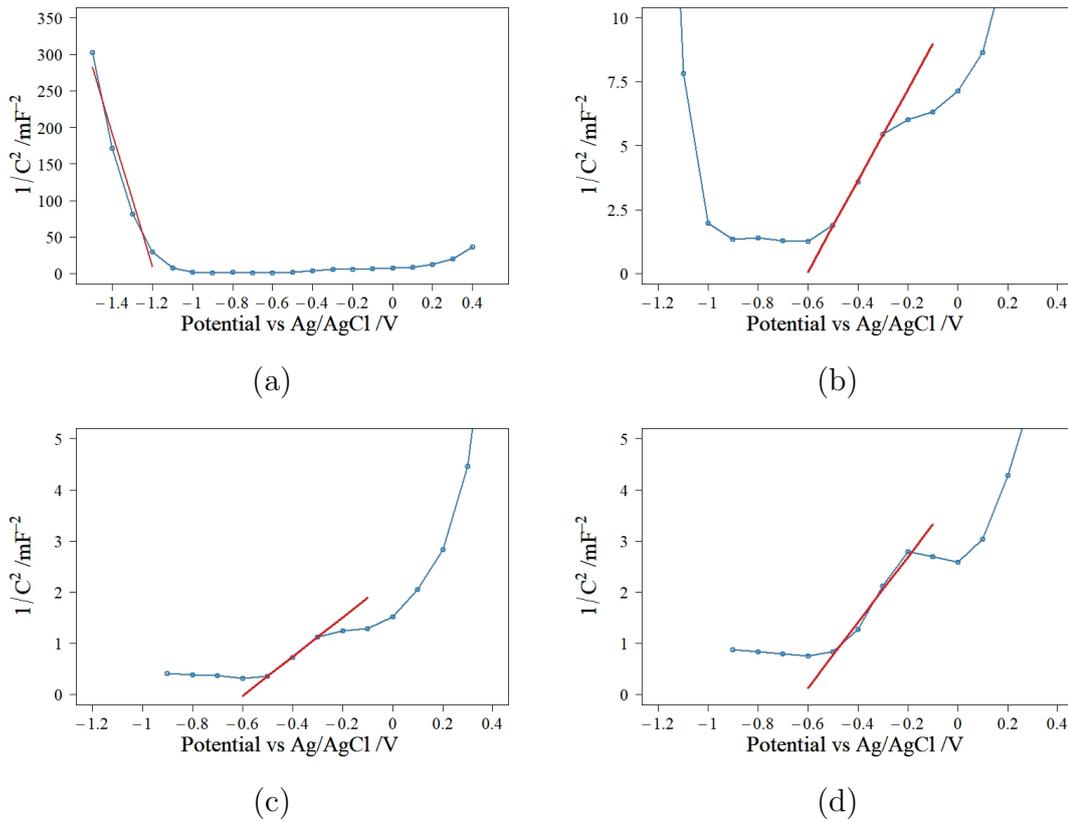
Figure 6.27: Mott-Schottky plots of (a) UO$_2$, (b) UO$_2$ with altered x and y-axis for clarity, (c) the 25 GWd/tU sample and (d) the 43 GWd/tU sample immersed in simulant pond water containing 0.5 mol dm^{-3} Na$_2$SO$_4$ as a supporting electrolyte, pH$\simeq$11.4.

Table 6.3 presents the N$_D$ and E$_{FB}$ values calculated using the Mott-Schottky equation (equation 6.1) for UO$_2$, 25 GWd/tU and 43 GWd/tU SIMFuels in simulant pond water with additional Na$_2$SO$_4$.

E$_{FB}$ for UO$_2$ is found to be -1.22 V. Again, this is similar to the value of -1.25 V found by Hocking *et al.* for UO$_2$ in 0.2 mol dm^{-3} Na$_2$SO$_4$ at pH$\simeq$10 [257, 258].

E$_{FB}$ for the n-type oxide layer formed on UO$_2$ at E>-0.4 V is -0.69 V. N$_D$ for the n-type oxide layer is an order of magnitude larger than that for the base p-type oxide, this is most likely a reflection of the level of incorporation of oxygen defects into the surface layer upon oxidation. This has been discussed in detail in section 6.2.2.1 above.

E$_{FB}$ values for the n-type material on the SIMFuels are ∼-0.68 V and ∼-0.67 V respectively for the 25 GWd/tU sample and the 43 GWd/tU and is very similar

to that formed on UO$_2$.

Compared with the values obtained in 0.5 mol dm^{-3} Na$_2$SO$_4$ the flat band potentials are generally more negative due to the pH dependence of E$_{FB}$. E$_{FB}$ is generally expected to vary by 0.059 V/pH for oxide semiconductors [258, 262]. This is due to the adsorption of H$^+$ and OH$^-$ ions at the semiconductor-electrolyte interface [262, 263]. The decrease is not as dramatic in this case. This could be due to the sorption of other ions within the space charge layer and is dependent on the concentration of such ions [262].

In the potential region where an n-type material is developing on the surface, the dopant density is lower for UO$_2$ than the SIMFuels. This shows the increased conductivity of SIMFuels and is consistent with the increased corrosion currents of the SIMFuels compared to UO$_2$, as seen in the CVs in Figure 6.15. Considering the region of n-type character, for UO$_2$ and SIMFuel samples N$_D$ values in 0.5 mol dm^{-3} Na$_2$SO$_4$ are approximately 10 times those found for the samples in simulant pond water. This is explained by the increase in pH leading to the formation of thicker oxide layers [111], as stated above the atoms have more space to rearrange themselves in a more stable structure resulting in a lower dopant density [260].

Sample	N$_D$ /m^{-3}	E$_{FB}$ /V vs Ag/AgCl
	p-type	
UO$_2$	1.16×10^{28}	-1.22
	n-type	
UO$_2$	5.2×10^{29}	-0.69
25 GWd/tU	2.6×10^{30}	-0.68
43 GWd/tU	1.49×10^{30}	-0.67

Table 6.3: Dopant densities and flat-band potentials for UO$_2$, 25 GWd/tU and 43 GWd/tU SIMFuels immersed in simulant pond water containing 0.5 mol dm^{-3} Na$_2$SO$_4$ as a supporting electrolyte, pH$\simeq$11.4.

Having now discussed the effects of pH on E$_{FB}$ and N$_D$, it is useful to also discuss its role in determining the presence of another phenomenon referred to earlier in this chapter - specifically the adsorption process on pure UO$_2$ inferred from the Nyquist plots of Figure 6.21 can be revisited and its natures explored.

A key observation here is that this putative adsorption process is not observed in the Nyquist plots describing the behaviour of UO$_2$ in simple electrolyte of pH 5.6. The adsorption process is therefore most likely due to the presence of hydroxide at the higher pond water pH of 11.4 which is not present at the lower pH value. The adsorption probably results in the formation of something akin to UO$_2$·OH on the surface of the UO$_2$ electrode via a process similar to that described in section 1.10.3.

However, despite the higher pH, the adsorption feature seen in the Nyquist plots recorded from UO$_2$ at pH$\simeq$11.4 is not present in the Nyquists obtained from directly analogous experiments in on SIMFuel materials. It is possible that this is a result of the different surface oxide forming on the surface of the UO$_2$ and SIMFuel samples - specifically U$_4$O$_9$ on SIMFuels compared with U$_3$O$_7$ on pure UO$_2$ (as discussed above and in section 6.2.2.1). Adsorption does not appear to be a dominant process on U$_4$O$_9$, so explaining the absence of the adsorbance derived semicircle in the SIMFuel Nyquists.

Section 6.3 shows that the OCPs of UO$_2$, 25 GWd/tU and 43 GWd/tU samples in simulant pond water are -0.01, 0.05 and 0.06 V respectively. Considering the position of the OCPs on the Mott-Schottky plot all three samples sit at a position where U$_4$O$_9$/U$_3$O$_7$ is beginning to oxidise and re-precipitate as UO$_3$·yH$_2$O protecting the surface from further dissolution.

6.3.2 Raman Spectroscopy Studies of Uranium Dioxide and AGR SIMFuels exposed to Simulant Pond Water

Based on the OCP results reported in section 6.3, UO$_2$, 25 GWd/tU SIMFuel and 43 GWd/tU SIMFuel have OCPs of -0.01, 0.05 and 0.06 V respectively. From the Mott-Schottky analysis of section 6.3.1 these OCPs are coincident with potentials at which U$_3$O$_7$/U$_4$O$_9$ is excepted to form. Therefore, long duration immersion experiments in simulant pond water of at least one week

were carried out to determine whether the formation of a U_3O_7/U_4O_9 layer could be confirmed using conventional Raman spectroscopic techniques. The resulting spectra can be seen in Figure 6.28.

The transformation from UO_2 to U_3O_7/U_4O_9 causes a broadening of the 455 cm^{-1} peak, a decrease in 530 cm^{-1} peak and a large ingrowth of the 630 cm^{-1} peak [241]. However, only minor differences are observed between freshly polished unimmersed samples and the samples after immersion in simulant pond water for a period of 1 week. For UO_2 there is a very slight broadening of the 455 cm^{-1} peak, with the FWHM value increasing from 21 cm^{-1} to 19 cm^{-1} after immersion. This is not the case for the SIMFuels where the FWHM values for the peak at 455 cm^{-1} are found not to change with immersion – 24 cm^{-1} for the 25 GWd/tU SIMFuel and 23 cm^{-1} for the 43 GWd/tU SIMFuel.
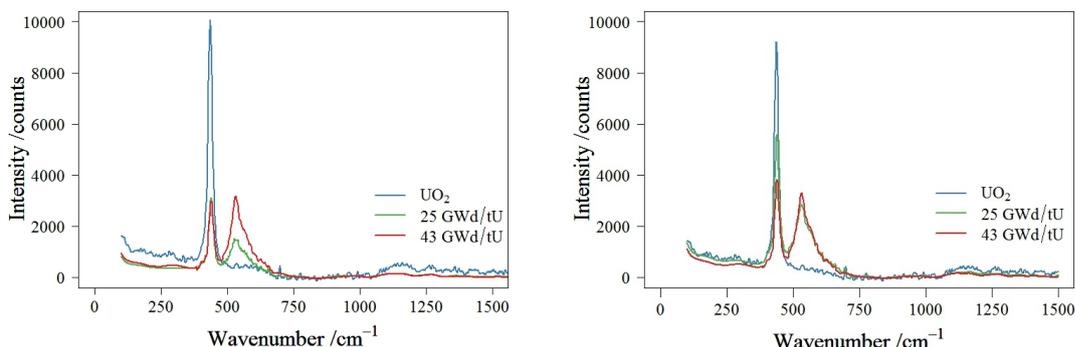
Figure 6.28: Raman spectra for UO_2, 25 GWd/tU and 43 GWd/tU SIMFuel (a) after submersion in simulant pond water and (b) after polishing, laser wavelength 633 nm.

However, the SIMFuels do show a notable post-immersion decrease in the measured intensity of the peak at 455 cm^{-1}. Such a decrease in intensity for this peak is commonly associated with further deviation from the perfect fluorite lattice (see above, section 6.1) and may be indicative of chemical alteration of the surface – most likely via an oxidation process given the OCP measured for these samples in the immersing pond water and their corresponding positions on the voltammetric traces recorded from same (see above). Such a decrease in the 455 cm^{-1} peak intensity is not seen for the UO_2 sample and may be indicative of

the greater corrosion susceptibility exhibited by the SIMFuels due to their higher matrix conductivity (see section 6.2 and 6.3 above).

There is no obvious ingrowth of the 630 cm^{-1} peak for either the UO$_2$ or the SIMFuel samples. Similarly, there is no noteworthy change in the intensity of the peak at 530 cm^{-1} upon immersion for the UO$_2$ and 43 GWd/tU SIMFuels. In contrast, the 25 GWd/tU SIMFuels exhibits a decrease in the 530 cm^{-1} peak. However, replotting the pre- and post-immersion spectra of 25 GWd/tU on the same axes after normalising the absorption profiles of both to the peak at 445 cm^{-1} indicates only minor changes in the structure of the feature at 530 cm^{-1}.

Thus, on balance, the changes to the Raman spectra of all three samples are minor at best and cannot be considered significant enough to confirm alterations to the surface uranium oxide phase to the higher oxides. However, it is worth mentioning that the penetration depth of the 785 nm laser used in the Raman spectroscopy reported here is $\sim$12 μm [180]. Any film likely to have grown on the surface of the immersed electrodes, higher oxides or otherwise, can be expected to be approximately 3-5 nm [130, 264–266]. Therefore, Raman spectroscopy is not a valid way of assessing the composition of the surface layer and the presence -or absence- of the anticipated U$_4$O$_9$ layer cannot be confirmed either way. A more sensitive surface analysis technique is necessary to show alterations to the surface phase, this is subject to further work. Such a technique may be Infrared-Visible Sum Frequency Generation Spectroscopy and this will be explored in follow on work.

6.4 Effect of Chloride Concentration on the Behaviour of Uranium Dioxide and AGR SIMFuels

Chloride has a pronounced effect on the corrosion behaviour of fuel cladding as seen in Chapters 3 and 4. Pourbaix diagrams for the U-H$_2$O-Cl system produced

using Medusa software are shown in Figure 6.29, from which it can be seen that chloride forms stable complexes with uranium, in the form of UO$_2$Cl$^+$, only at low pH and [Cl$^-$]$\geq$0.7 mmol dm^{-3}. This finding is in agreement with previous reports that chloride concentration does not affect the solubility of UO$_2$ through complex formation or ionic strength [267, 268]. To confirm there is no chloride driven corrosion, the effect of chloride concentration on the voltammetric behaviour was explored, Figure 6.30.

(a)   (b)
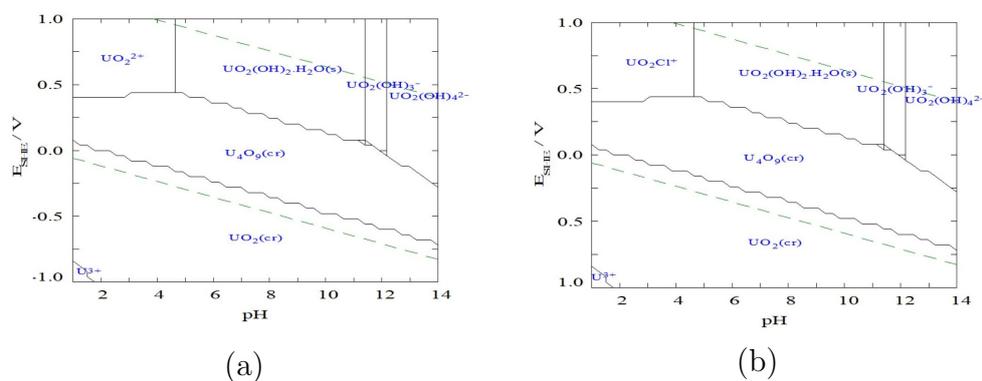
Figure 6.29: Pourbaix diagrams of uranium-water containing (a) 0.65 mol dm^{-3} and (b) 0.7 mmol dm^{-3} NaCl at 25 °C, produced using Medusa software [251].

Results obtained are similar to those seen from analogous experiments conducted using sodium sulphate rather than sodium chloride, see Figure 6.6 in section 6.2.1 above. As in the case of sodium sulphate experiments, peaks are seen to increase in height and/or broaden with increasing Cl$^-$ concentration. This behaviour is due only to the increased ionic strength of the solution, and thus greater associated non-faradaic background currents, and does not represent increased dissolution of the UO$_2$ matrix. Thus, Cl$^-$ concentration is considered to be inconsequential in the corrosion behaviour of SNF under interim storage conditions.

(b)

(b)

(c)
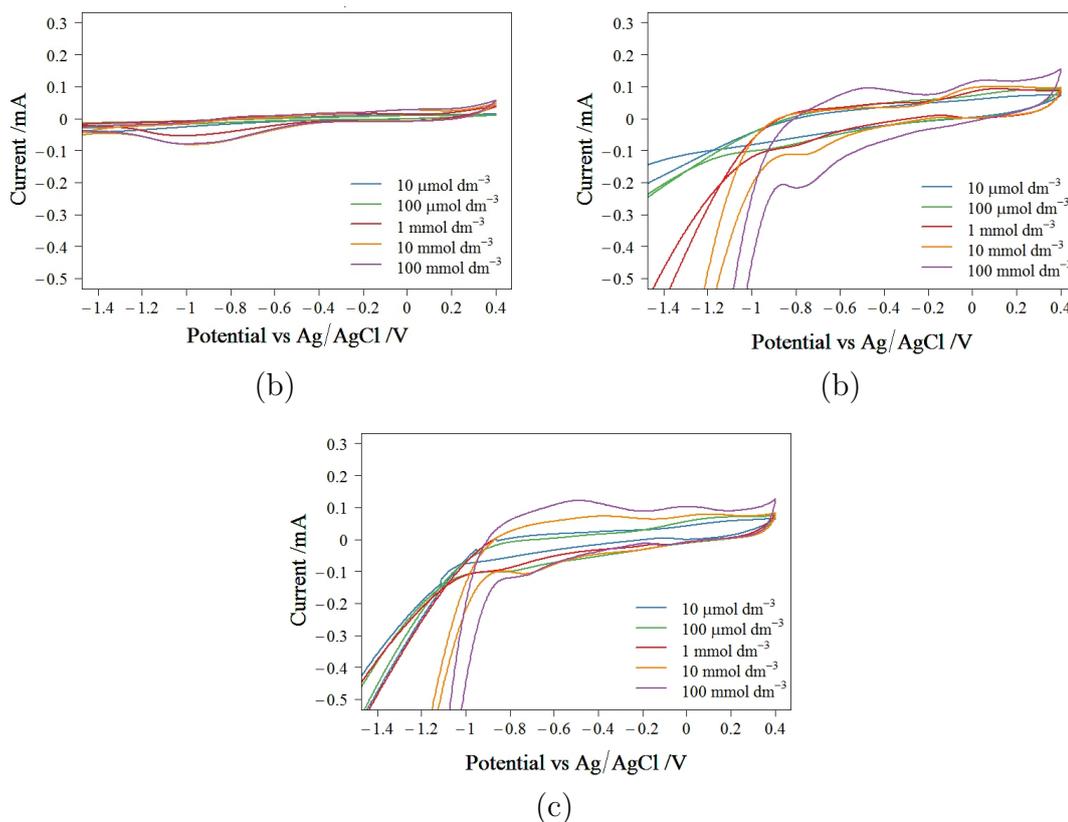
Figure 6.30: Effect of Cl$^-$ concentration on the cyclic voltammograms of UO$_2$, 25 GWd/tU and 43 GWd/tU.

6.5 Effect of Temperature of the Behaviour of Uranium Dioxide and AGR SIMFuels in Simulant Pond Water

As mentioned in previous chapters the interim storage pond water temperature is expected to increase under the new interim storage regime. Thus, as in the case of 20/25/Nb SS cladding studies described in Chapter 3-5, cyclic voltammetry experiments were carried out on the UO$_2$ and SIMFuel samples in simulant pond water at 45 °C, 60 °C and 90 °C. Figure 6.31 shows the resulting voltammograms.

At low potentials it is clear that H$_2$ evolution is enhanced with temperature. This is due to the decrease in pH with increasing temperature, pH∼11.4 at 24 °C

reduces to ~9.8 at 90 °C. H$_2$ evolution occurs at lower potentials at higher pH values.

The second noticeable difference with increasing solution temperature is the decrease in current between approximately -1 and -0.4 V. Previously oxidation in this region has been attributed to the oxidation of hyperstochiometric, UO$_{2+x}$ regions at the grain boundaries to UO$_{2.33}$. In the case of increased temperature, there appears to be enhanced passivation at the grain boundaries. Such enhanced passivation has been observed by Matzkel *et al.* [130] who report UO$_{2.33}$ growth due to accelerated diffusion of O^{2-} at elevated temperatures which increases film formation and growth, note this observation was reported for temperatures >100°C.

Thirdly, the onset of oxidation peaks II (UO$_2$ $\longrightarrow$ UO$_{2+x}$) and III (UO$_{2+x}$ $\longrightarrow$ UO$_3 \cdot y$H$_2$O) shift in the cathodic direction. Furthermore, for temperatures >45 °C the current observed at oxidation peak II and peak III increases with increasing temperature. This is indicative of activation-enhanced oxidation of U$_4$O$_9$ to U(VI) species and hence increased dissolution of the protective surface layer at higher temperatures. However, at 45 °C there is a reduction in the current at peak II compared to at 24 °C, this is more prominent for the SIMFuel samples. Considering potentials around 0.3 V, there is some evidence that the current is suppressed by deposition of UO$_3 \cdot y$H$_2$O onto the samples surface at 90 °C.
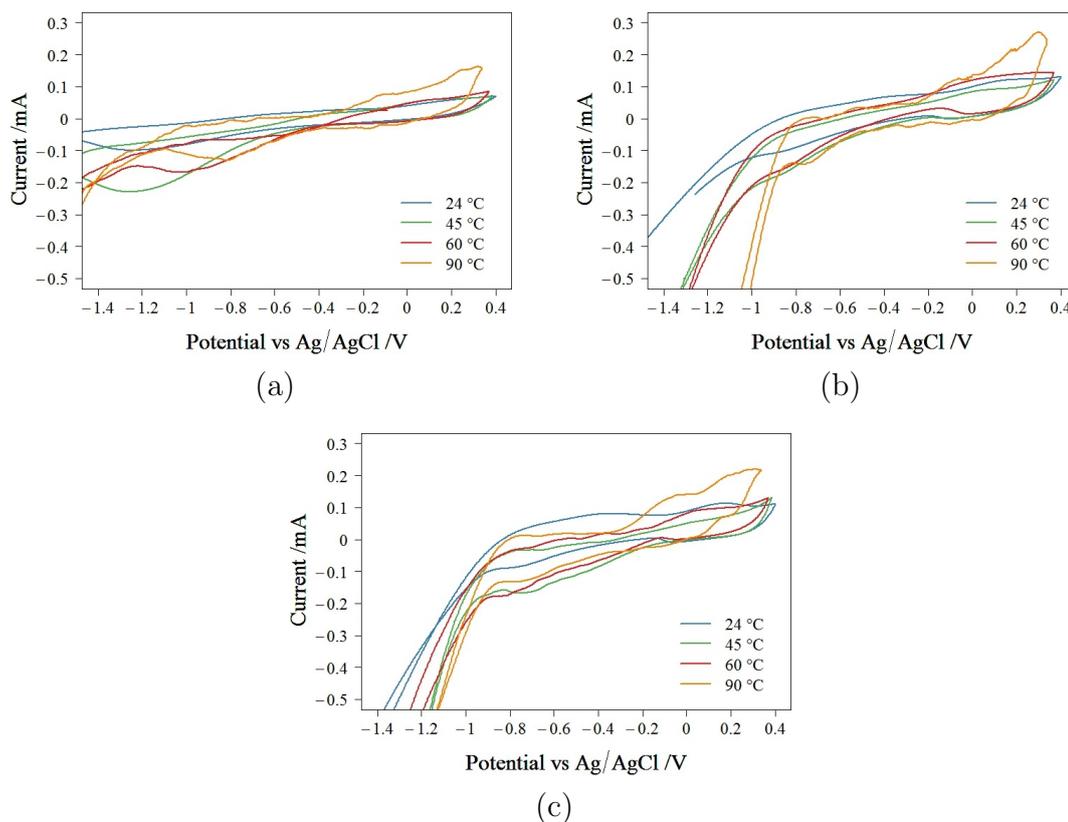
Figure 6.31: Cyclic Voltammetry demonstrating the effect of temperature on the corrosion behaviour of (a) UO_2, (b) 25 GWd/tU SIMFuel and (c) 43 GWd/tU SIMFuel in simulant pond water, pH$\simeq$11.4 at 24 °C.

The effect of solution temperature on the open circuit potential of each sample in simulant pond water is tabulated below, Table 6.4. As the temperature of the solution increases the OCP tends to decrease. As stated above temperature increases cause the oxidation of UO_2 to U_3O_7/U_4O_9 to occur at lower potentials. Thus, despite the decrease in OCP with temperature, the OCPs of UO_2 and SIMFuels lie in the potential range where a film of U_3O_7/U_4O_9 is expected to be developing on the surface at temperatures 24 - 90 °C. As previously mentioned, it is anticipated that the U_4O_9 layer will protect the surface from dissolution.

Sample	24 °C	45 °C	60 °C	90 °C
UO$_2$	-0.01	0.005	-0.05	-0.09
25 GWd/tU	0.05	-0.013	-0.006	-0.1
43 GWd/tU	0.07	-0.01	0.005	-0.1

Table 6.4: Open circuits potentials for UO$_2$, 25 GWd/tU and 43 GWd/tU samples in simulant pond water at 24 °C, 45 °C, 60 °C and 90 °C, pH$\simeq$11.4 at 24 °C.

6.6   Conclusions

This chapter reported the electrochemical corrosion behaviour of pure UO$_2$ and simulated AGR spent fuels under conditions relevant to the wet interim storage (pH$\simeq$11.4). These results can also be compared to their behaviour in a simple electrolyte of 0.5 mol dm^{-3} Na$_2$SO$_4$, of a lower pH, pH$\simeq$5.6. The principal conclusions are as follows:

- There are lower corrosion currents for all three samples in simulant pond water compared to those seen in the Na$_2$SO$_4$ solution. This suggests the growth of a thicker oxide layer in alkaline solutions.

- Similarly, the OCP for all samples under mild alkaline pond water conditions are more negative than those in the neutral sulphate-only bearing electrolyte. Particularly, the OCP for the SIMFuel samples moves from a region where active dissolution of the surface may be expected to an area where an oxide layer is developing, predicted through comparison with the results of CV experiments and previously published UO$_2$-H$_2$O Pourbaix diagrams. It is likely that this oxide layer then protects the surface from further dissolution.

- Mott-Schottky analysis is applicable here due to the semiconducting properties of UO$_2$ and SIMFuels. For the UO$_2$ sample there is a transition from p-type semiconductor behaviour at E<-1.1 to n-type semiconductor behaviour at E>-0.5 V. This is consistent with what is known about the electronic properties of these materials. Hydrogen evolution is catalysed by ε-particles in SIMFuel and thus, the region of p-type semiconductor

behaviour is masked by hydrogen evolution in the experiments on SIMFuel samples. Through Mott-Schottky analysis it was determined that in the region of n-type semiconductor behaviour, -0.5 to 0 V, the UO_2 matrix oxidises to U_3O_7 and SIMFuels oxidise to U_4O_9. This potential region corresponds with a region of increased resistance in the R_p vs E plots. Comparison of the OCP to the C^{-2} vs E plots reveals that the OCP of all three samples sit at a position where U_4O_9/U_3O_7 is beginning to oxidise and re-precipitate as $UO_3 \cdot yH_2O$ protecting the surface from further dissolution/oxidation.

In addition to the above, the following observations can be made in relation to the effects of chloride and temperature on the corrosion behaviour of UO_2 and AGR SIMFuel in wet storage conditions:

With respect to chloride concentration:

Although high levels of chloride proved to reduce the corrosion resistance of AGR fuel cladding, UO_2 and SIMFuels remain unaffected. At pond water pH values UO_2 chloro complexation will not occur and the oxidation of the surface layer proceeds without disruption from Cl^- ions.

With respect to temperature:

For pure UO_2 at OCP there is no significant changes in corrosion currents at temperatures ≤ 60 °C. However, for the SIMFuel samples at temperatures ≤ 60 °C there are small changes in the corrosion currents at OCP with temperature. Compared to the currents seen at 24 °C, at 45 °C the currents decrease and at 60 °C they increase. Increases in the current are a result of enhanced oxidation of the sample and it could be speculated that this would result in the formation of thicker oxide layers. However, further experiments are necessary to confirm whether a thicker oxide layer forms at higher temperatures and whether this thicker layer enhances corrosion resistance. At simulant pond water temperature of 90 °C there is a clear enhancement of the corrosion currents. However, at all temperatures studied the formation of a protective U_4O_9 layer is predicted.

These short duration electrochemical experiments provide initial evidence that for UO$_2$ and SIMFuels dosing pond water to a pH$\simeq$11.4, with an expected chloride concentration of $\sim$1 ppm, will result in passivation, and thus protection from surface dissolution, through the development of a protective U$_4$O$_9$/U$_3$O$_7$ surface film for simulant pond water temperatures between 24 and 90 °C.

Chapter 7

Conclusions and Further Work

7.1 Project Objectives

The key scientific objective of this thesis was to assess the corrosion behaviour of AGR SNF in wet interim storage. Specifically, the work carried out has an industrial application to the THORP Receipt and Storage pond at Sellafield, Cumbria. This pond is currently being converted into an interim storage facility where the SNF will be more densely packed than under current storage conditions leading to increases in the storage temperature. Thus, the key technical objective of the research presented in this thesis was to validate the corrosion safety during extended storage periods with a closer packing regime, as proposed by the NNL.

7.2 Conclusions

To achieve a comprehensive understanding of the corrosion behaviour of AGR SNF the project has been divided into three sections. In the first instance the corrosion of unsensitised 20/25/Nb SS fuel cladding under pond storage conditions was examined. Unsensitised cladding represents approximately 75 % of AGR spent fuel cladding. Secondly, the NNL are working towards the development of suitable analogues for RIS-affected stainless steel cladding and the corrosion behaviour of three of their most promising simulants to date has been investigated, under pond water conditions, in Chapters 4 and 5. Previously

published work on 20/25/Nb SS corrosion is limited and is especially sparse under the aqueous alkaline conditions relevant to interim storage. This thesis provides a combined XPS, voltammetric and impedance spectroscopic study of the fundamental surface structure and chemistry of unsensitised and heat treated 20/25/Nb SS and unsensitised and heat treated 304H SS in this environment.

Finally, AGR simulant SNF has been previously manufactured and studied under conditions relevant to geological disposal but never examined in environments consistent with wet interim storage. Thus, Chapter 6 has studied the behaviour of so-called SIMFuel under various conditions of pH and temperature consistent with that expected to exist in the new THORP pond storage regime.

7.2.1   Unsensitised 20/25/Nb Stainless Steel

Studies were first conducted on unsensitised 20/25/Nb SS cladding. The reasons for studying unsensitised material were threefold: (i) substantial amounts of cladding will not become sensitised in reactor (approximately 75 %); (ii) working on real irradiated cladding is challenging from both radiological safety and economic perspectives and (iii) representative analogues of RIS-affected 20/25/Nb SS, whilst under development, still do not fulfil all criteria required of such simulant materials.

The principal conclusions for unsensitised 20/25/Nb SS are as follows.

The OCP in simulant pond water (pH$\simeq$11.4) is found to be $\sim$0 V vs Ag/AgCl. Under these conditions, XPS data indicates that the protective oxide layer formed on the surface of 20/25/Nb SS consists predominately of Fe and Cr oxides. Resistance and capacitance data from EIS experiments shows that the source of this protection changes on application of an oxidative stress i.e. as the electrode potential is increased. Through comparative analysis with single metal samples of the main constituent elements of 20/25/Nb SS, Cr, Ni and Fe, it was found that this change occurs at $\sim$0.5 V whereupon the protection provided by

Cr_2O_3 is lost due to its oxidative dissolution as Cr(VI). At potentials greater than 0.5 V the surface behaviour is controlled by a Ni oxide layer with a potential contribution from $NiFe_2O_4$ or $FeCr_2O_4$. Transpassive dissolution of this (now predominantly nickel) oxide layer takes place at potentials above 0.75 V.

Voltammetric studies were used to investigate the robustness of this oxide layer. Tests under baseline conditions of pH=8 at 24 °C show a broad region of passivity from $\sim$-0.15 V vs Ag/AgCl to $\sim$0.65 V, punctuated by transient pitting events in the region of 0.4 V. However, at pH 11.4, not only are these pitting features eliminated, the window of passivity is also extended to $\sim$-0.3 V to 0.75 V – indicating that simple dosing of the system with NaOH provides significant corrosion protection on unsensitised 20/25/Nb SS samples under these conditions. This protection is maintained at pH 11.4 at 45 °C in the presence of 30 μmol dm^{-3} of both Cl$^-$ and H_2O_2, i.e. under future interim storage conditions, with a separation of over a volt between the potential of zero current and onset of transpassivity indicating that intergranular attack is unlikely – at least on unsensitised cladding.

7.2.2 Heat Treated 20/25/Nb Stainless Steel

Analogues for RIS-affected cladding aim to be representative of approximately 25 % of AGR spent fuel cladding. The first analogue for RIS-affected cladding studied was 20/25/Nb SS solution annealed for 0.5 hours at 1150 °C and then aged 48 hours at 600 °C. The principal conclusions for this heat treated 20/25/Nb SS are as follows.

The OCP in simulant pond water (pH$\simeq$11.4) is found to be $\sim$-0.1 V vs Ag/AgCl. Under these conditions, XPS data indicates that the protective oxide layer formed on the surface of 20/25/Nb SS consists predominately of Fe and Cr oxides, with Fe oxide being the more dominant of the two. As with unsensitised 20/25/Nb SS, resistance and capacitance data from EIS experiments shows that the source of this protection changes on application of an oxidative stress i.e. as

the electrode potential is increased. Through Mott-Schottky analysis it was found that this change occurs at ∼0.1 V whereupon the protection provided by Fe oxides is lost due to its oxidative dissolution and Cr oxides dominate until 0.6 V.

Voltammetric studies were again used to determine the robustness of this oxide layer. Studies under baseline conditions of pH=8 at 24 °C show a wide region of passivity from ∼-0.15 V vs Ag/AgCl to ∼0.6 V. However, at pH 11.4 the window of passivity is extended to ∼-0.3 V to 0.75 V – indicating that simple dosing of the system with NaOH provides significant added corrosion protection for heat treated 20/25/Nb SS samples under these conditions. This protection is maintained at pH 11.4 at 45 °C in the presence of 30 μmol dm^{-3} of both Cl$^-$ and H$_2$O$_2$, i.e. under future interim storage conditions, with a separation of approximately a volt between the E$_{ZC}$ and onset of transpassivity and as E$_{OCP}$ lies within this passive range intergranular attack is unlikely.

7.2.3   Unsensitised 304H SS

The purpose of studying unsensitised 304H SS is twofold. Firstly, heat treated 304H SS has been proposed as a RIS-affected AGR cladding analogue, therefore it is essential to understand the baseline behaviour of unsensitised 304H SS before analysis of its heat treated counterparts can be undertaken. Secondly, direct comparisons between 20/25/Nb SS and 304H SS can be made and inherent behavioural differences elucidated.

The key conclusions regarding the electrochemical corrosion behaviour of unsensitised 304H SS are as follows.

The OCP in simulant pond water (pH≃11.4) is found to be ∼-0.19 V vs Ag/AgCl. Under these conditions, XPS data indicates that the protective oxide layer formed on the surface of 304H SS consists predominately of Fe and Cr oxides/hydroxides, with Fe oxide/hydroxide being the more dominant of the two. Resistance and capacitance data from EIS experiments once again show that the

source of this protection changes on application of an oxidative stress i.e. as the electrode potential is increased. Through Mott-Schottky analysis it was found that this change occurs at ~0.2 V whereupon the protection provided by Fe oxides decreases due to its oxidative dissolution and Cr oxides dominate until ~0.8 V.

Voltammetric studies were used to determine the stability of this oxide layer. Studies under baseline conditions of pH=8 at 24 °C show a region of passivity from ~-0.25 V vs Ag/AgCl to ~0.2 V. However, at pH 11.4 the window of passivity is extended to ~-0.25 V to 0.8 V – indicating that simple dosing of the system with NaOH provides significant added corrosion protection for 304H SS samples under these conditions. This protection is maintained at pH 11.4 at 45 °C in the presence of 30 μmol dm^{-3} of both Cl$^-$ and H$_2$O$_2$, i.e. under future interim storage conditions, with a separation of approximately a volt between E$_{ZC}$ and onset of transpassivity. Since the measured E$_{OCP}$ for this steel lies in this passive region, it is unlikely that intergranular attack will occur under these pond/solution conditions.

7.2.4 Heat treated 304H SS

Heat treated 304H SS was used as an analogue for RIS-affected AGR fuel cladding. The corrosion behaviour of two heat treated 304H SS samples under possible storage pond conditions was examined in this section, one sample heated for 48 hours at 600 °C and one heated for 72 hours at 600 °C. The principal conclusions are as follows.

The OCP in simulant pond water (pH$\simeq$11.4) is found to be ~-0.16 V vs Ag/AgCl and ~-0.2 V vs Ag/AgCl for the sample heated for 48 hours at 600 °C and the sample heated for 72 hours at 600 °C respectively. Under these conditions, XPS data for the sample aged for 48 hours indicates that the protective oxide layer formed on the surface of heat treated 304H SS consists predominately of Fe and Cr oxides/hydroxides, with Fe oxide/hydroxides being the far more dominant of

the two. Just as for the other SS samples, resistance and capacitance data from EIS experiments shows that the source of this protection changes on application of an oxidative stress i.e. as the electrode potential is increased. Through Mott-Schottky analysis it was found that this change occurs at $\sim$0.1 V and 0.2 V for the sample aged for 48 hours and the sample aged 72 hours respectively, whereupon the protection provided by Fe oxides decreases due to its oxidative dissolution and Cr oxides dominate until 0.6 V.

Voltammetric studies were used to determine the robustness of this oxide layer. Studies under baseline conditions of pH=8 at 24 °C show a short region of passivity from $\sim$-0.2 V vs Ag/AgCl to $\sim$0.2 V for both heat treated sample. However, at pH 11.4 the window of passivity is extended to $\sim$-0.4 V to 0.75 V and $\sim$-0.3 V to 0.85 V for the sample aged for 48 hours and the sample aged 72 hours respectively – indicating that simple dosing of the system with NaOH provides significant added corrosion protection for heat treated 304H SS samples under these conditions. This protection is maintained at pH 11.4 at 45 °C in the presence of 30 μmol dm^{-3} of both Cl$^-$ and H$_2$O$_2$, i.e. under future interim storage conditions, with a separation of approximately a volt between the E$_{ZC}$ and onset of transpassivity and as E$_{OCP}$ lies within this passive range intergranular attack is unlikely.

7.2.5   Robustness of the Passive Oxide Layer

The extent of the envelope of protection identified in the above subsections, for each stainless steel sample examined, was studied as a function of key solution parameters such as chloride concentration, temperature and hydrogen peroxide concentration – including conditions relevant to future wet storage scenarios and their fault conditions. Results are summarised in the following subsections.

7.2.5.1 Effect of Chloride Concentration

In the absence of hydroxide i.e. at pH 8 close to neutrality, chloride readily attacks the passive layer on cladding and cladding analogue samples studied from concentrations as low as 30 μmol dm^{-3} with the exception of heat treated 20/25/Nb SS which does not exhibit localised corrosion behaviour until concentrations of 592 μmol dm^{-3}. Key features of this attack are a cathodic shift in the onset transpassivity and appearance of pitting corrosion in the passive range. For 304H SS samples, at [Cl$^-$]$\geq$28 mmol dm^{-3} there is no evidence of passivation thus the surface is expected to corrode freely. However, when the pH is increased to 11.4, i.e. the pH of dosed simulant pond water, chloride is only seen to induce either type of corrosion behaviour (shift in onset of transpassivity, pitting corrosion) at concentrations greater than 56 mmol dm^{-3} for 20/25/Nb SS samples and $\sim$28 mmol dm^{-3} for 304H SS samples. This is a significantly higher chloride concentration than expected under foreseen fault conditions, indicating that protection will be maintained under such.

7.2.5.2 Effect of Temperature

For all samples the onset of transpassivity moves towards more negative potentials with increasing temperature and generally there are increased uniform corrosion currents at elevated temperatures. However, passivation of the surface is expected to occur at the OCPs for pond water temperatures $\leq$60 °C, despite the changes in behaviour with temperature. Therefore, there seems to be no localised corrosion threat to fuel cladding as electrolyte/storage medium temperature is increased from 24 °C to 60 °C i.e. under the anticipated operating conditions. At 90 °C the protective oxide layer on the surface of SS samples breaks down and the OCPs lie in regions where the uninhibited dissolution of the samples is likely to proceed with the exception of unsensitised 304H whose OCP lies in the short potential passive window. Therefore, significant damage to the surface of the cladding would be expected if it were kept under such

maloperation conditions for any extended period of time.

7.2.5.3   Effect of Hydrogen Peroxide

Voltammetry indicates that H_2O_2 is simply oxidised at the surface of 20/25/Nb SS and 304H SS in the passive potential range. The associated oxidation current increases linearly with concentration values in the range $[H_2O_2]$ = 10 to 500 μmol dm^{-3}. At values higher than this, the associated current becomes invariant with concentration, indicating that the oxidation of peroxide at the steel surface is controlled by a surface adsorption process.

At simulant pond water temperatures between 45-90 °C the presence of peroxide promotes growth of a protective layer thus extending the potential passive window. For 20/25/Nb SS samples, at 90 °C the presence of peroxide suppresses the pitting corrosion that is observed at 0.2 V in the passive range at the same temperature in peroxide-free electrolytes - suggesting that peroxide actually has a protective action on 20/25/Nb SS at this temperature. However, for 304H SS samples, at 90 °C pitting corrosion is observed in the passive region and therefore the SS surface will be vulnerable to localised attack under this accident condition.

7.2.6   Comparison of the Corrosion Behaviour of the Stainless Steel Samples

7.2.6.1   Comparison of heat treated and unsensitised 20/25/Nb SS

Comparing the behaviour of heat treated 20/25/Nb SS to its unsensitised counterpart some further conclusions can be drawn. In general, under the conditions studied heat treated 20/25/Nb SS appears to be marginally more susceptible to transpassive corrosion and thus intergranular attack. This observation is consistent with oxalic etch and DL-EPR tests which show a greater susceptibility to intergranular attack and with XPS studies which showed

reduced Cr(III) oxide and Cr spinel content in the passive layer at OCP. EIS studies also show a decrease in contributions of chromium to the passive layer, all suggesting heat treatment results in net depletion of Cr at the grain boundaries. Interestingly heat treatment does not seem to increase susceptibility to pitting or general corrosion, in fact the unsensitised sample appears more vulnerable. As discussed in section 4.3, in neutral to alkaline conditions Fe oxides are less soluble than Cr oxides. During heat treatment some Cr is immobilised by the formation of chromium carbides and therefore unavailable to participate in oxide layer growth resulting in an Fe rich protective layer. Hence, general corrosion of heat treated 20/25/Nb SS occurs at a slower rate than for unsensitised 20/25/Nb SS.

With regards to pitting susceptibility, one could speculate that during heat treatment NbC inclusions, which provide pitting centres, are dissolved and Nb dispersed throughout the steel matrix. Therefore, there are fewer pitting centres on the SS surface and heat treated 20/25/Nb SS becomes less prone to pitting corrosion than unsensitised 20/25/Nb SS. This difference in behaviour is evident for the SS samples in simulant pond water containing peroxide at 90 °C. Unsensitised samples exhibit transpassive behaviour at 0.2 V likely initiated through pit formation whereas due to the dissolution of NbC pitting centres in the heat treated sample H_2O_2 is able to shut down the metastable pit and maintain some passivity.

7.2.6.2 Comparison of unsensitised 304H SS and unsensitised 20/25/Nb SS

Comparing the behaviour of unsensitised 304H SS to unsensitised 20/25/Nb SS some further insights can be gained. Generally, under the conditions studied, unsensitised 304H SS appears to be slightly more susceptible to transpassive corrosion and thus intergranular attack. This observation is consistent with oxalic etch and DL-EPR tests for 304H SS which show a greater susceptibility to intergranular attack compared to 20/25/Nb SS. This is also in agreement with

the XPS and EIS studies which showed reduced Cr(III) oxide content in the passive layer at OCP on 304H SS. This vulnerability to transpassive corrosion may also be due to the reduced nickel content in 304H SS which would presumably offer a thinner inner protective oxide/hydroxide layer compared to that formed on 20/25/Nb SS. This behaviour is most evident at elevated temperatures and in solutions containing high chloride concentrations. With regards to pitting susceptibility, one could speculate that since the NbC inclusions present in 20/25/Nb SS, which provide pitting centres, are not present in 304H SS this leaves 304H SS less vulnerable to this form of localised attack. This difference in behaviour is evident for the SS samples in simulant pond water containing $[Cl^-] \simeq 28$ mmol dm^{-3} and in simulant pond water at 90 °C. Uniform corrosion in the passive range occurs at almost the same rate for all studies at pH 11.4. This indicates that despite some compositional differences in the passive layers on 20/25/Nb and 304H SSs the mechanism for uniform loss of Fe and Cr oxides from the outer surface are concurrent and if the loss of the one oxide is more preferable to the other the residual oxide is able to compensate for this loss effectively in alkaline solutions.

7.2.6.3   Comparison heat treated 304H SS and unsensitised 304H SS

Heat treated 304H SS is more susceptible to general corrosion, pitting and transpassive corrosion than its unsensitised counterpart. This is suspected to be largely due to the depletion of chromium from the grain boundaries during heat treatment, this results in the formation of an inhomogeneous passive layer with reduced Cr oxide/hydroxide content leaving the heat treated samples more vulnerable to corrosion.

7.2.6.4 Comparison of heat treated 304H SS and heat treated 20/25/Nb SS

Comparing the behaviour of heat treated 304H SS to heat treated 20/25/Nb SS some further conclusions can be drawn. Generally, although heat treated 20/25/Nb SS exhibited less pitting susceptibility than unsensitised 20/25/Nb SS it is still more susceptible to this type of corrosion than heat treated 304H SS. This could indicate that perhaps not all of the NbC pitting centres were dissolved during heat treatment.

Heat treated 304H SS was more susceptible, than heat treated 20/25/Nb SS, to transpassive dissolution under the same experimental conditions. This indicates an inability of heat treated 304H samples to shut down pitting and/or other localised corrosion events compared with heat treated 20/25/Nb SS. This is possibly a result of the much lower Ni content of 304H SS and/or the lower contribution of Cr(III) oxide/hydroxide to the passive layer observed via XPS analysis.

7.2.7 Uranium dioxide and AGR Simulant Spent Nuclear Fuels

Previously published work on corrosion behaviour of undoped UO_2 and AGR SIMFuel materials, of different simulated burnups, is limited and is especially sparse under the aqueous alkaline conditions (pH$\simeq$11.4) relevant to interim storage. This thesis has provided a combined voltammetric and impedance spectroscopic study of the fundamental surface structure and chemistry of UO_2 and AGR SIMFuels in such environments.

Further, the results can have also been compared to the behaviour of UO_2 and AGR SIMFuels (with simulated burups of 25 GWd/tU and 43 GWd/tU) in a simple electrolyte of 0.5 mol dm^{-3} Na_2SO_4, of a lower pH, pH$\simeq$5.6. The principal

conclusions are as follows.

Lower corrosion currents were recorded for all three samples in simulant pond water compared to those seen in the Na_2SO_4 solution. This suggests the growth of a thicker oxide layer in alkaline solutions. Similarly, the OCP for all samples under mild alkaline pond water conditions are more negative than those in the neutral sulphate-only bearing electrolyte. Particularly, the OCP for the SIMFuel samples moves from a region where active dissolution of the surface may be expected to an area where an oxide layer is developing, predicted via comparison with the results of CV experiments and previously published UO_2-H_2O Pourbaix (E vs pH) diagrams. Said oxide layer potentially protects the surface from further dissolution.

In order to further understand the properties and development of this oxide layer EIS Mott-Schottky analysis was also performed under the same conditions. Such a technique is applicable here due to the semiconductor properties of UO_2 and SIMFuels. Results for the pure UO_2 sample have shown there is a transition from p-type semiconductor behaviour at E<-1.1 to n-type semiconductor behaviour at E>-0.5 V. This is consistent with what is known about the electronic properties of these materials. Hydrogen evolution is catalysed by ε-particles in SIMFuel and thus, the region of p-type semiconductor behaviour was shown to be masked by hydrogen evolution in the experiments on SIMFuel samples. Through further more detailed analysis it was determined that in the region of n-type semiconductor behaviour, -0.5 to 0 V, the UO_2 matrix oxidises to U_3O_7 and SIMFuels oxidise to U_4O_9. This potential region corresponds with a region of increased resistance in the R_p vs E plots, from standard EIS equivalent circuit fits. Comparison of the OCP to the C^{-2} vs E plots reveals that the OCP of all three samples sit at a position where U_4O_9/U_3O_7 is beginning to oxidise and re-precipitate as $UO_3 \cdot yH_2O$ providing the aforementioned surface protection from further dissolution/oxidation.

In addition to the above, experiments were also performed to determine the effects of chloride and temperature on the corrosion behaviour of UO_2 and AGR SIMFuel in wet storage conditions. While high levels of chloride have been shown

to reduce the corrosion resistance of AGR fuel cladding, UO_2 and SIMFuels remain relatively unaffected by increases in chloride concentration. Specifically, at pond water pH values UO_2 chloro complexation was shown not to occur and the oxidation of the uranium surface layer proceeds without disruption from Cl^- ions.

With respect to changes in temperature, for pure UO_2 at OCP no significant change in measured corrosion currents at temperatures ≤ 60 °C has been observed. However, for both SIMFuel samples at temperatures ≤ 60 °C there are small changes in the measured corrosion currents at OCP with temperature. Compared to the currents measured at 24 °C, at 45 °C the measured current decreased and at 60 °C the measured currents increased. Increases in the corrosion current are suggested to be a result of enhanced oxidation of the sample and it could be speculated that this would result in the formation of thicker oxide layers. However, further experiments are necessary to confirm whether a thicker oxide layer forms at higher temperatures and whether this thicker layer enhances corrosion resistance. Finally, at simulant pond water temperature of 90 °C there is a clear enhancement of the measured corrosion currents. Measured open circuit potentials lie within the potential range where U_3O_7/U_4O_9 is expected to exist for all samples and at all temperatures investigated.

In summary, these short duration linear sweep voltammetry experiments provide preliminary indications that dosing pond water to a pH$\simeq$11.4, with an expected chloride concentration of ~ 30 μmol dm^{-3} and hydrogen peroxide concentration of ~ 30 μmol dm^{-3}, provides corrosion protection to cladding samples at the temperatures studied, 24 °C (current conditions), 45 °C (projected future pond temperature) and 60 °C (predicted peak operating conditions). However, general corrosion rates of heat treated stainless steels are higher than those of their unsensitised counterparts and spent fuel stringers likely to be affected by RIS should be monitored more closely. In the improbable

event the temperatures of 90 °C are reached (potential maloperations / fault condition) degradation of the fuel cladding will be accelerated and it is of utmost importance to ensure operating conditions are returned to normal as soon as possible after the incident.

In the unlikely event the cladding is breached and the fuel itself is exposed to simulant pond water, the electrochemical experiments described in this thesis provide initial evidence that for UO_2 and SIMFuels dosing pond water to a pH$\simeq$11.4, with an expected chloride concentration of $\sim$1 ppm, will result in passivation, and thus protection from surface dissolution, through the development of a protective U_4O_9/U_3O_7 surface film for simulant pond water temperatures between 24 and 90 °C.

7.3 Further Work

Initial work has been carried out to investigate the corrosion susceptibility of AGR SNF under the proposed interim storage regime implemented on the closure of THORP. Further research is still necessary to gauge how well the cladding and fuel analogues represent actual irradiated cladding and SNF. As a result several key areas of further study are still outstanding:

1. Although sensitised stainless steel analogues with increased susceptibility to local corrosion have been developed, an ideal RIS-affected cladding analogue which meets all the required criteria has not been produced so far. Electrochemical studies should therefore be carried out on real irradiated fuel cladding. The cladding sample should be from a fuel stringer that has experienced temperatures likely to induce RIS, i.e. 350–520 °C.

2. Considering a substantial fraction of the fuel cladding will remain unsensitised, an irradiated cladding sample that is unaffected by RIS could be analysed to compare to as-received 20/25/Nb SS. This would allow other possible radiation induced effects that could influence the corrosion

behaviour of fuel cladding to be elucidated.

3. Carbon deposits on the fuel cladding surface are likely to occur during its time in reactor. It is possible carbon deposits may result in the precipitation of chromium-rich carbides at the grain boundaries. Separately, 20/25/Nb SS oxidised in CO_2 has been shown to form an outer spinel phase and an inner chromia rich phase, however the oxides formed appear to be sensitive to temperature and pressure [269] [270]. As such, the influence of a pre-existing oxide layer and carbide deposits on the corrosion behaviour in interim storage should be investigated by carrying out electrochemical experiments on 20/25/Nb SS pre-oxidised in CO_2.

4. A new batch of SIMFuels with grain size and porosity closer to that of real spent nuclear fuel have since been manufactured by the NNL. Electrochemical studies performed on these new SIMFuels will provide a more representative picture of the corrosion behaviour of AGR SNF.

5. To assess the legitimacy of using SIMFuels, experiments should be performed on real spent nuclear fuel. The likeness of AGR SIMFuels to real irradiated fuel could be evaluated by comparing the electrochemical corrosion behaviour of SIMFuels to that of real fuel samples.

6. The surface composition of the UO_2 and SIMFuels was determined to be U_3O_7/U_4O_9 through Mott-Schottky analysis. Confirmation of the compositional characterisation should be carried out using XPS or Infrared-Visible Sum Frequency Generation Spectroscopy. Unfortunately, due to time and access restrictions this was not carried out as part of the project presented in this thesis.

7. If the surface layer of SIMFuels is indeed U_4O_9 studies on the corrosion behaviour of U_4O_9 must be considered. This could be investigated by carrying experiments on U_4O_9 thin films deposited on piezoelectric quartz

crystal electrodes. Electrochemical Quartz Crystal Microbalance (EQCM) studies allow mass losses and gains to be measured over the potential range of interest.

8. Given that the spent fuel matrix will be in intimate contact with the cladding in interim storage, it is entirely possible that the electrochemistries of these two materials may couple in a manner that accelerates the corrosion processes of one or the other. In the event that the fuel cladding is perforated, both fuel and cladding will be simultaneously exposed to pond water. Interrogating the binary systems of SIMFuels and cladding, and a cross-section of real SNF will provide valuable insight into whether the corrosion of fuel cladding is accelerated, inhibited or unaffected by the presence of SNF and vice versa.

Bibliography

[1] J Kyffin. The Technical Case for Interim Storage of AGR Fuel, 2014.

[2] G.O.H Whillock, B.J Hands, and T Carey. Assessed efficacy of sodium hydroxide as a corrosion inhibitor for AGR fuel at elevated temperatures. Technical report, National Nuclear Laboratory, Sellafield Ltd, 2014.

[3] Radioactivity.eu.com. Radioactive Waste.

[4] U.S.NRC. *Stages of the Nuclear Fuel Cycle.* https://www.nrc.gov/materials/fuel-cycle-fac/stages-fuel-cycle.html.

[5] World Nuclear Organisation. *Nuclear fuel cycle.* http://www.world-nuclear.org/information-library/nuclear-fuel-cycle.aspx, 2017.

[6] Nuclear Fuel Cycle Information System, IAEA-TECDOC-1613. Technical report, IAEA-TECDOC-1613, 2009.

[7] G Rossiter and M Mignanelli. The characteristics of LWR fuel at high burnup and their relevance to AGR spent fuel. Technical report, National Nuclear Laboratory, 2011.

[8] JM McKibben, DF Chostner, and EG Orebaugh. Plutonium-uranium separation in the Purex process using mixtures of hydroxylamine nitrate and ferrous sulfamate. Technical report, Savannah River Laboratory, 1983.

[9] Sergio Peraza. *Lecture Notes: Purex.* The University of Utah, The University of Utah, 2015.

[10] Nuclear matters. *Multi-barrier disposal of radioactive waste.* http://nuclearmatters.co.uk/2011/02/multi-barrier-disposal-of-radioactive-waste/, 2011.

[11] BEIS. Implementing Geological Disposal - Annual Report. Technical report, 2018.

[12] Wikipedia. *Advanced Gas-cooled Reactor.* https://en.wikipedia.org/wiki/Advanced_Gas-cooled_Reactor.

[13] B.D Murphy. ORIGEN-ARP Cross-Section Libraries for Magnox, Advanced Gas-Cooled, and VVER Reactor Designs. Technical report, Nuclear Science and Technology Division, Oak Ridge National Laboratory, 2004.

[14] S Jones. *Ceramics - Art or Science?* 2014.

[15] A Keshmiri. Three-dimensional Simulation of a Simplified Advanced Gas-cooled Reactor Fuel Element. *Nuclear Engineering and Design*, 241(10):4122–4135, 2011.

[16] IAEA-TECDOC-944. Further analysis of extended storage of spent fuel. Technical report, 1997.

[17] IAEA-TECDOC-1012. Durability of spent nuclear fuels and facility components in wet storage. Technical report, 1998.

[18] P.N Standring. The Long-term Storage of Advanced Gas-Cooled Reactor (AGR) Fuel. In *Storage of Spent Fuel from Power Reactors*. International Atomic Energy Agency - IAEA-TECDOC-1089, 1999.

[19] C Heng Phuah. *Corrosion of Thermally-aged Advanced Gas-Cooled Reactor Fuel Cladding.* PhD thesis, Imperial College London, 2012.

[20] A.B Johnson. Impacts of Reactor-Induced Cladding Defects on Spent Fuel Storage. Technical report, PNL-SA-6917, Pacific Northwest Laboratories - NEA Seminar on the Storage of Spent Fuel Elements, 1978.

[21] A.B Johnson. Behaviour of Spent Nuclear Fuel in Water Pool Storage. Technical report, Pacific Northwest Laboratories, BNWL-2256, 1977.

[22] K.M Wasywich and C.R Frost. Examination of used CANDU fuel following 27 years of storage under water. In *Proceedings of the third international conference on nuclear fuel reprocessing and waste management.* Japan Atomic Industrial Forum, 1991.

[23] J.F Walker. The Long-Term Storage of Irradiated CANDU Fuel under Water. Technical report, Atomic Energy of Canada Limited, AECL-6313, 1979.

[24] J.R Davis. *Corrosion: Understanding the Basics.* ASM International, 2000.

[25] D Landolt. *Corrosion and Surface Chemistry of Metals.* EPFL Press, 2007.

[26] E McCafferty. *Introduction to Corrosion Science.* Springer Science & Business Media, 2010.

[27] Corrosion Clinic. *Lecture 11: Electrochemical Techniques.* http://www.corrosionclinic.com/corrosion_online_lectures/ME303L11.HTM.

[28] B Beverskog and I Puigdomenech. Revised Pourbaix Diagrams for Iron At 25-300C. *Corrosion Science*, 38(12):2121–2135, 1996.

[29] M Pourbaix. *Atlas of electrochemical equilibria in aqueous solutions.* NACE, 1974.

[30] B Beverskog and I Puigdomenech. Revised Pourbaix Diagrams for Chromium At 25-300C. *Corrosion Science*, 39(1):43–57, 1997.

[31] C.O.A Olsson and D Landolt. Passive films on stainless steels—chemistry, structure and growth. *Electrochimica Acta*, 48(9):1093–1104, apr 2003.

[32] Aalco. Stainless Steel : Alloying in Elements Stainless Steel. Technical report, http://www.aalco.co.uk/datasheets/Stainless-Steel_Alloying-Elements-in-Stainless-Steel_98.ashx, 2013.

[33] E. Zumelzu, O. Opitz, C. Cabezas, A. Parada, and L. Goyos. High-chromium (22-34 per cent) cast iron alloys and their simulated behaviour at the sugar industry. *Journal of Scientific and Industrial Research*, 62(6):583–588, 2003.

[34] H.K.D.H Bhadeshia. *Bainite in Steels: Theory and Practice.* CRC Press, 3rd editio edition, 2015.

[35] B Beverskog and I Puigdomenech. Revised Pourbaix Diagrams for Nickel At 25-300C. *Corrosion Science*, 39(5):969–980, 1997.

[36] R.J Wilbraham. *Surface Decontamination by Photocatalysis.* PhD thesis, Lancaster University, 2011.

[37] WebCorr Corrosion Consulting Services. *Different Types of Corrosion.* http://www.corrosionclinic.com/types_of_corrosion/.

[38] B Nimmo and G Hinds. Beginners Guide to Corrosion. Technical report, NPL, 2003.

[39] E Mattsson. *Basic Corrosion Technology for Scientists and Engineers.* Institute of Materials, 2nd editio edition, 1996.

[40] R.H Jones, M.J Danielson, and D.R Baer. Microchemistry and Mechanics Issues in Stress Corrosion Cracking. In R.P Wei and R.P Gangloff, editors, *Fracture Mechanics: Perspectives and Directions (Twentieth Symposium)*, pages 209–232. ASTM International, 1989.

[41] P. Marcus, V. Maurice, and H. H. Strehblow. Localized corrosion (pitting): A model of passivity breakdown including the role of the oxide layer nanostructure. *Corrosion Science*, 50(9):2698–2704, 2008.

[42] King Fahd University of Petroleum and Minerals. *Forms of Corrosion.* http://faculty.kfupm.edu.sa/ME/hussaini/Corrosion Engineering/04.11.02.html.

[43] D Kopeliovich. *Pitting Corrosion.* http://www.substech.com/, 2015.

[44] D Talbot and J Talbot. *Corrosion Science and Technology.* CRC Press, 1997.

[45] Sacome. *How to avoid intergranular corrosion? "L" or "Ti" Stainless Steel?* https://www.sacome.com/en/avoid-intergranular-corrosion/, 2017.

[46] J Woodtli and R Kieselbach. Damage due to hydrogen embrittlement and stress corrosion cracking. *Engineering Failure Analysis*, (7):427–450, 2000.

[47] J.R Galvele. Transport processes in passivity breakdown—II. Full hydrolysis of the metal ions. *Corrosion Science*, 21(8):551–579, 1981.

[48] M. K. Nieuwoudt, J. D. Comins, and I. Cukrowski. Analysis of the composition of the passive film on iron under pitting conditions in 0.05 M NaOH/NaCl using Raman microscopy in situ with anodic polarisation and MCR-ALS. *Journal of Raman Spectroscopy*, 43(7):928–938, 2012.

[49] J Horvath and H.H Uhlig. Critical for Pitting Corrosion of Ni, Cr-Ni, Cr-Fe and Relaed Stainless Steels. *Journal of Electrochemical Society*, 115(8):791–795, 1968.

[50] H.P Leckie and H.H Uhlig. Environmental Factors Affecting the Critical Potential for Pitting in 18-8 Stainless Steel. *Journal of Electrochemical Society*, 113:1262–1267, 1966.

[51] S Haupt and H.H Strehblow. A combined surface analytical and electrochemical study of the fomation of passive layers on Fe/Cr alloys in 0.5 M H2SO4. *Corrosion Science*, 37:43–54, 1995.

[52] P Schmutz and D Landolt. In-situ microgravimetric studies of passive alloys: potential sweep and potential step experiments with Fe-25Cr and Fe-17Cr-33Mo in acid and alkaline solution. *Corrosion Science*, 41:2143–2163, 1999.

[53] S-H Jung, J Yeon, and K Song. Effect of pH , temperature , and H 2 O 2 on the electrochemical oxidation behavior of iron in perchlorate solutions. pages 333–339, 2014.

[54] J.G.N Thomas. The Electrochemistry of Corrosion. Technical report.

[55] S. Ningshen, U.K. Mudali, and R.K. Dayal. Electrolyte and temperature effects on pitting corrosion of type 316LN stainless steels. *British Corrosion Journal*, 36(1):36–41, 2001.

[56] M.A.M Ibrahim, S.S Abd El Rehim, and M.M Hamza. Corrosion behaviour of some austenitic stainless steels in chloride environments. *Materials Chemistry and Physics*, 115:80–85, 2009.

[57] J.H. Wang, C.C. Su, and Z Szklarska-Smialowska. Effects of Cl Concentration and Temperature on Pitting of AISI 304 Stainless Steel. *Corrosion*, 44:732–737, 1988.

[58] J C Langevoort, I Sutherland, L J Hanekamp, and P J Gellings. On the Oxide Formation on Stainless Steels Aisi 304 and Incoloy 8Ooh Investigated With Xps. *Applied Surface Science*, 28:167–179, 1987.

[59] G.R Choppin, J-O Liljenzin, and J Rydberg. *Radiochemistry and Nuclear Chemistry*. Butterworth-Heinemann, 2002.

[60] K Bobrowski. Radiation Chemistry of Liquid Systems. In *Applications of Ionizing Radiation in Materials Processing*, pages 81–116. 2017.

[61] S Sunder. Alpha, Beta and Gamma Dose Rates in water in Contact with Used CANDU UO2 Fuel. Technical report, Atomic Energy of Canada Ltd, 1995.

[62] D.W Shoesmith. Fuel corrosion processes under waste disposal conditions. *Journal of Nuclear Materials*, 282(1):1–31, nov 2000.

[63] E.C Buck, R.S. Wittman, F.N. Skomurski, K.J. Cantrell, B.K. McNamara, and C.Z. Soderquist. Radiolysis Process Modeling Results for Scenarios : Used Fuel Disposition. Technical report, Pacific Northwest National Laboratory for US Department of Energy, Separations/Waste Form Campaign, 2002.

[64] Sophie Le Caër. Water Radiolysis: Influence of Oxide Surfaces on H2 Production under Ionizing Radiation. *Water*, 3(4):235–253, 2011.

[65] C Patrício and M Lousada. *Reactions of aqueous radiolysis products with oxide surfaces: An experimental and DFT study.* PhD thesis, KTH Chemical Science and Engineering, 2013.

[66] S Sunder, N.H Miller, and D.W Shoesmith. Corrosion of uranium dioxide in hydrogen peroxide solutions. *Corrosion Science*, 46:1095–1111, 2004.

[67] I Štefanić and J.A LaVerne. Temperature dependence of the hydrogen peroxide production in the γ-radiolysis of water. *Journal of Physical Chemistry A*, 106(2):447–452, 2002.

[68] D Swiatla-Wojcik. Computation of the effect of pH on spur chemistry in water radiolysis at elevated temperatures. *Nukleonika*, 53(SUPPL. 1), 2008.

[69] R Venkatachalapathy, G.P Davila, and J Prakash. Catalytic decomposition of hydrogen peroxide in alkaline solutions. *Electrochemistry Communications*, 1:614–617, 1999.

[70] J.O'M. Bockris and L F Oldfield. The Oxidation-Reduction Reactions of Hydrogen Peroxide at Inert Metal Electrodes and Mercury Cathodes. *Transactions of the Faraday Society*, 51:249–259, 1955.

[71] B. R. Leavitt. In Situ Iron Oxidation using Hydrogen Peroxide. In *Proceedings America Society of Mining and Reclamation*, pages 551–569, 2010.

[72] I.M Kolthoff and A.I Medalia. The Reaction between Ferrous Iron and Peroxides. I. Reaction with Hydrogen Peroxide in the Absence of Oxygen. *Journal of the American Chemical Society*, 71:3777–3783, 1949.

[73] K. C. Namkung, A. E. Burgess, and D. H. Bremner. A fenton-like oxidation process using corrosion of iron metal sheet surfaces in the presence of hydrogen peroxide: A batch process study using model pollutants. *Environmental Technology*, 26(3):341–352, 2005.

[74] T.H Song and I.S Kim. Effect of H2O2 on the Corrosion Behaviour of 304L Stainless Steel. *Journal of the Korean Nuclear Society*, 27(4):453–462, 1995.

[75] A Sharma and V Kumar. Behavior of Steels against Corrosion in Peroxide Solutions. *Journal of Materials and Environmental Science*, 3(1):76–84, 2011.

[76] R Sundara. Hot peroxide bleaching. *Canadian Chemical News*, 50:15–17, 1998.

[77] T Miyazawa, T Terachi, S Uchida, T Tsukada, Y Satoh, and Y Wada. Effects of Hydrogen Peroxide on Corrosion of Stainless Steel , (V) Characterization of Oxide Film with Multilateral Surface Analyses. *Journal of Nuclear Science and Technology*, 43(8):884–894, 2006.

[78] Y Wada, A Watanabe, M Tachibana, N Uetake, S Uchida, K Akamine, S Suzuki, K Ishigure, Y Wada, A Watanabe, M Tachibana, and K Ishida. Effects Of Hydrogen Peroxide On Intergranular Stress Corrosion Cracking Of Stainless Steel in High Temperature Water , (IV) Effects of Hydrogen Peroxide on Intergranular Stress Corrosion Cracking of Stainless Steel in High Temperature Water , (IV) Eff. *Journal of Nuclear Science and Technology*, 38(3):183–192, 2001.

[79] D. Herbert, G.O.H. Whillock, and S.E Worthington. Zero Resistance Ammetry - Its Application in Preventing the Corrosion of Stainless Steel

in Cooling Waters. In *Electrochemical Methods in Corrosion Research V, Materials Science Forum*, pages 469–476. Trans Tech Publications, 1995.

[80] C. Anwyl, C. Boxall, R.J Wilbraham, D. Hambley, and C. Padovani. Corrosion of AGR Fuel Pin Steel Under Conditions Relevant to Permanent Disposal. *Procedia Chemistry*, 21:247–254, 2016.

[81] P. Ernst, N.J. Laycock, M.H. Moayed, and R.C. Newman. The mechanism of lacy cover formation in pitting. *Corrosion Science*, 39(6):1133–1136, 1997.

[82] G.O.H. Whillock, B.J Hands, T.P Majchrowski, and D I Hambley. Investigation of thermally sensitised stainless steels as analogues for spent AGR fuel cladding to test a corrosion inhibitor for intergranular stress corrosion cracking. *Journal of Nuclear Materials*, 498:187–198, 2018.

[83] G.P Marsh and I.W Cavell. Corrosion inhibitors for CAGR fuel storage. Technical report, AERE G3-203, AGR-FSCWP P83, 1984.

[84] C.A English, S.M Murphy, and J.M Perks. Radiation-induced Segregation in Metals. *Journal of the Chemical Society, Faraday Transactions*, 86(8):1263–1271, 1990.

[85] T.R Allen, J.Y Busby, G.S Was, and E.A Kenik. On the mechanism of radiation-induced segregation in austenitic Fe–Cr–Ni alloys. *Journal of Nuclear Materials*, 255:44–58, 1998.

[86] G.S Was, J.P Wharry, B Frisbie, B.D Wirth, D Morgan, J.D Tucker, and T.R Allen. Assessment of radiation-induced segregation mechanisms in austenitic and ferritic–martensitic alloys. *Journal of Nuclear Materials*, 411:41–50, 2011.

[87] J.F Bates, R.W Powell, and E.R Gilbert. Reduction of Irradiation-Induced Creep and Swelling in AISI 316 by Compositional Modifications. In *Effects of Radiation on Materials: Proceedings of the Tenth International Symposium*, pages 713–734. ASTM International, 1980.

[88] D.I.R Norris, C Baker, and J.M Titchmarsh. A Study of Radiation-Induced Sensitisation in 20/25/Nb Steel by Compositional Profile Measurements. In *Materials for nuclear reactor core applications: proceedings of the international conference*, pages 277–283. British Nuclear Energy Society, 1987.

[89] C Taylor, R Sumerling, and D Rhodes. The Development of Sensitised Structures in CAGR Fuel Pin Cladding: a Brief Summary of Recent WNL Observations. Technical report, UKAEA, 1982.

[90] D.I.R Norris, C Baker, C Taylor, and J.M Titchmarsh. Radiation-Induced Segregation in 20Cr/25Ni/Nb Stainless Steel. In R.E Stoller, A.S Kumar, and D.S Gelles, editors, *Effects of Radiation on Materials: Proceedings of the 15th International Symposium*, pages 603–620. ASTM International, 1992.

[91] I.E. Wilson and A.D. King. Post-Storage Examination of Pond Stored CAGR Fuel: Progress Report on Work Carried Out at WL. Technical report, UKAEA, 1987.

[92] R Singh. Influence of cold rolling on sensitization and intergranular stress corrosion cracking of AISI 304 aged at 500 C. *Journal of Materials Processing Technology*, 206:286–293, 2008.

[93] N Parvathavarthini. Sensitization and Testing for Intergranular Corrosion. In H.S Khatak and B Raj, editors, *Corrosion of Austenitic Stainless Steels: Mechanism, Mitigation and Monitoring*, page 117. Alpha Science International, 2002.

[94] D.I.R Norris. Radiation-induced sensitisation of stainless steels. In *Symposium on radiation-induced sensitisation of stainless steels, United Kingdom*. Central Electricity Generating Board, London (UK), 1987.

[95] Outokumpu. High Performance Austenitic Stainless Steel - Technical Report. Technical report, https://www.outokumpu.com/en/austenitic-grades, 2013.

[96] ATI. ATI 20-25+Nb Stainless Steel: Technical Data Sheet. Technical report, ATI metals, 2013.

[97] G.O.H. Whillock, B.J Hands, and T Carey. AGR cladding corrosion: Development of a non-active analogue for use in inhibitor tests at elevated temperatures. Technical report, National Nuclear Laboratory, Sellafield Ltd, 2015.

[98] Z Hiezl. *Processing and Microstructural Characterisation of UO2-based Simulated Spent Nuclear Fuel Ceramics for the UK's Advanced Gas-cooled Reactors.* PhD thesis, Imperial College London, 2015.

[99] D.W Shoesmith, S. Sunder, and W.H Hocking. Electrochemistry of UO2 Nuclear Fuel. In J. Lipkowski and P.N. Ross, editors, *Electrochemistry of Novel Materials: Frontiers of Electrochemistry*, pages 297–338. VCH Publishers, 1994.

[100] H He, Z Qin, and D. W Shoesmith. Characterizing the relationship between hyperstoichiometry, defect structure and local corrosion kinetics of uranium dioxide. *Electrochimica Acta*, 56(1):53–60, 2010.

[101] J. M. Elorrieta, L. J. Bonales, N. Rodríguez-Villagra, V. G. Baonza, and J. Cobos. A detailed Raman and X-ray study of UO$_{2+x}$ oxides and related structure transitions. *Phys. Chem. Chem. Phys.*, 18(40):28209–28216, 2016.

[102] H He, M.E Broczkowski, K O'Neill, D Ofori, O Semenikhin, and D.W Shoesmith. Corrosion of Nuclear Fuel (UO2) Inside a Failed Nuclear Waste Container, A Review of Research Conducted Under the Industrial Research Chair Agreement Between NSERC, NWMO and Western University (January 2006 to December 2010). Technical report, Nuclear Waste Management Organisation, 2012.

[103] B.T.M Willis. Structures of UO2, UO2+x andU4O9 by neutron diffraction. *Journal de Physique*, 25(5):431–439, 1964.

[104] B. T.M. Willis. The defect structure of hyper-stoichiometric uranium dioxide. *Acta Crystallographica Section A*, 34(1):88–90, 1978.

[105] N. A. Brincat, M. Molinari, S. C. Parker, G. C. Allen, and M. T. Storr. Computer simulation of defect clusters in UO2and their dependence on composition. *Journal of Nuclear Materials*, 456:329–333, 2015.

[106] H He and D.W Shoesmith. Raman spectroscopic studies of defect structures and phase transition in hyper-stoichiometric UO2+x. *Physical Chemistry Chemical Physics*, 12(28):8108, 2010.

[107] L Wu. *The Electrochemistry of Hydrogen Peroxide on Uranium Dioxide and the Modelling of Used Nuclear Fuel Corrosion under Permanent Disposal Conditions*. PhD thesis, Western University, London, Ontario, Canada, 2014.

[108] H Lim, Y Yun, K Park, and K.W Song. Electronic Structure of Uranium Dioxide. *Journal of Nuclear Science and Technology*, 39(sup3):110–113, 2002.

[109] A. Seibert, D. H. Wegen, T. Gouder, J. Römer, T. Wiss, and J. P. Glatz. The use of the electrochemical quartz crystal microbalance (EQCM) in corrosion studies of UO2thin film models. *Journal of Nuclear Materials*, 419(1-3):112–121, 2011.

[110] B.G. Santos, J.J Noel, and D.W. Shoesmith. The effect of pH on the anodic dissolution of SIMFUEL (UO2). *Journal of Electroanalytical Chemistry*, 586:1–11, 2006.

[111] S Sunder, D.W. Shoesmith, R.J Lemire, M.G. Bailey, and G.J. Wallace. The effect of ph on the corrosion of nuclear fuel (UO2) in oxygenated solutions. *Corrosion Science*, 32(4):373–3886, 1991.

[112] M.E Torrero, E Baraj, J Pablo, J Gimenez, and I Casas. Kinetics of corrosion and dissolution of uranium dioxide as a function of pH. *International Journal of Chemical Kinetics*, 29(4):261–267, 1997.

[113] M.J. Nicol and C.R.S. Needes. The anodic dissolution of uranium dioxide—I in perchlorate solutions. *Electrochimica Acta*, 20(8):585–589, 1975.

[114] J. Engelhardt, F. Feldmaier, M. Laske, and G. Marx. Impedance measurements on U02+ x in saturated NaC1 solutions. *Journal of Nuclear Materials*, 238:104–109, 1996.

[115] I Grenthe, J Fuger, R.J Konings, A.B Muller, C Nguyen-Trung, and H Wanner. *Chemical Thermodynamics of Uranium*. Nuclear Energy Agency, 2004.

[116] W.H Hocking, J.S Betteridge, and D.W Shoesmith. The Cathodic Reduction of Dioxygen on Uranium Oxide in Dilute Alkaline Aqueous Solution. Technical report, Atomic Energy of Canada Ltd, 1991.

[117] J.S Betteridge, N.A.M Scott, D.W Shoesmith, L.E Bahen, W.H Hocking, and P.G Lucuta. Effects of Hyperstoichiometry and Fission Products on the Electrochemical Reactivity of UO2 Nuclear Fuel. Technical report, Atomic Energy of Canada Ltd., 1997.

[118] M. E. Torrero, I. Casas, J. de Pablo, L. Duro, and J. Bruno. Oxidative dissolution mechanism of uranium dioxide at 25C. In *Goldschhmidt Conference*, Toulouse, 1998. MINERALOGICAL MAGAZIN.

[119] D.W Shoesmith, S. Sunder, L. Johnson, and M. Bailey. Oxidation of Candu UO2 Fuel by the Alpha-Radiolysis Products of Water. In *MRS Proceedings*, page 309, 1985.

[120] J. Gimenez, E. Baraj, M.E. Torrero, I. Casas, and J. de Pablo. Effect of H202, NaC10 and Fe on the dissolution of unirradiated UO 2 in NaC1 5

mol kg-1. Comparison with spent fuel dissolution experiments. *Journal of Nuclear Materials*, 238:64–69, 1996.

[121] D.W Shoesmith and S Sunder. An electrochemistry-based model for the dissolution of UO2. Technical report, SWEDISH NUCLEAR FUEL AND WASTE MANAGEMENT CO, 1991.

[122] F. Clarens, J. de Pablo, I. Casas, J. Gimenez, and M. Rovira. The oxidative dissolution of unirradiated UO2 by hydrogen peroxide as a function of pH. *Journal of Nuclear Materials*, 345:225–231, 2005.

[123] M Amme, B Renker, B Schmid, M.P Feth, H Bertagnolli, and W Döbelin. Raman microspectrometric identification of corrosion products formed on UO2 nuclear fuel during leaching experiments. *Journal of Nuclear Materials*, 306(2-3):202–212, dec 2002.

[124] C. Corbel, G. Sattonnay, S. Guilbert, F. Garrido, M.-F. Barthe, and C. Jegou. Addition versus radiolytic production effects of hydrogen peroxide on aqueous corrosion of UO2. *Journal of Nuclear Materials*, 348(1-2):1–17, jan 2006.

[125] National Nuclear Laboratory. Personal Communications with D.I. Hambley, 2017.

[126] S. Meca, V. Marti, J. de Pablo, J. Gimenez, and I. Casas. UO2 dissolution in the presence of hydrogen peroxide at pH > 11. *Radiochim. Acta*, 96:535–539, 2008.

[127] G.F Thomas and G Till. The Dissolution of Unirratiated UO2 Fuel Pellets under Simulated Disposal Conditions. *Nuclear and Chemical Waste Management*, 5:141–147, 1984.

[128] M-P Lahalle, R Guillaumont, and G.C Allen. Surface Behaviour of Uranium Dioxide after Immersion in Mineral Water studied by X-Ray Photoelectron

Spectroscopy. *Journal of the Chemical Society Faraday Transactions*, 86(14):2641–2644, 1990.

[129] O.N Batuk, S.N Kalmykov, V.V Krivetsov, M Klimenkov, and E.V Zakharova. Oxidation Behavior of Uranium Dioxide Powder Samples in Simulated Groundwater under Different Temperatures. In *Programme and Abstracts 38 Journees des Actinides together with the 7 School on the Physics and Chemistry of the Actinides*, page 140. 2008.

[130] Hj Matzke. Analysis of the structure of layers on UO2 leached in H2O. *Journal of Nuclear Materials*, 238:58–63, 1996.

[131] P.D.W. Bottomley, D.H. Wegen, and M. Coquerelle. Construction of an electrode for irradiated UO 2 fuel and preliminary results concerning its use in aqueous solutions. *Journal of Nuclear Materials*, 238:23–37, 1996.

[132] D.W Shoesmith, S Sunder, M.G Bailey, and N.H Miller. Corrosion of used nuclear fuel in aqueous perchlorate and carbonate solutions. *Journal of Nuclear Materials*, 227:287–299, 1996.

[133] S.A. Steward and W.J. Gray. Comparison of Uranium Dissolution Rates from Spent Fuel and Uranium Dioxide. In *International High Level Radioactive Waste Management Conference, American Nuclear Society*, 1994.

[134] P.G. Lucuta, Hj. Matzke, R.A. Verrall, and H.A. Tasman. Thermal conductivity of SIMFUEL. *Journal of Nuclear Materials*, 188:198–204, 1992.

[135] H He, P.G Keech, M.E Broczkowski, J.J Noël, and D.W Shoesmith. Characterization of the influence of fission product doping on the anodic reactivity of uranium dioxide. *Canadian Journal of Chemistry*, 85(10):702–713, 2007.

[136] Z Hiezl, D.I. Hambley, C Padovani, and W.E. Lee. Processing and microstructural characterisation of a UO 2 -based ceramic for disposal studies on spent AGR fuel. *Journal of Nuclear Materials*, 456:74–84, 2015.

[137] D.W Shoesmith. The Role of Dissolved Hydrogen on the Corrosion/Dissolution of Spent Nuclear Fuel. Technical report, Nuclear Waste Management Organisation, 2008.

[138] M Razdan and D.W Shoesmith. Influence of Trivalent-Dopants on the Structural and Electrochemical Properties of Uranium Dioxide (UO 2). *Journal of The Electrochemical Society*, 161(3):105–113, 2014.

[139] J . V. C Rum, D. M. S Trachan, and M. Zumhoff. Initial Evaluation of Processing Methods for an Epsilon Metal Waste Form - PNNL-21350. Technical report, Pacific Northwest National Laboratories, 2012.

[140] G. F. Álvarez, M. Mamlouk, and K. Scott. An Investigation of Palladium Oxygen Reduction Catalysts for the Direct Methanol Fuel Cell. *International Journal of Electrochemistry*, 2011:1–12, 2011.

[141] J.W Lee and B.N Popov. Ruthenium-based electrocatalysts for oxygen reduction reaction-a review. *Journal of Solid State Electrochemistry*, 11(10):1355–1364, 2007.

[142] J. S. Goldik, J. J. Noël, and D. W Shoesmith. The Effects of Simulated Fission Products in the Reduction of Hydrogen Peroxide on Simulated Nuclear Fuel Electrodes. *Journal of The Electrochemical Society*, 153:151–159, 2006.

[143] M Trummer, S Nilsson, and M Jonsson. On the effects of fission product noble metal inclusions on the kinetics of radiation induced dissolution of spent nuclear fuel. *Journal of Nuclear Materials*, 378(1):55–59, 2008.

[144] S Nilsson and M Jonsson. On the catalytic effect of Pd(s) on the reduction of UO22+ with H2 in aqueous solution. *Journal of Nuclear Materials*, 374:290–292, 2008.

[145] C.M. Lousada, M Trummer, and M Jonsson. Reactivity of H2O2 towards different UO2-based materials: The relative impact of radiolysis products revisited. *Journal of Nuclear Materials*, 434:434–439, 2013.

[146] M E Broczkowski, P G Keech, J J Noël, and D W Shoesmith. The role of dissolved hydrogen on rare earth-doped uranium dioxide corrosion in the presence of hydrogen peroxide. *Journal of the Electrochemical Society*, 158(12):C439–C444, 2011.

[147] N Rauff-Nisthar, C Boxall, D.I Hambley, Z Hiezl, W.E Lee, C Padovani, and R.J Wilbraham. Corrosion Behaviour of AGR SIMFUELS. *ECS Trans.*, 66(17):85–94, 2015.

[148] D.A. Miller and J.A. Roscow. A Heat Treatment Procedure to Produce Small Grain Size Artificially Sensitised Structure in CAGR Fuel Cladding. Technical report, CEGB, 1983.

[149] T.C. Underwood. The Sensitization of Agr Fuel Cladding. Technical report, CEGB, 1982.

[150] M. Deighton. No Title. *The Journal of the Iron and Steel Institute*, 205:535, 1967.

[151] Outokumpu. High Temperature Austenitic Stainless Steel - Technical Report. Technical report, https://www.outokumpu.com/en/austenitic-grades, 2013.

[152] Aalco. Stainless Steel Data Sheet 304H. Technical report, http://www.aalco.co.uk/datasheets/?gId=5, 2015.

[153] Atlas Steels. Grade Data Sheet 304, 304L, 304H. Technical report, http://www.atlassteels.com.au/, 2011.

[154] A.F. Alshater. *Intergranular corrosion of sensitized 20Cr-25Ni-Nb stainless steel nuclear fuel cladding material.* PhD thesis, Manchester University, 2010.

[155] S. Sunder, L.K. Strandlund, and D.W. Shoesmith. Anodic Dissolution of UO2 in Slightly Alkaline Sodium Perchlorate Solutions. Technical report, Atomic Energy of Canada Limited, 1996.

[156] D. Sawyer, A. Sobkowiak, and J. Roberts. *Electrochemistry for Chemists.* Wiley-Interscience, 2nd editio edition, 1995.

[157] L Albright. *Albright's Chemical Engineering Handbook.* CRC Press, 2008.

[158] F Scholz. *Electroanalytical Methods: Guide to Experiments and Applications.* Springer Science and Business Media, 2009.

[159] T.J.A. Richardson. *Shreir's Corrosion.* Elsevier, 2009.

[160] ASTM International. Standard Practices for Detecting Susceptibility to Intergranular Attack in Austenitic Stainless Steels- A262. Technical report.

[161] T. Amadou, H. Sidhom, and C. Braham. Double loop electrochemical potentiokinetic reactivation test optimization in checking of duplex stainless steel intergranular corrosion susceptibility. *Metallurgical and Materials Transactions A*, 35(11):3499–3513, 2004.

[162] R Baboian, editor. *Corrosion Tests and Standards: Application and Interpretation.* ASTM International, 2nd editio edition, 2005.

[163] ASTM International. Standard Test Method for Electrochemical Reactivation (EPR) for Detecting Sensitization of AISI Type 304 and 304L Stainless Steels - ASTM G108.

[164] S Krause. Impedance Methods. In *Encyclopedia of Electrochemistry.* Wiley-VCH Verlag GmbH & Co. KGaA, 2007.

[165] NPTEL. *Fuel Cell Technology: In-situ characterization.* http://nptel.ac.in/courses/103102015/fuel cell characterization/in situ characterization.html, 2012.

[166] K.M Chew, R Sudirman, N Seman, and C.Y Yong. Relaxation frequency and relaxation time estimation for phantom modeling by proposed fitting linear models. *2012 IEEE-EMBS Conference on Biomedical Engineering and Sciences, IECBES 2012*, (December):911–915, 2012.

[167] C.M.A Brett and A.M.O Brett. *Electrochemistry: Principles, Methods and Applications*. New York: Oxford University Press Inc., 1993.

[168] Libretexts. *Fermi Energy Levels*. https://photon.libretexts.org/.

[169] Libretexts. Chapter 10: Electronic Properties of Materials: Superconductors and Semiconductors. In *Inorganic Chemistry*. https://chem.libretexts.org/Textbook_Maps/Inorganic_Chemistry/, 2016.

[170] K Rajeshwar. Fundamentals of Semiconductor Electrochemistry and Photoelectrochemistry. In A. J. Bard, editor, *Encyclopedia of Electrochemistry*. 2007.

[171] I. Tiginyanu, S. Langa, H. Foell, and V. Ursachi. *Space Charge Layer in Semiconductors -Porous III-V Semiconductors*. http://www.porous-35.com/electrochemistry-semiconductors-8.html, 2009.

[172] A.S. J. L Bachmeier. *Metalloenzymes as Inspirational Electrocatalysts for Artificial Photosynthesis: From Mechanism to Model Devices*. Springer, 2016.

[173] UniversityofUlm. *The semiconductor-electrolyte interface*. Https://www.uni-ulm.de/fileadmin/website_uni_ulm/nawi.inst.251/Lehre/.

[174] Nanoscience Instruments. *Scanning Electron Microscopy*. https://www.nanoscience.com/techniques/scanning-electron-microscopy/.

[175] *Encyclopaedia Britannica*. https://www.britannica.com/technology/scanning-electron-microscope.

[176] R Smart, S McIntyre, M Bancroft, and I Bello. X-ray Photoelectron Spectroscopy ray Photoelectron Spectroscopy.

[177] P van der Heide. *X-ray Photoelectron Spectroscopy: An introduction to Principles and Practices.* John Wiley and Sons, 2012.

[178] Nanophoton. *What is Raman Spectroscopy?* https://www.nanophoton.net/raman/raman-spectroscopy.html.

[179] BW-TEK. *Theory of Raman Scattering.* http://bwtek.com/raman-theory-of-raman-scattering/.

[180] F Adar. *Depth Resolution of the Raman Microscope: Optical Limitations and Sample Characteristics.* 2010.

[181] F. Pointurier and O. Marie. Identification of the chemical forms of uranium compounds in micrometer-size particles by means of micro-Raman spectrometry and scanning electron microscope. *Spectrochimica Acta - Part B Atomic Spectroscopy*, 65(9-10):797–804, 2010.

[182] C.M. Chan, D.L. Engelberg, and W.S. Walters. Performance Characterisation of AGR Fuel Cladding Relevant to Long-term in-Pond Storage in pH-moderated Aqueous Environment. In *Reactor Fuel Performance - TopFuel 2015 Proceedings - Part II.*, pages 120–129, 2015.

[183] A.V Naumkin, A Kraut-Vass, S.W Gaarenstroom, and C.J Powell. NIST X-ray Photoelectron Spectroscopy Database: NIST Standard Reference Database 20, Version 4.1, 2012.

[184] J. J. Yeh and I. Lindau. Atomic subshell photoionization cross sections and asymmetry parameters: 1 - Z -103. *Atomic Data and Nuclear Data Tables*, 32(1):1–155, 1985.

[185] B Beverskog and I Puigdomenech. Pourbaix Diagrams for the Ternary System of Iron-Chromium-Nickel. *Corrosion*, 55(11):1077–1087, 1999.

[186] T.E Jones, T.C.R. Rocha, A Knop-Gericke, C Stampfl, R Schlögl, and S Piccinin. Insights into the Electronic Structure of the Oxygen Species Active in Alkene Epoxidation on Silver. *ACS Catalysis*, 5(10):5846–5850, 2015.

[187] J.M Francis. Structure of Surface Oxides formed on a 20%Cr/25%Ni/Nb-Stabilised Steel in Carbon Dioxide at High Temperatures. *British Corrosion Journal*, 3:113–119, 1968.

[188] I Betova, M Bojinov, T Laitinen, K Mäkelä, P Pohjanne, and T Saario. The transpassive dissolution mechanism of highly alloyed stainless steels I. Experimental results and modelling procedure. *Corrosion Science*, 44(12):2675–2697, 2002.

[189] S Zhang, H Zhao, F Shu, W He, and G Wang. Microstructure and Corrosion Behavior of Simulated Welding HAZ of Q315NS Steel in Sulfuric Acid Solution. *Metals*, 7(6):194, 2017.

[190] N Mahato and M. M.Singh. Investigation of Passive Film Properties and Pitting Resistance of AISI 316 in Aqueous Ethanoic Acid Containing Chloride Ions using Electrochemical Impedance Spectroscopy(EIS). *Portugaliae Electrochimica Acta*, 29(4):233–251, 2011.

[191] H. Luo, C. F. Dong, X. G. Li, and K. Xiao. The electrochemical behaviour of 2205 duplex stainless steel in alkaline solutions with different pH in the presence of chloride. *Electrochimica Acta*, 64:211–220, 2012.

[192] J Pan, C Leygraf, R.F.A. Jargelius-Pettersson, and J Linden. Characterization of High-Temperature Oxide Films on Stainless Steels by Electrochemical-Impedance Spectroscopy. *Oxidation of Metals*, 50:431–455, 1998.

[193] H Luo, H Su, C Dong, K Xiao, and X Li. Electrochemical and passivation behavior investigation of ferritic stainless steel in simulated concrete pore media. *Data in Brief*, 5:171–178, 2015.

[194] X Zhang, G Xiao, C Jiang, B Liu, N Li, R Zhu, and Y Lu. Influence of process parameters on microstructure and corrosion properties of hopeite coating on stainless steel. *New Journal of Chemistry*, 39:5813–5822, 2015.

[195] R Zhang, L Wang, and W Shi. Variable corrosion behavior of a thick amorphous carbon coating in NaCl solution. *RSC Advances*, 5(116):95750–95763, 2015.

[196] C. J. Li and M. Du. The growth mechanism of calcareous deposits under various hydrostatic pressures during the cathodic protection of carbon steel in seawater. *RSC Advances*, 7(46):28819–28825, 2017.

[197] R Blair, B Pesic, J Kline, I Ehrsam, and K Raja. Threshold chloride concentrations and passivity breakdown of rebar steel in real concrete solution at different pH conditions with the addition of glycerol. *Acta Metallurgica Sinica English Letters*, 30(4):376–389, 2017.

[198] T.P. Moffat and R.M. Latanision. An Electrochemical and X-Ray Photoelectron Spectroscopy Study of the Passive State of Chromium. *Journal of The Electrochemical Society*, 139(7):1869–1879, 1992.

[199] M. Metikoš-Huković and M Ceraj-Ceric. p-Type and n-Type Behavior of Chromium Oxide as a Function of the Applied Potential. *Journal of the Electrochemical Society*, 134(9):2193–2197, 1987.

[200] J.A. Bastos, M.R. Barbosa, J. Gregori, J.J. García-Jareño, and F. Vicente. Nickel Mouldable Electrodes: Mott-Schottky Analysis of Ni(OH)2 Deposited Layers on Nickel Powder-Epoxy Resin Composite Electrodes. *ECS Transactions*, 6(8):229–243, 2007.

[201] Z. Grubač, Ž. Petrovića, J. Katića, M. Metikoš-Hukovića, and R. Babića. The electrochemical behaviour of nanocrystalline nickel: A comparison with polycrystalline nickel under the same experimental condition. *Journal of Electroanalytical Chemistry*, 645(2):87–93, 2010.

[202] X.H Chan, J.R Jennings, M.A Hossain, K.K.Z Yu, and Q Wang. Characteristics of p-NiO Thin Films Prepared by Spray Pyrolysis and Their Application in CdS-sensitized Photocathodes. *Journal of The Electrochemical Society*, 158(7):H733–H740, 2011.

[203] S Seo, I.J Park, M Kim, S Lee, C Bae, H.S Jung, N-G Park, J.Y Kim, and H Shin. An ultra-thin, un-doped NiO hole transporting layer of highly efficient (16.4%) organic–inorganic hybrid perovskite solar cells. *Nanoscale*, 8(22):11403–11412, 2016.

[204] J Williamson and O. B Isgor. The effect of simulated concrete pore solution composition and chlorides on the electronic properties of passive films on carbon steel rebar. *Corrosion Science*, 106:82–95, may 2016.

[205] M. da Cunha Belo, B. Rondot, C. Compere, M.F. Montemor, A.M.P. Simões, and M.G.S. Ferreira. Chemical composition and semiconducting behaviour of stainless steel passive films in contact with artificial seawater. *Corrosion Science*, 40(2-3):481–494, feb 1998.

[206] I Olefjord and B.O. Elfstrom. The Composition of the Surface during Passivation of Stainless Steels. *Corrosion*, 38(1):46–52, 1982.

[207] Z Wang, P.K. Nayak, J.A. Caraveo-Frescas, and H.N Alshareef. Recent Developments in p-Type Oxide Semiconductor Materials and Devices. *Advanced Materials*, 28:3831–3892, 2016.

[208] E Stefan. *Development of spinel-based electrode supports for solid oxide fuel cells.* PhD thesis, University of St. Andrews, 2013.

[209] M Stoica and C.S Lo. P-type zinc oxide spinels: application to transparent conductors and spintronics. *New Journal of Physics*, 16:5, 2014.

[210] FHWA. An FHWA Special Study: Post-Tensioning Tendon Grout Chloride Thresholds. Technical Report FHWA-HRT-14-039, Federal Highway Administration, 2014.

[211] S. Jin and A. Atrens. ESCA-studies of the structure and composition of the passive film formed on stainless steels by various immersion times in 0.1 M NaCl solution. *Applied Physics A Solids and Surfaces*, 45:83–91, 1988.

[212] S E Ziemniak, M E Jones, and K E S Combs. Solubility and Phase Behavior of Cr (III) Oxides in Alkaline Media at Elevated Temperatures. *Journal of Solution Chemistry*, 27(1):33–65, 1998.

[213] C.J. Donohoe. The effect of ionising radiation on the corrosion resistance of ILW containers. Technical report, National Nuclear Laboratory, 2009.

[214] *Instrumental methods in electrochemistry*. Southampton Electrochemistry Group, Ellis Horwood, 1990.

[215] A.J Bard and L.R Faulkner. *Electrochemical Methods: Fundamentals and Applications*. John Wiley & Sons, Inc., 2nd edition, 2001.

[216] S.B Hall, E.A Khudaish, and A.L Hart. Electrochemical oxidation of hydrogen peroxide at platinum electrodes. Part 1. An adsorption-controlled mechanism. *Electrochimica Acta*, 43(5-6):579–588, 1997.

[217] L Gorton. A carbon electrode sputtered with palladium and gold for the amperometric detection of hydrogen peroxide. *Analytica Chimica Acta*, 178:247–253, 1985.

[218] C Yu, T.D Nguyen, J Zhang, and D.J Young. Sulfur Effect on Corrosion Behavior of Fe-20Cr-(Mn, Si) and Fe-20Ni-20Cr-(Mn, Si) in CO2-H2O at 650C. *Journal of The Electrochemical Society*, 163(3):C106–C115, 2016.

[219] T Gheno, D Monceau, J Zhang, and D.J Young. Carburisation of ferritic FeCr alloys by low carbon activity gases. *Corrosion Science*, 53:2767–2777, 2011.

[220] D Macdonald Digby, K.M Ismail, and E Sikora. Characterization of the Passive State on Zinc. *Journal the Electrochemical Society*, 145(9):3141–3149, 1998.

[221] S.S Kulkarni and C.D Lokhande. Structural, optical, electrical and dielectrical properties of electrosynthesized nanocrystalline iron oxide thin films. *Materials Chemistry and Physics*, 82(1):151–156, 2003.

[222] K Nomura and Y Ujihira. Analysis of oxide layers on stainless steel (304 , and 316) by conversion electron Mossbauer spectrometry. *Journal of Material Science*, 25:1745–1750, 1990.

[223] M.W.A Rashid, M Gakim, Z.M Rosli, and M.A Azam. Formation of Cr23C6 during the sensitization of AISI 304 stainless steel and its effect to pitting corrosion. *International Journal of Electrochemical Science*, 7(10):9465–9477, 2012.

[224] R.C. Woodhouse, R.J Wilbraham, and C Boxall. Fixed Contamination on Steel Surfaces: First Use of Quartz Crystal Microgravimetry to Measure Oxide Growth on Process Steels Under Conditions Typical of Nuclear Reprocessing. *MRS Proceedings*, 1383:mrsf11–1383–a07–04, jan 2012.

[225] G.H Kelssall, C.I House, and F.P Gudyanga. Chemical and electrochemical equilibria and kinetics in aqueous Cr(III)/Cr(II) Chloride solutions. *Journal of Electroanalytical Chemistry and Interfacial Electrochemistry*, 244(1-2):179–202, apr 1988.

[226] M.D Asaduzzaman, C Mohammad, and I Mayeedul. Effects of concentration of sodium chloride solution on the pitting corrosion behavior of AISI 304L

austenitic stainless steel. *Chemical Industry and Chemical Engineering Quarterly*, 17(4):477–483, 2011.

[227] K.K. Sagoe-Crentsil and F.P. Glasser. "Green rust", iron solubility and the role of chloride in the corrosion of steel at high pH. *Cement and Concrete Research*, 23(4):785–791, 1993.

[228] P.M Gil, M Palomar-Pardavé, M de Oca-Yemha, M Guadalupe, M.T Ramírez-Silva, C Ángeles-Chávez, and M Romero-Romo. Effect of carbonate and chloride ions on the corrosion susceptibility of pipeline steel samples artificially aged. *International Journal of Electrochemical Science*, 13(2):1844–1858, 2018.

[229] R.N Clark. *Mapping of corrosion sites in advanced gas-cooled reactor fuel cladding for long term pond storage*. PhD thesis, Swansea University, 2018.

[230] B MacDougall and M Cohen. Anodic Oxidation of Nickel in Neutral Sulfate Solution. *Journal of The Electrochemical Society*, 121(9):1152–1159, 1974.

[231] C. Q. Cui and J.Y. Lee. Nickel deposition from unbuffered neutral chloride solutions in the presence of oxygen. *Electrochimica Acta*, 40(11):1653–1662, 1995.

[232] C. Albu, D. Deconinck, L. Hotoiu, J. Deconinck, and V. Topa. Steady-state analysis of the nickel oxide in neutral and weakly alkaline solutions. *Electrochimica Acta*, 89:114–121, 2013.

[233] M Okuyama and S Haruyama. Passive film formed on nickel in a neutral solution. *Corrosion Science*, 14(1):1–14, 1974.

[234] N Attarzadeh and A. Fattah-Alhosseini. The Mechanism of Transpassive Dissolution of AISI 321 Stainless Steel in Sulphuric Acid Solution. *International Journal of Electrochemistry*, 2011, 2011.

[235] J Stewart and D.E Williams. The initiation of pitting corrosion on austenitic stainless steel: on the role and importance of sulphide inclusions. *Corrosion Science*, 33(3):457–474, 1992.

[236] M.A Baker. *Investigation into the Initiation of Pitting Corrosion on Stainless Steels using Auger Electron Spectroscopy*. PhD thesis, University of Surrey, 1990.

[237] D.G Li, Y.R Feng, Z.Q Bai, J.W Zhu, and M.S Zheng. Influence of temperature, chloride ions and chromium element on the electronic property of passive film formed on carbon steel in bicarbonate/carbonate buffer solution. *Electrochimica Acta*, 52(28):7877–7884, 2007.

[238] N.N Krot, V.P Shilov, A.M Fedoseev, N.A Budantseva, M.V Nikonov, A.B Yusov, A.Yu Garnov, I.A Charushnikova, V.P Perminov, L.N Astafurova, T.S Lapitskaya, and V.I Makarenkov. Development of Alkaline Oxidative Dissolution Methods for Chromium(III) Compounds Present in Hanford Site Tank Sludges. Technical report, PNNL, 1999.

[239] N Usui, M Fuse, H Hosokawa, and S Uchida. Effects of Hydrogen Peroxide on Radioactive Cobalt Deposition on Stainless Steel Surface in High Temperature Water. 42(1):75–81, 2005.

[240] WorldWideScience.org. *Sample records for nickel ferrite NiFe2O4*. https://worldwidescience.org/topicpages/n/nickel+ferrite+nife2o4.html.

[241] A Orlov. *Corrosion Product Deposition on Fuel Element Surfaces of a Boiling Water Reactor*. PhD thesis, 2011.

[242] M Sadiq. *Toxic Metal Chemistry in Marine Environments*. CRC Press, 1992.

[243] R. J. Wilbraham, N. Rauff-Nisthar, C. Boxall, E. Howett, D. Hambley, Z. Hiezl, W. Lee, and C. Padovani. Raman Studies of Advanced Gas-Cooled Reactor Simulated Spent Nuclear Fuels. *Progress in Nuclear Science and Technology*, pages 213–216, 2018.

[244] J Lee, J Kim, Y Youn, N Liu, J Kim, Y Ha, D.W Shoesmith, and J Kim. Raman study on structure of U1-yGdyO2-x (y=0.005,0.01, 0.03, 0.05 and 0.1) solid solutions. *Journal of Nuclear Materials*, 486:216–221, 2017.

[245] L Desgranges, Y Pontillon, P Matheron, M Marcet, P Simon, G Guimbretie, C E A D E N Dec, Bat Cadarache, and Saint Paul. Miscibility Gap in the U- Nd-O Phase Diagram : a New Approach of Nuclear Oxides in the Environment? *Inorganic Chemistry*, 51:9147–9149, 2012.

[246] Z Talip, T Wiss, P.E Raison, J Pallier, D Manara, J Somers, and R.J.M Konings. Raman and X-ray Studies of Uranium–Lanthanum-Mixed Oxides Before and After Air Oxidation. *Journal of the American Ceramic Society*, 98(7):2278–2285, 2015.

[247] L Desgranges, G Baldinozzi, P Simon, G Guimbretiere, and A Canizares. Raman spectrum of U4O9: a new interpretation of damage lines in UO2. *Journal of Raman Spectroscopy*, 43(3):455–458, 2011.

[248] S. Sunder, D. W. Shoesmith, M. G. Bailey, F. W. Stanchell, and N. S. McIntyre. Anodic oxidation of UO2. Part I. Electrochemical and X-ray photoelectron spectroscopic studies in neutral solutions. *Journal of Electroanalytical Chemistry and Interfacial Electrochemistry*, 130:163–179, 1981.

[249] S Sunder, D.W. Shoesmith, M.G. Bailey, and G.J. Wallace. Anodic oxidation of UO2: Part II. Electrochemical and X-ray photoelectron spectroscopic studies in alkaline solutions. *Journal of Electroanalytical Chemistry and Interfacial Electrochemistry*, 150:217–228, 1983.

[250] M.E Broczkowski, J.J Noel, and D W Shoesmith. The inhibiting effects of hydrogen on the corrosion of uranium dioxide under nuclear waste disposal conditions. *Journal of Nuclear Materials*, 346:16–23, 2005.

[251] I Puigdomenech. Hydra/Medusa Chemical Equilibrium Database and Plotting Software, 2004.

[252] L.E. Thomas, R.E. Einziger, and H.C. Buchanan. Effect of fission products on air-oxidation of LWR spent fuel. *Journal of Nuclear Materials*, 201:310–319, 1993.

[253] J.T. Waber. A Review of the Corrosion Behavior of Uranium. Technical report, Los Alamos Scientific Lab, 1956.

[254] J.S Morrell and M.J Jackson. *Uranium Processing and Properties*. Springer New York, New York, NY, 2013.

[255] R.K Willardson, J.W Moody, and H.L Goerin. The Electrical Properties of Uranium Oxides. *Journal of Inorganic and Nuclear Chemistry*, 6(1):19–33, 1958.

[256] S. Roy Morrison. *Electrochemistry at Semiconductor and Oxidized Metal Electrodes*. Plenum Press, 1980.

[257] W.H Hocking, D.W Shoesmith, and J.S Betteridge. Reactivity effects in the oxidative dissolution of UO2 nuclear fuel. *Journal of Nuclear Materials*, 190:36–45, 1992.

[258] R Memming. Processes at Semiconductor Electrodes. In *Comprehensive Treatise of Electrochemistry - Vol 7*, page 529. 1983.

[259] J Cai and D. F. Gervasio. The nature of surface oxides on corrosion-resistant nickel alloy covered by alkaline water. *Nanoscale Research Letters*, 5(3):613–619, 2010.

[260] P Lu, S Sharifi-Asl, B Kursten, and D.D. Macdonald. The Irreversibility of the Passive State of Carbon Steel in the Alkaline Concrete Pore Solution under Simulated Anoxic Conditions. *Journal of The Electrochemical Society*, 162(10):572–581, 2015.

[261] Resources for Electrochemistry. *Inductance.* http://www.consultrsr.net/resources/eis/induct1.htm.

[262] X Yong and M.A.A. Schoonen. The absolute energy positions of conduction and valence bands of selected semiconducting minerals. *American Mineralogist*, 85(3-4):543–556, 2000.

[263] S Al-Hilli and M Willander. The pH response and sensing mechanism of n-type ZnO/electrolyte interfaces. *Sensors*, 9:7445–7480, 2009.

[264] T. L. Martin, C. Coe, P. A.J. Bagot, P. Morrall, G. D.W. Smith, T. Scott, and M. P. Moody. Atomic-scale Studies of Uranium Oxidation and Corrosion by Water Vapour. *Scientific Reports*, 6(October 2015):1–10, 2016.

[265] R J McEachern and P Taylor. A Review of the Oxidation of Uranium Dioxide at Temperatures Below 400 C. Technical Report January, AECL, 1997.

[266] W Siekhaus and J Crowhurst. Optical Propertiesof a Mechanically Polished and Air-Equilibrated [111] UO2 Surface by Raman and Ellipsometric Spectroscopy. *IOP Conference Series: Materials Science and Engineering*, 9(1), 2010.

[267] O.L Gaskova and M.B Bukaty. Solubility of Uranium Dioxide during Underground Disposal of Radioactive Wastes and Spent Nuclear Fuel. *Chemistry for Sustainable Development*, 12:649–655, 2004.

[268] K Ollila. Solubility of UO2 in the High pH Range in 0.01 to 0.1 M NaCl Solution Under Reducing Conditions. Technical report, Posiva, 2008.

[269] R.K Wild. Surface Analysis in an industrial Environment. *Analytical Proceedings*, 30:19–27, 1993.

[270] G. C. Allen, P. A. Tempest, J. W. Tyler, and R. K. Wild. Oxidation behavior of 20%Cr/25%Ni/Nb stabilized stainless steel in CO2 environments. *Oxidation of Metals*, 21(3-4):187–203, 1984.

Appendix A

Outer Surface Behaviour of Unsensitised 20/25/Nb SS in Simulant Pond Water

Figure A.1 shows the effect of simulant pond water temperature variations on the corrosion behaviour of the surface of the unsensitised 20/25/Nb SS cladding, as opposed to the cross-section which has been interrogated throughout the thesis. The differences in behaviour between the outer surface and the cross section are as follows. For all temperatures studied, E_{ZC} is more negative for the cross section sample than for the surface sample. At room temperature general corrosion currents are lower in the case of the cross section samples, transpassive currents are higher for the surface sample and the onset of transpassivity occur at approximately the same potential. For T$\geq$45 °C, general corrosion and transpassive currents are greater for the cross section sample than for the surface sample and the onset of transpassivity is more negative in the case of the cross section sample. Overall the corrosion behaviour of the cross section sample in simulant pond water is largely representative of that of the surface sample in the same conditions and where significant differences exist the cross section sample offers a conservative view of the cladding behaviour.
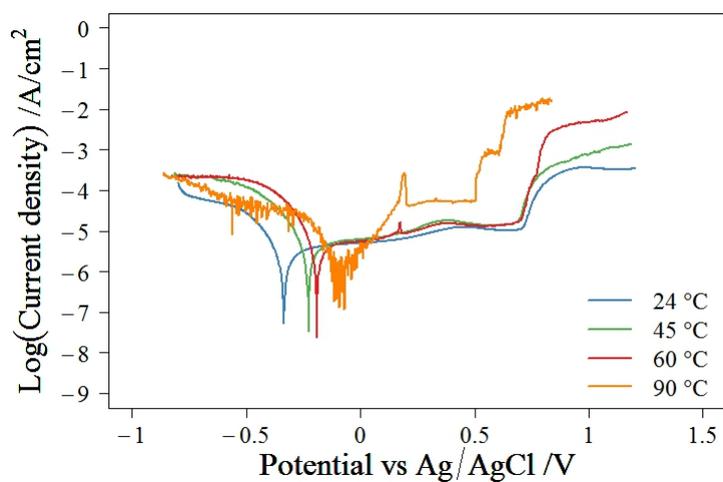
Figure A.1: The effect of simulant pond water temperature on the corrosion behaviour of the outer surface of 20/25/Nb SS, pH$\simeq$11.4 at 24 °C.

Appendix B

Resistance and Capacitance Data for UO_2 and SIMFuels

Potential	R_s	R_{UO_2}	CPE_{UO_2}	R_p	$CPE_{SC/UO2+x}$
-1.5	326	1200	1.26×10^{-8}	18838	2.15×10^{-5}
-1.4	320	1215	2.36×10^{-8}	22496	0.00015134
-1.3	320	1215	1.55×10^{-8}	27765	0.00033779
-1.2	326	1210	2.99×10^{-8}	4.63×10^{11}	0.00038225
-1.1	326	1210	2.92×10^{-8}	3.42×10^{11}	0.00063017
-1	326	1210	2.84×10^{-8}	1.05×10^{11}	0.0011383
-0.9	334	1210	1.86×10^{-8}	4.94×10^{10}	0.0020454
-0.8	330	1220	2.92×10^{-8}	3.13×10^{10}	0.0028354
-0.7	330	1220	2.79×10^{-8}	5.27×10^{10}	0.0030976
-0.6	330	1228	2.78×10^{-8}	1.30×10^{10}	0.0032577
-0.5	334	1230	2.81×10^{-8}	3.50×10^{10}	0.00326
-0.4	334	1240	2.81×10^{-8}	5.56×10^{10}	0.0030464
-0.3	334	1250	2.75×10^{-8}	1.08×10^{11}	0.0025534
-0.2	334	1250	2.59×10^{-8}	2.57×10^{11}	0.0021138
-0.1	334	1250	2.39×10^{-8}	4.50×10^{11}	0.0020157
0	334	1255	2.41×10^{-8}	1.18×10^{11}	0.0020658
0.1	334	1260	2.30×10^{-8}	5.96×10^{10}	0.0019777
0.2	334	1260	2.27×10^{-8}	9.87×10^{10}	0.0019977
0.3	334	1265	2.35×10^{-8}	4.26×10^{10}	0.0020844
0.4	326	1268	2.18×10^{-8}	6.13×10^{10}	0.0020076

Table B.1: Resistance (Ω) and capacitance (F) data for UO_2 in 0.5 mol dm^{-3} Na_2SO_4.

Potential	R$_s$	R$_{SIM}$	CPE$_{SIM}$	R$_p$	CPE$_{SC/UO2+x}$
-0.9	16.77	22	0.0049898	7.64×10^9	0.0055506
-0.8	16.77	24	0.0058027	$3.10E \times 10^9$	0.0068833
-0.7	16.77	24	0.006039	1.46×10^{10}	0.0074356
-0.6	16.77	24	0.0057617	4.03×10^9 0.0077906	
-0.5	16.77	24	0.0061162	1.18×10^{10}	0.0079663
-0.4	16.77	24	0.0059892	5.01×10^9	0.0076507
-0.3	16.77	24	0.0053884	12406	0.0066205
-0.2	16.77	26	0.0050637	2543	0.0055154
-0.1	16.77	26	0.0045306	2841	0.0048565
0	16.77	26	0.0035868	2.19×10^7	0.0046408
0.1	16.77	22	0.0021606	3.51×10^{10}	0.0042463
0.2	16.77	22	0.0015536	3.37×10^{10}	0.0040149
0.3	16.77	26	0.0021117	4.29×10^9	0.0040917
0.4	16.77	28	0.0023214	18086	0.004109

Table B.2: Resistance (Ω) and capacitance (F) data for the 25 GWd/tU sample in 0.5 mol dm^{-3} Na$_2$SO$_4$.

Potential	R$_s$	R$_{SIM}$	CPE$_{SIM}$	R$_p$	CPE$_{SC/UO2+x}$
-0.9	38.61	0.83053	4.24×10^{-5}	2123	0.0016227
-0.8	38	0.98608	4.95×10^{-5}	21961	0.001596
-0.7	38	1.025	5.21×10^{-5}	49366	0.0014634
-0.6	38	1.04	5.54×10^{-5}	4.97×10^4	0.0013749
-0.5	38	0.94944	5.38×10^{-5}	91380	0.0013782
-0.4	38	0.94944	5.51×10^{-5}	92135	0.0011684
-0.3	38	0.94944	5.81×10^{-5}	47063	0.00093988
-0.2	38	0.99306	5.86×10^{-5}	37629	0.00085701
-0.1	38	0.99306	5.66×10^{-5}	37382	0.00082769
0	38	0.99306	5.77×10^{-5}	47475	0.00078984
0.1	38	0.99306	5.89×10^{-5}	81576	0.00074499
0.2	38	0.99306	5.82×10^{-5}	177810	0.00074344
0.3	38	0.99306	5.53×10^{-5}	28001	0.00079155
0.4	38	0.99306	5.68×10^{-5}	1005	0.00085573

Table B.3: Resistance (Ω) and capacitance (F) data for the 43 GWd/tU sample in 0.5 mol dm^{-3} Na$_2$SO$_4$.

Potential	R_s	R_p	$CPE_{SC/UO_{2+x}}$	R_{ads}	CPE_{ads}	R_{UO_2}	CPE_{UO_2}
-1.5	300	48251	5.75×10^{-5}	6435	6.00×10^{-6}	2573	4.80×10^{-8}
-1.4	300	85217	7.64×10^{-5}	6878	9.15×10^{-6}	2257	4.29×10^{-8}
-1.3	300	742990	0.00011086	6564	1.04×10^{-5}	2137	4.15×10^{-8}
-1.2	300	9.86×10^{11}	0.00018331	6292	1.19×10^{-5}	2029	3.96×10^{-8}
-1.1	300	3.15×10^{11}	0.00035721	5767	1.25×10^{-5}	1999	4.04×10^{-8}
-1	300	1.23×10^{11}	0.00071244	5389	1.30×10^{-5}	1967	3.99×10^{-8}
-0.9	300	52007	0.00086491	5044	1.27×10^{-5}	1931	3.89×10^{-8}
-0.8	300	1.41×10^7	0.00084378	4855	1.16×10^{-5}	1904	3.82×10^{-8}
-0.7	300	35629	0.00088148	4603	9.71×10^{-6}	1938	4.09×10^{-8}
-0.6	300	131630	0.0008876	4478	8.16×10^{-6}	1958	4.27×10^{-8}
-0.5	300	4.36×10^7	0.00072987	4415	6.94×10^{-6}	1991	4.48×10^{-8}
-0.4	300	21691	0.00052879	4408	5.83×10^{-6}	2026	4.73×10^{-8}
-0.3	300	120140	0.00042858	4305	4.59×10^{-6}	2091	5.14×10^{-8}
-0.2	300	53365	0.00040742	4339	4.10×10^{-6}	2138	5.60×10^{-8}
-0.1	300	41402	0.00039806	4257	3.87×10^{-6}	2252	6.32×10^{-8}
0	300	19764	0.00037415	4080	3.74×10^{-6}	2475	7.49×10^{-8}
0.1	300	21602	0.00034007	3807	3.60×10^{-6}	2804	8.77×10^{-8}
0.2	300	16243	0.00028327	3372	3.86×10^{-6}	3371	1.05×10^{-7}
0.3	300	10015	0.00022066	2397	7.15×10^{-6}	4773	1.13×10^{-7}
0.4	300	15160	0.0001659	3267	3.39×10^{-6}	3955	9.38×10^{-8}

Table B.4: Resistance (Ω) and capacitance (F) data for UO_2 in simulant pond water containing 0.5 mol dm^{-3} Na$_2$SO$_4$.

Potential	R$_s$	R$_{SIM}$	CPE$_{SIM}$	R$_p$	CPE$_{SC/UO2+x}$
-0.9	30	20	0.00021079	7061	0.0015553
-0.8	30	20	0.00021586	8724	0.0016218
-0.7	30	20	0.00021978	12444	0.0016613
-0.6	30	20	0.00021974	12937	0.001789
-0.5	30	20	0.00020932	9042	0.0016638
-0.4	30	20	0.00019149	4344	0.0011767
-0.3	30	20	0.00016869	3920	0.00094236
-0.2	30	20	0.00014481	4199	0.00089594
-0.1	30	20	0.00012136	5577	0.00088279
0	30	20	0.00010593	5702	0.00081301
0.1	30	20	9.66×10^{-5}	5327	0.00069907
0.2	30	20	9.16×10^{-5}	4282	0.00059394
0.3	30	20	8.44×10^{-5}	3595	0.00047378
0.4	30	20	7.70×10^{-5}	3641	0.00034827

Table B.5: Resistance (Ω) and capacitance (F) data for the 25 GWd/tU sample in simulant pond water containing 0.5 mol dm^{-3} Na$_2$SO$_4$.

Potential	R$_s$	R$_{SIM}$	CPE$_{SIM}$	R$_p$	CPE$_{SC/UO2+x}$
-0.9	44	1.3	0.00329	242010	0.0010725
-0.8	44	1.3	0.0061643	304250	0.0010974
-0.7	44	1.3	0.0084494	1.88E+05	0.0011246
-0.6	44	1.3	0.011611	87615	0.0011491
-0.5	44	1.3	0.02811	266950	0.0010943
-0.4	44	1.3	2.831	88978	0.00088817
-0.3	44	1.3	0.024993	20604	0.00068763
-0.2	44	1.3	0.026422	20269	0.00059874
-0.1	44	1.3	0.040869	25448	0.00060908
0	44	1.3	0.0062743	29790	0.00062145
0.1	44	1.3	0.0050704	21285	0.00057418
0.2	44	1.3	0.0047295	10417	0.00048335
0.3	44	1.3	0.0043581	5174	0.00041269
0.4	44	1.3	0.0039707	3812	0.00041499

Table B.6: Resistance (Ω) and capacitance (F) data for the 43 GWd/tU sample in simulant pond water containing 0.5 mol dm^{-3} Na$_2$SO$_4$.